POLITECNICO

MILANO 1863

Engineering of titanium oxide and nitride nanostructures for plasmonic applications

Doctoral Dissertation of:
BEATRICE ROBERTA BRICCHI

Advisor:
Prof. Andrea Li Bassi

Tutor:
Prof. Carlo S. Casari

The Chair of the Doctoral Program:
Prof. Vincenzo Dossena

Abstract

Plasmonics is a fascinating field which offers the attractive potential of manipulating light at nanoscale. Plasmonic response occurs when an electromagnetic wave interacts with a metal and, as a consequence, the conduction electrons resonate with the incident electric field, giving rise to collective oscillations. Interesting phenomena involve surface plasmon polaritons (SPP) at metal-dielectric interfaces, and localized surface plasmon resonance (LSPR) in assemblies of metal nanoparticles (NPs), which lead to a strong intensification of the electric field close to the metal surface and the sub-wavelength confinement of light. These peculiar features make plasmonics appealing for several application fields, such as waveguides, sensing, surface enhanced Raman scattering (SERS) and photoconversion (e.g. photocatalysis and photovoltaics), in which plasmonic NPs can enhance the photoresponse of the employed photoanode. However, noble metals are not the best choice for any plasmonic application. Indeed they exhibit high optical losses in the infrared, difficulty in finely tuning their optical properties, poor hardness, low chemical stability and resistance to high temperature, difficulty in the realization of metallic ultrathin films (i.e. <10 nm) and non-compatibility with standard silicon manufacturing process. In response to these limitations, alternative plasmonic materials have been searched. Among them, transparent conductive oxides (TCOs) have demonstrated a tunable plasmonic response in near-IR and mid-IR range depending on carrier density, while transition metal nitrides are refractory, stable and hard materials which provide a tailored plasmonic response in the visible and near-IR range, in principle controlled by stoichiometry and crystalline quality.

This PhD thesis project concerns an experimental investigation for the development of nanostructured thin films based on titanium oxides and nitrides, aimed to achieve a fine control of their physical properties (i.e. morphology, structure, composition) and the understanding of their relation with the material optical and electrical behavior. The specific systems investigated were Au NPs integrated with TiO_2 hierarchical nanostructured thin films (aimed to enhance light harvesting of the oxide for photoanode applications); thin/ultrathin films based on Ta-doped TiO_2 (Ta:TiO_2, a high performance TCO); thin films and NPs assemblies based

on TiN. These systems were grown mainly via pulsed laser deposition, followed by post-deposition thermal treatments to crystallize the materials in the desired phase. Au NPs were uniformly distributed in nanostructured TiO_2 and their LSPR was modulated by means of synthesis conditions and Au content. Conductive $Ta:TiO_2$ thin films were obtained down to a thickness of 10 nm, while the optical response demonstrated to be controlled by doping content, and a first exploration of the optical behavior in IR was performed. For TiN, the tuning of optical response was performed for both compact films and NPs assemblies, and a peculiar condition of broadband absorption was observed for specific synthesis conditions. Finally, the $Au-TiO_2$ system properties were optimized in view of selected plasmonic applications (e.g. SERS and photoconversion), while the resulted tunable optical and electrical behavior of $Ta:TiO_2$ and TiN thin films paves the way to applications usually unaffordable for noble metals (e.g in the IR range or at high temperature/power conditions); moreover they can be employed as building blocks for sub-wavelength optical structures (metameterials) with engineered plasmonic behavior and for nanoelectronics.

Sommario

L'interesse nello studio della plasmonica è dovuto all'attraente possibilità di manipolare la luce alla nanoscala. Quando un'onda elettromagnetica interagisce con un metallo, gli elettroni di conduzione possono entrare in risonanza con il campo elettrico incidente, generando oscillazioni collettive di elettroni chiamati plasmoni. I polaritoni plasmonici di superficie (SPP), che si presentano all'interfaccia metallo-dielettrico, e la risonanza plasmonica di superficie localizzata (LSPR), che si verifica in gruppi di nanoparticelle metalliche, sono due fenomeni interessanti che portano ad una forte intensificazione del campo elettrico vicino alla superficie del metallo e al confinamento della luce al di sotto della sua lunghezza d'onda. Queste caratteristiche rendono la plasmonica accattivante per certe applicazioni, ad esempio per le guide d'onda, i sensori, la spettroscopia Raman amplificata da superfici (SERS) e per la fotoconversione (in fotocatalisi e fotovoltaico), nella quale le nanoparticelle plasmoniche possono contribuire all'aumento dell'efficienza dei fotoanodi.

Nonostante la loro elevata risposta plasmonica nel visibile, i metalli nobili non emergono come i migliori candidati in certe applicazioni. Infatti, risulta difficile regolarne finemente le proprietà ottiche, inoltre presentano perdite ottiche elevate nell'IR, hanno scarsa durezza, stabilità chimica e resistenza alle alte temperature; la realizzazione di film metallici ultra-sottili (cioè <10 nm) non è banale e non sono compatibili con il processo standard per la produzione del silicio. In risposta a questi limiti, sono stati cercati materiali plasmonici alternativi, come gli ossidi conduttivi trasparenti (TCO) e i nitruri di metalli di transizione. I primi hanno dimostrato un comportamento plasmonico nel vicino e medio IR, regolabile attraverso la densità di carica del materiale; i secondi sono materiali refrattari, stabili ad elevata durezza che permettono una risposta plasmonica nel visibile e nel vicino IR controllata dalla stechiometria e della qualità cristallina del materiale.

Questo progetto di dottorato consiste in una ricerca sperimentale per lo sviluppo di film sottili e nanostrutturati basati su ossidi e nitruri di titanio, con l'obiettivo di controllare le loro proprietà (morfologia, struttura e composizione) e di capire la loro relazione con il comportamento elettrico e ottico di questi film. Nello specifico, i sistemi studiati sono: nanoparticelle di oro integrate con film sottili di

ossido di titanio nanostrutturato (Au-TiO$_2$), per aumentare l'assorbimento della luce da parte dell'ossido come fotoanodo; film sottili e ultra-sottili di ossido di titanio drogato con tantalio (Ta:TiO$_2$) e, infine, film sottili compatti o formati da nanoparticelle assemblate di nitruro di titanio (TiN). Questi sistemi sono stati sintetizzati principalmente con la tecnica di deposizione a laser pulsato, seguita da trattamenti termici specifici per cristallizzare i materiali nella fase desiderata. Per i sistemi Au-TiO$_2$ è stato possibile ottenere nanoparticelle di oro uniformemente distribuite lungo tutto lo spessore del film di TiO$_2$, in aggiunta la loro risonanza plasmonica è stata modulata attraverso le condizioni di sintesi e la quantità di oro utilizzata. I film sottili di Ta:TiO$_2$ sono stati ottimizzati dal punto di vista delle proprietà elettriche e sono risultati conduttivi fino a spessori ultra-sottili di 10 nm, inoltre la risposta ottica di questi film si è dimostrata controllabile attraverso il contenuto di drogante ed, infine, si è iniziato ad esplorare il comportamento ottico di questo materiale nell'IR. Per quanto riguarda i film di TiN, è stato possibile modularne la risposta ottica sia per i film compatti sia per le nanoparticelle assemblate, inoltre, per una particolare condizione di sintesi, sono stati ottenuto film nanostrutturati capaci di assorbire più del 90% della luce incidente su un ampio intervallo (dall'UV al vicino IR).

Infine, le proprietà dei sistemi Au-TiO$_2$ sono state ottimizzate in prospettiva di applicazioni plasmoniche di fotoconversione e SERS. Inoltre, i film sottili di Ta:TiO$_2$ e TiN hanno dimostrato di avere proprietà elettriche e ottiche controllabili in un certo intervallo, estendendo il campo delle possibili applicazioni plasmoniche, ad esempio nell'IR o ad alta temperatura/potenza (applicazioni non accessibili ai metalli nobili). In conclusione, i film sottili di questi materiali possono essere impiegati in nanoelettronica e per lo sviluppo di nanostrutture ottiche con dimensioni minori della lunghezza d'onda della luce (i metamateriali), il cui comportamento plasmonico può essere ingegnerizzato.

Contents

Introduction

Nowadays, the explosive spreading of nanotechnology has brought researchers' attention to plasmonics, a fascinating field which offers the attractive potential of manipulating light at the nanoscale. Plasmonic response occurs when an electromagnetic wave (e.g. solar radiation) interacts with a metal and, as a consequence, the conduction electrons resonate with the incident electric field, giving rise to collective oscillations. Interesting possibilities arise when considering plasmonic phenomena at metal-dielectric interfaces, in which surface plasmon polaritons (SPP) are originated, or in assemblies of metal nanoparticles, resulting in localized surface plasmon resonance (LSPR). These phenomena involve the strong intensification of the electric field close to the metal surface and the sub-wavelength confinement of light. These peculiar features make plasmonics appealing for several application fields, such as for imaging below diffraction limit by near-field spectroscopy, sensing and nano-sensing up to single molecule recognition, surface enhanced Raman scattering (SERS), waveguides and photoconversion. For the latter, the device efficiency could be improved by incorporating plasmonic functionalities into the photoanode; this is usually made of semiconducting oxide materials (e.g. TiO_2) which are responsible for the light absorption aimed at charge carrier separation, that can be employed for electricity production (i.e. photovoltaic cells) or chemical reactions (i.e. photocatalysis). A possible improvement approach includes the integration of noble metal nanoparticles (NPs) (e.g. Au and Ag), whose plasmonic properties are known to be tunable through their size distribution, density, shape as well as surrounding dielectric medium. In particular, LSPR excitation and subsequent decay enable peculiar mechanisms exploitable for this purpose. Namely, plasmonic NPs can induce an antenna-like effect (also known as plasmon-induced resonant energy transfer, PIRET) when the extinction wavelength of plasmonic NPs overlaps with the intrinsic absorption range of the semiconductor material and the spectrum range of the illuminating source. Moreover, the plasmon resonance can dissipate either radiatively, implying photons re-emission (scattering), or non-radiatively, generating electron-hole pairs in the metal that can be injected in the semiconductor band (hot electron/hole injection). The latter effect gives rise to the possibility for the semiconductor

to absorb photons with energy lower than its band gap, usually limited to the light absorption in the UV range of the solar spectrum.

However, noble metals are not the best choice for any plasmonic application. Indeed, metals exhibit high optical losses in the infrared, restricting possible applications in this range, together with the difficulty of finely tuning their optical properties, limiting the development of devices such as optical modulators (i.e. active devices in which the optical response is controlled by the application of an external stimulus, e.g. bias or light). In addition, some technological challenges arise for the industry application of metallic materials due to poor hardness, low chemical stability and resistance to high temperature, as well as the difficulty in the realization of ultrathin metallic films (i.e. film thickness of few nanometers, appealing for sub-wavelength optical structures and nanoelectronics) and non-compatibility with standard silicon manufacturing process (i.e. complementary metal-oxide semiconductor, CMOS). In response to such limitations, different classes of materials have been proposed as an alternative. Semiconductors have been considered since they can achieve metal-like optical properties through doping. Among them, transparent conductive oxides (TCOs) have gained increasing attention. They are a well-known class of materials, widely employed as transparent electrodes for many optoelectronic applications. TCOs have been recently studied in the plasmonic field because they have demonstrated a tunable plasmonic response in near-IR and mid-IR range depending on carrier density, which is controlled in turn by adding dopants or by engineering oxygen defects. Moreover, TCOs can be grown into thin films and in other different nanostructures, polycrystalline and crystalline structures, patterned by standard fabrication procedures and integrated with many other standard technologies.

Among TCOs, Ta doped TiO_2 (Ta:TiO_2) has been already demonstrated to be a performing oxide with low resistivity and high mobility, while ensuring the advantages of TiO_2, i.e. low-cost, non-toxicity and chemical stability. Another alternative to noble metals involves transition metal nitrides. Among them, titanium nitride (TiN) is a unique material which goes beyond the aforementioned limitations, providing a tailored plasmonic response in the visible and near-IR range which in principle can be controlled through stoichiometry and crystalline quality. Metal nitrides are refractory, stable and hard materials and have the technological advantage to be currently used in CMOS technology. As a final consideration, the study of alternative plasmonic materials, which provide similar or, in some cases, enhanced properties, paves the way to other applications, e.g. in the field of IR vibrational spectroscopy, waste heat management, sensors and telecommunications.

In such context, this PhD thesis project concerns an experimental investigation for the development of nanostructured thin films based on titanium oxides and nitrides, aimed to achieve a fine control of their physical properties as well as the understanding of the material's optical and electrical behavior and their potential applications, with particular attention to the plasmonic field. The investigated systems are grown via physical vapor deposition techniques, in particular pulsed laser deposition (PLD), followed by post-deposition thermal treatments in order to crystallize the materials in the desired phase, or to modify their functional prop-

erties. The reasearch activities and the specific investigated system are reported in the present doctoral dissertation as follows:

Chapter 1 - Fundamentals of plasmonics and applications: a brief description of the electrical and optical properties of metals is presented, followed by an introduction of the main ingredients of plasmonics excitations. Finally, an overview on potential applications in this field is discussed, with a focus on the field involving plasmonic nanostructures (e.g. Au NPs) coupled with semiconductors (e.g. TiO_2) in order to improve their photoresponse.

Chapter 2 - Alternative materials for plasmonics: the limitations of traditional plasmonic materials are discussed and the alternative materials proposed in literature as a solution are presented, i.e. transparent conductive oxides (TCOs) and metal nitrides. Particular attention is given to tantalum doped titania ($Ta:TiO_2$) and titanium nitride (TiN), objects of this work. Electrical and optical properties of thin films of these materials are discussed as well as their state-of-the-art in plasmonic field and applications.

Chapter 3 - Thesis goal and methods: after the overview on the scientific framework of this work, the specific objectives are explained, followed by the description of the employed experimental methods. In particular, a brief description of the synthesis technique, i.e. pulsed laser deposition (PLD), is presented.

The following three chapters include my original researches with the related experimental results:

Chapter 4 - Integration of Au nanoparticles in TiO_2 hierarchical films: a PLD co-deposition approach for the synthesis of integrated Au NPs-TiO_2 hierarchical films is presented, while tuning the film porosity and Au content. The morphology, structure and optical properties of the systems were controlled by synthesis parameters. Finally selected samples were tested for photocatalytic applications and as a substrate for SERS.

Chapter 5 - Tantalum-doped TiO_2 thin films: after the first step of optimization of the synthesis parameters to find the conditions for maximizing the electrical conductivity of $Ta:TiO_2$ thin films, film properties were studied as a function of Ta content and thickness (down to ultrathin films, i.e. 10 nm, interesting for sub-wavelength optical structures and nanoelectronics), with a particular focus on electrical and optical behavior. Finally, more complex $Ta:TiO_2$-based systems are investigated, namely Au NPs integrated with $Ta:TiO_2$ and $Ta:TiO_2$ NPs assemblies.

Chapter 6 - Titanium nitride thin films: the correlation between synthesis process parameters and TiN thin films morphology (i.e. from compact to NPs assemblies) and stoichiometry/composition is established, while handling the non-trivial oxidation-issue of nanoporous TiN thin films. In addition, the investigation of the

influence of composition and structure on the optical response is presented with the aim of tuning and understanding the plasmonic behavior.

Chapter 7 - Conclusions and perspectives: the main achievements of this PhD thesis are summarized and some possible future developments are highlighted.

The original contents of this Ph.D. thesis have actively contributed to the publication of the following peer-reviewed papers, ordered by year:

- B. R. Bricchi et al., "Integration of plasmonic Au nanoparticles in TiO_2 hierarchical structures in a single-step pulsed laser codeposition" *Materials & Design*, 156, 311-319, (2018).

- R. Matarrese, B. R. Bricchi et al., "Integrated Au/TiO_2 nanostructured photoanodes for photoelectrochemical organics degradation" *Catalysts*, 9, 340 (2019).

- A. Brognara, B. R. Bricchi et al. "Highly sensitive detection of estradiol by a SERS sensor based on TiO_2 covered with gold nanoparticles" *Beilstein J. Nanotechnol.*, 11, 1026-1035 (2020).

- B. R. Bricchi et al., "Effect of doping and thickness on optical and electronic properties of $Ta:TiO_2$ thin and ultra-thin films", in preparation.

In addition, I presented the results achieved in this work in several in several international conferences:

- 6th workshop Plasmonica (4-6 July 2018, Florence, Italy), Poster presentation "Synthesis of Au NPs with tuned plasmonic properties and integration in TiO_2 hierarchical structures via single-step pulsed laser co-deposition".

- International Conference on Nanoscience + Technology (ICN+T) 2018 (22-27 July 2018, Brno, Czech Republic), Oral presentation "Integration of plasmonic Au nanoparticles in hierarchically-organized TiO_2 films for advanced light harvesting and photocatalytic applications".

- European Materials Research Society (E-MRS) Fall meeting 2019 (16-19 September 2019, Warsaw, Poland), Oral presentation "Tuning of electrical and optical properties of ultrathin $Ta:TiO_2$-based plasmonic films".

Fundamentals of plasmonics and applications

Plasmonics is known as a fascinating field of *nanophotonics*, based on the inter-action processes between electromagnetic radiation and conduction electrons of metals. In the past, people started to use plasmonics before knowing the actual plasmonic mechanisms and related physics. A famous example involves the *Lycur-gus cup* of the Roman age, 4th century AD, which exhibits a different color if it is illuminated from the front (i.e. red light is reflected) or from the back (i.e. green light is transmitted). The mystery of Lycurgus cup was then explained by the plasmonic properties exhibited by noble metal nanoparticles (i.e. Au-Ag alloy of 30-70 nm) embedded in the glass matrix. Another example consists in the stained glass which adorn medieval cathedrals, whose vibrant colors were obtained from interaction between light and metal nanoparticles with precise size embedded in the glass matrix; the Sainte-Chapelle in Paris (France) is a gorgeous example. At the beginning of 20th century, plasmonics and its main elements were clearly described, but it took the century to appreciate the interlinked nature of different phenomena and applications of this field.

Nowadays, with the explosive spreading of nanotechnolgy, plasmonic field has gained much attention because of its potentiality to manipulate light at the nanoscale. In order to understand this peculiar field, it is fundamental first to discuss how electrons behave in a metallic structure and how they react to an external perturbation such as an electromagnetic wave. In this chapter a brief description of electrical and optical properties of metal is presented, followed by a presentation of main ingredients of plasmonics excitations. Finally, an overview on potential application in this field is given.

1.1   Electrostatic properties of metals

According to solid state physics, the bright and reflective surface of metals, as well as their electrical conductivity, are properties related to the motion of electrons in a crystal lattice. Under proper assumptions, it is possible to describe electrons'

behavior by means of classical motion equations, avoiding complex quantum mechanics details. This treatment is known as *semiclassical dynamics* and allows to describe electron motion in a periodic potential (related to the presence of positive ions in the crystal lattice) by classic Newton's law. Anyway, the effect of the periodic potential is taken into account by introducing the *effective mass* (*m**), a simple parameter which strongly depends on band structure $E(k)$ of solid media [1, 2]. In a one dimensional crystal, m^* is defined as

$$m^* = \frac{\hbar}{\frac{d^2 E(k)}{dk^2}} \tag{1.1}$$

Semiclassical dynamics can describe electrons at the bottom of the conduction band, whose dispersion relation can be approximated as parabolic. Mathematically, m^* is the parabolic approximation applied to the real band structure $E(k)$. In the framework of semiclassical approach, electrical conduction of metals can be well described by a very simple model, i.e. Drude model [3]. Here, conduction electrons are considered as a cloud of independent particles (i.e. electron-electron scattering is neglected), where the effect of periodic potential of crystal lattice is taken into account with the implementation of the effective mass. However, electrons can collide with static (e.g. impurities) or dynamics defects (e.g. phonons) with a characteristic frequency $\gamma = 1/\tau$, where τ is the average scattering time between collisions. After each scattering event, electrons are scattered in a random direction, therefore their overall contribution to current flow is zero. On the other hand, when an electric field is applied, the average velocity of electrons becomes [3]

$$\mathbf{v} = -\frac{e\mathbf{E}\tau}{m*} \tag{1.2}$$

and the current density j with n electrons per unit volume (*carrier density*) becomes

$$\mathbf{j} = -ne\mathbf{v} = \frac{ne^2\tau}{m*}\mathbf{E} \tag{1.3}$$

Considering the Ohm law $j = \sigma\mathbf{E}$, conductivity can be written as

$$\sigma = \frac{ne^2\tau}{m*} = en\mu \tag{1.4}$$

where $\mu = \frac{e\tau}{m*}$ is the *carrier mobility*, which indicates how easily a particle moves inside a material. Drude model is very convenient since these results are the same as those obtained by using a more complete treatment such as the Boltzmann equation (still in relaxation time approximation) [2, 3].

1.2 Optical properties of metals

The interaction of a metal with electromagnetic field can be described within classical theory based on Maxwell's equations, even in case of metallic nanostructures because of high density of free carriers [4]. The *plasma model* (i.e the counterpart of Drude model in an oscillating electric field with a certain frequency) is

employed to describe optical properties of metals over a wide frequency range, involving a gas of free electrons which moves against a fixed background of positive ions cores. Even in this context, the relaxation time approximation is employed, and the lattice potential effect on electrons is again considered through m^* [5]. The electrons oscillate in response to the applied electromagnetic field and their motion can be described with the equation:

$$m\ddot{\mathbf{x}} + m\gamma\dot{\mathbf{x}} = -e\mathbf{E} \tag{1.5}$$

where $\mathbf{E}$ is the external electric field and γ is the dumping term related to the collision frequency of electrons, as already defined. If we assume a harmonic time dependence $\mathbf{E}(t) = \mathbf{E_0}e^{-i\omega t}$ of the driving field, a particular solution of the equation describing the oscillation of the electron is $\mathbf{x}(t) = \mathbf{x_0}e^{-i\omega t}$. The overall computation gives the *dielectric function* (or *complex relative permittivity $\epsilon(\omega)$*)

$$\epsilon(\omega) = 1 - \frac{\omega_p^2}{\omega^2 + i\gamma\omega} \tag{1.6}$$

$$\omega_P = \sqrt{\frac{ne^2}{\epsilon_0 m^*}} \tag{1.7}$$

where ω_P is the *plasma frequency* of the free electron gas. From a physical point of view, ω_P corresponds to the frequency of a collective longitudinal oscillation of conduction electrons versus the fixed positive background of ions, moving all together with the same phase (assuming small damping, $\epsilon(\omega_P) = 0$). The quanta of these charge oscillations are called *plasmons* or *volume plasmons* (to distinguish them from *surface* and *localized* plasmons, which will be discussed in the next sections). Due to the longitudinal nature of the excitation, volume plasmons do not couple with transverse electromagnetic waves. Moreover, ω_P has another important physical role. When $\omega < \omega_P$, no electromagnetic wave can propagate inside the material (i.e. reflection occurs), while for $\omega > \omega_P$ the transverse electromagnetic wave can be sustained (i.e. transmission occurs) and the dispersion relation of traveling waves is $\omega^2 = \omega_P^2 + k^2c^2$.

For practical reasons, it can be convenient to rewrite Eq.1.6 by isolating the real and imaginary parts of dielectric function according to $\epsilon(\omega) = \epsilon_1(\omega) + i\epsilon_2(\omega)$, since these two quantities are related to the ability of a material to store and lose incident electric field, respectively. We then obtain

$$\epsilon_1(\omega) = 1 - \frac{\omega_p^2\tau^2}{1 + \omega^2\tau^2} \tag{1.8}$$

$$\epsilon_2(\omega) = \frac{\omega_p^2\tau}{\omega(1 + \omega^2\tau^2)} \tag{1.9}$$

In some cases, optical properties of a material are described through *complex refractive index* (N), defined as the square root of dielectric function [6]. In particular, $N(\omega) = n(\omega) + i\kappa(\omega)$, where n in known as *index of refraction* and κ is the extinction coefficient. Both real and imaginary parts of refractive index have a physical meaning, namely n is given by the ratio of the speed of light in vacuum and the phase velocity of light in a medium, while κ is related to the
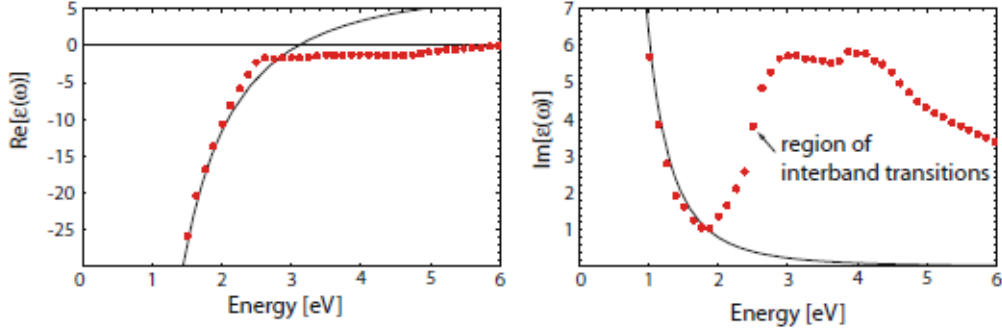
Figure 1.1: *Dielectric function of the free electron gas (solid line) fitted to the literature values of dielectric data for gold (red dots) [5, 7].*

exponential decay of an electromagnetic wave propagating in a medium due to optical absorption. Finally, real and imaginary parts of complex dielectric function and refractive index are related to each other according to

$$\epsilon_1 = n^2 - \kappa^2 \tag{1.10}$$

$$\epsilon_2 = 2n\kappa \tag{1.11}$$

Back to the plasma model, for noble metals (e.g. Au, Ag, Cu) an extension to this approach is needed in the region $\omega > \omega_P$, where the response is dominated by free s electrons, but the additional polarization due to bound electrons of d band should be taken into account through the use of a dielectric constant ϵ_∞

$$\epsilon\left(\omega\right) = \epsilon_\infty - \frac{\omega_p^2}{\omega^2 + i\gamma\omega} \tag{1.12}$$

Nonetheless, real metals experience interband transitions that should be considered in order to well describe their optical behavior. However, Drude model adequately describes the optical response of metals only for photon energies below the threshold of transition between electronic bands. As an example, Fig.1.1 shows the real and imaginary part of dielectric function of Au and the Drude model fits to the data. Clearly, a more general approach is required for describing both ϵ_1 and ϵ_2 at high frequency. Therefore, Eq.1.5 should be corrected with a resonant term at frequency ω_0 associated to characteristic oscillation of bound electrons, where interband electron excitations occur

$$m\ddot{\mathbf{x}} + m\gamma\dot{\mathbf{x}} + m\omega_0^2\mathbf{x} = -e\mathbf{E} \tag{1.13}$$

this equation leads to a number of equations which describe $\epsilon\left(\omega\right)$ and correspond to each separated contribution of the total polarization. Each resonance leads to a Lorentz-oscillator $\frac{A_i}{\omega_0^2 - \omega^2 - i\gamma\omega}$ term to be added to free-electron result (i.e. Eq.1.6). The overall model is called *Drude-Lorentz model* and a resonant response is expected in the perturbed material at ω_0 due to the presence of an external driving force (e.g. electromagnetic radiation) [5,8].

1.3 Plasmonic excitation

As previously mentioned, volume plasmons cannot be excited by electromagnetic waves. However, under particular conditions, free electrons can couple with electromagnetic field, leading to particular optical phenomena which allow light confinement below the diffraction limit and strong intensification of the electromagnetic fields. These plasmonic excitations involve surface plasmon polaritons (SPPs) and localized surface plasmon resonance (LSPR).

1.3.1 Surface plasmon polaritons

Surface plasmon polaritons are electromagnetic excitations propagating at the interface between a conductor and a dielectric, while wave confinement occurs in the perpendicular direction (see Fig.1.2 for a schematic illustration). SPP takes place when an electromagnetic field couples to the oscillation of the conductor's free electrons [10]. The requirement for SPP propagation is

$$\epsilon_m + \epsilon_d < 0 \tag{1.14}$$

where ϵ_m and ϵ_d are the dielectric functions of metal and dielectric, respectively. This condition implies that the dielectric functions to have opposite signs, and it happens when $\epsilon_m < 0$, i.e. for $\omega > \omega_P$. Moreover, boundary conditions require incident radiation with transverse-magnetic (TM) polarization. However, SPP excitation cannot occur directly from an electromagnetic radiation because of the momentum difference with respect to the incident photon, therefore phase-matching techniques are required, e.g. grating or prism coupling. When all conditions are satisfied, the resonance frequency of SPP excitation is given by

$$\omega_{SPP} = \frac{\omega_P}{\sqrt{1 + \epsilon_d}} \tag{1.15}$$

In real metals, the imaginary part of dielectric function is not zero and interband transitions cannot be neglected. Therefore, the traveling SPPs are damped with a propagation length, typically between 10 and 100 μm in the visible regime, depending on metal/dielectric coupling and frequency involved. Moreover, confinement at the interface is not perfect, as shown schematically in Fig.1.2 (right).
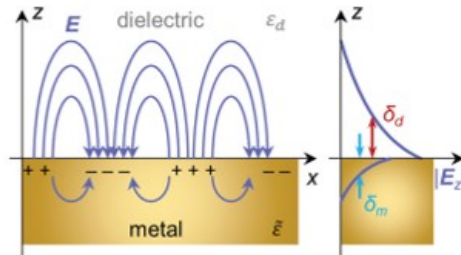

Figure 1.2: *On left, schematic illustration of surface plasmon polariton propagating along metal-dielectric interface, electromagnetic wave and surface charges are highlighted; on right, electric field component perpendicular to interface which decays exponentially with distance [9].*
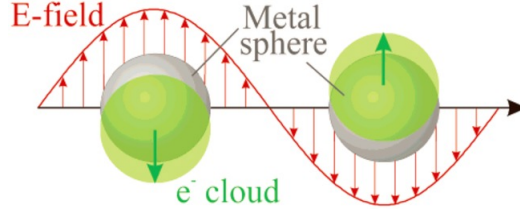
Figure 1.3: *Schematic illustration of conduction electrons oscillations of plasmonic nanospheres caused by external oscillating electric field [11].*

In the dielectric, the field falls off over distances from hundreds nanometers to micrometers, while in the metal propagation is on the order of 20 nm. However, the better the confinement, the lower the propagation length. Therefore, there is a trade-off between localization and loss and, typically, confinement below diffraction limit of half the wavelength can be achieved close to ω_{SPP} in the dielectric [5, 10].

1.3.2 Localized surface plasmons

The second fundamental plasmonic excitation consists in localized surface plasmons, which are non-propagating excitations of the conduction electrons of a metallic nanostructure coupled to the electromagnetic field [12]. For example, in the case of sub-wavelength nanoparticles (NPs) exposed to an oscillating electromagnetic field, the curved surface excerts an effective restoring force on the conductive electrons and a resonance (*localized surface plasmon resonance*) arises, leading to a field amplification next to the particle surface. A schematic illustration of the mechanism is shown in Fig.1.3. This type of plasmonic excitation can be triggered by direct light illumination, in contrast to propagating SPP. The interaction of a particle with an electromagnetic field can be analyzed using the *quasi-static approximation* if the particle is much smaller than the wavelength of light in the surrounding medium (i.e. $d << \lambda$) [12]. This means that over the particle volume, the harmonically oscillating electromagnetic field exhibits a practically constant phase, therefore the spatial field distribution can be calculated considering the particle subjected to an electrostatic field. Then, the harmonic time dependence can be added to the solution. For the sake of simplicity, we consider a homogeneous, isotropic sphere with radius a in a uniform static electric field. The surrounding medium is isotropic and non-absorbing, with dielectric constant ϵ_d. In these conditions, nanoparticles act as electric dipole whose polarization induced by the electrostatic field is given by

$$\alpha = 4\pi a^3 \frac{\epsilon - \epsilon_d}{\epsilon + 2\epsilon_d} \tag{1.16}$$

which means that polarizability α experiences a resonant enhancement when denominator goes to zero [5]. A consequence of the resonant condition is a concomitant enhancement in the efficiency with which a metal nanoparticle scatters or absorbs light. Here, the results for the scattering and absorption cross sections in

the quasi-static approximation are presented

$$\sigma_{sca} = \frac{8\pi}{3}k^4a^6 \left[\frac{\epsilon - \epsilon_d}{\epsilon + 2\epsilon_d} \right]^2 \qquad (1.17)$$

$$\sigma_{abs} = 4\pi k a^3 \text{Im} \left[\frac{\epsilon - \epsilon_d}{\epsilon + 2\epsilon_d} \right] \qquad (1.18)$$

Notably, scattering and absorption cross sections scale with a^6 and a^3, respectively, suggesting big particles prefer to scatter, while small ones favor absorption. While this theory is strictly valid only for sub-wavelength particles, such calculations provide a reasonably good approximation for spherical or ellipsoidal particles with dimensions below 100 nm, illuminated with a visible or near-infrared radiation. On the other hand, for particles of larger dimensions, the quasi-static approximation is not applicable due to significant phase-changes of the field over the particle volume, therefore an electrodynamic approach is required. The *Mie theory* allows to expand the internal and scattered fields into a set of normal modes described by vector harmonics; then, the quasi-static results are recovered by a power series expansion of the absorption and scattering coefficients and considering only the first term. Besides, when the two contributions cannot be distinguishable in the plasmonic response, it is convenient to consider *extinction*, which consists in the sum of both scattering and absorption sections (i.e. $\sigma_{ext} = \sigma_{sca} + \sigma_{abs}$). If extinction cross-section is plotted as a function of frequency, a peak will occur at the resonance frequency ω_{LSPR}, which is defined as

$$\omega_{LSPR} = \frac{\omega_P}{\sqrt{1 + 2\epsilon_d}} \qquad (1.19)$$

As a consequence, LSPR frequency is affected by surrounding medium via ϵ_d, while the effect of the metal involved is included in its plasma frequency ω_P. In Fig.1.4 the extinction spectra of Au, Ag and Cu NPs are shown and the variation of the resonance frequency with metal involved is visible. Besides, the quasi-static approximation is not suitable for particles larger than 100 nm and an electro-dynamic approach is required due to the phase change of the driving field over particle volume. Moreover, NPs smaller than 10 nm required a different analysis too, since particle size is appreciably smaller than the mean free path of oscillating electrons [5, 12]. Finally, this simplified picture does not take into account other important parameters which affect ω_{LSPR}, i.e. NPs size, shape and coupling effect (in the case of metallic NPs close enough to interact with each other) [14, 15]. To properly describe these factors, it is necessary to relax the quasi-static approximation, leading to higher order terms whose mathematical derivation and physical discussion will not be discussed in this work. However, the general effect of these parameters on ω_{LSPR} are here summarized:

- the increase of NPs size leads to a red-shift of resonance frequency. For example, this trend is evident in Fig1.5a, where the experimental absorption spectra of Au nanosphere as a function of size are shown. Intuitively, this is justified considering that the distance between the charges at opposite interface of the particle increases with its size, thus leading to a smaller restoring force and therefore a lowering of resonance frequency [14, 16].
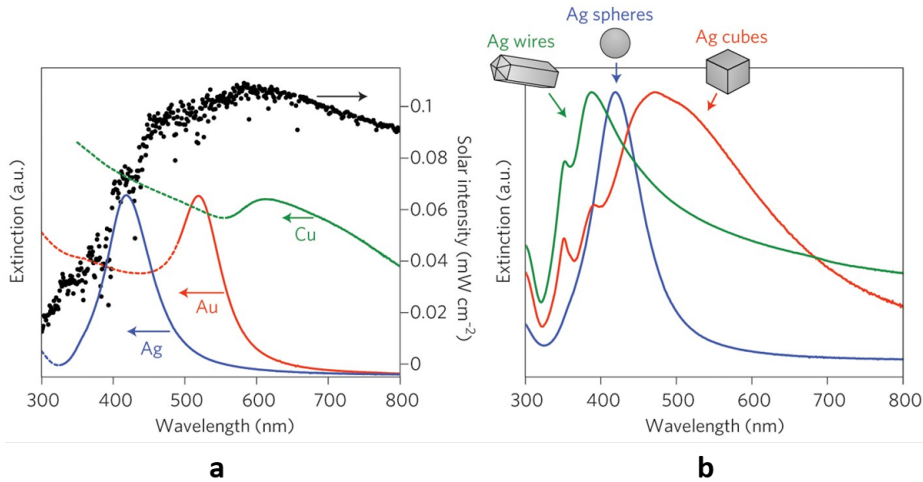
Figure 1.4: *(a) Extinction spectra of Ag, Au and Cu NPs showing their respective plasmonic resonance peaks plotted with the solar spectrum; (b) extinction spectra of Ag NPs as a function of NP shape [13].*
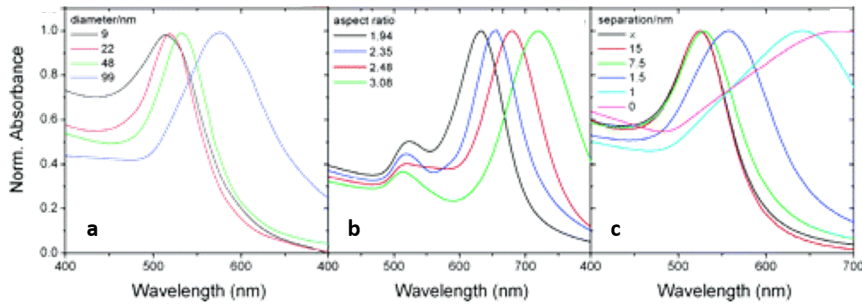

Figure 1.5: *Experimental absorption spectra of (a) Au nanospheres as a function of size, (b) Au nanorods as a function of the aspect ratio between lateral and transverse size and (c) multilayer films of glass-coated Au nanospheres as a function of interparticle distance; reproduced from [16].*

- shape affects the direction of oscillation of electrons under incident electric field and in general the effect of anisotropic shape of NP consists in a red-shift of plasma frequency with respect to the corresponding spherical one. In Fig.1.4b the extinction spectra of Ag NPs with different shape are reported. Notably, an interesting behavior occurs for rod-like structure. In this case, two kinds of oscillations are expected, one longitudinal and one transverse with respect to incident electric field. Polarizability along principal axes are different, therefore multiple LSPRs can occur. Fig.1.5b shows absorption spectra of Au nanorods as a function of aspect ratio between main sizes which affect main resonant peak's position and secondary peak's intensity [13,16].

- in NPs ensembles, shifts in resonance frequency are expected due to electro-magnetic interactions between localized modes and, in first approximation, an ensemble can be treated as interacting dipoles. Depending on polarization direction of the exciting light, this leads to a blue- or red-shift of resonance
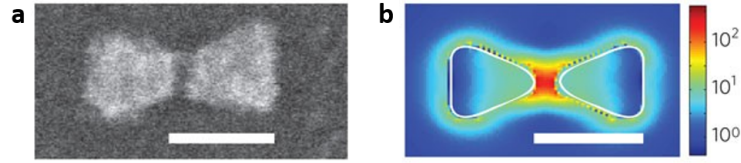
Figure 1.6: *(a) SEM image of a gold bowtie nanoantenna and (b) related result of FDTD calculation of local intensity enhancement. In both pictures, scale bar corresponds to 100 nm. In [17] this system is exploited to enhance single-molecule fluorescence.*
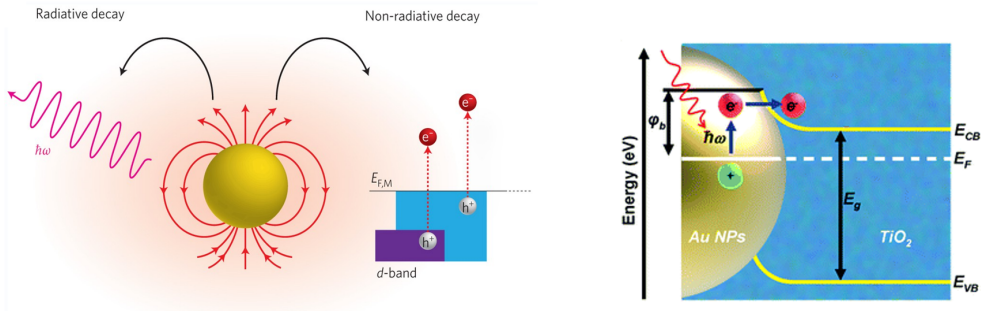

Figure 1.7: *On left, decay of LSPR excitation radiatively via re-emitted photons or non-radiatively via excitation of hot electrons within the conduction band or through interband transitions, e.g. from d band to conduction band [18]. On right, schematic illustration of the band-bending effect of the Schottky junction between Au NP and the TiO_2 layer surrounding it. The mechanism of injection of a hot electron from conduction band of Au NPs to TiO_2 is shown [19].*

frequency for the excitation of transfer and longitudinal modes, respectively. In Fig.1.5, glass-coated Au nanospheres present a blue-shift of the resonance peak by incrasing interpaticle distance [16]. Moreover, technological interest is attributed to the interparticle junctions where an hot-spot for field enhancement takes place [17]. Fig.1.6 shows the scanning electron microscopy image (SEM) of gold bowtie nanoaltenna and the related finite-difference-time-domain (FTDT) calculation of a local intensity enhancement.

Finally, in addition to the resonant frequency, another important parameter which characterizes the plasmonic response of a particle consists in the peak line-width (i.e. the region around which the resonance peak extends, often indicated as full-width half-maximum, FWHM or Γ). This element takes into account both technological factors, e.g. a broad NP size distribution results in a overall broad response, and physical parameters, summarized by plasmon life time. This is associated to the radiation damping caused by two competing processes: a radiative decay process into photons, dominating for large particles, and a non-radiative process due to absorption, favored in small particles and induced by the creation of electron-hole pairs via either intraband excitations within the conduction band or interband transitions, as schematically represented in Fig.1.7. Therefore, the linewidth of plasma resonance can be related to damping processes via the introduction of a dephasing time T

$$\Gamma = \frac{2\hbar}{T} \tag{1.20}$$

T takes into account both radiative and non-radiative energy loss processes, but also scattering events that do not change electron energy but its momentum [5, 20, 21]. The dominant contribution to T depends on the NPs material, size and shape. For very small particles (i.e. radius smaller than 10 nm) there is an additional damping process due to elastic scattering at the particle surface, since particle size is smaller than electron mean free path [12]. Finally, NPs with radius smaller than 1 nm cannot be analyzed with a classical treatment because quantum effects begin to set in, however this condition is not considered because beyond the goal of this work.

Beyond SSP and LSPR, the last peculiar condition that is worth discussing for the aim of this work is the change of behavior of the electron free gas when it is confined in two-dimensions, namely when the free motion of electrons in one direction is hindered by the small size of the system [22]. For very low thickness (few nanometers), plasma frequency dispersion becomes

$$\omega_{2D} = \frac{\omega_P}{\epsilon k d/(\epsilon_1 + \epsilon_2)} \tag{1.21}$$

where ϵ_1 and ϵ_2 are dielectric constant of the substrate and surrounding medium, respectively, k is the in-plane wavevector and d the film thickness.

1.4 Applications

The implementation of plasmonic functionalities in several devices has attracted interest because of the possibility of confining light below the diffraction limit and of the intensification of electric field close to metal's surface [23]. Studies of this kind involve devices for imaging below diffraction limit by near-field spectroscopy [24–26], sensing and nano-sensing up to single molecule recognition [17, 27, 28], surface enhanced Raman scattering (SERS) [29, 30], waveguides [10, 31], photo-conversion systems [11, 32] and more.

In this framework, it is useful to define a quality factor (Q), or figure-of-merit, to compare the performance of various materials employed in different applications over a wide frequency band [33]. Since the field distribution and losses in a material depend on ϵ_1 and ϵ_2 respectively, quality factors of a plasmonic material are generally function of them. Considering that different applications can have different definition for Q, this discussion is focused on devices based on LSPR and SPP effects (Q_{LSPR} and Q_{SPP}). Both phenomena involve local-field enhancement at metallic surface, therefore the quality factor can be defined as the ratio of enhanced local field and incident field. In case of LSPR, the enhancement depends on the NP shape, e.g. for a sphere is given by

$$Q_{LSPR}(\omega) = \frac{-\epsilon_1(\omega)}{\epsilon_2(\omega)} \tag{1.22}$$

For SPP, the quality factor can be defined as the ratio of real part of the propagation wavevector and the imaginary part and, considering the absolute value of the real part of dielectric function of metal being much higher than dielectric one
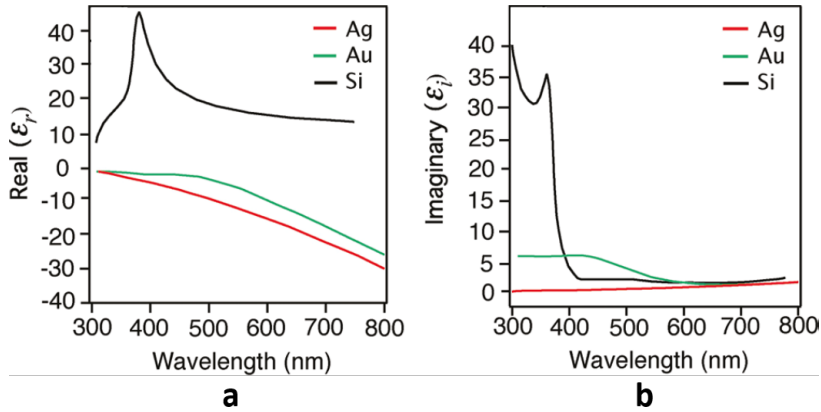
Figure 1.8: *(a) Real ϵ_1 and (b) imaginary ϵ_2 parts of the dielectric constant of Ag, Au and Si [34]. ϵ_2 of Au increases below 500 nm due to interband transitions, while Ag curve remains zero.*

(i.e. $|\epsilon_{1m}| \gg \epsilon_d$), Q_{SPP} can be simplified as

$$Q_{SPP}\left(\omega\right) = \frac{\epsilon_{1m}\left(\omega\right)^2}{\epsilon_{2m}\left(\omega\right)} \tag{1.23}$$

It may be noted that Q_{SPP} has the same form as Q_{LSPR} for spheroid NPs [33].

Typically, gold and silver are the most employed metals for plasmonic applications because of their plasmonic resonance in the visible and near-IR range. In particular Ag is characterized by a stronger plasmonic response and higher quality factor, prompted by interband transitions occurring at much higher frequencies [34]. Conversely, Au plasmonic excitations in visible are limited by interband transitions below a wavelength of 500 nm, as shown in Fig.1.8 where ϵ_2 of Au presents an increment in this range. However, in several cases the choice of Au can be convenient due to its high chemical and physical stabilty (e.g. in aqueous environment, which implies limited corrosion under photocatalytic conditions), biocompatibility and the ease of surface functionalization with organic and biological molecules [15, 35].

Besides, a fascinating application field involves plasmonic nanostructures coupled with semiconductors in order to improve their photoresponse. This coupling has a technological interest in devices where the semiconductor constitutes the photoanode, i.e. the material which enables the generation of charge carrier by absorbing light. These photogenerated carriers can be employed for electricity production (i.e.photovoltaic cells [32, 36, 37]) or chemical energy (i.e. photoelectrochemical cell, in solar water splitting or photocatalysis [38, 39]). In particular, LSPR excitation and subsequent decay enable peculiar mechanisms exploitable for this purpose. As previously discussed, LSPR excitation is associated to a large dipole moment which can be coupled with the semiconductor absorption band for electron-hole pair generation. This effect is called *plasmon-induced resonant energy transfer* (PIRET) and it is useful when the extinction wavelength of plasmonic NPs overlaps with the intrinsic absorption range of the semiconductor material and the spectrum range of the illuminating source, leading to
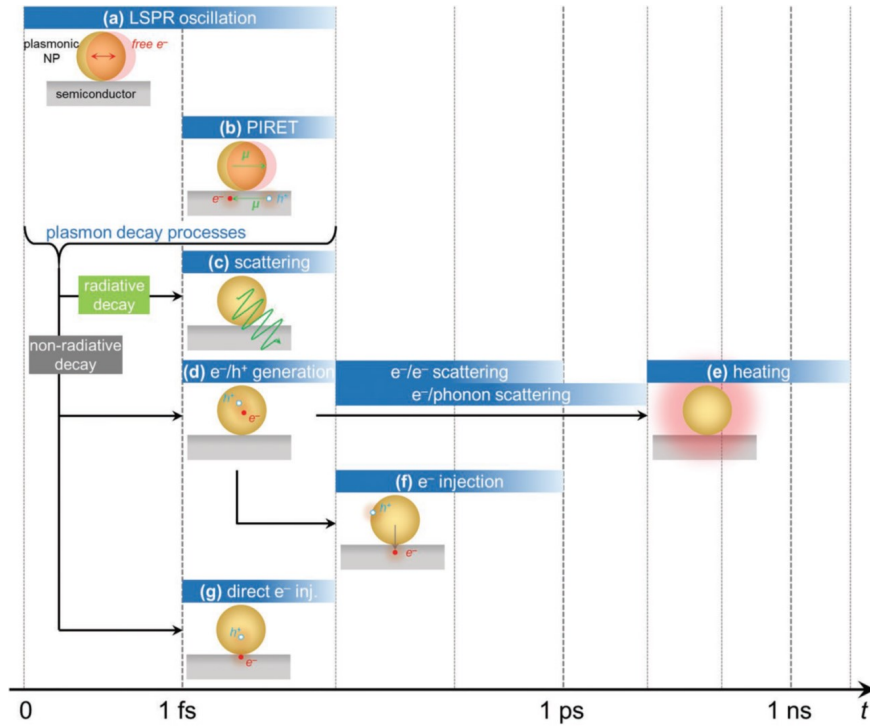
Figure 1.9: *Schematic illustration summarizing LSPR-excitation-induced processes occurring in a plasmonic nanostructure/semiconductor coupling with relative time evolution [9].*

an antenna-like effect [9, 40]. Subsequently, the plasmon resonance can dissipate either radiatively or non-radiatively. The first case implies photons re-emission and this process is known as *scattering* [41]. If the plasmon energy is higher than semiconductor band gap, scattering provides light absorption enhancement, aimed to free carriers generation in photoconversion applications. On the other hand, non-radiative decay (known also as *Landau damping*) generates electron-hole pairs (with a non-thermal distribution) in the metal. Then, two situations can happen. First, hot carriers rapidly relax to a thermal distribution via electron-electron and electron-phonon scattering, resulting in the heating of plasmonic material, which finally cools through heat transfer into the surrounding medium. Alternatively, in the case of plasmonic nanostructures coupled with semiconductors, a Shottky barrier forms among work functions of the two materials and, if the work function of plasmonic metal is higher, hot carriers can be extracted before thermal relaxation and injected into the semiconductor bands [15, 42]. A schematic illustration of this mechanism is shown in Fig.1.7. This process is called *hot electron (or hole) injection* and its interest lies in the possibility for the photoanode to absorb photons with energy lower than the semiconductor band gap. An important role of this mechanism is played by the interface between NPs and the semiconductor, which can induce recombination centers. Fig.1.9 summarizes the possible LSPR-excitation-induced mechanisms discussed and their time evolution [9].

Thimsen et al. and Thomann et al. integrated Au NPs in hematite ($\alpha - Fe_2O_3$) in order to improve its performance as a possible photoanode material for photoelectrochemical cell aimed to solar-to-fuel conversion [43, 44]. The limit of a
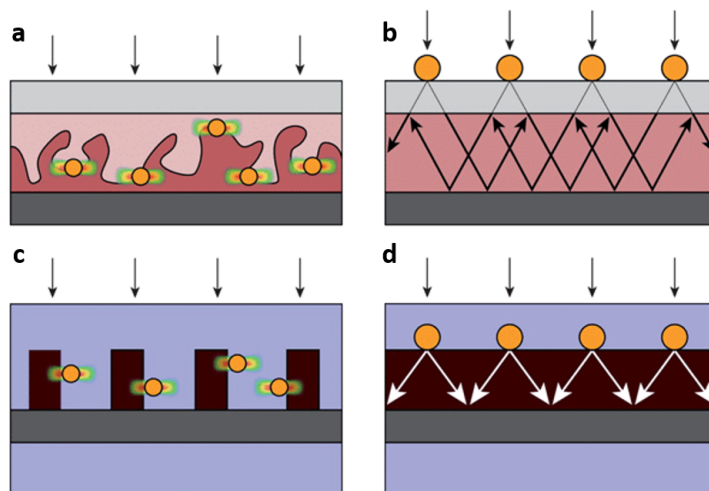
Figure 1.10: *Device design for (a,b) solar cell and (c,d) photoelectrochemical cell with plasmonic NPs integrated to promote (a,c) near field carrier generation by PIRET or (b,d) light trapping by scattering. In these figures, transparent conducting oxide electrodes are light grey, metal electrodes are dark grey, plasmonic metal nanoparticles are yellow, water is blue, and the semiconductor is red [54].*

$\alpha - Fe_2O_3$ based photoanode is the mismatch between the length scales over which photons are absorbed and the holes diffusion length. If the Au NPs resonance overlaps the absorption range of hematite (and this is possible by selecting a proper NP size and shape which tune plasmonic resonance), PIRET effect occurs, allowing an antenna-like effect which can be exploited to locate the charge carrier generation in the semiconductor nearby the surface. In principle, the PIRET effect is exploitable between many metallic NPs/semiconductors couples, thank to the tuneability of metallic NPs plasmonic responce, as reported in different works [45–53].

As explained before, a scattering mechanism is expected in the case of metallic particles larger than 100 nm. In practice, scattering can be exploited by photoanodes through waveguiding modes or reflection mode [32, 54]. When a plasmonic particle is placed at the interface of two dielectrics, e.g. a photoanode and an electrolyte, the light will scatter preferentially into the dielectric with larger permittivity. For this reason, metal NPs at the surface of the photoanode can act as an antireflection layer and, if the cell has a reflecting metal back contact, the incident light can pass several times through the semiconductor film, increasing the effective path length. However, particular attention should be given to such a design because deconstructive interference of scattered light should be avoided. Fig. 1.10 shows possible device design for solar and photoelectrochemical cells exploiting antenna-like effect and light scattering for overall performance enhancement [54].

Among all semiconductors, titanium dioxide (TiO_2) has gained particular attention for photoanode application because of its chemical stability, its availability and lack of toxicity. However, the high recombination rate of photogenerated charge carriers constitute significant limitations for its successful employment, while the wide band gap (3.2 eV for the anatase phase) allows the absorption of

the solar light in the UV range, limiting its activity under the visible light irradia-
tion which is crucial for example in photocatalysis. [55,56]. A strategy to improve
the photoresponse is the integration of NPs in order to exploit potential hot elec-
tron injection, since the TiO_2 band gap limits the possibility of other plasmonic
enhancement mechanisms (except for TiO_2-based dye-sensitized solar cell where
scattering can be employed to improve dye absorption). This hypothesis was ver-
ified by Tian and Tatsuma in a photoelectrochemical cell (PEC) which involves a
photoanode of Au NPs-TiO_2 and Ag NPs-TiO_2 by soaking mesoporous TiO_2 in a
solution containing NPs of Au or Ag with size of 5-20 nm [57,58]. They found a
higher value of incident photon to current conversion efficiency (IPCE, i.e. flux of
collected electron per flux of incident photons) in the visible range with respect
to bare TiO_2, in particular at the resonant wavelength of the two materials. They
ascribed this behavior to hot electron injection. Moreover, they observed that
the photocurrent of the Au-TiO_2 photoanode was stable in time, while it was
less stable in the Ag-TiO_2 photoanode, presumably because Ag rapidly oxidized
under anodic conditions used for PEC characterization. The mechanism of hot
electron injection when coupling metallic NPs and TiO_2 was studied by many
other authors [19,59,60].

So far, the applications based on LSPR and SPP mechanisms have been dis-
cussed. Besides, other possible phenomena can take place and be exploited for
peculiar applications, such as in the field of *transformation optics*. This fascinat-
ing field involves metamaterials, i.e. materials arranged in repeating patterns at a
scale smaller than the wavelength of the interacting electromagnetic field, which
present unique properties (e.g. negative index of refraction), exploitable for the
development of peculiar applications, e.g. superlenses, hyperlenses, optical invis-
ibility cloaks and light concentrations [61,62]. Finally, plasmonic excitations can
boost nonlinear optical effects when the electronic motion in a strong electromag-
netic field cannot be considered as harmonic and instead a power series expansion
is needed and, with regard to possible applications, the most important effects
occur at second and third order. The role of plasmonics in nonlinear optics is
threefold: enhancement of effective nonlinearity of conventional photonics by al-
lowing the use of reduced optical power; scaling down nonlinear components in
size, which is of interest for developing fully functional nanophotonic circuitry;
and since the response time of plasmonic excitations is ultrafast, the possibility to
manipulate optical signals on femtosecond timescales [63,64]. However, a deeper
discussion of these fields is beyond the goal of this work.

This chapter presented the main ingredients of plasmonics as well as the po-
tential applications, mainly in the framework of traditional plasmonic materials,
namely noble metals (i.e. Au, Ag, Cu and so on). In the next chapter, limitations
of these materials will be outlined, then alternative materials will be proposed
as a solution to overcome these limits, aiming to the access to applications not
feasible in traditional conditions.

Alternative materials for plasmonics

In Chapter 1, an overview on fundamentals of plasmonics has been presented, considering electrical and optical properties of metals as well as main aspects of plasmonic excitation, concluding with potential applications. In particular, noble metals have been taken into account so far. However, some technological challenges arise for metal industry application, combined with high optical losses in the frequency range of applicability, therefore research efforts have focused to find a better plasmonic candidate, depending on considered application. In this chapter, limitations of traditional plasmonic materials will be presented and alternative materials will be proposed as a solution, i.e. transparent conductive oxides (TCOs) and metal nitrides. Particular attention will be given to one material for each considered class, namely tantalum doped titania (Ta:TiO$_2$) and titanium nitride (TiN), because this thesis work is focused on the development of nanostructured thin films based on titanium oxides and nitrides. First, electrical and optical properties of TCOs will be discussed as well as their state-of-the-art in plasmonic field and applications. Then, an overview on properties of TiO$_2$-based TCOs will be presented, focusing on Ta-doped TiO$_2$. Since Ta:TiO$_2$ has been already studied in our research group as transparent electrode for phovoltaics, a brief resume of previous achievements on its synthesis and properties will be presented. Second, discussion will switch to metal nitrides and TiN. Since TiN is a well-established material in various industrial sectors, its electrical and optical properties have been investigated in several works, therefore the state-of-the-art of these TiN properties as well as the achievements of TiN films and NPs in plasmonics will be presented. Finally, we will deal with the synthesis of TiN thin films and nanostructures, which has proven to be a critical issue in the definition of material properties, and particular attention will be given to oxidation problem.

2.1   Limitations of convetional plasmonic materials

Metals (e.g. Au and Ag) are commonly used for plasmonic applications because of their small ohmic losses or high DC conductivity. Optical losses (represented by imaginary part of dielectric function ϵ_2, see section 1.2) depend on interband transition, intraband transition and scattering due to defects. The last two contributions decrease with a smaller charge carrier concentration n. As an example, intraband losses (or Drude losses) in gold are very high in the near-IR range, because of its high charge carrier density ($\sim 10^{23}$ cm^{-3}), and are lower for shorter wavelength where, however, interband losses occur from d band to sp band [7,33,65]. Furthermore, the reduction of n could be convenient for the development of transformation optics (TO) devices, because the real part of dielectric function (ϵ_1) of both metal and dielectric should be of the same order of magnitude and from Eq.1.8 we know that ϵ_1 decreases with n [66]. However, metal optical properties cannot be tuned so easily. Carrier concentration of metals cannot be changed much with the application of moderate electric or optical fields. Therefore, metals are not the convenient choice in applications where switching or modulation of optical properties is required (e.g. in optical modulators, consisting in active devices in which the optical response is controlled by the application of an external stimulus, such as bias or light). In addition to optical losses and not adjustable dielectric permittivity, metals suffer also technological problems for synthesis and integration in several devices. Indeed, metals have a percolation threshold when deposited on common substrates such as silicon, quartz, sapphire or glass, making the realization of ultra-thin films (i.e. films thick few nanometers) extremely challenging [66,67]. However, ultra-thin films result particular attractive for sub-wavelength optical structures and in nanoelectronics. Another technological challenge for their integration in nanoelectronics consists in non-compatibility with standard silicon manufacturing process (i.e. complementary metal-oxide semiconductor, CMOS), since nobel metals can diffuse into silicon to form deep traps which severely affect the performance of device [68]. Finally, other issues to consider in the context of realistic devices include poor hardness, low chemical stability and resistance to high temperature [69].

In response to the mentioned limitations, different class of materials have been proposed as an alternative. Semiconductors have been considered since they can achieve metal-like optical properties through doping [70]. Among them, transparent conductive oxides (TCOs) have gained increasing attention. They are a well-known class of materials, widely employed as transparent electrodes for many optoelectronic applications [71–74]. TCOs have been recently studied in the plasmonic field because they have demonstrated a tunable plasmonic response in near-IR and mid-IR range (i.e. frequency range where metals suffer high optical losses) depending on carrier density, which is controlled in turn by adding dopants or by engineering oxygen defects [66,70,75,76]. Moreover, TCOs can be grown into thin films and many different nanostructures, polycrystalline and crystalline structures, patterned by standard fabrication procedures and integrated with many other standard technology.

Another promising alternative to metals consists in transition metal nitrides

and, among them, titanium nitride (TiN) is a unique material which goes beyond the aforementioned limitations, providing a tailored plasmonic response in the visible and near-IR range which in principle can be controlled by stoichiometry and crystalline quality. Metal nitrides are refractory, stable and hard materials and have the technological advantage to be currently used in silicon CMOS technology [77].

As a final consideration, the study of alternative plasmonic materials (i.e. TiN and TCOs), which provide similar or, in some cases, enhanced properties, paves the way to other applications, e.g. in the field of IR vibrational spectroscopy, waste heat management, sensors and telecommunications [66, 78].

2.2 Transparent conductive oxides

Transparent conducting oxides (TCOs) are fascinating materials because of their unique properties which allow good conductivity and transparency in the visible region. These peculiar properties allow to employ TCOs as electrodes in opto-electronic devices, including photodetectors [72], solar cells [71], light-emitting diodes [74], and flexible displays [73]. The most employed TCO for consumer products is Sn-doped indium oxide (ITO) because of its high optical transparency in the visible range and very low resistivity $(1-2 \cdot 10^{-4} \, \Omega cm)$, however the limited availability of In has been driving the research toward alternative materials, e.g. Al-doped ZnO (AZO) and TiO_2 based TCO [75, 79–81]. TCOs consist in highly doped oxides, but in this work only n-type materials will be considered since most of them belong to this category. There are two main strategies to n-dope an oxide to obtain a wide band gap conductor: introducing intrinsic defects (e.g. oxygen vacancies) or substitutional element with more valence electrons than the metal in the compound, in this case higher carrier concentration is obtained [75]. Considering the dependence of plasma frequency on charge carrier density explained in section 1.2, n should not be too high, because a plasma resonance close to visible range is not appreciated in case of TCOs. Moreover, the excessive doping can lead to pass the limit of solid-solubility, resulting in phase separation or compound of dopants. On the other hand, there is a lower limit of n too, because it is necessary to provide enough free carriers in order to conduct electrical current in a similar way to metals [66].

Thin films of TCOs can be deposited by many physical-vapor and chemical-vapor deposition techniques, in particular highly conductive TCO films can be produced by techniques such as pulsed laser deposition (PLD) and sputtering. Usually, an optimization of synthesis parameters is required to achieve highest possible carrier concentration and lowest possible losses. Among them, substrate temperature and oxygen partial pressure during deposition play a key role for this purpose [69].

2.2.1 Optical and electrical properties of TCOs

The optical response of a TCO differs from the corresponding pristine oxide because the introduction of high carrier density leads to an increase in the optical band gap and a decrease in the plasma frequency. The first effect is known as
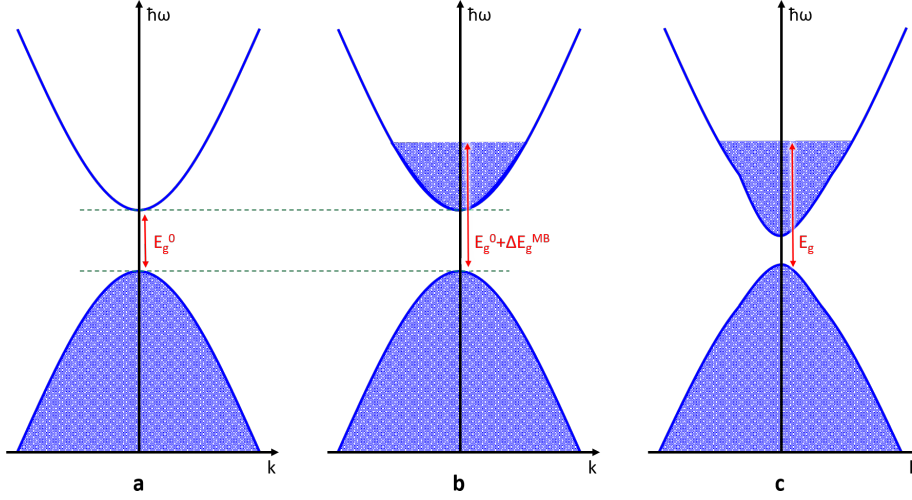
Figure 2.1: *Schematic band gap structure of (a) a direct gap semiconductor with parabolic bands separated by E_g^0; (b) increase of optical gap by amount ΔE_g^{MB} due to heavy doping and consequent Moss-Burstein effect; (c) perturbed band structure due to many-body affect, resulting in optical gap E_g. Occupied states are represented by shaded area.*

Moss-Burstein (MB) and it occurs when a metal is doped over the degeneracy limit, leading to the occupation of the bottom of the conduction band [82]. As a consequence, only photons with higher energy can be absorbed and the optical band gap increases, as schematically represented in Fig. 2.1a,b for a direct gap semiconductor. Considering a simple free electron approximation, the MB shift can be calculated by

$$\Delta E_g = \frac{\hbar^2 k_F^2}{2m^*} \tag{2.1}$$

where k_F is the Fermi wavevector and m^* is the effective mass. However, for very high carrier concentration, other effects such as many-body interactions came into play, introducing distortion of the dispersion relation and shrinkage of the band gap (see Fig.2.1c), as a consequence this simple calculation of MB shift is no longer valid [83].

Fig.2.2 reports modeled real and imaginary part of refractive index as well as modeled transmittance, reflectance and absorbance of a TCO with carrier concentration of $5 \cdot 10^{20}\, cm^{-3}$, effective mass of $0.4\, m_e$, high-frequency permittivity of 4, mobility of $50\, cm^2/Vs$ and film thickness of 500 nm, taken from [84]. Notably, in real materials there is not a sharp decrease of reflectance in favor of transmittance increment above the plasma frequency, but rather a slow increase, spanning even over hundreds of nanometers. Since the transmittance decrease does not perfectly match the reflectance increase, an absorption peak occurs around the plasma wavelength (see Fig.2.2b). However, absoption peak cannot be confused as an excitation of volume or surface plasmons, because it is not possible under simple light irradiation (as explained in section 1.3). Indeed, this peak is often called *free carrier absoption*, because absoption in this region is given by the particular dispersion acquired by the dielectric constant due to the presence of free electrons and related relaxation time. In Fig.2.2a, the plasma wavelength λ_{PW}
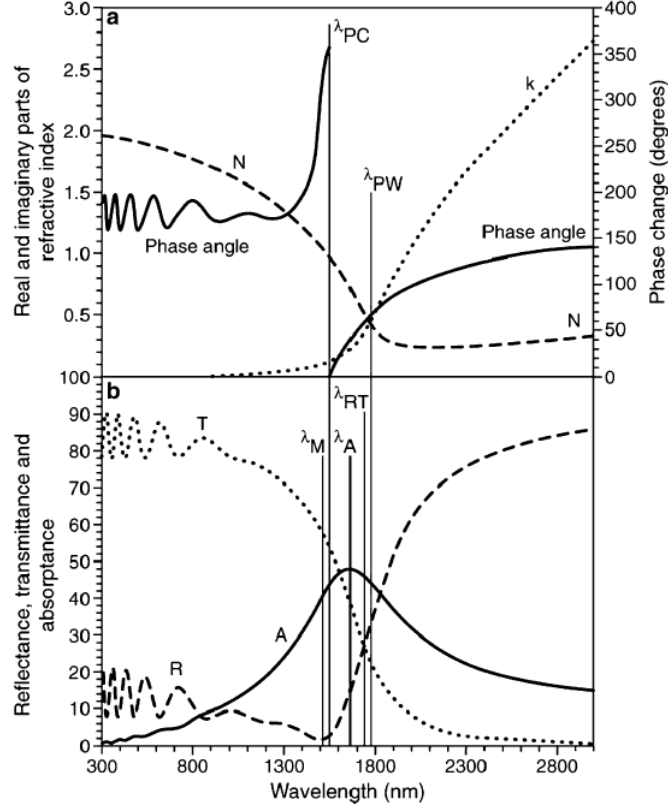
Figure 2.2: *(a) Modeled real and imaginary parts of refractive index and phase change on reflection. (b) Modeled transmittance, reflectance and absorbance. Carrier concentration was $5 \cdot 10^{20} \, cm^{-3}$, effective mass was $0.4 \, m_e$, high-frequency permittivity was 4, mobility was $50 \, cm^2/Vs$ and film thickness was 500 nm. Reproduced from [84].*

corresponds to $N = k$ (i.e. $\epsilon = 0$), which does not correspond exactly to minimum in reflectance or maximum in absorbance, because their position depends on relaxation time specific for each material, however they can be an indication of λ_{PW}, as widely employed in experimental studies of TCOs [85, 86].

Charge transport in TCOs is similar to metals, consequently the Drude model presented in section 1.1 is appropriate to describe their conductivity. The main differences lie in charge carrier density (already discussed) and in the scattering mechanisms which limit carrier mobility. The last ones involve electron-phonon scattering, ionized impurity scattering, grain boundary scattering and surface scattering [84]. The first one is always present at room temperature, while the last one is relevant for films thinner than 100 nm. Moreover, ionized impurity scattering is unavoidable in TCOs because their doping requires the introduction of aliovalent element in the materials, for example this mechanism becomes the dominant one in doped ZnO for $n > 5 \cdot 10^{21} \, cm^{-3}$ [87]. Also charged oxygen vacancies (when acting as double electron donors) can be virtually considered as ionized scattering centers [84]. Notably, higher carrier concentration requires higher doping, which leads to a lower mobility, and the optimal condition is searched in the middle. Finally, grain boundary scattering becomes relevant in polycrystalline films. Here, different orientation of neighboring crystal grains give rise to dislo-
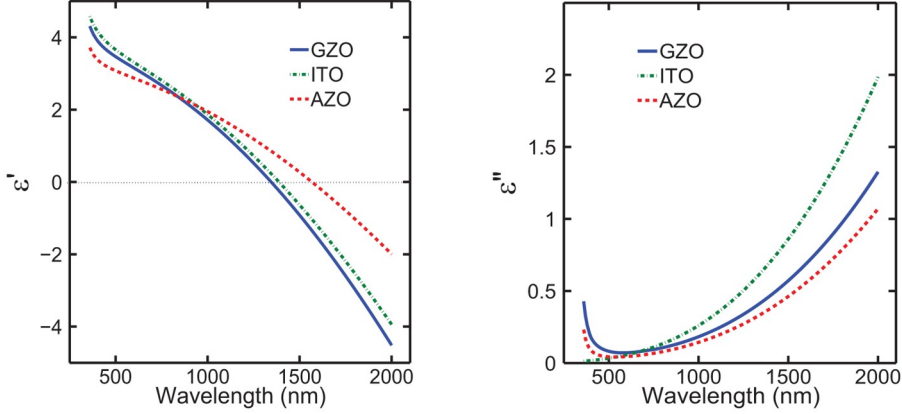
Figure 2.3: *Comparison of optical properties of pulsed laser deposited ITO, AZO and GZO films on glass substrate [69].*

cations, misplaced atoms, vacancies, distorted bond angles and bond distance at the interfaces [88]. The various types of defect introduce extra electronic states spatially localized, which may have energy in the band gap and trap carriers. Their behavior depends on their energy position relative to the bands of the bulk crystal: shallow defects close to the conduction band tend to act as electron traps, defects close to the valence band act as hole traps, while deep defects levels near the center of the band gap may trap either type of carrier, acting as recombination centers. These traps states influence the potential distribution close to the grain boundary. In case of n-type material, the defect levels within the band gap are usually distributed so that the local neutrality level (i.e. the level up to which the states are filled when the interface is neutral) lies closed to the center of the band gap than the Fermi level of the doped semiconductor. These states trap electrons, giving rise to a plane of fixed negative charge at the interface, and a layer of positive space charge on either side where the n-type material had been depleted. The electrostatic force sets up a potential barrier which opposes further migration of electrons. For p-type material the situation is analogous and a barrier opposing hole flow is established [88].

2.2.2 TCOs for plasmonics

The investigation on TCOs for plasmonic application is an emerging field, which has attracted attention because of the possibility to supply some limitations of traditional plasmonic materials, under specific doping conditions as already explained. Fig.2.3 reports the real and imaginary parts of dielectric function extracted from elipsometric measurements of three different TCOs, namely indium-tin-oxide (ITO), Ga:ZnO (GZO) and Al:ZnO (AZO). All the films were deposited by pulsed laser deposition and ellipsometric data were fitted by a Drude-Lorentz model, showing a metal-like optical behavior in near-IR. For a better comparison between optical properties of these materials, Fig. 2.4 shows the cross-over frequency (i.e. when $\epsilon_1 = 0$) and the Drude damping rate (γ) as a function of dopant concentration [69]. Notably, AZO films showed lower losses with higher doping because of good crystallinity of highly doped films, while the highest cross-over
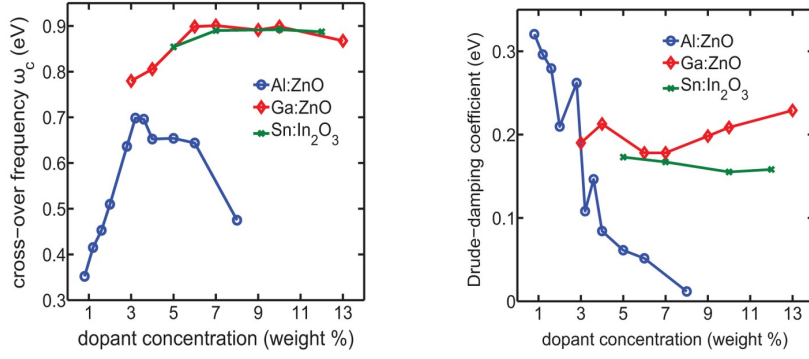
Figure 2.4: *Cross-over frequency (i.e. $\epsilon_1 = 0$) and Drude damping coefficient (γ) of pulsed laser deposited ITO, AZO and GZO films as a function of respective doping concentration [69].*
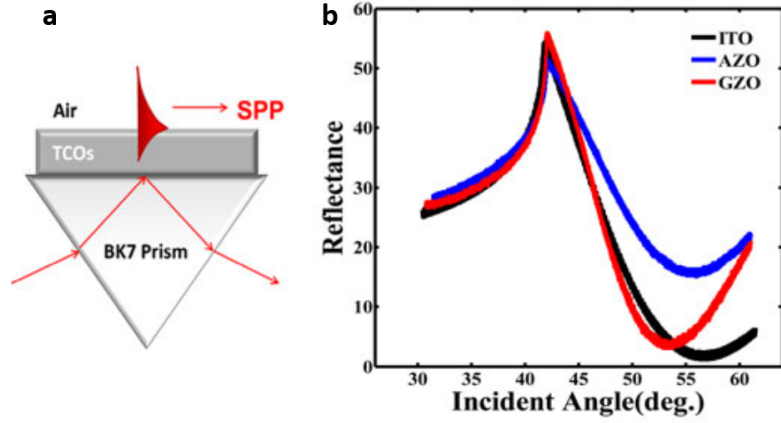

Figure 2.5: *(a) Schematic representation of the experimental setup for SPP excitation in attenuated total reflection; (b) reflectance curve as a function of the angle of incident light (at $\lambda = 1548 nm$) for ITO, AZO and GZO films [93].*

frequency reached is smaller with respect to GZO and ITO because of lower carrier density available. This difference was related to the different dopant solubility limit among materials as well as the effectiveness of doping itself. Moreover, TCOs demonstrated to support SPP excitation at the interface with dielectric materials in many research works [89–93]. Fig.2.5 reports the reflectivity measurements at different incident light angle at fixed wavelength (i.e. at $\lambda = 1548$ nm) for films of ITO, GZO and AZO by exploiting Kretschmann geometry to set the excitation (schematically reported in Fig.2.5a). The dips in the curves correspond to the SPP excitation which occurs in the near-IR range.

Besides, LSPR excitation of doped metal oxide nanocrystal is an expanding research area. Indeed, in case of TCOs, LSPR is tuned not only by size and shape like in traditional plasmonic materials, but also charge carrier density and doping level can play a role. Della Gaspera *et al.* synthesized ZnO nanocrystals doped by three different metal cations, namely Al, Ga and Ir [94]. They found a blue-shift of LSPR from about 7.5, to 5, to 3 μm for AZO, GZO and IZO nanocrystals respectively. This blue-shift was correlated to the increase in carrier density, because each doping element has a different doping efficiency.

Optical metamaterials and optical modulators are emergent fields which can include TCOs in the form of either compact thin films or nanoparticles. In the first field, very thin films can be involved, therefore the study of optical properties of TCO thin films should consider the dependence on thickness, especially for films thinner than 50 nm [66]. In the second field, TCOs are convenient choice because they have demonstrated the ability to switch from dielectric to plasmonic behavior by the application of a moderate electric field. For example, Feigenbaum *et al.* showed that refractive index of ITO and In-doped ZnO (IZO) changes on the order of one in the visible range when subjected to an external electric field [95]. For this experiment, they built a capacitor by sandwiching 300 nm of a TCO film and 100 nm of silicon oxide between two gold layers. The application of a voltage produced an accumulation of carriers at the TCO/silicon oxide interface. A 5 nm-thick layer accumulates electrons at the interface, which exhibits a refractive index change on the order of one at visible frequencies. This *active modulation* of material properties is an interesting feature of TCOs, and besides electric field applications, it is possible with other external stimuli such as light or solvents. Instead, the tuning of plasmonic response as well as other properties by means of varying morphology, dopant (what and how much) and defect stoichiometry is known as *passive modulation*.

Other important characteristics of TCOs useful for the application in plasmonic field are the possibility of their deposition on many different substrates, including flexible polymers as well as patterning on the micro- and nanoscale using standard fabrication techniques [93, 96–98]. In particular nanostructured TCOs can be made by means of electron-beam lithography followed by reactive-ion etching, wet chemical etching or lift-off. This would be an advantage in applications where features of nanosize can determine the material's behavior. For example, Fig.2.6 reports nanodisk array of GZO obtained by etching, which sustains LSPR excitation, while distance between nanodisk play a role in the tuning of resonance peak width.

Finally, another fascinating perspective is the integration of nanostructures of traditional plasmonic materials in TCO thin films. The aim is the possibility to tune the LSPR frequency of embodied nanostructures (e.g. Au NPs) by changing the dielectric constant of the surrounding TCO matrix, which can be modulated in turn in the active way or passive way, as already explained [99, 100]. On this basis, plasmonic nanostructured sensor can be developed by exploiting LSPR dependency on dielectric constant of the surrounding, which depends in turn on change in environment in case of TCOs [101]. Moreover, the embedding of plasmonic metallic nanostructures in TCOs would be interesting also to implement plasmonic functionalities in the visible range as well as improve TCO's electrical conductivity, keeping high transparency, in devices where these materials have already a key role [102–104]. However, the employment of a TCO matrix as a mean to further tailor the LSPR of embedded plasmonic nanostructures is scarcely studied so far, but the knowledge already acquired about these materials can be combined in perspective of multifunctional devices.
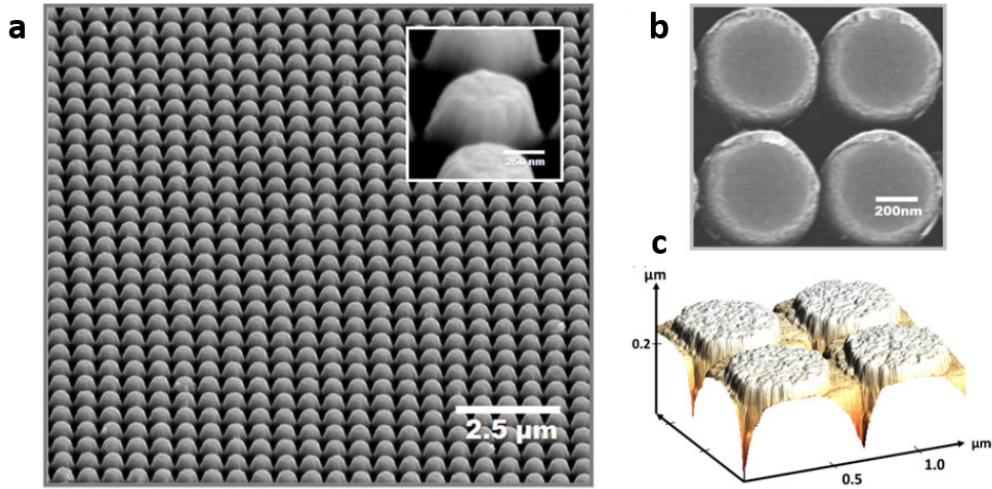
Figure 2.6: *(a,b) Tilted and top view SEM images of an array of GZO nanodisks with a mean diameter of 500nm and height of 270nm and (c) AFM scan of the same system [93].*

2.2.3 Titanium dioxide based TCOs

Titanium dioxide has been widely investigated for energy conversion and photo-catalytic applications because of its activity, low-cost, non-toxicity and chemical stability [55]. In addition, TiO_2 is commonly employed as photoanode in dye sensitized solar cells thanks to its electronic band alignment with the active component of the cell, and it is a promising photo-absorbing material for photovoltaics and photocatalysis [105–107]. TiO_2 can be synthesized by both chemical and physical processes: sol-gel methods, spry pyrolysis, molecular beam epitaxy (MBE), chemical vapour deposition (CVD), sputtering, and pulsed laser deposition (PLD) [108]. However, TiO_2 based TCOs have been predominantly produced only through the latter two techniques [109–112].

The most common crystalline phases of TiO_2 are rutile, anatase and brookite. Rutile is the stable form and has a cubic cell, while anatase and brookite are metastable with thetragonal cell [113], as represented in Fig.2.7. Among TiO_2 allotropes, anatase is the most attractive because of its band gap equal to 3.2 eV and low conduction-band effective mass, around $1\,m_e$ (even if the actual value depends on direction since the anisotropy of structure, as discussed below) while rutile presents 3.0 eV and $20\,m_e$, respectively [55, 114]. TiO_2 conductivity can be improved by n-type doping, which consists in substitutional dopant atoms whose excess electrons are transferred to the conduction band of the matrix [116]. Nb- and Ta-doped anatase are the most studied TiO_2-based TCO. Experimentally both films epitaxially grown via pulsed laser deposition (PLD) showed very similar resistivity, around $2 - 3 \cdot 10^{-4}\,\Omega cm$, suggesting almost identical electrical conduction mechanism, with a resistivity comparable to commercial polycrystalline ITO [109, 110]. However, the resistivity of Nb and Ta:TiO_2 polycrystalline films resulted higher than corresponding epitaxial films and strongly dependent on dopant content and film structural properties, which implies a correlation on synthesis conditions. Moreover, electrical properties demonstrated to be depen-
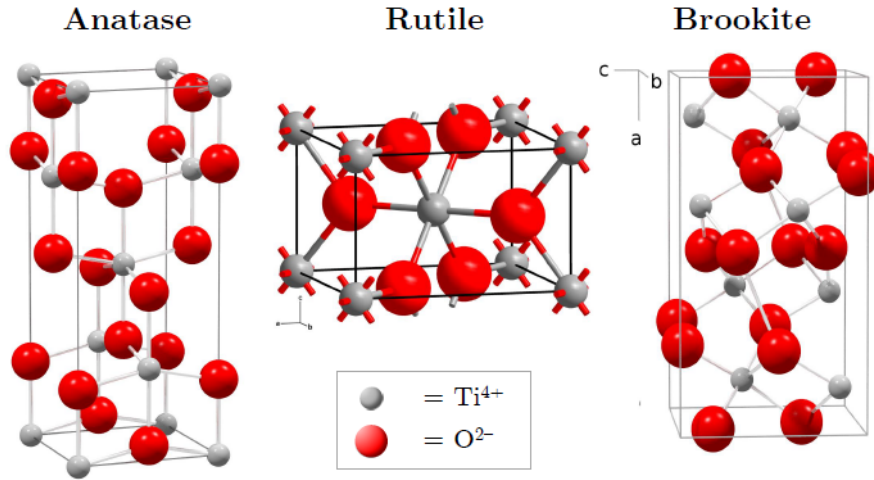
Figure 2.7: *Unit cells of* TiO_2 *allotropes: anatase (left), rutile (middle) and brookite (right). Reproduced from [115].*

dent on oxygen stoichiometry and, in particular, the optimal values occurred for a certain amount of oxygen deficiency. Indeed, the formation energy of $Nb:TiO_2$ and $Ta:TiO_2$ was calculated very low under Ti-rich-O-poor condition, while oxygen-rich conditions promote electron acceptor defects, namely cationic vacancies and oxygen interstitials, which reduce conductivity [116–119].

$Nb:TiO_2$ has gained greater attention because computational studies reported lower distortion of the crystal lattice than $Ta:TiO_2$, which means potentially better charge carrier mobility and crystal growth. On the other hand, Ta is reported to have both higher solubility in anatase and lower effective mass in band structure than Nb, which favors the mobility [120, 121]. Even if this can be moderately relevant for transparent electrode applications, because optimum electrical properties are often associated to a rather low doping density, it would be crucial in plasmonic field, where high doping density is often required, in fact increasing the carrier density is the only practical way to increase the plasma frequency of the material. However, an increase of the effective mass works in the opposite direction (see Eq.1.7), for this reason $Ta:TiO_2$ is a more promising material for plasmonics. In addition, as already mentioned, the effective mass (m^*) of electrons in the conduction band of anatase single crystals is expected to show anisotropy, because of the anisotropy of the anatase tetragonal crystal structure. In literature, theoretical calculations of m^* for both Nb- and Ta-doped anatase and experimental work on Nb-doped TiO_2 confirmed anisotropy [121–123]. In particular, theoretical calculation for $Ta:TiO_2$ films reported an orthogonal effective mass (m_x^*) and a parallel one (m_z^*) with respect to tetragonal axis (also called $\vec{c}$), which resulted equal to 0.4-0.6 m_e and higher than 3.5 m_e, respectively. Moreover, calculations predict an increase of m_z^* with charge carrier concentration [121].

The effects of effective mass anisotropy on the plasmonic responce have been discussed by Dahlman *et al.* for the LSPR of Nb-doped anatase nanocrystals [124]. Here, the high mobility along x-axis scatters more the incident field than the z-axis, indeed the IR absorption of a dilute solution of $Nb:TiO_2$ nanocrystals

in tetrachloroethylene demonstrated to depend on the averaged projection on the incident field in the anatase unit cell orientation for each particle. In fact, nanocrystals oriented with the maximal projection of the incident field along x-axis ($\vec{E} \perp \vec{c}$) have significantly higher amplitude and energy LSPR absorption than nanocrystals oriented with a minimal projection along the x-axis ($\vec{E} \parallel \vec{c}$). Furthermore, the simulated isotropic averaged spectrum have a similar peak energy and broadness to the $\vec{E} \perp \vec{c}$ projection spectrum, but with only about 70% of amplitude. This study indicates that the observed broadness and low peak energy of LSPR absorption in n-doped TiO_2 nanocrystals can be attributed primarily to crystalline anisotropy and intrinsic scattering. As a consequence, the particle orientation presents an additional source of IR modulation for birifringent semiconductor nanocrystals.

Sine in this work polycrystalline Ta-doped anatase thin films are considered, the effect of anisotropic effective mass is expected mediated by different crystallites orientations, however it was taken into account when considering optical properties in Chapter 5.

2.2.3.1 Polycrystalline Ta:TiO_2 thin films and previous works

A previous study of Ta-doped TiO_2 thin films was performed by P. Mazzolini in our research group as transparent electrode for solar cell application [112, 125–127]. Here, we report main achievements of this work, that would be functional for the purpose of this thesis. Ta:TiO_2 thin films were deposited via PLD on soda-lime glass and Si (100) substrates, followed by an ad hoc annealing treatment in vacuum in order to obtain polycrystalline films in anatase phase. Films thick ~ 200 nm with a nominal content of Ta equal to 5% at. were studied in order to find the optimal condition of electrical properties and transparency. A strong dependence of electrical and optical properties on background pressure of oxygen during deposition was found (see Fig.2.8), indeed oxygen stoichiometry of the films was affected by such synthesis parameter as well as post-deposition thermal treatment atmosphere. In particular, oxygen sub-stoichiometry demonstrated to favor Ta:TiO_2 films conductivity, therefore annealing in vacuum was necessary, while annealing in atmosphere where oxygen is present turned out detrimental for electrical properties. The lower resistivity corresponded to $5 \cdot 10^{-4}\,\Omega$cm and it raised at 1.25 Pa, while it increases gradually with pressure (up to 2.25 Pa) as well as it falls down at lower pressure (i.e. 1 Pa). The resistivity trend could be explained by measured charge carried density and mobility behavior (Fig.2.8). For pressures lower than 1.50 Pa, the carrier density is almost constant, with a value of $\sim 10^{21}$ cm^{-3}. Above such threshold, the number of carriers monotonically decreases with increasing pressure. Even mobility decreases with pressure above optimal value (~ 10 cm^2/Vs), and the falling down of electrical properties at 1 Pa was related to the appearance of macroscopic cracks which break down carrier mobility. To the best of our knowledge, the optimal value of resistivity found in this work is still the state of the art value for polycrystalline Ta:TiO_2 films. Then, the possibility of depositing films with increasing carrier density was exploited to evaluate the effect of Moss-Burstein on material properties. Optical band gap was calculated by means of Tauc plot and a shift from bare anatase gap was found as a
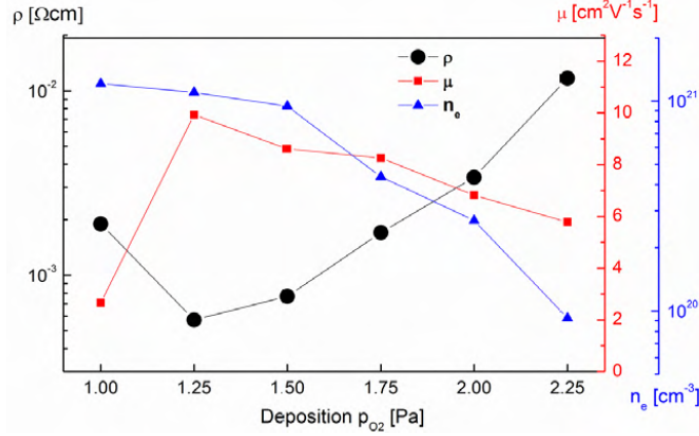
Figure 2.8: *Electrical properties (i.e. resistivity ρ, charge carrier density n and Hall mobility μ) of* Ta:TiO$_2$ *thin film as function of oxygen partial pressure during deposition. Electrical measurements were performed after thermal treatment in vacuum [125].*

function of carrier density, as expected from Moss-Burstein effect. This shift was exploited to estimate effective mass according to the Eq.2.1, finding $m^* = 2.9\, m_e$, which in turn was employed to estimate plasma wavelength (see Eq.1.7), resulting equal to 4160 nm. These preliminary results of optical properties will be take into account and further investigated in this work in Chapter 5. Finally, another result that cannot be ignored consists in the modification of anatase Raman spectrum as a function of carrier density. The typical anatase spectrum presents six well known Raman peaks: $E_g(1)$ at $144\,cm^{-1}$, $E_g(2)$ at $197\,cm^{-1}$, $B_{1g}(1)$ at $399\,cm^{-1}$, $B_{1g}(2)$ at $519\,cm^{-1}$, A_{1g} at $513\,cm^{-1}$, and $E_g(3)$ at $638\,cm^{-1}$. Since the A_{1g} and the $B_{1g}(2)$ peak are very close, they cannot be distinguished at room temperature. Fig. 2.9a reports the typical Raman spectrum of Ta:TiO$_2$, both as deposited (i.e. amorphous), and after annealing, where anatase peaks are clearly visible. Mazzolini P. et al. noticed that the most intense peak of anatase Raman spectrum (i.e. $E_g(1)$) acquired a non-negligible shift to higher wavenumber as the carrier density was increased. An almost linear dependence of the peak position on the carrier density was reported, and it turned out to be essentially independent on the doping concentration and on the type of dopant (see Fig.2.9b). In this framework, Raman spectroscopy can be employed not only for structural investigation (since anatase has spectrum which differs clearly from other allotropies of TiO$_2$) but also to have a qualitative evaluation of doping efficiency in doped TiO$_2$ films.

2.3 Titanium nitride

In section 2.1 transition metal nitrides have been presented as a class of material studied to supply limitations of traditional metals used in plasmonic field. Among them TiN is the most interesting candidate because its unique properties that are potentially advantageous in plasmonic applications.

The most stable and durable phase of TiN is B1-TiN (also known as δ-TiN, with Fm3m symmetry) characterized by a cubic rocksalt structure and bright yel-
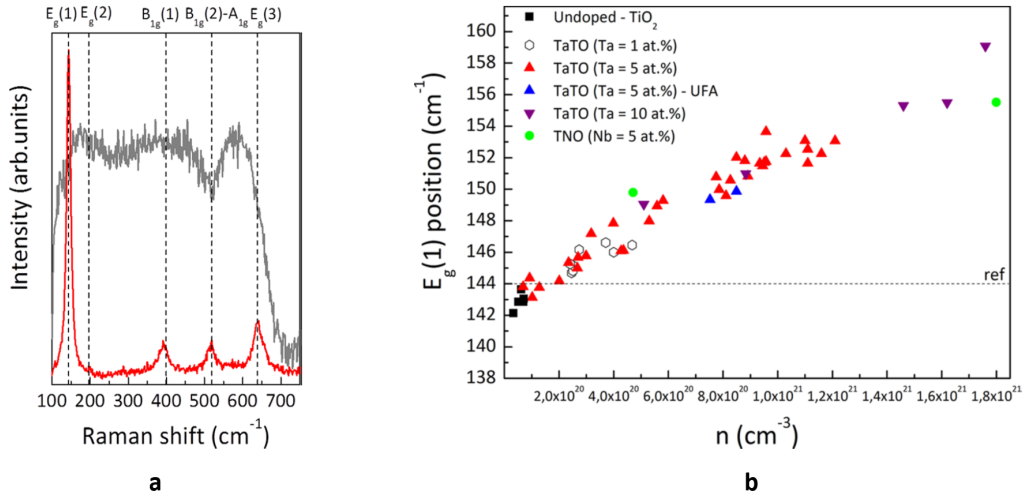
Figure 2.9: *(a) Raman spectra of* Ta:TiO$_2$ *as deposited (grey) and after vacuum annealing (red), anatase's Raman active peak positions are indicated as well (dash lines); (b)* $E_g(1)$ *peak position as a function of measured charge carrier density. Both pictures are reproduced from [126].*

low color. This material is a well-established in various industrial sector because it is characterized by very high hardness, strong resistance towards abrasion and corrosion, relative inertness, low friction coefficient and high chemical and thermal stability (i.e. melting point is equal to $\sim 3000°$C) [128, 129]. Therefore, TiN has already found application as protective coatings and cutting tools as well as it is an appealing material for decorative applications due to its gold-like bright yellow appearance and color tunability by simply varying stoichiometry [130, 131]. Another important application involves semiconductor industry, where TiN is widely employed as diffusion barrier in CMOS manufacturing process [132]. In addition, TiN presents metal-like electron conductivity and mobility that, combined with refractority, make it a valid candidate for Ohmic and Schottky contacts in microelectronic devices [133, 134]. Finally, TiN can be used to protect underlying materials in orthopedic prosthesis thanks to its non-cytotoxical nature [135]. The study of TiN for plasmonic applications is more recent, but promising results have been already reported in literature. For example, TiN was found an active and stable plasmonic material with LSPR ranging from UV to IR and, combined with its refractory character, it results suitable for high temperature/high power plasmonics, photothermal applications and, considering TiN low work function (~ 3.75 eV), plasmon-enhanced electron emitters [136–140].

Such application are not affordable by noble metals due to their lower melting point as well as higher work function [141].

Before moving forward, we need to highlight the most stable phase of TiN will be considered for this work, i.e. B1-TiN (also known as δ-TiN), which is a cubic rocksalt crystalline structure. Other crystalline phases, such as Ti$_2$N and Ti$_3$N$_4$, will not be taken into consideration because they are less stable and present very different material properties [78].
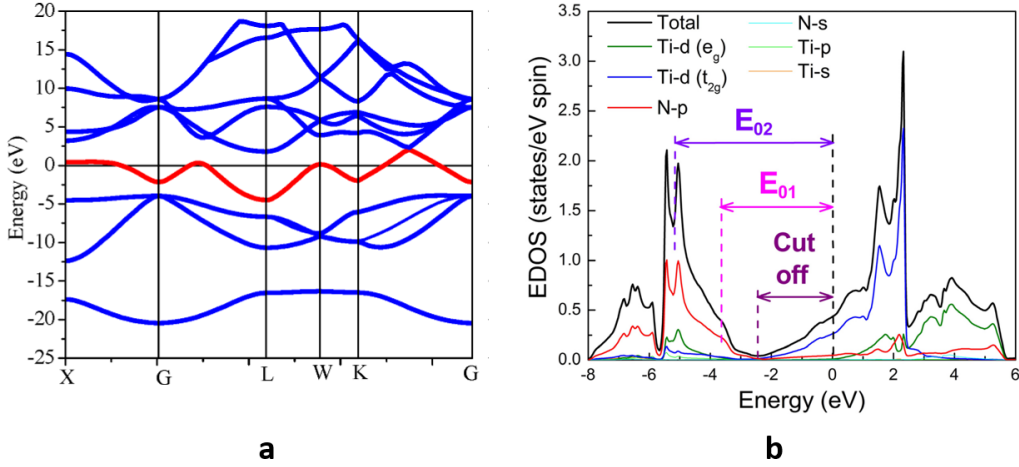
Figure 2.10: *(a) Band structure and (b) energy density of state (EDOS) of B1-TiN, where the zero energy corresponds to Fermi level. Reproduced from [143] and [77], respectively.*

2.3.1 Optical and electrical properties of TiN

TiN and other transition metal nitrides exhibit electronic conductivity due to the partially filled valence d orbitals that are not completely hybridized with N-$2p$ electrons [142, 143]. Moreover, under favorable synthesis conditions, TiN emerges as a good optical conductor too, which means that interband transitions are distant from the region where optical plasmonic performance are desired (i.e. valence electrons are strongly bound and have quite deep energy with respect to Fermi energy, E_F), implying ϵ_1 negative with a clear steep crossing positive values, while ϵ_2 smallest as possible in the entire spectrum in order to minimize optical losses. The overlap between intraband and interband absorption leads to a flatter slope of ϵ_1 and higher values of ϵ_2 in the visible range [78]. This behavior can be understood by considering B1-TiN electronic structure. Fig.2.10 reports TiN band structure and the calculated electron density of states (EDOS). Notably, two main energy regions of occupied states are distinguishable. The first one occurs from -8 eV to -3 eV (zero energy corresponds to E_F). Here the hybridization between Ti-$3d$ and N-$2p$ is strong and, as a consequence, EDOS shows a shoulder and a peak around -3.5 eV and -5.5 eV, marked with E_{01} and E_{02} respectively in Fig.2.10b. They are responsible for two absorption bands in TiN absorption spectra, mainly due to N-p electrons going to the unoccupied metal-d states above Fermi level. In particular, EDOS is non-zero starting from about -2.5 eV (below E_F) and this represents the threshold at which the dielectric losses contribute to the optical response of TiN, called *cut-off energy*. The second region is from -3 eV to E_F, in which d-electrons of Ti are present in greater number and, those not involved in the bond with N, are responsible for electronic conductivity of TiN, because of this interception of d-electron valence band with Fermi level.

A fascinating feature of TiN consists in the significant variation of optical properties as a function of films stoichiometry and composition because of their role over electron losses and density, as showed in Fig.2.11, where some examples of ϵ_1 reported by several groups in literature are collected. This scattering of the ϵ_1
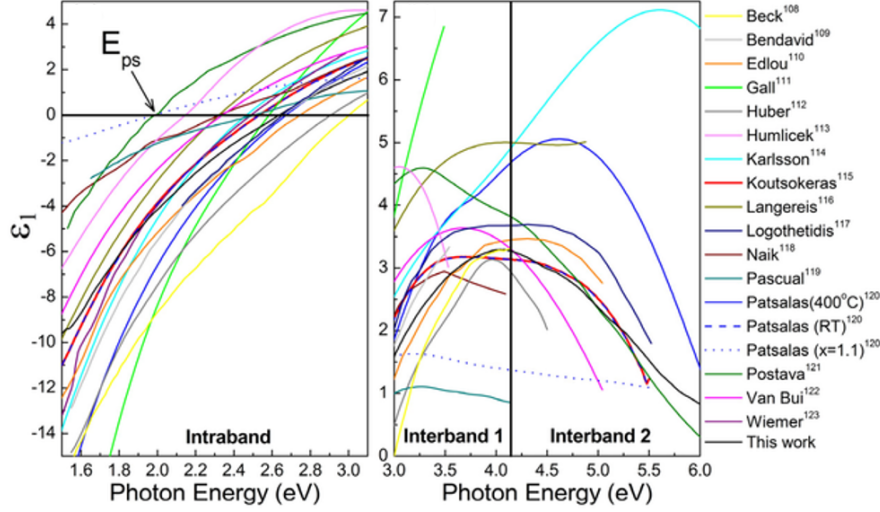
Figure 2.11: *Real part of dielectric constant (ϵ_1) of TiN reported by several groups. For citations in the picture, refer to [77].*

experimental values and the high tailoring potential of TiN are two of the main reasons why this material is the most studied transition metal nitride for plasmonics. However, in addition to stoichiometry, TiN electrical and optical properties are affected by other properties such as crystallinity and surface oxidation, which strictly depend in turn on synthesis conditions, as explained later. All these contributions make challenging the understanding and the fine tuning of electrical and optical properties of TiN, which consists in a open issue of this work.

According to the important role of interband transition on optical behaviour, the energy where $\epsilon_1 = 0$ is called *screened plasma energy* (E_{ps}), which coincides with *unscreened plasma energy* considered in Eq.1.7 only in case of ideal conductors (i.e. without any bound electrons). As explained in section 1.2, for energy higher than E_{ps} (where $\epsilon_1 > 0$) light can propagate in the material, while for energy lower than E_{ps} (where $\epsilon_1 < 0$) reflection occurs due to the interaction between light and conduction electrons. TiN stoichiometry affects directly E_{ps} value, that has been reported ranging from 2 to 2.95 eV, affecting the color. At stoichiometric conditions (i.e. TiN_x with x=1), E_{ps} was found equal to 2.65 eV and TiN surface shows bright-yellow appearance, while overstoichiometric TiN (x>1) appears reddish-brown and more opaque as well as substoichiometric one (x<1) tends to a more grey aspect [78, 144]. Indeed, the increase of nitrogen content means that the number of free electrons decreases, reducing the light reflected by the film as well as its brightness. Moreover, since the unscreened plasma frequency is proportionally depending on the carrier density, a higher nitrogen content leads to a lower free electrons density and, as follows, to a red-shifted plasma reflectance edge [145].

Braic et al. studied the effect of composition on TiN film optical properties, focusing on how oxygen content of titanium oxynitride TiO_xN_Y films affects epsilon-near-zero behavior (i.e. around $\epsilon_1 = 0$, ENZ) [146]. In particular, they grew films via reactive magnetron sputtering at different levels of residual oxygen in the background vacuum. They found that for oxygen partial pressure
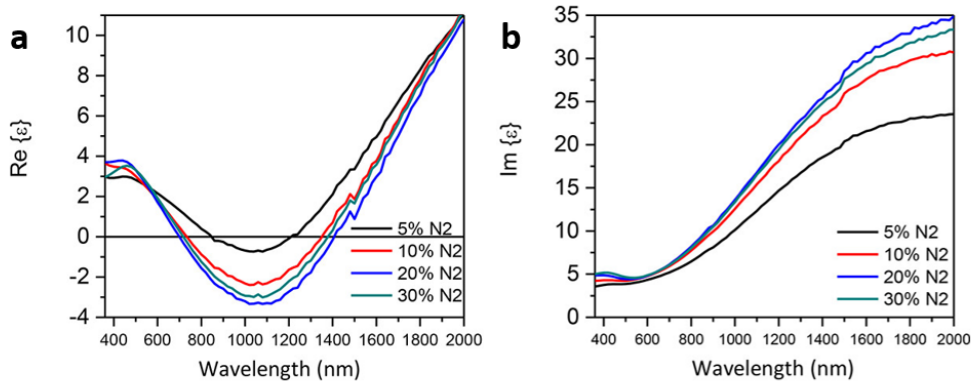
Figure 2.12: *(a) Real and (b) imaginary parts of the dielectric constant of* TiO_xN_y *films deposited at different nitrogen partial pressure [146].*

(P_{O2}) above $2.67 \cdot 10^{-6}$ Pa, the films exhibit nonmetallic behaviour; for P_{O2} below $6.67 \cdot 10^{-7}$, films show a metallic behavior, while between these two ranges, authors discovered an unusual double-ENZ in visible near-IR range, whose positions were tunable by the level of residual oxygen and partial pressure of nitrogen during deposition, as shown in Fig.2.12. This peculiar behavior could be exploited for designing the enhanced nonlinear optical response and metasurfaces.

Naturally, electrical properties of TiN show a dependence on stoichiometry as well, due to the way they rule on free electrons, as already discussed. Moreover, even crystallinity and microstructure play an important role in the definition of the overall film resistivity. Meng et al. deposited TiN films via DC reactive magnetron sputtering and they investigated the effect of nitrogen partial pressure on film properties [147]. X-ray diffraction analysis found that by increasing the nitrogen pressure, the (111) TiN peak intensity decreases, while the (200) diffraction peak intensity increases, suggesting a modification of the film crystallographic orientation, as well as an improved stoichiometry. The preferred orientation may affect resistivity because electronic bands may be varied with crystal orientation. Moreover, they found that even grain size enlarged as the nitrogen partial pressure increases. Indeed, the lowest resistivity was measured for higher pressure of N, which exhibit quite stoichiometry and larger crystal domains (see Fig.2.13a). Reflectivity measurements agreed with these results (see Fig.2.13b), reflectance intensity increases with nitrogen partial pressure as well as minimum red-shift. The effect of microstructure and stoichiometry on electrical and optical properties was studied by several other authors, testing also different synthesis techniques or involving other synthesis parameters (e.g. temperature) [148–151]. Composition plays a key role too. Mihailescu et al. deposited TiN films via laser reactive ablation and studied the effect of N background pressure [152]. In the range of 0.7-7 Pa, N atoms resulted enough to nitride all ablated Ti, while oxygen contamination was limited to film surface. Conversely, for higher pressure TiN presence gradually vanishes because oxygen progressively accommodate in the crystal lattice, leading to the formation of oxynitride compound TiN_xO_{1-x}. From electrical measurements, they found a conductivity of 2-$5 \cdot 10^4 \, \Omega^{-1} cm^{-1}$ for film deposited
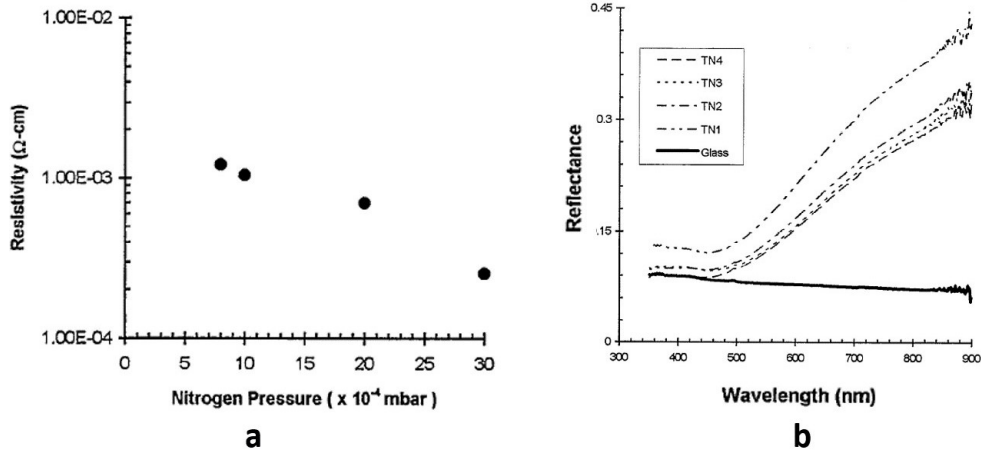
Figure 2.13: *TiN films (a) resistivity and (b) optical reflectance (b) as a function of nitrogen partial pressure. In (b) TN1, TN2, TN3 and TN4 correspond to N pressure of 0.3, 0.2, 0.1, 0.08 Pa, respectively [147].*

at low N pressure, while it decrease of one order of magnitude at 10s of Pa, up to non-measurable films at 100s Pa. This study highlights the extremely high chemical activity of Ti in presence of oxygen contamination and the subsequent strong impact on material properties, which is crucial point in the choice of synthesis parameters in order to obtain a good TiN films. This important item will be discussed deeply in section 2.3.3.2.

2.3.2 TiN for plasmonics

TiN has been studied as a possible candidate to substitute noble metals in visible and near-IR, as a matter of fact TiN films and NPs showed the ability to sustain SPP and LSPR excitations. As a first comparison, optical properties of TiN films deposited with three different methods (i.e. PLD, DC magnetron sputtering and non-reactive sputtering) are reported in Fig.2.14 against Au, W and Mo. First, it is clear how TiN offers an additional degree of freedom in the tuning of plasmonic responce due to its non-stoichiometric nature. Then, TiN shows smaller absolute value of negative real permittivity ϵ_1 than Au, but TiN presents also higher ϵ_2 explained with its larger relaxation rates than most noble metals, which increases the losses due to scattering (Ohmic losses) [153]. Naik et al. demonstrated 30 nm-thick TiN film sustains SPP in the near-IR [154]. Angular reflectance was taken at two wavelength, i.e. 900 and 1000 nm, and dips in reflectance was found at 30° and 25°, respectively. Moreover, authors compared the SPP performance in terms of propagation length and confinement width of TiN and Au films interfacing with air (see Fig. 2.15a,b). In particular, two type of Au were considered, ideal one and with loss factor of 3.5 (commonly observed in nanopatterned gold structures). TiN showed a slightly better confined than lossy Au, but propagation length for TiN resulted smaller. In the same way, Fig. 2.15c compares the figure of merit M_1^{1D}, defined as the ratio of propagation length to confinement width for one dimensional SPP waveguides, of TiN against Au and
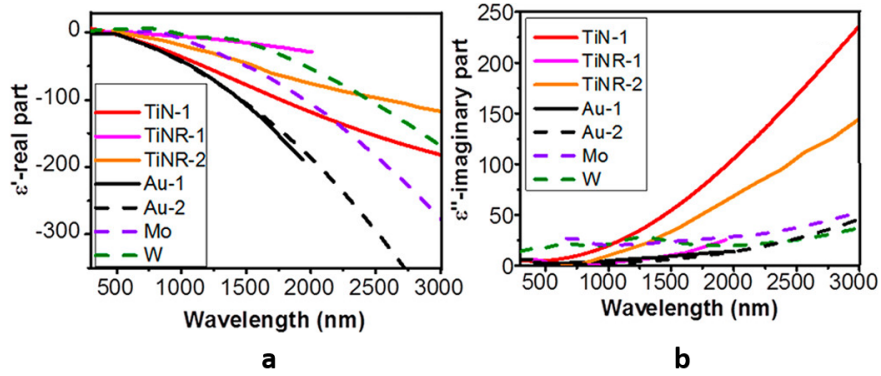
Figure 2.14: *(a) Real and (b) imaginary parts of the dielectric constant of three TiN films deposited via different synthesis methods and Au,W and MO films [153].*
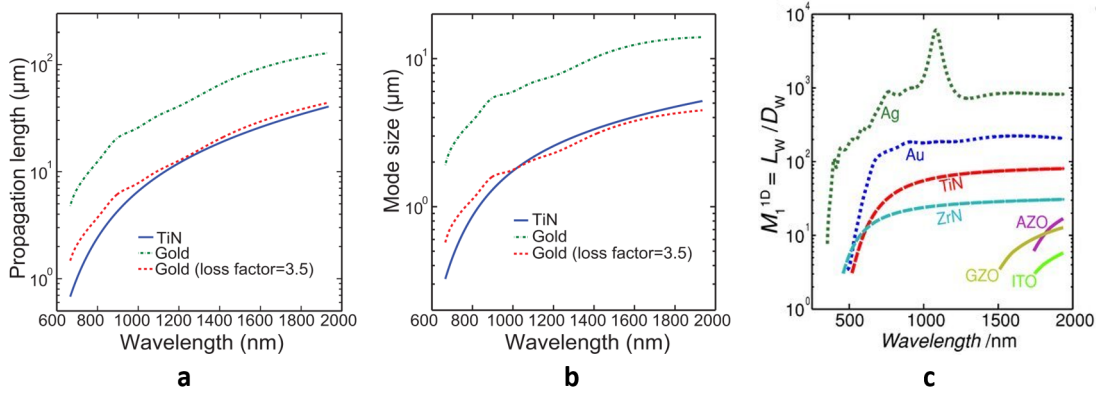
Figure 2.15: *Comparison of the performance of SPP waveguides based on TiN with respect to other materials, in terms of (a) propagation length, (b) mode size, and (c) specific figure-of-merit M_1^{1D} calculated for 1D-waveguides. Reproduced from [66, 154].*

Ag [66]. From Fig.2.15a-c, it is clear how noble metals outperform nitrides for waveguiding applications. Despite worse performance than conventional materials (i.e. Au and Ag), TiN remains a valid alternative where these materials cannot be employed for technological issue, as well as TiN offers more tunability of plasmonic responce.

Naik et al. calculated the enhancement at surface of TiN NPs due to LSPR by using quasistatic dipole approximation and compared results with Au NPs [154]. The resonant wavelength obtained for TiN NPs was red-shifted compared to Au, as expected from smaller absolute real permittivity (see Fig.2.14), while the magnitude of field enhancement was slightly smaller than that of Au. However, the overall performance of each material was comparable, making TiN NPs a realistic alternative for LSPR plasmonic applications. Guler et al. compared the optical transmittance of disk-shaped NPs (30 nm-thick) of TiN and Au in the visible and near-IR [136]. Fig 2.16 shows the results for two Ti NPs array grown at two different temperature (i.e. 400 and 800°C), clearly showing the tunability of TiN nanostructures by varying growth parameters. In these graphs, the biological
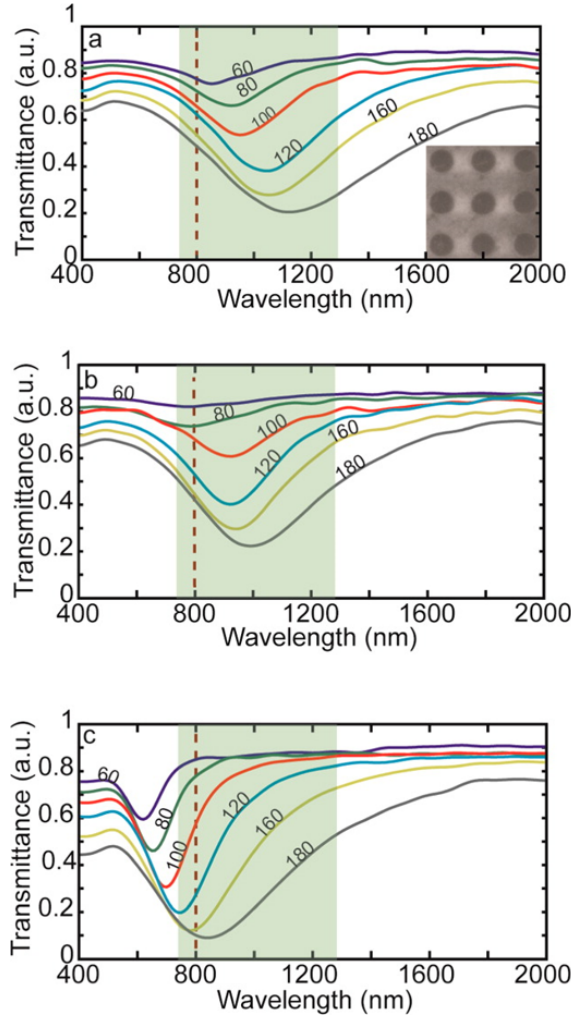
Figure 2.16: *Transmittance spectra of 30 nm-thick disk array of TiN grown at (a) 400°C, (b) 800°C and (c) Au. Disk's diameters are indicated in nm on curves with different colors; green regions indicate the biological transparency; inset in (a) shows nanodisk pattern [136].*

transparency window is indicated in green, because authors intended to evaluate TiN NPs as alternative local heat plasmonic sources in this specific region of the electromagnetic spectrum. It is evident that LSPR peak of TiN can cover better this region with respect to gold, playing with NPs size and growth condition.

For far field applications, it could be convenient to measure the performance of TiN NPs with respect to gold in terms of scattering efficiency; on the other hand, in case of devices based on local heating, the quality factor considered is the absortion efficiency [145]. Fig.2.17 shows that in both cases, Au and TiN NPs peak intensities are rather similar, but TiN NPs have a much broader peak whose resonance elongates towards the near-IR, emerging as a better candidate for this range. Moreover, the very high melting point of TiN should be taken into account for high temperature and power applications. For example, Li et al. fabricated a braodband absorber (i.e. 95% light absorption in the range 400-800 nm) using three layer TiN metamaterial schematically represented in Fig. 2.18a.
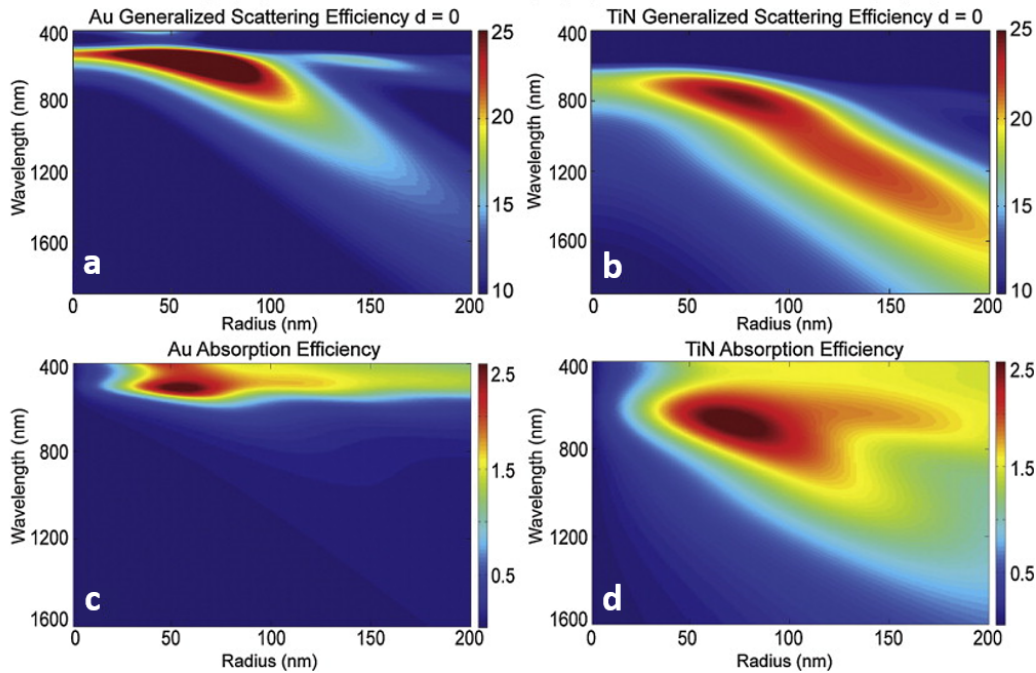
Figure 2.17: *Near field intensity efficiencies, showing the field enhancement at NP surface, and absorption efficiency calculated for (a,c) spherical Au and (b,d) TiN NPs, varying radius [145].*

The top layer is composited by 30 nm-thick TiN square ring-like unit cells, with outer and inner side length of 250 and 150 nm, respectively, and periodically distributed along x and y-directions with a pitch of 300 nm. Second layer consist in 60 nm-thick SiO_2 film and the back layer consist in a TiN film thicks 150 nm. In contrast with noble metals which utilize only plasmonic resonance to achieve high absorption, the TiN broad absorption is due to the combination of both intrinsic losses of the material and the plasmonic resonances due to a plasma frequency (here in the visible range). Furthermore, due to its high melting point and the combined absorption mechanisms, the TiN absorber can work at high temperatures and under strong light illumination not affordable to noble metals, as shown in Fig. 2.18b-e.

2.3.3 Synthesis of TiN thin films and nanostructures

Titanium nitride demonstrated to be a very tunable material in terms of microstructure as well as electrical and optical properties, due to its non-stoichiometric nature strongly dependent on the employed synthesis technique. For this reason a deeper discussion on fabrication of TiN thin films, NPs and nanostructers is important for the purpose of this work. Besides synthesis methods, in this section another critical issue of TiN synthesis will be treated, the oxidation.

2.3.3.1 Deposition of TiN thin films

TiN films can be grown by a wide variety of techniques, that could be both physical and chemical, including magnetron sputtering (MS), cathodic vacuum arc, ion
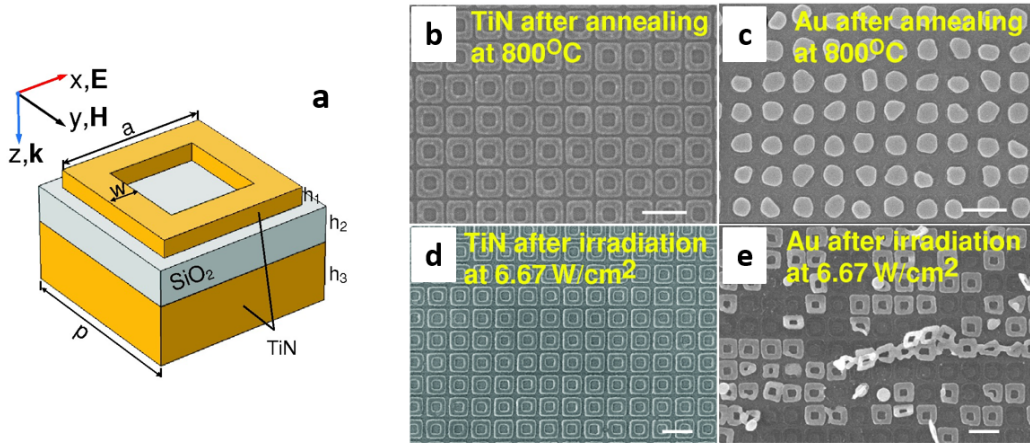
Figure 2.18: *(a) Schematic representation of unit cell of TiN-based metamaterial absorber with dimension a=250 nm, w=50 nm, p =300 nm, h_1=30 nm, h_2=60 nm and h_3=150 nm; SEM images of (b,d) TiN- and (c,e) Au-based absorber after annealing at 800° or shot by a laser with intensity of $6.67 \, W/cm^2$. Scale bars correspond to 400 nm. Adapted from [155].*

beam assisted deposition, atomic layer deposition and pulsed laser deposition (PLD) [151, 156–159]. Since in this work the main synthesis method is PLD, in the following, we will focus on the main features of TiN films deposited by this technique. However, some MS results will be taken into account as an indication of conditions and deposition mechanisms involved, being a physical vapor deposition too.

MS is the most used deposition method for TiN films, thanks to its capability to form uniform and high quality films with rather high deposition rate. Moreover, MS gives a certain degree of tunability of TiN properties by varying deposition parameters, i.e. power and pressure. However, their variability is quite limited, since too high flux of nitrogen or oxygen may contaminate the target surface, loosing its conductivity. As a consequence, MS presents some limitations such as the impossibility to deposit highly porous or nanostructured thin films, and the difficulty to obtain the desired stoichiometry. On the other hand, PLD can overcome these issues thanks to its feature of reproducing easily target stoichiometry/composition and its possibility to obtain nanostructured films built up with NPs assemblies by playing with deposition pressure and laser energy density. More details of PLD working principle are presented in section 3.2.

In literature there are several works that discuss the pulsed laser deposition of TiN films, either from TiN or metallic Ti target, and in this last case we talk about reactive laser ablation, necessarily in nitrogen atmosphere [152, 160–162]. Then, the properties of the obtained TiN films were investigated as function of synthesis parameters, e.g. laser fluence at target surface, N_2 background pressure and substrate heating. Summarizing, the optimal values of laser fluence and N_2 pressure were found in the range of 5-7 J/cm^2 and 1-7 Pa, respectively. Moreover, the substrate was found to present a key role to determine TiN films crystallinity. If lattice matching is provided (e.g. in case of Al_2O_3 and MgO), epitaxial film growth can be achieved, otherwise polycrystalline or amorphous films

are obtained [163, 164]. In addition, substrates heating during deposition can favor high crystallinity and stoichiometry due to the higher ad-atoms diffusion, while limiting oxygen incorporation during film growth. However, oxidation could be a trickier issues related to many variables, e.g. poor vacuum environment or low film compactness, as discuss later [165, 166]. As an alternative to substrate heating, post-deposition thermal treatments can be performed to promote TiN film crystallization [167, 168]. Annealing atmosphere should avoid the presence of any oxygen compound or contamination, therefore thermal treatments in vacuum, pure nitrogen, or a reducing atmosphere with a partial pressure of H_2 are privileged [169–172]. However, even in vacuum conditions, TiN films can suffer nitrogen depletion, probably because nitrogen atoms diffuse from the bulk to surface and desorb, then residual oxygen atom present in the chamber may replace them [172]. It was found that for already crystalline TiN films, vacuum annealing leads to a slight oxidation without any improvement of material properties; on the other hand, thermal treatment represents a way to improve electrical and optical properties of amorphous films. As a consequence, the choice of the optimal temperature for annealing may be challenging, because a good compromise between good crystallization and little oxidation extent has to be found.

However, these synthesis parameters should be taken in consideration just as a starting point, because PLD setups can vary significantly one from the other. For example different laser wavelength can be employed as well as distances among components (e.g. target-to-substrate distance or angle, optics positions).

2.3.3.2 Oxidation issue

An extremely crucial issue when depositing TiN consists in the difficulty to obtain a purely stoichiometric compound, due to titanium higher reactivity with oxygen rather than with nitrogen [169]. Therefore, it is important to know the effect of partial oxidation on structure, electrical and optical properties as well as the identification of synthesis parameters which cause this variation in composition. In this section, oxidation effects on Raman spectra, electrical and optical properties of TiN thin films will be presented, being functional for the characterization and discussion of results of TiN films and nanostructures synthesized in this work.

Trenczek-Zajac et al. studied the effect of oxygen doping on TiN film structure and optical properties [173]. TiON films were obtained by reactive magnetron sputtering and oxygen flow rate η_{O_2} varied from 0 to 1.65 sccm. X-ray photoelectron spectroscopy (XPS) analysis showed that at highest oxygen flow rate (i.e. 1.65 sccm) the excess of oxygen cannot be accommodated anymore in TiN_xO_y, therefore precipitation of crystalline anatase TiO_2 occurred. This work has a significant role showing the modification of Raman spectra with the gradually increase of oxidation, showed in Fig. 2.19a. Before continuing, a specification about Raman characterization of TiN films is needed, even if more details are presented in Chapter 6. In principle, first-order Raman scattering is not allowed in an ideal crystal with rock-salt cubic structure like TiN. However, films deposited by MS or PLD present defects that may be generated from energetic ions or species in deposition mechanism, leading to a reduction of crystal symmetry which induces first-order Raman modes [174]. As a consequence, Raman spectroscopy would be
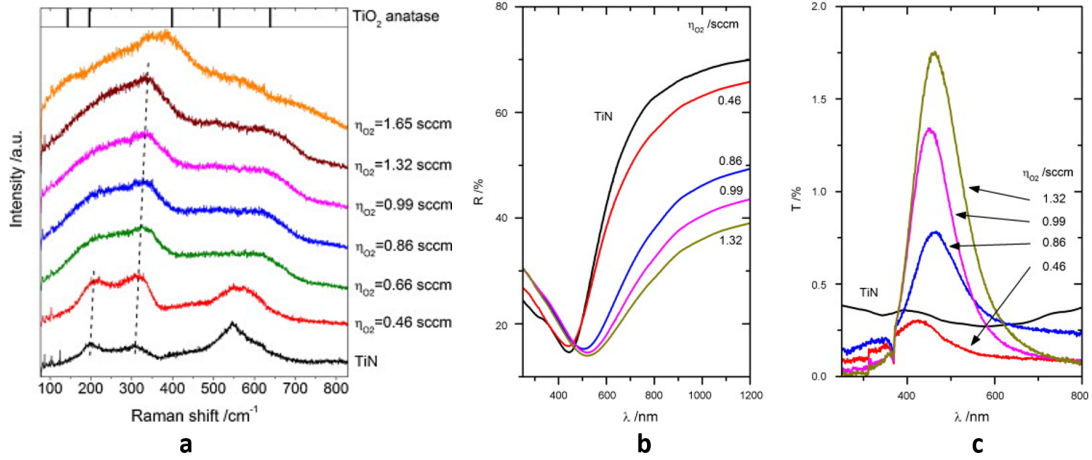
Figure 2.19: *(a) Raman spectra, (b) optical reflectance and (c) transmittance of TiN and oxygen-doped* TiN_xO_y *deposited by reactive magnetron sputtering at different oxygenn flow rate, i.e.* η_{O_2}*=0-1.65 sccm* [173].

a useful technique to check qualitatively the composition of deposited films, considering the relative intensity of acoustic and optical bands as an indication of film stoichiometry. Indeed, acoustic bands occur at $\sim$ 200-215 cm^{-1} and $\sim$ 300-330 cm^{-1} due to transverse acoustic (TA) and longitudinal acoustic (LA) phonons, respectively, and are associated to vibrations of Ti^{4+} ions due to nitrogen vacancies, while optical mode (TO) at $500-600\,cm^{-1}$ is associated to Ti vacancies and vibration of N^{3-} ions. In addition, another peak can be observed at $\sim 440-450\,cm^{-1}$ corresponding to second order scattering of the TA mode [175–177]. However, TiN Raman peaks consist in large bands, lacking sensitivity to the difference between crystalline, defective or amorphous TiN films, therefore also a qualitative interpretation is not straightforward (see section 6.1).

Back to Fig. 2.19a, at η_{O_2}=0-0.46 sccm an increase in the relative intensity of the acoustic bands over the optical band and a shift towards higher frequencies of the transversal and longitudinal acoustic modes indicated a deviation from TiN stoichiometry. In fact, according to many literature papers, a higher $I_{acoustic}/I_{optical}$ ratio is related to a higher number of nitrogen vacancies (i.e. lower N^{3-} ions vibrating) and therefore to a less stoichiometric titanium nitride. At η_{O_2}=0.66-1.32 sccm, Raman bands broad significantly due to the increase of N vacancies, which are easily filled by O, and progressive amorphisation of the film. According to XPS measurements, N/Ti ration was estimated from 0.8 down to 0.35 in these increasing oxygen flow rate conditions. Finally, at η_{O_2}=1.65 sccm, the shape of Raman spectrum changes, indicating the appearance of TiO_2 largely in amorphous phase. On the other hand, when the deposition atmosphere is highly oxidizing, Raman peaks of anatase, rutile or a mixture of the two may appear [178, 179].

Optical properties were studied as a function of η_{O_2} too (see Fig.2.19b,c). At η_{O_2}=0-0.46 sccm, reflectivity spectrum of TiN films did not change, remaining similar to pure TiN. At η_{O_2}=0.66-1.32 sccm, reflectance minimum red-shifted as well as a less steep reflectance edge at long wavelength were observed, up to η_{O_2}=1.65 sccm, where the reflectance dip was lost due to amorphous TiO_2 formation. On

the other hand, stoichiometric TiN is almost opaque with a transmission coefficient of $\sim 0.3 - 0.4\%$, which does not depend on wavelength. While, in case of oxidation a maximum in transmittance appears, which rises and red-shifts upon increasing η_{O_2} (see Fig.2.19c).

Radecka et al. studied the variation structural and electrical properties of TiN films deposited by DC-pulsed reactive magnetron sputtering in Ar:N$_2$:O$_2$ atmosphere, as a function of η_{O_2} too [180]. They used impedance spectroscopy analysis to measure electrical properties and they found a transition from metallic to semi-conducting behavior between the range η_{O_2}=0.46-0.66 sccm, due to TiN$_x$O$_y$ formation and film amorphisation. At $\eta_{O_2} > 1.5$ sccm insulating electrical behavior was found due to formation of amorphous TiO$_2$ precipitates.

By the way, it has to be underlined that a very thin film of native oxide is unavoidable on TiN surface upon air exposure [181,182]. In case of compact TiN films, limited surface oxidation does not affect material properties, while it starts to play an important role in case of porous structure and NPs where the ratio between surface and volume increases, leading to a higher oxidation extent.

TiN nanoparticles

TiN NPs can be synthesized with many different techniques, including direct nitridation of metal powder or metal hydrides, microwaves and thermal plasma techniques and laser ablation in solution [183–186]. Several authors studied the effect of NPs size and stoichiometry on LSPR position and intensity [187,188]. However, few studies treat the oxidation issue related to TiN NPs. Barragan et al. investigated the oxidation of TiN NPs prepared via plasma-enhanced chemical vapor deposition looking at extinction peaks [189]. In particular, he found an unexpected blue-shift of extinction peak by increasing TiN NPs size, contrary to what is expected from Mie theory. This unusual behavior was explained with a different degree of oxidation of NPs surface. Indeed, XPS measurements after air-exposure showed that smaller NPs were nitrogen-deficient and oxygen-rich, while bigger ones were almost stoichiometric and had a lower O content, mostly on surface. In support of this, FTDT simulation of absorption efficiency of TiN NPs with diameter of 10 nm were performed as a function of different degree of oxidation (0-60%). These simulations highlighted the detrimental effect of oxidation on LSPR excitation, showing how plasmonic peak red-shifts, broadens and decreases in intensity. A method proposed to prevent oxidation consisted in a capping layer of silicon-oxynitride, which led to blue-shift, narrowing and enhancement of plasmonic peak with respect to uncoated TiN NPs, combined to a increased thermal stability of optical properties upon air-annealing.

2.3.3.3 Nanostructured and nanoporous TiN thin films

In this section, nanostructured films refers to assemblies of NPs with various size, shape and architectures. Their high surface area combined with nanoporosity make them extremely interesting for several applications. However, nanostructured (or nanoporous) films are very prone to external agents and, in case of TiN, the exposure to air could be detrimental for material properties.
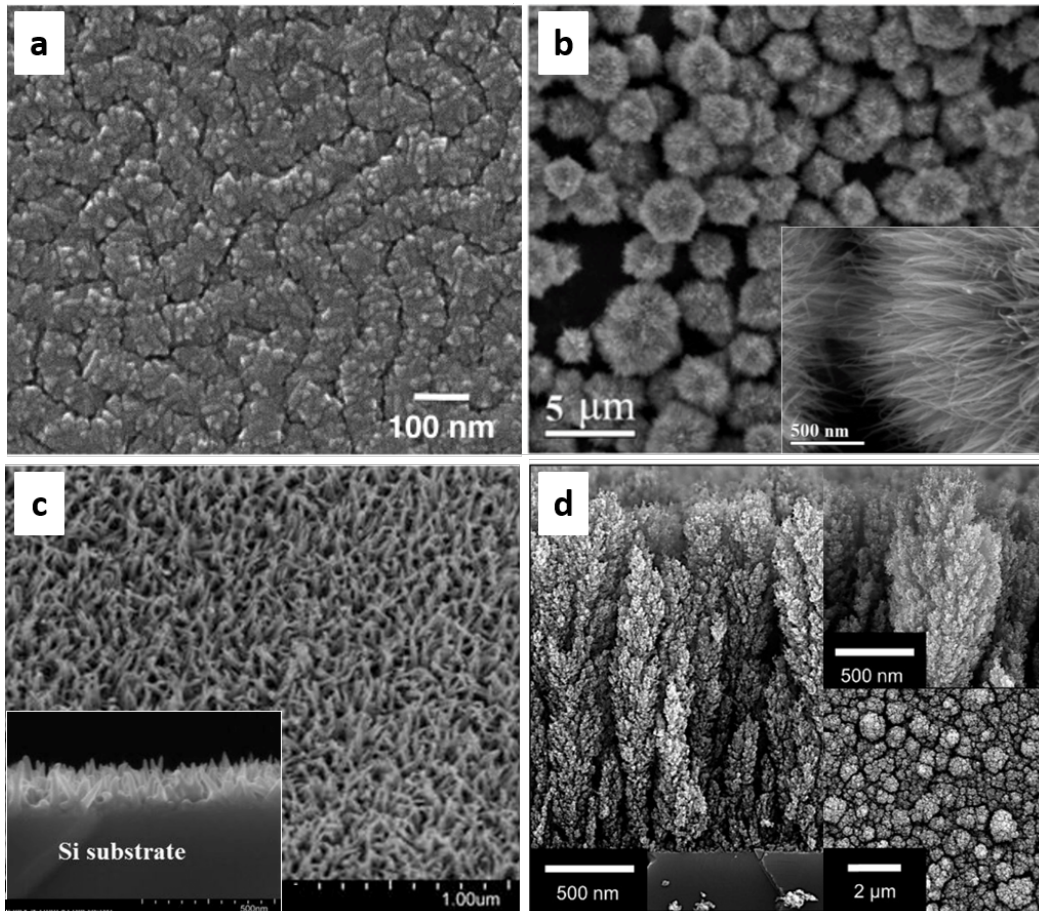
Figure 2.20: *Top view SEM images of (a) wrinkly, (b) hierarchical TiN films, (c) TiN nanotubes and cross-section of (d) tree-like nanostructures, taken from [190, 192, 193] and [194], respectively. Insets show magnification of images taken from another point of view.*

In literature there are some examples of nanostructured TiN films for SERS applications. Kaisar et al. deposited TiN films via reactive sputtering onto a silicone oil coated Si substrate, followed by silicone oil evaporation, obtaining a wrinkled morphology (see Fig.2.20a) [190]. SERS measurements were performed on a probe molecule (i.e. R6G) and a signal enhancement of $\sim 1.3 \cdot 10^4$ was achieved. This result is due to both high porosity and large surface area of this peculiar morphology, which provides a large number of absorption sites, combined with local electric field enhancement at high curvature regions. A very similar result was obtained by Dong et al., that synthesized nanostructured TiN films via nitridation of sol-gel derived TiO_2, focusing to SERS application [191]. A nanoporous structure was obtained thanks to the decomposition of the residual polyvinylpyrrolidone, employed in sol-gel process, during nitridation. Here, the Raman intensity enhancement reached $\sim 4.1 \cdot 10^3$. Xu et al. synthesized three TiN thin films with different morphology for biosensing applications, i.e. flat (f-TiN), roughened (R-TiN) and perforated with nanoholes (NH-TiN) [195]. In particular, TiN was chosen for its biocompatibility and its capability to be directly antibody fictionalized, which is an interesting feature in application of immuno-detection.

R-TiN and NH-TiN were deposited on glass substrate via RF magneto-sputtering, combined with a peculiar procedure which involves sacrificial Au NPs. In both cases, an Au film was deposited on glass substrate followed by thermal treatment, leading to NPs formation because of thermal meral dewetting. Moreover, Au NPs resulted partially sunk into glass substrate because temperatures reached during annealing allowed glass transition from glassy to rubbery state. For R-TiN, Au NPs were removed leaving a glass rough surface which implied deposition of rough TiN films; for NH-TiN, Au NPs were removed after TiN film deposition, leaving nanoholes. Biosensing tests showed that both roughness and localized plasmon fields due to the presence of nanoholes improve sensing performance of TiN, but the plasmonic enhancement was proven to be superior with the capability to detect to detect smaller molecules.

In these examples, TiN nanostructured films were obtained by using a template which should be removed at the end. However, template removal could be hazardous, time and energy consuming as well as difficult to be achieved completely. In literature there are other examples of TiN nanostructured films which employ different methods, although not for plasmonic applications. Liu et al. developed a 3D hierarchical TiN films by means of a solvothermal process and subsequent high temperature nitriding process of TiO_2 precursor [192]. They obtained plentiful and highly interconnected nanowires, exhibiting both high surface area and effective charge transfer in catalytic process (see Fig. 2.20b). Gbordzoe et al. synthesized TiN nanowires by using PLD on Si substrates with Au nanodots serving as catalyst (see Fig. 2.20c) [193]. They studied the effect of substrate temperature (i.e. 600,700 and 800°C) on nanowire diameter and length, showing an increase of both sizes with temperature. Moreover, they found that nanowires grew with no preferred orientation due to lattice mismatching between TiN and Si substrate. Finally, they performed destructive and non-destructive corrosion tests in comparison with TiN thin films, showing TiN nanowires corrode faster and, consequently, this kind of system turned out as a potential choice for biodegradable implants. Perego et al. used PLD to synthesize hierarchical nanostructured TiN-based electrode for electrochemical application [194]. Tree-like nanostructures with tunable posity were obtained by varing $N_2 - H_2$ background gas pressure during deposition from 15 to 100 Pa (see Fig. 2.20d). High-angle annular dark field STEM found a content of oxygen higher than 35% at., probably due to large oxidized surface of this particular architecture. Moreover, Raman spectra suggested a slight substoichiometry, while high resolution transmission electron microscopy (HR-TEM) and XRD measurements showed the presence of nanocrystalline domains of TiN (i.e. TiN cubic crystals of 7-8 nm) immersed into an amorphous matrix.

In conclusion, this chapter presented typical limitations of traditional plasmonic material as well as suggestions to overcome them by employing alternative materials, i.e. transparent conductive oxides and transition metal nitrides. In particular, we focused on two Ti-based materials, namely Ta-doped titanium dioxide and titanium nitride, that will play a main role in this thesis work. The discussion developed about their electrical and optical properties, plasmonic behavior and applications as well as synthesis conditions underlie objectives and choices

presented in the next chapters.

Thesis goal and methods

This chapter contains the objectives of this thesis as well as the research methodology followed to achieve them. Specifically, section 3.1 includes the precise goals of this work, keeping in mind the motivations exposed in previous chapters, and the collaborations established for these purposes. The sample synthesis approach is illustrated in section 3.2. In particular, pulsed laser deposition is described from the point of view of mechanism and specific apparatus, with a focus on the critical parameters that play a role in the deposition of nanostructures (see subsection 3.2.1). Then, the different annealing treatments employed for this work are described in detail (see subsection3.2.2). Finally, section 3.3 is devoted to the description of the characterization techniques employed, with a focus on optical and electrical characterizations that play a major role in this work.

3.1 Objectives of this work

This PhD thesis project concerns an experimental investigation for the development of nanostructured thin films based on titanium oxides and nitrides, aimed to achieve a fine control of their physical properties as well as the understanding of the material optical and electrical behavior and their potential applications, with particular attention to the plasmonic field. Keeping in mind the motivations explained in previous chapters, the specific tasks of this thesis involve:

1. The integration of plasmonic Au NPs in semiconducting oxide (i.e. TiO_2) nanostructured thin films, featured by a peculiar hierarchical morphology, which offers the possibility of tuning the system's structure and nanoporosity as well as its optical properties by varying process parameters. The interest in this kind of system lies in the extent of light harvesting up to the visible range, for example in a photoanode application (as extensively discussed in section 1.4).

2. The synthesis and characterization of thin films based on alternative plas-

monic materials, namely Ta:TiO_2 and TiN. In particular, the main purpose consists in the tuning of electrical, optical and plasmonic properties of the films as a function of specific material properties, namely composition/stoichiometry, morphology (i.e. from compact thin films to nanoparticles assemblies), structure (i.e. crystalline phase and crystalline domain size) and thickness.

The investigated systems are grown via physical vapor deposition techniques, in particular pulsed laser deposition (PLD); this is an effective and versatile method for the production of nanostructured films (both compact and nanoporous) of several materials with controllable morphological, structural and functional properties by means of process parameters (e.g. laser fluence, background gas pressure). Post-deposition thermal treatments are employed to crystallize the materials in the desired phase, or to modify their functional properties. The effects of different annealing atmosphere, temperature and duration are investigated. The developed systems have been characterized from the point of view of morphology, structure, electrical and optical properties with techniques available at the laboratory (i.e. the Micro and Nanostructured Materials Laboratory, NanoLab, of the Department of Energy at Politecnico di Milano) or by establishing collaborations, especially for the exploration of possible applications and functional properties.

Task (1) represents the first part of the project and related results are reported in Chapter 4. Specifically, TiO_2 nanostructured films with quasi-1D morphology (having been previously studied at NanoLab [196, 197]) were employed for Au NPs integration via an original single-step pulsed laser co-deposition procedure. This approach allows to obtain TiO_2 hierarchical films with a porosity which is tuned by varying the oxygen background pressure during deposition, while ensuring a fine dispersion of Au NPs through the whole thickness of the TiO_2 film. In particular, the effect of Au content (i.e. from 0.5 up to 5 % at.) was studied for different TiO_2 porosities, obtained by depositing at 5 and 8 Pa of O_2. Then, the effect of post-deposition air thermal treatments has been investigated in order to control TiO_2 crystallization and the nucleation/growth of Au NPs. Finally, selected samples were tested for the photodegradation of pollutants and as substrates for surface enhanced Raman scattering (SERS) in collaborations with the Department of Information Engineering, Chemistry for Technologies Laboratory of the University of Brescia and the Laboratory CSPBAT of Université Paris 13, respectively. Specifically, SERS measurements and related development of Au-TiO_2 samples were performed by a master student, who I supervised for his thesis project [198].

Task (2) can be divided in two main parts according to the material under investigation, Ta:TiO_2 and TiN, whose results will be presented in Chapters 5 and 6, respectively. First, considering Ta:TiO_2, we need to remind that Ta:TiO_2 thin films were previously studied at our laboratory by Mazzolini as transparent electrode for solar cell application, whose main achievements of our interest have been reported in section 2.2.3.1. However, since the laser wavelength employed in PLD changed from 266 to 532 nm, the optimization procedure of PLD parameters (i.e. O_2 background pressure and laser fluence at target surface) was repeated for the goals of this thesis, in order to obtain Ta:TiO_2 thin films as conductive as those in

Mazzolini's work. Once optimal deposition conditions were accessed, the electrical and optical properties of synthesized films were investigated as a function of film thickness (i.e. from 200 down to 10 nm) and Ta content (i.e. 5, 10 % at.). Such a systematic study is presently lacking, despite being essential for a better comprehension of the material behavior in view of possible applications, as well as for the achievement of the thinnest films without degradation of TCO properties. The relation between electrical and optical properties has been analyzed with a focus on the plasmonic response. Ellipsometric measurements have been performed (from UV to near-IR range) in collaboration with CNR-SPIN of Genova, in order to investigate dielectric function (real and imaginary) as a function of doping content and thickness and to evaluate material's properties, such as electronic effective mass and plasma frequency. Moreover, since plasmonic response of Ta:TiO$_2$ films was expected in near- and mid-IR range, Fourier-transform infrared spectroscopy (FTIR) measurements were performed in order to study film transmittance in this specific range. Finally, more complex Ta:TiO$_2$-based systems were developed, in collaboration with two master thesis students [199, 200], (i) Au NPs integrated in compact Ta:TiO$_2$ thin films, aimed to tune the visible plasmonic frequency of Au NPs by changing the dielectric constant of the surrounding TCO matrix, and (ii) Ta:TiO$_2$ NPs assemblies in thin films.

The second part of task (2) involves TiN thin films, whose optical and electrical properties are extremely sensitive to stoichiometry/composition and the understanding of their relation is still an open issue, especially in the case of thin films grown by pulsed laser deposition. In addition, different morphologies were studied, from compact to NPs assemblies, which is a quite new and promising system in the plasmonic framework. In particular, the oxidation issue during synthesis represents a non-trivial problem (see section 2.3.3.2), as been addressed in the thesis of another master student which I supervised [201]. In parallel, I spent three months at the Oak Ridge National Laboratory (ORNL, Tennessee, USA) in the framework of a user project aimed to the development of novel TiN films for advanced plasmonic applications, in cooperation with the Center for Nanophase Materials Sciences (CNMS). Here, I focused on PLD dynamics for TiN synthesis, which resulted in the development of TiN NPs systems. Specifically, the mechanism of plasma plume expansion, which occurs when the laser pulses hit the material target (i.e. TiN) during PLD process, was investigated with specific in-situ characterization techniques available at CNMS as a function of background atmosphere and laser fluence. Once the synthesis process was understood, material properties such as composition, morphology and structure were monitored with several characterization techniques down to nanometer resolution. Then, I continued the study of TiN NPs assemblies back at Nanolab, focusing on oxidation control. For this purpose two strategies were employed: (i) covering the TiN NPs assemblies with a capping layer, in order to reduce surface oxidation due to air exposure; (ii) deposition at high laser fluence, leading to higher nitrogen radicals reactivity in the plasma plume and reduction of oxygen incorporation during deposition.

This PhD thesis project was performed at the Micro and Nanostructured Ma-

terials Laboratory (NanoLab) of the Department of Energy, in the framework of the research field Micro and Nanostructured Materials of the STEN doctoral program. In addition to those already mentioned, external collaborations for specific characterizations not available at Nanolab involve: optical characterizations through UV/Vis/near-IR spectrophotometer at the Center for Nano-Science and Technology of Italian Institute of Technology (IIT), ellipsometric measurements at CNR-SPIN of Genova for Ta:TiO$_2$ thin films and at Regional Centre of Advanced Technologies and Materials (Palacký University) of Olomouc for TiN thin films, Fourier-transform infrared spectroscopy (FTIR) measurements at Department of Physics of Politecnico di Milano, X-ray diffraction (XRD) at Department of Chemistry, Materials, and Chemical Engineering *Giulio Natta* of Politecnico di Milano and transmission electron microscopy (TEM) analysis at Department of Materials Science & Metallurgy of University of Cambridge.

3.2 Material synthesis

3.2.1 Pulsed laser deposition

Pulsed laser deposition (PLD) is a physical vapor deposition technique, in which the material to be deposited is brought at the vapor phase by means of a physical process. Briefly, the fundamental process of a nanosecond PLD involves a high-energy pulsed nanosecond laser that hits a solid target leading to laser ablation. Here, a small part of target surface is vaporized and expands in the form of a supersonic plasma with a characteristic plume shape. Laser ablation can be performed either in vacuum or in presence of a background gas, which could be inert or reactive (this last case is known as *Reactive PLD*). The ablated species, constituting the plasma plume, include atoms, ions, molecules, electrons as well as small aggregates; they are collected by the substrate, where film growth takes place. For a more complete treatment of the physical processes involved in PLD, the reader can refer to [202, 203].

Fig. 3.1 shows a schematic picture of typical PLD apparatus. The laser is placed closed to the vacuum chamber, which hosts the target and the substrate. Laser pulses are focused onto target surface by an optical system. The chamber is evacuated to high vacuum condition by a pumping system and, subsequently, it can be filled with a background gas at controlled pressure and flow. Target and substrate move and rotate thanks to remote-controlled motors. Target-to-substrate distance (d_{TS}) can be varied. The target follows a roto-translation motion ensuring uniform ablation from laser, while the substrate is positioned with an off-set with respect to plasma plume and rotates in order to deposit uniform and homogeneous films over several cm^2.

Two critical PLD parameters play a key role in the deposition of nanostructured thin films, due to their effect on plume expansion dynamics, namely laser fluence and background atmosphere. The *laser fluence* (or energy density at target surface) consists in the ratio between the pulse energy and the size of focused spot. Typically for nanosecond PLD, the laser power at the target is of the order of 10-100 MW, the size of the spot is of the order of millimeters, as a consequence the corresponding fluence values of several J/cm^2. At fixed laser
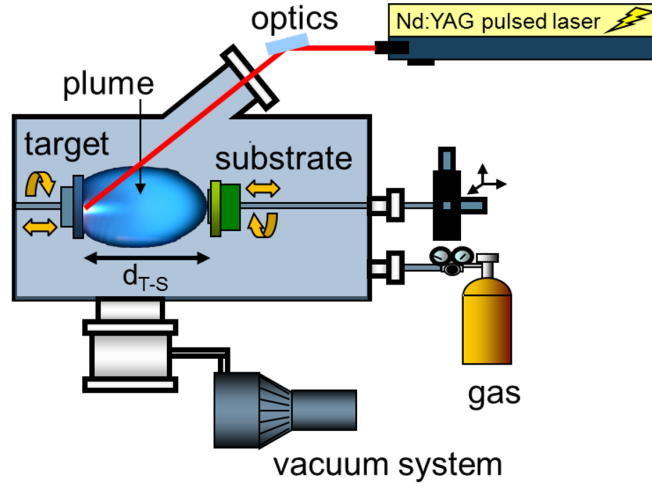
Figure 3.1: *Schematic picture of PLD apparatus. The laser path is indicated with a red line.*
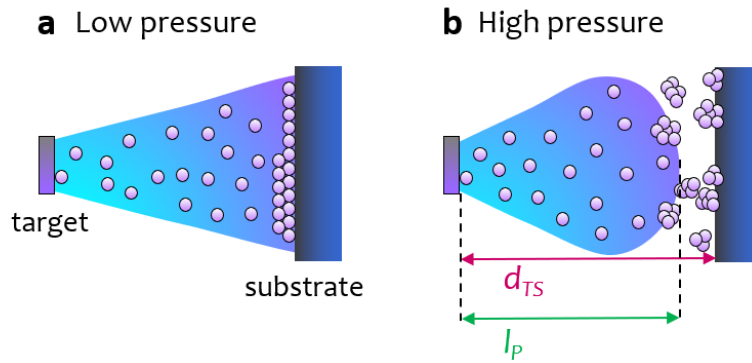
Figure 3.2: *Schematic picture of PLD conditions for (a) low and (b) high pressure regime. d_{TS} is the target-to-substrate distance and l_P is time-integrated visible plume length.*

fluence, the background atmosphere (i.e. gas type and pressure) controls the plume shape as well as its length and ionization degree, allowing to chose between different deposition regimes. Fig.3.2 illustrates deposition regimes schematically, while Fig.3.3 and 3.4 show pictures of plasma plume taken at different PLD setup. By introducing a non-dimensional parameter L, defined as the ratio between d_{TS} and time-integrated visible plume length (l_P) at each laser pulse, PLD deposition regimes are defined as follow

- **Low pressure regime** ($L < 1$). Ablated species proceed from target to substrate with a forward directed flow, almost without collisions and reach the substrate with high kinetic energy (tens of eV/atom [204]). In this condition, substrate is placed in plume, leading to atom-by-atom deposition of compact and bulk-like films (see Fig.3.2a and3.3a).

- **Transition regime**. A strong momentum is transferred to the background gas, forming a shock wave at the front of the expanding plume. Specifically,
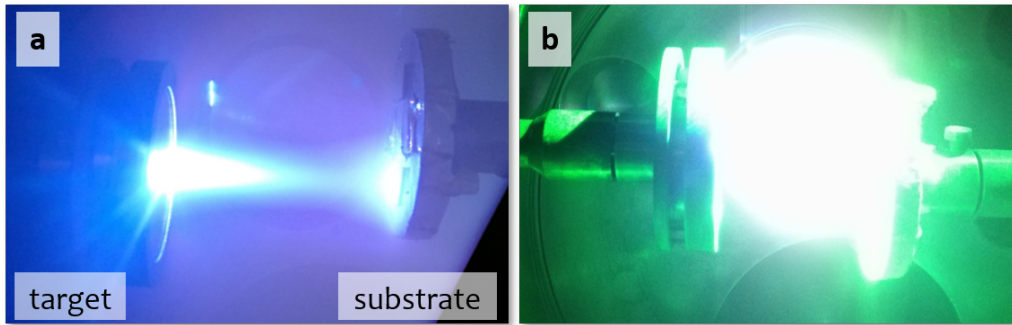
Figure 3.3: *Pictures of PLD plasma plume during depositions performed by means of (a) IR (1064 nm) laser at low pressure condition $L < 1$ and (b) green laser (532 nm) at intermediate condition $L \simeq 1$. Pictures taken at NanoLab.*

when pressure is increased, the background gas molecules and the ablated species undergo collisions which can lead to the spatial confinement of the ablation plume (see Fig.3.4 . The plume edge corresponds to the traveling shock wave front, which slows down until it reaches the so-called stopping distance. Upon collisions, clusters are formed and reach the substrate with lower kinetic energy.

- **High pressure regime** ($L > 1$), characterized by diffusion of the ablated particles (i.e. clusters) and further decrease of kinetic energy (fraction of eV/atom [204]). Substrate is placed out of plume, while plume confinement, induced by collisions, favors cluster nucleation and leads to the deposition of cluster-assembled nanostructured materials (see Fig.3.2b).

A peculiar condition occurs at the intermediate situation, when $L \simeq 1$, namely substrate is at the plume edge (see Fig.3.3b). This condition can favor the growth of film with hierarchical morphology (or tree-like) extensively investigated at NanoLab [196, 204]. Another important role of background atmosphere occurs in case of reactive deposition, in particular, in this work it is exploited for the deposition of oxides and nitrides. For example, when an oxide target is ablated in O_2, oxygen atoms can interact with ablated species affecting the stoichiometry of final deposited film. This has been exploited for the deposition of TiO_2 and Ta:TiO_2 thin films, that need a certain degree of oxygen substoichiometry to favor conductivity (this topic is treated in detail in section 5.1).

In conclusion, PLD is a synthesis methods which allows a fine control of stoichiometry, composition, morphology (i.e. from compact thin films to NPs assemblies) and structure (i.e. crystalline phase and crystalline domain size). However, PLD has some drawbacks, including the limitation in producing large area uniform thin films, due to inhomogeneous flux and angular energy distribution within the ablation plume, as well as the ejection of molten particles (i.e. droplets, from hundreds of nm to several μm) from the target during ablation process, that are detrimental in case low surface roughness is required.

Fig.3.5 shows the PLD apparatus employed in this work. The laser is a Continuum-Quantronix Powerlite 8010 pulsed Q-switched Nd:YAG laser, which generates ns pulses (7 ns) at the fundamental wavelength $\lambda = 1064$ nm (IR), with

Figure 3.4: *Pictures of PLD plasma plume during depositions performed by means of UV (248 nm) laser by varying background pressure from vacuum to 100 Pa (N$_2$). It is clear how pressure affects plasma plume confinement and, as a consequence, deposition regime. Pictures taken at CNMS.*
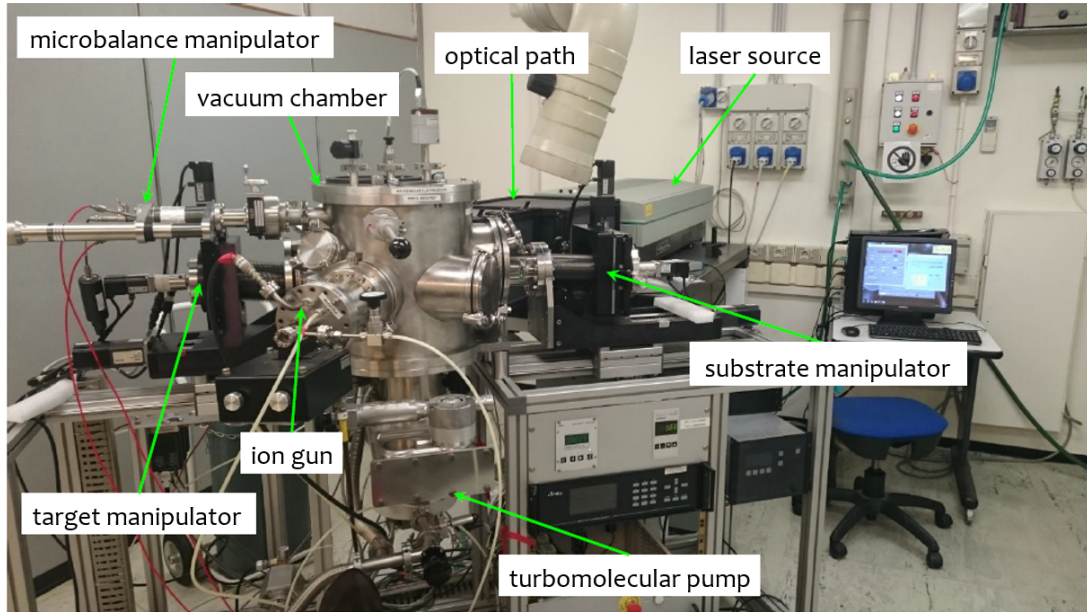
Figure 3.5: *Photo of PLD apparatus at NanoLab, adapted from [115].*

a maximum repetition rate of 10 Hz. Pulse energy ranges between 350 mJ and 1800 mJ by modifying the delay time between pulse generation and the maximum efficiency of the amplification module. A non-linear crystal is employed to double the fundamental wavelength, obtaining $\lambda = 532$ nm (i.e. green), which is the one employed in this work. The laser beam impinges on the target at an angle of 45°, so its projection is elliptical. The beam is focused by a plano-convex lens with focal length of 50 mm. The pumping system is made up of a primary scroll pump and a turbomolecular pump (TMP), which allow to reach a base pressure of the order of 10^{-3} Pa before gas injection (in the range of 4-6·10^{-3} Pa for all deposition performed in this work and, in particular, for TiN film deposition the base pressure was always set between 4-5 ·10^{-3} Pa). All samples were deposited at d_{TS}=5cm. In addition, during my stay at CNMS of ORNL, the employed PLD apparatus was very similar, but with a pulsed KrF laser ($\lambda = 248$ nm); pictures of the related plasma plume are reported in Fig.3.4.

3.2.2 Annealing treatments

In this work, annealing treatments were employed to tune thin film composition, stoichiometry and crystalline structure. In particular, TiO_2-based films deposited via PLD resulted amorphous, therefore thermal treatments at temperature higher than 400°C are needed to obtain TiO_2 in anatase phase. In addition, the choice of annealing atmosphere affects film composition and stoichiometry. In this project different systems were developed, therefore different annealing atmospheres, temperature and duration were employed

- For Au-TiO_2 hierarchical films, annealing were performed in air at temperature ranges between $250 - 700$°C, 2-6 hours dwell, heating ramp 4°C/min. Air-annealing provides crystalline and stoichiometric TiO_2. Different temper-
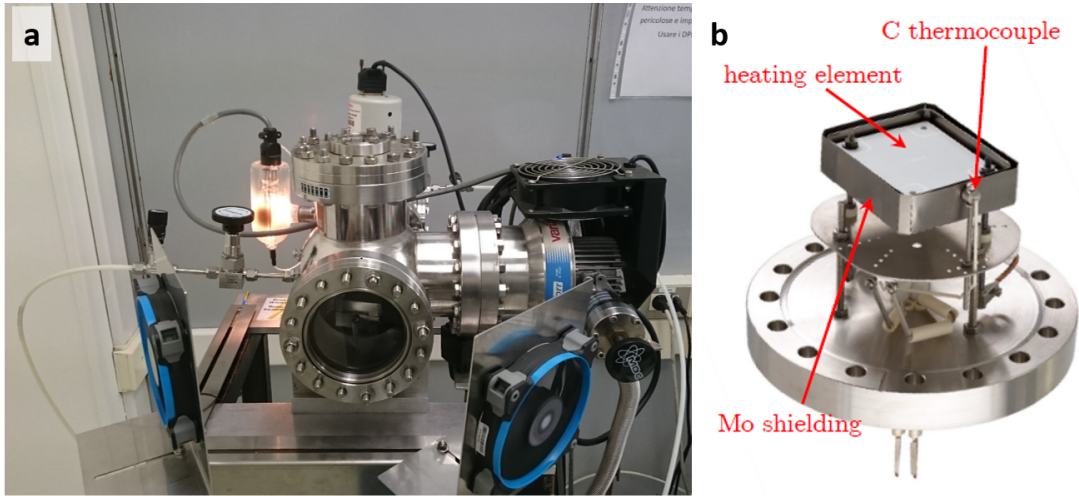
Figure 3.6: *Pictures of (a) home-made furnace for thermal treatments in vacuum and controlled atmosphere and (b) its internal heater stage.*

ature and duration were tested to study and control nucleation and growth of Au NPs embodied in TiO_2 tree-like films.

- For $Ta{:}TiO_2$ films, annealing treatment was performed in vacuum, at 550°C for 1 hour dwell, ramp 10°C/min. This condition was set by Mazzolini in previous works and, here, it is considered the *standard annealing* for $Ta{:}TiO_2$ compact films [112, 125, 127]. Vacuum-annealing crystallizes anatase phase while ensuring sub-stoichiometric TiO_{2-x}. Indeed, oxygen-poor conditions, leading to oxygen vacancies, (needed to obtain conductive TiO_2 and $Ta{:}TiO_2$ films) are tuned by the combination of PLD synthesis in a oxygen-poor atmosphere and subsequent vacuum annealing.

- For TiN films, annealing treatments were performed both in vacuum and over-pressure (1050 mbar) of N_2/H_2 ($95 - 5\%$). A reducing atmosphere was chosen according to literature that reports how easily TiN thin films oxidize in presence of few oxygen contaminations, as discussed in section 2.3.3.2. Annealing temperatures chosen were equal to 300 and 550°C, 1hour dwell and heating ramp 10°C/min.

A Lenton Muffle furnace (ECF type, maximum operating temperature of 1200°C) was employed for air annealing. The temperature uniformity is provided by two side wall-heating elements manufactured from high temperature resistance wire spirals embedded into cast refractory slabs. An exhaust chimney is also present, while the annealing chamber is insulated from the outside environment with an insulating door. The annealing temperature, dwell and heating ramp were set up with a PID controller (Lenton type 3216). Thermal treatments in vacuum or controlled atmosphere were performed in a home-made furnace which includes a high vacuum chamber connected to a pumping system and a heater stage connected to a PID controller (see Fig.3.6a). The heater stage, its power supply and its controller are provided by Tectra (see Fig.3.6b). The heating element is made of

pyrolitic boron nitride and pyrolitic graphite, that are a dielectric ceramic material and electrical conductor, respectively. By flowing an electrical current through the graphite contacts and exploiting the Joule effect, it is possible to bring the system to the desired temperature, measured by a C thermocouple. A standard PID controller (Yudian AI-518P) is employed for system regulation. A molybdenum shield, covering the heating element, can be installed to reduce the irradiated power, keeping the other components safe and to ensure a more uniform temperature distribution. This system can reach very high temperatures (i.e. maximum operating temperature is 1200°C) with heating ramps up to 100°C/min. The vacuum chamber equipped with a gas inlet ensures the possibility to introduce a gas flow during annealing treatments to perform them in a desired atmosphere (e.g. N_2/H_2) or, also, to speed up the cooling process. The base pressure used for vacuum annealing or reached before gas injection is of the order of 10^{-5} Pa (in the range of of 4-5·10^{-5} Pa for all thermal treatment performed with this set up in this work).

3.3 Materials characterization techniques

The synthesized materials have been characterized from the morphological, structural, compositional/stoichiometric, electrical and optical point of view by exploiting different techniques. For this purpose, I personally carried out systematically measurements by means of scanning electron microscope (SEM), energy dispersive X-ray (EDX) spectroscopy, Raman spectroscopy, four-point probe resistivity and Hall effect measurements, and UV-vis-NIR spectroscopy (at the Center for Nano-Science and Technology of the Italian Institute of Technology, IIT).

Specifically, the employed SEM is a high resolution Field Emission-SEM Zeiss Supra 40 based on the Gemini column, equipped with an Oxford EDX spectrometer. The accelerating voltage ranges from 1 kV up to 30 kV (in this work, the used voltages are 5-10 kV to acquire SEM images and 10-20 kV for EDX measurements). The sample holder is connected with five software-controlled motors (x, y, z, rotation and tilt). The EDX detector is a solid-state silicon lithium detector protected by a beryllium window with an energy resolution of about 10 eV. The SEM images were obtained acquiring secondary electrons with an In-Lens detector. For Raman spectra, a Renishaw InVia Raman spectrometer has been used. The exciting radiation is the 514.5 nm line produced by a Ar^+ laser. Spectra have been acquired by a 1800 greeds/mm grating, a super-notch filter (cutoff at 100 cm^{-1}) and a Peltier-cooled CCD camera, allowing a spectral resolution of about 3 cm^{-1}. Laser power on samples was kept below 1 mW to avoid thermal modification of samples.

In the following sections, details about the employed electrical and optical characterizations of sample will be given.

3.3.1   UV-Vis-NIR spectroscopy

Optical characterization is of paramount importance for this project. Indeed, it allows to detect the transition from transmittance to reflectance when probing metal-like films (which is an indication of plasma frequency), or it enables
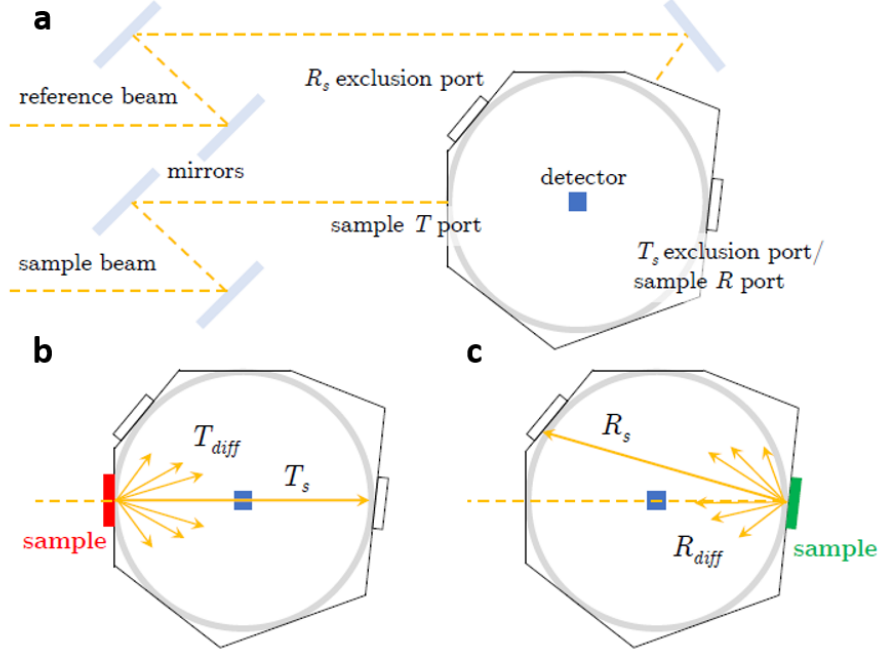
Figure 3.7: *(a) Schematic representation of the Perkin Elmer Lambda 1050 spectrophotometer with integrated sphere, (b) in trasmittance and (c) reflectance measurements configuration. Reproduced from [115].*

to identify the LSPR excitation when probing plasmonic NPs (associated to a minumun in trasmittance in visible range), or even to evaluate the optical band gap of semiconducting films in the UV range. Ultraviolet-visible-near infrared (UV-Vis-NIR) spectroscopy is a non-destructive technique which allows to probe optical transitions of molecules and solids. UV-Vis-NIR spectroscopy employs a spectrophotometer, which measures the intensity of light passing through (or reflected from) the sample (I) and compares it to the intensity of a reference beam, not interacting with the sample (I_0). The ratio I/I_0 is called (total) transmittance (T) or (total) reflectance (R), depending on type of I measured. The fraction of light absorbed by the sample, called absorbance, can be estimated as

$$A = 1 - (T + R) \tag{3.1}$$

Specifically, some samples can induce light scattering, therefore $T_{tot} = T_{diff} + T_S$ as well as $R_{tot} = R_{diff} + R_S$, where T_S and R_S are the specular components (i.e. the one transmitted or reflected with the same angle as the incident one). For scattering samples, the fraction of scattered light can be evaluated by means of *Haze Factor*, which can be defined both from transmittance and reflectance as

$$H = \frac{T_{diff}}{T_{tot}} \tag{3.2}$$

$$H = \frac{R_{diff}}{R_{tot}} \tag{3.3}$$

Moreove, in semiconductors it is possible to estimate the optical band gap of the material from transmittance and reflectance measured in its proximity. First, the

absorption coefficient α is determined from Lambert-Beer's law

$$\alpha = -\frac{1}{d}\ln\left(\frac{T}{1-R}\right) \tag{3.4}$$

where d is the thickness of the films. Then, the theoretical value of α for photons of energies $h\nu$ just above the optical bandgap E_g is given by

$$\alpha = C\left(h\nu - E_g\right)^{1/r} \tag{3.5}$$

where C a constant dependent on the optical transition matrix element and r indicates the type of transition in the considered material, namely $r=2$ for direct bandgap transition, while $r=1/2$ for indirected transitions. Since from Eq. 3.5, α^r should have a linear behavior as a function of $h\nu$, the optical bandgap of measured material correspond to the intercept of its linear fit with energy axis (i.e. $\alpha=0$ for $h\nu=E_g$). This calculation method is known as Tauc plot [205]. In some case, $(\alpha h\nu)^r$ is plotted instead of α^r, this depends on properties of the constant C (Eq. 3.5) which, in the case of a heavily filled and energy dispersed conduction band needs to be multiplied by $h\nu$ for a more accurate realization of the Tauc plot [206]. In this work, a Perkin Elmer Lambda 1050 spectrophotometer with a 150 mm diameter Spectralon®-coated integrating sphere ($R > 95\%$ in the range 250-2000 nm, $R > 99\%$ in the range 400-1500 nm) was employed. The total and diffuse transmittance as well as total reflectance spectra were measured in the wavelength range between 250 and 2000 nm. A schematic illustration of the instrumentation and of the transmittance and reflectance measurement configurations is shown in Fig. 3.7. For reflectance measurements, the sample was mounted with a 8° inclination to let R_S light to be detected. Finally, all measurements presented in this work were normalized to the substrate according to

$$T_{norm} = \frac{T_{measured}}{T_{glass}} \tag{3.6}$$

$$R_{norm} = R_{measured} - \left(R_{glass} \cdot T_{norm}^2\right) \tag{3.7}$$

3.3.2 Van der Pauw method for resistivity and Hall effect measurements

Resistivity is an intrinsic property of a material, which does not depend on the size or shape of a sample. The related extrinsic property measured is the resistance (R) and there are a variety of methods to calculate resistivity (ρ) from R measurements. In 1958 van der Pauw published a work showing his method to determine ρ of 2D-samples from R without knowing sample physical size [207]. The 4-point probe van der Pauw configuration is the most diffuse electrical characterization approach for thin films. The requirement is that 4 contacts are on the edge of the sample and are mathematically point contact, moreover film must have uniform thickness and no holes within it. This method consists in measuring the voltage drop between electrodes when a known current is flowing through the other two, as shown in Fig 3.8. 8 measurements are performed, corresponding to 4 configurations available, each one measured at two current directions. Considering symmetry and reciprocity constrains, the resistance values extracted from
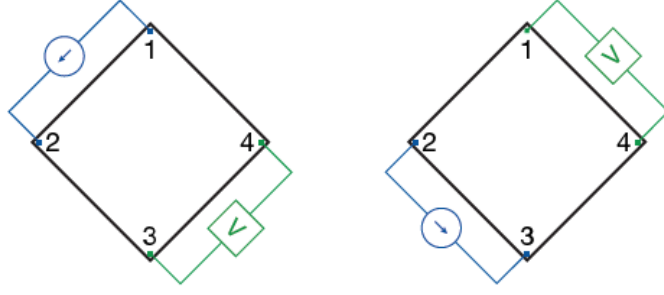
Figure 3.8: *Schematic illustration of 4-point probe van der Pauw configuration showing connections for resistivity measurements. Reproduced from [208].*

measurements must satisfy the following conditions

$$R_{21,34} = R_{12,43}$$
$$R_{32,41} = R_{23,14}$$
$$R_{43,12} = R_{34,21}$$
$$R_{14,23} = R_{41,32}$$
$$R_{21,34} + R_{12,43} = R_{43,12} + R_{34,21}$$
$$R_{32,41} + R_{23,14} = R_{14,23} + R_{41,32}$$

(3.8)

Defining R_a and R_b as the average resistances measured on each side of the sample, it is possible to calculate the sheet resistance R_S, which is the resistance of a sample of unitary area (i.e. resistivity multiplied by the thickness d), according to the equation

$$e^{-\pi \frac{R_a}{R_S}} + e^{-\pi \frac{R_b}{R_S}} = 1$$

(3.9)

Then, resistivity ρ can be calculated as

$$\rho = R_S d$$

(3.10)

Hall effect measurements can be performed by using the same configuration. Fig. 3.9a shows the fundamental aspects of Hall effect in, for example, a conductor slab. In a current I is flowing in a material in x direction and an external magnetic field B is applied in (positive) z direction, then an electric field is induced in y direction. This electric field is proportional to the current and magnetic field. The force on the current by the electric field is balanced by a force (i.e. the Lorentz force). The integral of the electrical field across the width of the sample is the *Hall voltage* V_H, that can be either positive or negative.

$$V_H = \frac{IB}{qdn}$$

(3.11)

where n is the carrier density and q is the charge of the carrier. Since q is positive in case of hole conduction, while it is negative for electron conduction, the sign of V_H gives information also on type of carriers in the material. The Hall mobility μ_H can be calculated too according to Eq. 1.4. For Hall measurements, a current is applied to two contacts in cross configuration, as shown in Fig. 3.9b and a
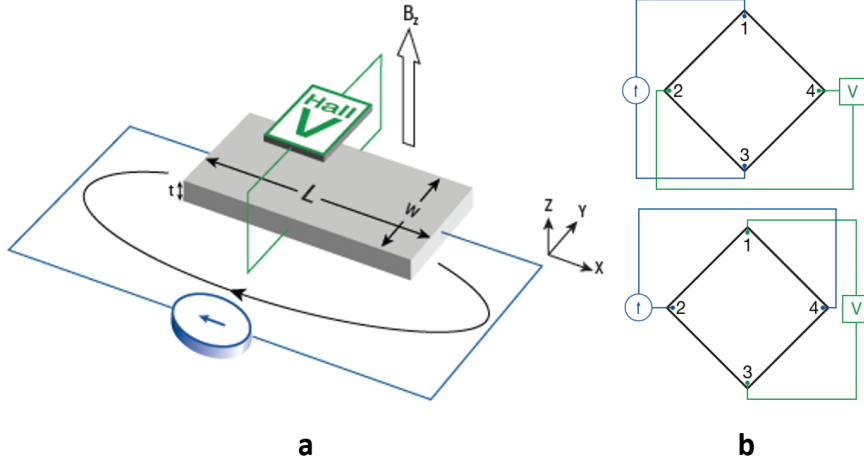
Figure 3.9: *(a) Scheme of Hall effect in a conductor slab; (b) 4-point probe configurations for Hall effect measurements. Reproduced from [208].*

voltage is measured at other two. Since two contact connection configurations are possible, 4 values of voltage are measured considering two current directions. Actually, measurements are repeated by inverting the direction of magnetic field too, with a total of 8 measurements. The inversion of magnetic field aims to isolate Hall voltage contribution from the one due to the current flow by a simple subtraction. Indeed, Hall voltage changes in sign as B is inverted, while voltage due to current flow stays the same.

The apparatus used in this work consists in a Keythley 2400 SourceMeter, used as a current source (from 100 nA to 10 mA), an Agilent 34970A voltage meter and a 0.57 T Ecopia permanent magnet, coupled with a Keysight 34972A LXI Data acquisition unit controlled remotely with a computer to record the voltage measurements. The different configurations required in the measurement were selected using an home-made switch. Five data were collected for each configuration and then averaged before proceeding with the calculations described above. The raw data was analyzed with an ad-hoc Matlab code. In order to obtain an error bar, each sample was measured three times. Notice that in the case of polycrystalline or nanostuctured thin films, the value of carrier density and mobility obtained with this method are to be taken as effective values, rather than real material properties. In case of ultra-thin films (i.e. thickness about 10 nm), porous thin films or partially oxidized TiN thin films, results of Hall measurements could be unreliable. Therefore, a Figure-of-Merit (FoM) was defined, providing an indication of error on the measured carrier density and Hall mobility

$$FoM = \frac{ZeroCheck}{V_H} \qquad (3.12)$$

where $ZeroCheck$ is the reference potential measured with no applied magnetic field, averaged over the four possible configurations. Ideally, $ZeroCheck$ should be zero, but for non-ideal systems this term must be as small as possible, at least smaller than V_H. Therefore, obtained data are considered reliable when $FoM<1$.

Integration of Au nanoparticles in TiO$_2$ hierarchical films

As discussed in section 1.4, a strategy to improve the photoresponse of oxide photoanodes involves the integration of metal nanoparticles (NPs). Among semiconducting oxides, TiO$_2$ is largely investigated for this purpose due to its chemical stability, availability and lack of toxicity [56, 107]. Nevertheless, TiO$_2$ provides wide band gap (3.2 eV for the anatase phase [55]), limiting light absorption in UV range, as well as high recombination rate of the photogenerated charge carriers, however both these limitations can be overcome via the integration of plasmonic metal NPs in TiO$_2$. In literature, there are examples of integration of Au NPs in TiO$_2$ films using either chemical or physical methods. However, chemical approaches have some drawbacks including the use of aggressive solvents and the presence of remaining contaminants [209], while requiring a two steps procedure, namely the synthesis of Au NPs and subsequent infiltration in the TiO$_2$ films, and a proper dispersion of NPs within TiO$_2$ structures is difficultly achieved, especially in case of nanoporous TiO$_2$ [210, 211]. On the other hand, a physical method of synthesis allows the production of highly pure NPs without the presence of contaminants, keeping a good control of size distribution [19, 60].

In this chapter, a PLD co-deposition approach for the synthesis of integrated Au NP-TiO$_2$ films has been successfully performed with a single-step procedure involving the ablation of a composite TiO$_2$-Au target. Specifically, we managed to finely disperse Au NPs through the whole thickness of TiO$_2$ film, while tuning its porosity as well as the Au content. In particular, the integration was performed with peculiar TiO$_2$ nanostructured films with a so-called hierarchical morphology previously studied at our research group, obtained via PLD in the condition where plasma plume edge tangets to substrate (i.e. $L \simeq 1$, see section 3.2.1). Therefore, the porosity and density of TiO$_2$ hierarchical films can be controlled by PLD process parameters, obtaining large surface area (from tens to hundreds m^2/g) [197, 212, 213] and a peculiar vertically-oriented morphology that can facilitate

Figure 4.1: *Pictures of targets employed for Au-TiO$_2$ co-depositions. The number of Au plates varies from 1/4 to 5.*

the transport of photogenerated charge carriers as well as produce an effective visible light scattering [214]. Because of these features, these structures have been studied as photoanodes for photocatalysis [197, 215], photovoltaics [196, 212, 216] and photoelectrochemical water splitting [213, 217].

Section 4.1 reports in detail the synthesis strategy adopted for this peculiar integrated Au-TiO$_2$ system, then sections 4.2, 4.3 deal with morphological, structural and optical characterization of the films obtained. Section 4.4 summarizes preliminary tests for the application of these systems for photodegradation of pollutants, photoanode for water splitting and as substrate for surface enhanced Raman scattering (SERS). For this last, further investigation on thermal treatment, testing other temperatures and duration, as well as higher porosity effect were performed aimed to the specific application. Finally, section 4.5 sums up overall conclusions and perspectives of these systems. The main results of this chapter are published in [218].

4.1 Synthesis strategy

Co-deposited films of TiO$_2$ and Au have been synthesized by ablating a 2 inch TiO$_2$ target (99.9% pure, provider *Kurt J. Lesker*) partially covered with Au plates (99.99% pure, provider *MaTeck*) attached on the target surface. Au plates have been placed in order to have some subsequent laser shots on gold only, during the target motion (see Fig.4.1). The laser pulse energy was set at 170 mJ, corresponding to a laser fluence on the target of 3.5 J/cm². The employed substrates were Si (100) and soda-lime glass mounted on a rotating sample holder at a fixed target-to-substrate distance of 50 mm. Depositions were performed at room temperature with a pure O$_2$ background gas at two different pressures, 5 and 8 Pa (referred to as 5Pa-films and 8Pa-films, respectively), in order to

# Au plates	Au target area (%)	Au % at. - 5 Pa	Au % at. - 8 Pa
5	6.6	5	3.9
3	4.0	3.5	2.9
2	2.7	2.5	2.4
1	1.3	1.1	1.0
1/2	0.7	0.8	0.7
1/4	0.3	0.6	0.5

Table 4.1: *Atomic percentage of Au measured by EDX in Au-TiO_2 films deposited at different pressures. Corresponding number of Au plates and target area are reported.*

study two different film porosities, keeping a nominal film thickness of 1 μm. The Au content of the co-deposited films was controlled by varying the number of Au plates on target, as shown in Fig. 4.1, and the Au atomic percentage (%at.) in the deposited films was estimated by EDX with accelerating voltage of 15 kV. Table 4.1 lists the Au amounts at the two deposition pressures and the corresponding target area covered by Au plates. Notably, by varying the deposition pressure, the same Au target area corresponds to a different Au atomic percentage in the films because the deposition rate of species changes with background pressure and, therefore, the same thickness (1 μm) is achieved with different deposition times and so different shot numbers. However, these EDX results of Au atomic percentage are semiquantitative measurements and they can be used to obtain relative information among different samples. The order of magnitude is reliable (the reliability limit of Au detection with EDX is of the order of tenths of percent) and, for samples deposited at the same pressure but with different Au target area, the ratio of the Au contents is trustworthy, likewise the higher amount of Au in sample deposited at 5 Pa than 8 Pa at the same Au target area.

Post-deposition annealing treatments were performed in air at 500°C for 2 hours (as described in detail in section 3.2.2), in order to obtain anatase crystallization.

4.2 Morphology and structure

First, as-deposited Au-TiO_2 films are considered, i.e. films before thermal treatment. Fig.4.2 a-d show the SEM cross-section images of bare TiO_2 and Au-TiO_2 films deposited at 5 and 8 Pa. The effect of O_2 background pressure on TiO_2 deposition has been already studied in previous works [196, 197, 219], the higher the pressure, the higher the porosity and the lower the density (Fig.4.2a,b). The effect of Au addition in the film induces a slightly more compact structure (Fig.4.2c,d), indeed, if the deposition time is kept constant, the obtained thickness decreases with increasing Au content. Furthermore, Au plays a role on the morphological organization as well. Specifically, 5Pa-films (Fig.4.2c) show a layered structure in which TiO_2 is separated by Au-rich layers which are originated by the target geometry (with alternated ablation of Au and TiO_2 target regions), combined with the fact that in these deposition conditions the pressure is not enough to induce significant Au NP nucleation and growth, as it was found in the
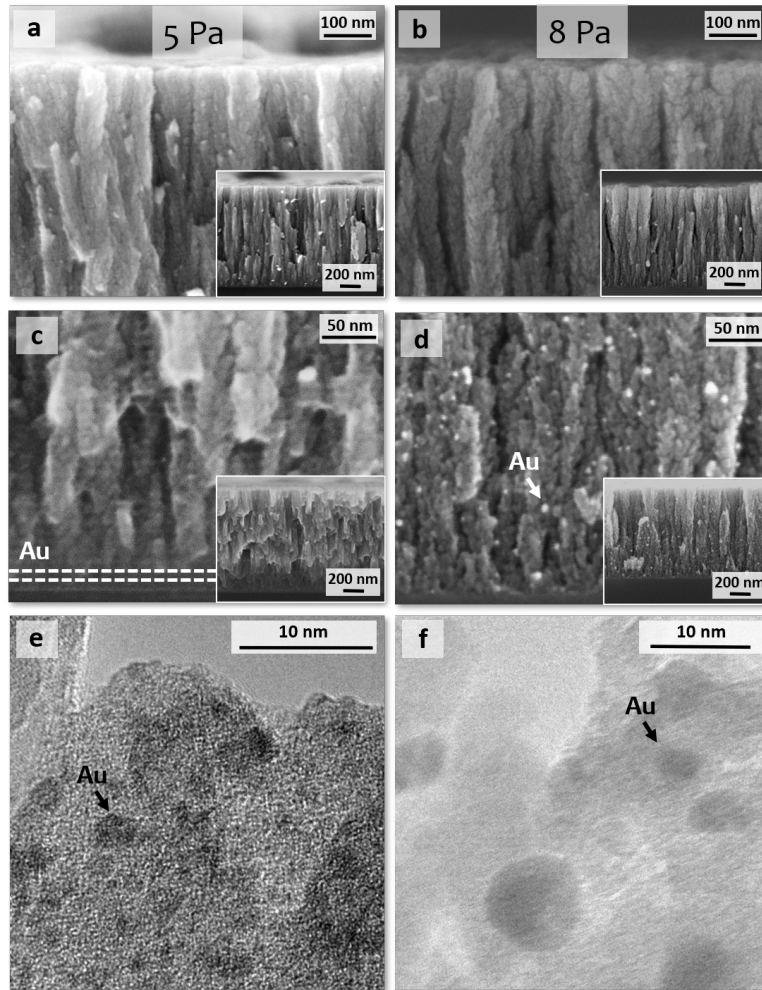
Figure 4.2: *(a-d) SEM and (e, f) TEM images of Au-TiO_2 films deposited at 5 and 8 Pa with different Au contents. Bare TiO_2 film and with 3.5 % at. Au, deposited at 5 Pa, are reported in (a) and (c, e), respectively; while (b) and (d, f) report bare 8 Pa TiO_2 film and with 2.9 % at. Au, respectively. Adapted from [218].*

previous work on PLD of Au NPs [220]. In addition, TEM analysis[1] has been carried to study the nanoscale organization of Au NPs and TiO_2 films. TEM image in Fig.4.2e shows that the Au layer is not continuous, but is formed by very small Au NPs ($<$3 nm) very close to each other. On the other hand, 8Pa-films show Au organized in the form of NPs with an average diameter smaller than 10 nm and homogeneously distributed in the porous TiO_2 nanostructures (Fig.4.2d), which indicates that the cluster-assembled growth promoted at 8 Pa leads to the formation of dispersed Au NPs. From TEM analysis (Fig.4.2f) also smaller NPs are visible and so the average diameter was estimated around 5 nm. The results

---

[1] Transmission electron microscopy (TEM) analysis was performed thanks to the collaboration with C. Ducati at the Department of Materials Science & Metallurgy, University of Cambridge, using a FEI Tecnai F20 FEG-TEM with acceleration voltage of 200 kV. The microscope is equipped with a Gatan OneView camera for image acquisition. Specimens of Au-TiO_2 films were removed from the Si substrates and deposited on TEM Cu grids. The average diameter of Au NPs has been estimated by a statistical analysis on many TEM images with the open source software *ImageJ*.
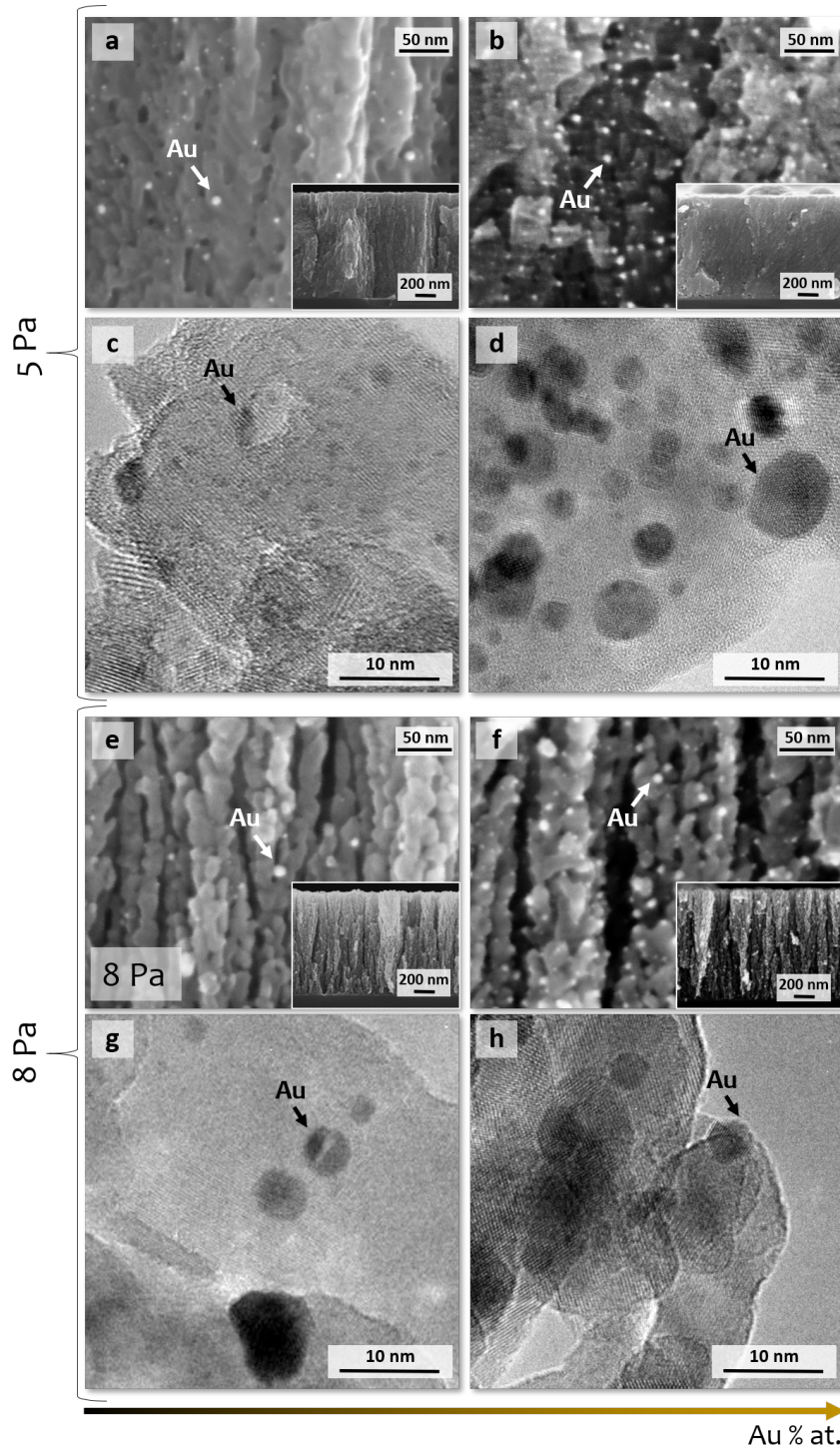
Figure 4.3: *(a,b,e,f) SEM and (c,d,g,h) TEM images of 5Pa- and 8Pa-films with different Au contents: 5Pa-films with 0.8 and 3.5%at. Au are reported in (a, c) and (b, d), respectively; 8Pa-films with 0.7 and 2.9%at. Au are shown in (e, g) and (f, h), respectively. Adapted from [218].*

of statistical analysis of Au NPs size are reported in Table 4.2.

Fig.4.3 shows SEM and TEM images of selected samples after air-annealing

Pressure (Pa)	Au content (% at.)	Themal treatment	Mean Au NPs size (nm)	SD (nm)	# Au NPs
5	3.5	No	2.4	2.3	111
	3.5	Yes	4.7	3.5	79
	0.8	Yes	2.4	1.3	51
8	2.9	No	5.0	1.9	27
	2.9	Yes	3.0	1.4	102
	0.7	Yes	3.4	2.3	66

Table 4.2: *Results of statistical analysis of Au NPs size on TEM images, including the mean size, the standard deviation and the number of particles on which statics has been performed.*

treatment. The effect on TiO$_2$ involves the formation of TiO$_2$ nanocrystals with an average size of few tens nm partially merged with each other due to sintering effects [213, 217]. In addition, the thermal treatment affects the Au morphological organization as well, providing the energy for the diffusion of Au atoms. The mechanisms governing the NPs formation and coarsening during a thermal treatment are Ostwald ripening and NPs diffusion and subsequent coalescence [221–223]. From the statistical analysis of different TEM images, it was possible to estimate the size of the observed Au NPs, reported in Table 4.2. The annealed 5Pa-films with 3.5%at. Au (Fig.4.3d) shows larger Au NPs than the corresponding as-deposited film (Fig.4.2e), indeed the average diameter increases from <3 nm to around 5 nm after thermal treatment. Conversely, an apparent decrease in the average Au NP diameter, from 5 nm down to 3 nm, is observed in 8Pa-films with 2.9%at. Au after thermal treatment. As an hypotesis, Au atoms or very small Au atomic clusters, probably already present before annealing but not visible by TEM, aggregate and grow upon thermal treatment thus becoming detectable. Furthermore, the effect of Au content on NP size in annealed films was investigated, 5Pa-films show a slight increase in Au NPs size vs. Au content: films with 0.8%at. (Fig.4.3c) and 3.5%at. Au (Fig.4.3) exhibit NPs with average diameter of 3 and 5 nm, respectively. Instead, 8Pa-films with Au content of 0.7%at. (Fig.4.3g) and 2.9%at. (Fig.4.3h) reveal Au NPs with almost constant average size, around 3 nm. As expected, at both deposition pressures, the Au NPs number density increases with the amount of Au (Fig.4.3a-b, e-f). In addition, it was possible to analyze the spacing of the characteristic lattice plane fringes of Au NPs and TiO$_2$ domains of the annealed films. The spacing for Au NPs is equal to 0.236 nm, compatible with Au [111] face centered cubic (FCC) structure, while TiO$_2$ was confirmed in anatase phase.

Further structural analysis of Au-TiO$_2$ films has been performed by means of XRD[2] and Raman spectroscopy. Fig.4.4a,b reports the XRD analysis of 5Pa- and 8Pa-films respectively, with different amounts of Au as well as before and after the annealing treatment. The characteristic Au peaks, located at 38.19 and 44.39° (corresponding to Au (111) and (200) reflections, respectively), were detectable

---

[2]X-ray diffraction patterns have been acquired by G. Terraneo at the Laboratory of Nanostructured Fluorinated Materials, Department of Chemistry, Materials and Chemical Engineering *G. Natta* (Politecnico di Milano), using a Bruker D8 Advance X-ray diffractometer at 293 K (CuKα1 radiation - 1.5406Å). The measurements were carried out in Bragg-Brentano geometry with a step-scan technique in 2θ range of 10-75°. Data were acquired by Lynx Eye detector in continuous scanning mode with a step size of 0.038° and time/step of 0.15 s.
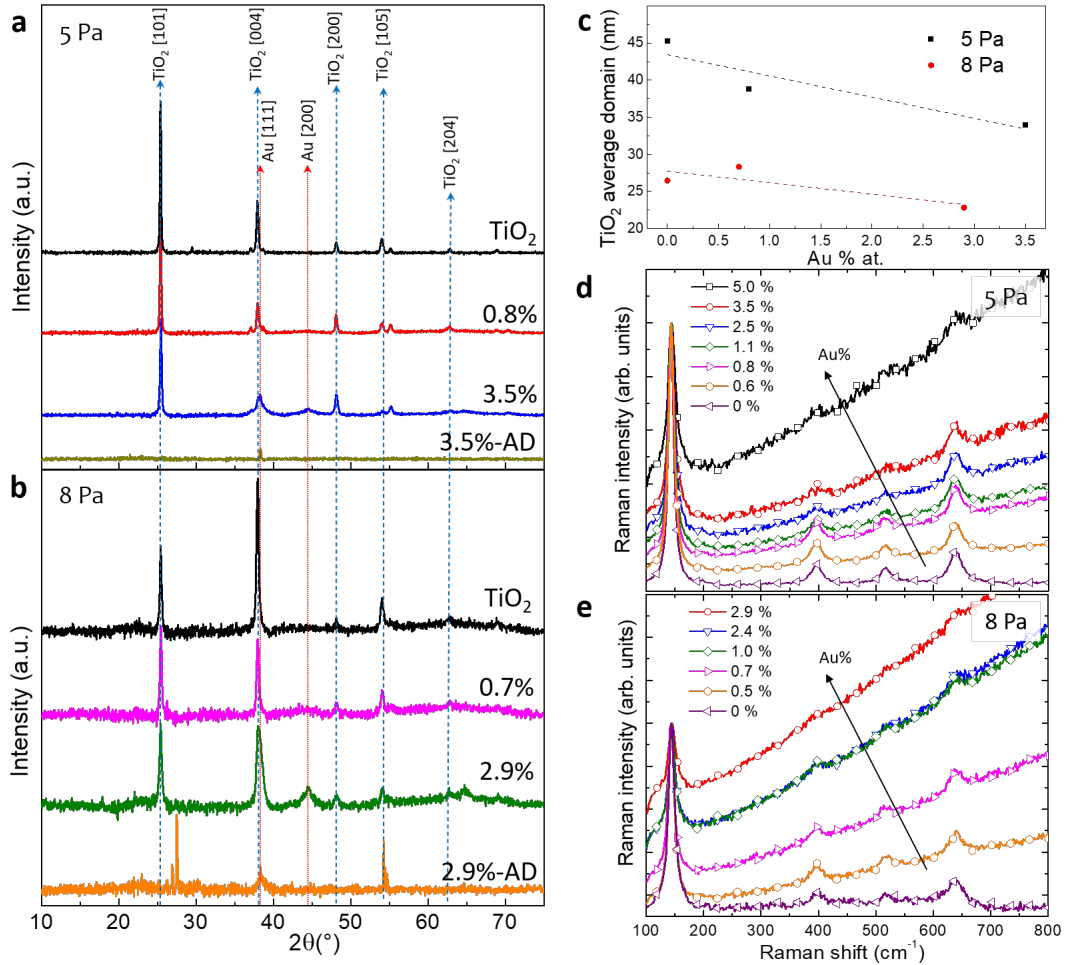
Figure 4.4: *XRD diffractograms of (a) 5Pa- and (b) 8Pa-films with different Au content as deposited (AD) and after air-annealing. The characteristic peaks of TiO_2 (anatase) and Au are highlighted; (c) TiO_2 average crystalline domain sizes for different deposition pressures and Au content calculated with Scherrer's equation. Raman spectra of air-annealed (d) 5Pa- and (e) 8Pa-films with different Au content. Adapted from [218].*

only for the highest Au contents, pointing out the presence of crystalline Au [224]. Specifically, the Au (111) peak of as-deposited films has a very low intensity, corresponding to very small Au crystalline domains (smaller than 3 nm), while the anatase peaks are not detected, suggesting an amorphous TiO_2 structure, as expected [197, 217]. The Au crystalline domain size after annealing was estimated equal to 8 and 12 nm for 5Pa- and 8Pa-films, respectively, through Pawley fitting[3]. The difference between Au size evaluated by XRD and TEM is not unexpected, indeed TEM allows a direct observation of selected NPs, while XRD provides the mean scattering domain size. Furthermore, these techniques are sensitive to different orders of magnitude of investigated material volume and, finally, XRD is sensitive to larger NPs whereas the smallest ones are simply not detected.

At both pressures, annealed films show the characteristic TiO_2 anatase peaks

---

[3]Pawley method was carried out using the program-suite TOPAS from Bruker.

(Fig.4.4a,b); no shift is detected despite the presence of Au, which rules out a possible doping effect [225]. On the other hand, a slight variation of the full width at half maximum (FWHM) occurs, which means that the Au content affects the TiO$_2$ crystalline domain size. Fig.4.4c shows the average TiO$_2$ domain size (τ) evaluated through Scherrer's equation based on the analysis of anatase (101) peak.

$$\tau = \frac{K\lambda}{\beta cos\theta} \tag{4.1}$$

where K is the shape factor (equal to 0.9), λ is the x-ray wavelength, β is the FWHM in radians and θ is the Bragg angle. Notably, the average size is strongly dependent on deposition pressure, being equal to about 40 and 25 nm for TiO$_2$ films deposited at 5 and 8 Pa, respectively, in agreement with a stronger sintering effect in more compact films [197]. Then, the average crystalline domain size decreases with the increase of Au content at both deposition pressures, namely from 45 to 35 nm for 5Pa-films with 3.5%at. Au; from 26 to 22 nm for 8Pa-films with 2.9%at. Au. In addition, the Raman analysis of the annealed Au-TiO$_2$ films confirms XRD results (see Fig.4.4d,e). Indeed, the characteristic anatase Raman peaks are detected, but a slight increase (2 cm^{-1}) in the $E_g(1)$ peak FWHM is observed when moving from bare nanoporous TiO$_2$ to Au-TiO$_2$ films with 3.5%at. Au (at 5 Pa) and 2.9%at. Au (at 8 Pa), suggesting more disordered structure.

4.3 Optical properties

Figs.4.5a,b,d,e show the transmittance spectra in the UV-Vis.NIR range (300-2000 nm) of 5Pa- and 8Pa-films as a function of Au content, before and after the thermal treatment. The decrease of transmittance in the UV range is related with TiO$_2$ absorption [55]; conversely, in the visible-IR range there is a high-transparency region showing fringes as a consequence of interference phenomena, which depend on sample morphology, thickness and optical properties [226]. Before annealing (4.5a,b), the addition of Au to TiO$_2$ film leads to a transmittance decrease in the visible range at both deposition pressures. Specifically, 8Pa-films (Fif.4.5b) show a clear LSPR peak around 540 nm for the highest Au contents, for which Au NPs are observed in the as-deposited films (Fig.4.2d). On the other hand, at lower Au contents, Au cluster size and density are too small to produce LSPR and a clear plasmonic effect. The 5Pa-films (Fig.4.5a) do not show a characteristic plasmonic absorption for any Au content, which also can be related to the Au morphological organization in layers composed by very small clusters and limited crystallinity, as discussed above. Notably, for the highest Au content (i.e. 5%at.) the transmittance decreases strongly and this phenomenon is associated with the large amount of Au which absorbs significantly in the analyzed range [220]. In addition, since the optical reflectance of Au-TiO$_2$ films is almost constant (around 20% and 10% for 5Pa- and 8Pa-films, respectively, see Fig.4.5c) for all the wavelengths, the observed decrease in transmittance can be associated to optical absorption of the system.

The thermal treatment leads to a slight decrease in the film transmittance, as already observed for bare TiO$_2$ films [212, 217]. For Au-TiO$_2$, annealed 5Pa-films
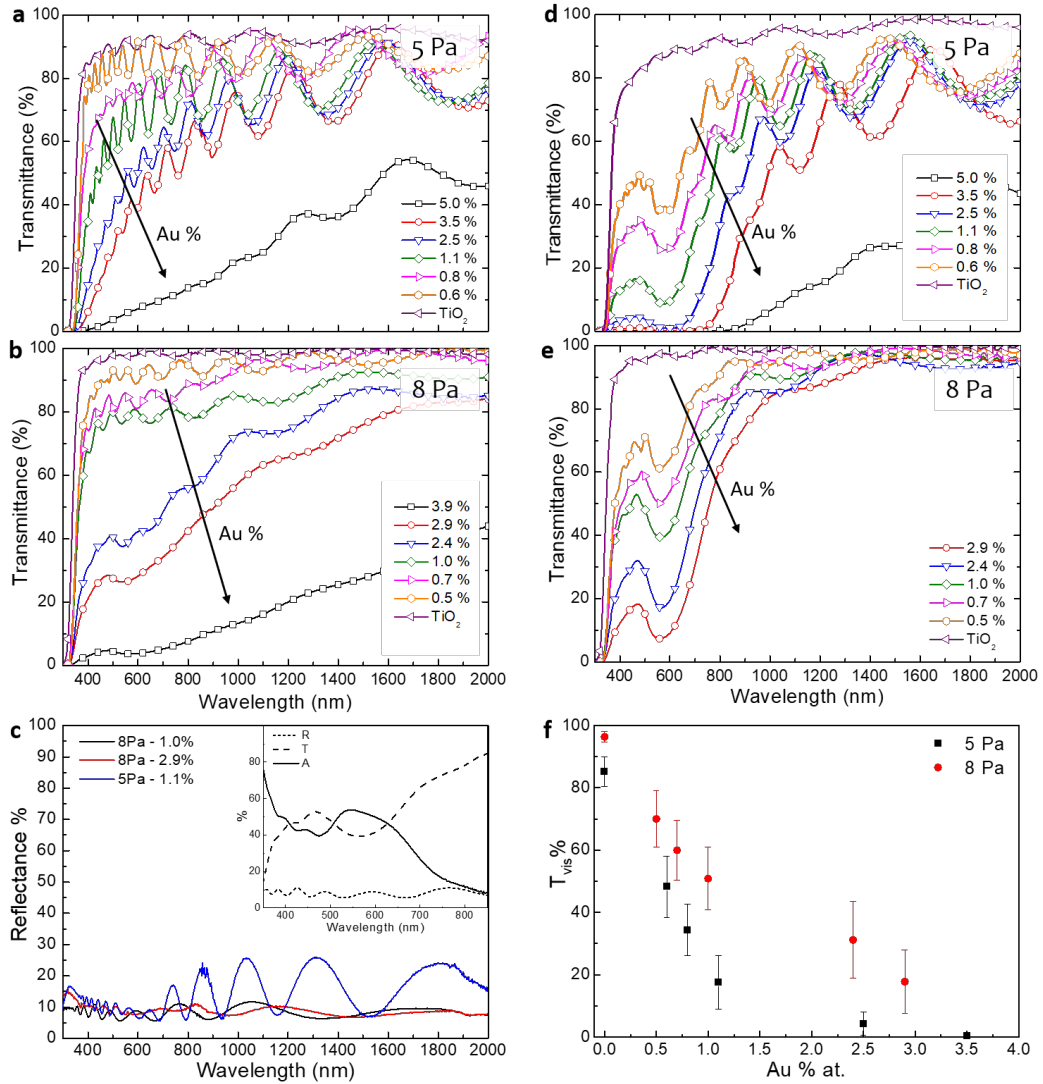
Figure 4.5: *Optical transmittance of 5Pa- and 8Pa- Au-TiO₂ with different Au contents (a,b) before and (d,e) after thermal treatment. (c) Reflectance of selected annealed Au-TiO₂ films; the inset reports reflectance, transmittance and absorbance of a 8Pa-film with 1.0%at. Au. (f) Average transmittance of annealed samples in the visible range (390-750 nm) as a function of Au content at both deposition pressures. Adapted from [218].*

(Fig. 5a) exhibit a plasmonic peak around 575 nm, while annealing on 8Pa-films (Fig. 5b) induces a more intense and well-defined plasmonic peak with respect to the corresponding as-deposited films, red-shifted to 560-570 nm. These effects can be related to the plasmonic behavior of Au NPs which aggregate and grow upon thermal treatment. Moreover, the crystallization of TiO₂ leading to an increase of refractive index of the matrix (from 2.0-2.2 for amorphous TiO₂ up to 2.5 for anatase [227]), which may contribute to the red-shift [228]. Notably, the LSPR position (i.e. the transmission minimum) of annealed Au-TiO₂ films is similar at both deposition pressures as a consequence of comparable Au NP
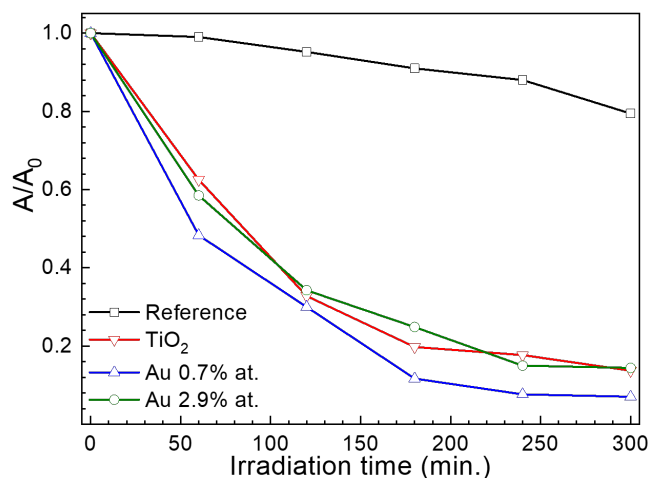
Figure 4.6: *A/A_0 as a function of time for bare TiO_2 and Au-TiO_2 films with 0.7 and 2.9%at. Au deposited at 8 Pa. The error bars are included within the point size. Adapted from [218].*

size,while the Au content mainly affects the absorption intensity. Fig.4.5f shows that the average transmittance of annealed samples in the visible range (390-750 nm) decreases with Au content at both deposition pressures. For 8Pa-films, transmittance decreases from 96%, for bare TiO_2, to 17% for films with 2.9%at. Au, while for 5 Pa films it drops from 85% to almost zero with 3.5%at. Au.

4.4 Application of Au NPs-TiO_2 hierarchical films

4.4.1 Photodegradation activity

TiO_2 nanostructures are widely exploited for assisting the photodegradation of environmental pollutants, therefore the photocatalytic properties of both TiO_2 and Au-TiO_2 nanostructured developed in this project were tested in photodegradation tests of organic dyes, in particular methyl orange (MO) was selected as degradation target, because of its mutagenic nature and high persistency [229]. For this test, annealed 8Pa-films were employed because of their high porosity, which makes them suitable in view of photocatalytic applications; Au contents were chosen equal to 0.7 and 2.9%at. because of their defined plasmonic peak (see Fig.4.5e). The experiments were performed in collaboration with I. Alessandri at the Department of Information Engineering, Chemistry for Technologies Laboratory of the University of Brescia, and carried out with a solar simulator, in order to study the behavior of the samples under natural sunlight and the photocatalytic activity was evaluated by monitoring the decrease in intensity of the MO main absorbance band in the visible (λ=460 nm) [230]. Fig.4.6 shows the progress of MO photodegradation, expressed in terms of the A/A_0 ratio, where A_0 is the absorbance of the initial MO solution (concentration of 10^{-5} M, pH=4.2) and A is the absorbance at a given irradiation time. The MO self-degradation in the absence of any catalytic support was also considered as a reference. Be-

fore starting irradiation, the three samples were kept under dark for 60 min to take the adsorption effect into account. Importantly, all the MO samples were simultaneously irradiated under the same conditions, in order to ensure a reliable comparison among absorbance data from different samples. Moreover, the temperature of the MO solution during irradiation was around 33°C,which excludes thermal effects as a primary cause of degradation. Notably, the bare nanostructured TiO$_2$ films exhibit already good photocatalytic efficiency, allowing to reduce the concentration of the MO solution to about 60% of its initial value in the first 60 min of irradiation and to about 20% in 240 min. These data are relevant with respect to literature [231–233], due to the very small amount of TiO$_2$ that is loaded on the thin film support, in the order of 10^{-1} mg [219]. Moreover, these results were compared to a reference planar TiO$_2$ thin film with the same geometric area synthesized with atomic layer deposition, resulting in a significantly higher photocatalytic activity of PLD tree-like samples. Since the fraction of UV light in the solar lamp output is around 4% of the total irradiation, this activity may be associated to the presence of surface defects (oxygen vacancies, Ti^{3+} sites), as well as to the hierarchical tree-like TiO$_2$ structures which favours photoconversion by combining nano/mesoscale porosity beneficial for the penetration of the organic molecules, a very large surface area and strong light scattering effects [197, 234]. The integration of 0.7%at. Au in the TiO$_2$ nanostructures leads to a further improvement of the photocatalytic activity of the films, reducing the concentration of MO to <50% of its initial value after 60min and to about 10% in 240 min. Although the study of the catalytic mechanisms is beyond the scope of this work, these results suggest that the presence of Au NPs can improve the catalytic activity of bare TiO$_2$ or favor the production of superoxide radicals [235]. Indeed, the presence of Au NPs is expected to make the e$^-$/h$^+$ separation more efficient, moreover plasmonic-related effects such as increased light scattering or hot electron generation can contribute to the enhanced photocatalytic activity [236]. 8Pa-films with 2.9%at. Au were also tested, leading to a decrease of the photocatalytic activity with respect to the one with 0.7%at. Au, which may be related to excessive light absorption by Au or reduction of the active TiO$_2$ surface. Further tests are necessary to elucidate the photocatalytic mechanisms and find the optimal conditions (i.e. Au content and porosity) to develop thin-film photocatalytic supports with superior efficiency.

4.4.2 Surface enhanced Raman scattering of MBA

Further investigations on thermal treatment on 8Pa-films, testing other temperatures ($250 - 700$°C) and duration (2-6 hours), as well as higher porosity (i.e. Au-TiO$_2$ films deposited at 10 and 12 Pa) were performed in collaboration with a Master student for his thesis project [198]. The effect of TiO$_2$ crystallization, the increase of Au NPs size upon annealing, which affects LSPR resonance, and the increased porosity were studied in perspective to develop substrates for surface enhanced Raman scattering (SERS) application. Indeed, the obtained samples were tested at the Laboratory CSPBAT of Université Paris 13 for SERS of 4-Mercaptobenzoic acid (MBA), a molecule used in literature to analyze SERS performance.
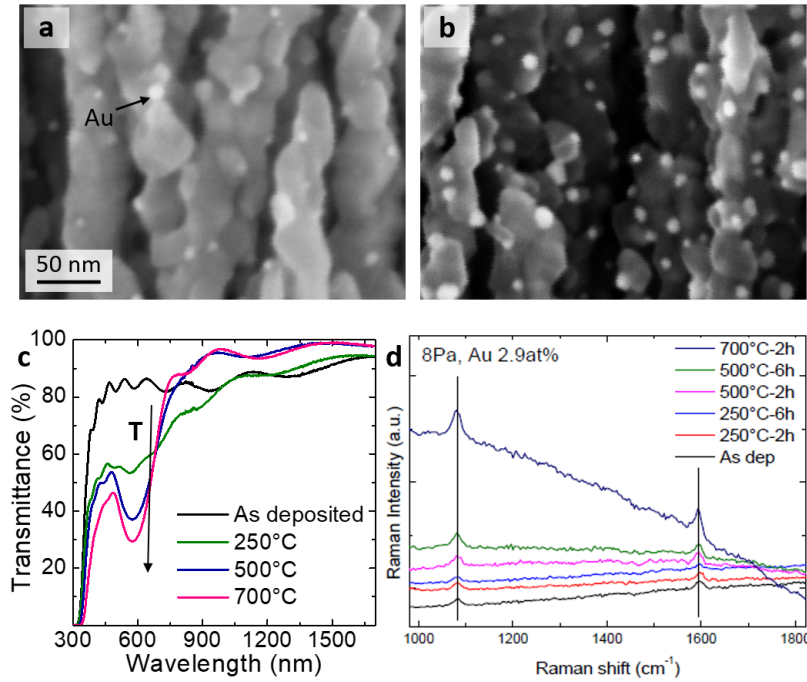
Figure 4.7: *SEM cross-section images of 8Pa-films annealed at 700°C for 2 hours with Au content of (a) 1.0%at. and (b) 2.9%at. (c) Optical trasmittance and (d) SERS measurements of MBA of 8Pa-films with 2.9%at. Au after different thermal treatment. Adapted from [198].*

For the effect of annealing parameters, two Au contents were considered, namely 1.0 and 2.9%at. (see Fig.4.7a,b). Au NPs size and distribution (i.e. number of particles) increased with temperature, while the effect of annealing duration resulted negligible. TiO₂ crystalline structure exhibited a dependence on annealing temperature, since films annealed at 250°C remained amorphous, while at 500°C and 700°C films crystallize in anatase phase. Optical properties were affected by thermal treatment parameters, indeed Au NPs resonance peak became more well-defined with temperature, while a red-shift occurs moving from 250 to 500°C (see Fig.4.7c). In conclusion, thermal treatments showed to be an effective strategy to tune Au NPs morphology and film crystal structure, tuning in turn the optical properties and LSPR resonance of the whole system. These results were interesting toward the application of these systems as high surface area (nanoporous) substrate for SERS, where hierarchical TiO₂ could provide scattering effect, increasing optical path of incident light, as well as its porous surface could favor molecules attachment. For this purpose, films with higher porosity were studied as well, aiming to increase also the analyte molecules penetration within the films.

Au-TiO₂ films were deposited at 10 and 12 Pa of O₂ and the target with three Au plates was employed (corresponding to 4% Au target area, i.e. 2.9%at. Au for 8Pa-films, see Table 4.1), and air-annealing at 500°C for 2 hours were performed. Considering morphology, besides the effect of depositing TiO₂ films with higher porosity, Au NPs size and distribution seemed to be affected by higher deposition pressure too. Indeed, for both as deposited 10Pa- and 12Pa-films, no NPs were observable by SEM (see Fig.4.8a), while after thermal treatments, Au NPs form
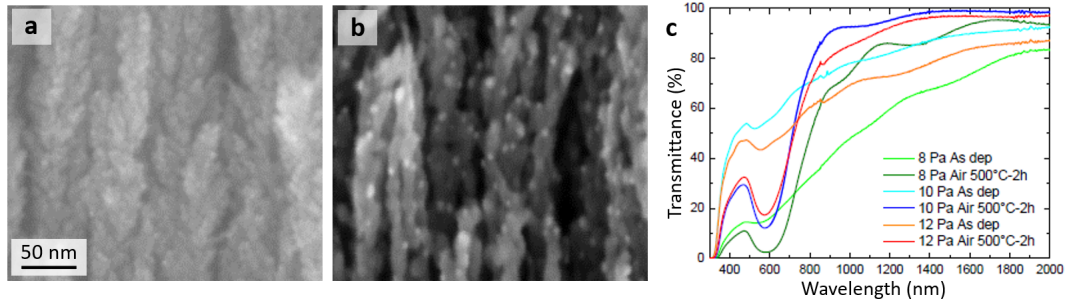
Figure 4.8: *SEM cross-section images of 12Pa-films (a) before and (b) after thermal treatment; (c) optical trasmittance of 10Pa- and 12Pa-films with before and after thermal treatment. Adapted from [198].*

(see Fig.4.8b). Optical transmittance spectra showed that the higher the deposition pressure, the higher the transmittance of the whole films (see Fig.4.8c). This behavior was associated both to higher sample porosity and to a difference in Au content, since the sample thickness was kept constant and equal to 1μm, meaning a shorted deposition time for more porous samples (i.e. lower Au content deposited). After thermal treatment, resonance peaks of Au NPs became well-defined for all samples, the intensity and FWHM decreases by increasing deposition pressure, and peak position slightly differ in all three cases. This behavior suggests Au NPs with similar size, but smaller size dispersion with pressure, which led to sharper peaks.

Then, SERS measurements on MBA were performed. Au-TiO$_2$ samples were soaked in a solution of MBA powder dissolved in pure ethanol for a whole night, to ensure bonds formation between MBA and Au NPs, while allowing MBA organization in self-assembled monolayers [237]. After sample preparation, SERS measurements were carried out with a Horiba LabRAM 300 spectrometer, equipped with a laser of wavelength equal to 632 nm and power of 1.3 mW.

First, 8Pa-films annealed with different thermal treatment parameters were tested. For films with 2.9%at. Au, both MBA peaks at 1080 and 1590 cm^{-1} (for which the enhancement effect was expected) were clearly detectable for each sample (see Fig.4.7d). As a main result, peak intensities increased with sample annealing temperature and this was associated to the combination of two effects: first, annealing temperature promote Au NPs formation and size growth, therefore larger content of MBA molecules can stick on them; second, the NPs size increment leads to red-shift of plasmonic resonance, closer to laser excitation wavelength 632 nm. Then, SERS measurements were repeated also for films at 8 Pa with 1.0%at. of Au. Unfortunately, it was not possible to measure any MBA peak with these samples, likely because of too low content of Au NPs where MBA can attach. Finally, SERS measurements on 10Pa- and 12Pa-films were performed as well, and peak intensities showed an increment with porosity, even though they have the same order of magnitude found for 8Pa-films.

Lastly, co-deposited Au NPs-TiO$_2$ hierarchical films were tested as photoanodes for water splitting and bisphenol A (BPA) oxidation, in collaboration with De-

partement of Mechanical, Chemical and Materials Engineering of Universitá degli studi of Cagliari and Laboratory of Catalysis and Catalytic Processes of Politecnico di Milano. In particular, 8Pa-film with 3.9%at. Au was compared with other Au NPs-TiO$_2$ architectures (i.e. Au NPs on top, on bottom, or both together, of hierarchical TiO$_2$) obtained by different synthesis strategies (i.e. hierarchical TiO$_2$ by PLD, while Au NPs by PLD or thermal evaporation, depending on the architecture). I personally contributed to the fabrication of these samples, however I did not participate to the performing of the functional tests, whose results are reported in [238]. In particular, the advantage of co-deposited Au NPs-TiO$_2$ resulted in a lower corrosion effect on the Au NPs, because of the protection effect of the embedding in TiO$_2$.

4.5 Conclusions

In this chapter, the development and investigation of integrated Au NP-TiO$_2$ hierarchical films, aimed to enhance the oxide photoresponse, was presented. The integration was successfully achieved with an original single-step synthesis procedure by means of pulsed lases co-deposition approach, which ensure homogeneous Au NPs distribution through the whole TiO$_2$ thickness. Specifically, the effect of the Au content (0.5-5%at.) was studied for different TiO$_2$ porosities by depositing at different oxygen background pressures, namely at 5 and 8 Pa. From SEM and TEM analyses, it was observed that the deposition pressure affects the morphological organization of both TiO$_2$ and Au, i.e. 5Pa-films show a layered structure in which TiO$_2$ is separated by Au-rich layers (composed by Au NPs smaller than 3 nm and very close to each other), while 8Pa-films show Au in form of NPs (average diameter of 5 nm) homogeneously distributed in a more porous TiO$_2$. This result is particularly relevant since it is difficult to obtain with other physical vapor deposition techniques without any thermal treatments. Then the effect of post-deposition air-annealing was studied on the point of view of morphology and structure. At temperatures higher than 500°C, TiO$_2$ crystallizes in anatase phase, while Au species start to diffuse, leading to Au NPs formation and growth. The combination of Au content, deposition pressure and thermal treatments demonstrated to offer the opportunity for tuning Au NPs size and distribution, which affect in turn optical properties of the whole system.

Optical analysis showed that for as deposited 5Pa-films, the absorption in the visible range increases with Au content, but a well-defined plasmonic resonance is not observed; while, after annealing, absorption further increases and a plasmonic peak clearly appears around 575 nm, associated to Au NPs formation and growth. For as deposited 8Pa-films, a plasmonic peak at about 540 nm is visible for high Au amount, while annealing induces an increase in the plasmonic absorption for all Au contents and a red-shift of about 20 nm with respect to as deposited films.

Finally, preliminary tests were performed for the application of these systems for photodegradation of pollutants, photoanode for water splitting and as substrate for surface enhanced Raman scattering (SERS). For this last, further investigations on thermal treatment on 8Pa-films, testing other temperatures $(250 - 700°C)$ and duration (2-6 hours), as well as higher porosity (i.e. Au-TiO$_2$

films deposited at 10 and 12 Pa) were performed. These results showed the limited tunability of Au NPs size distributions and, as a consequence, of LSPR position by these process parameters. On the other hand, the role of Au content resulted more effective. Indeed, while for SERS applications a high content is favorable (e.g. good results were achieved for 8Pa-films with 2.9%at. Au), for the photocatalytic activity this can be detrimental for overall system effectiveness and lower Au amounts are preferred (e.g. 8Pa-films with 0.7%at. Au. for photodegradation of MO). However, more studies are needed to understand physical and chemical mechanism involved, such as quantum efficiency tests.

In conclusion, the overall results of this chapter demonstrate the feasibility of one-step synthesis of Au NPs-TiO$_2$ integrated nanostructures via PLD and suggest the potentiality of this approach to be extended to other NP/oxide systems with controlled properties thanks to the versatility of the laser ablation process. In particular, the fascinating possibility of tunable plasmonic response paves the way toward novel plasmonic-based devices. Moreover, these systems can be exploited for other plasmonic applications, especially those requiring nanoscale porosity and light scattering, such as chemical sensors and light management. In addition, Au NPs-TiO$_2$ hierarchical nanostructures are a promising SERS substrate to detect molecules that cannot bind directly to Au NPs, but with TiO$_2$, such as silane molecules, as a way to provide SERS enhancement also to a this kind of molecules [239].

Tantalum-doped TiO$_2$ thin films

As discussed in section 2.2.2, transparent conductive oxides (TCOs) are a well-known class of materials already employed as transparent electrodes in several optoelectronic devices. More recently, TCOs have demonstrated plasmonic response in near- and mid-IR by tuning charge carrier density. This feature is particular attractive since traditional plasmonic metals suffer from high optical losses in this range and difficult tunability, as well as other limitations that TCOs can supply (see section 2.1). Among them, Ta-doped TiO$_2$ has already demonstrated good conductivity while ensuring advantages typical of TiO$_2$, namely chemical stability, availability and lack of toxicity. Previous studies of Ta:TiO$_2$ films were performed at our research group by P. Mazzolini as transparent electrode for solar cell applications [112, 125–127]. However, a systematic investigation on electrical and optical properties, their relation as well as a study focused on plasmonic response, currently lacks. In particular, the effect of Ta content and film thickness, down to ultrathin films (i.e. 10 nm), is essential for a better comprehension of material behavior in view of possible applications. Indeed, thin and ultrathin TCOs films have been proposed for implementation in sub-wavelength nano-optics structures [23], replacing metals which present a percolation threshold.

In this chapter, the development of Ta:TiO$_2$ thin films and the study of their properties is presented. In section 5.1, the optimization of synthesis parameters to obtain uniform and conductive Ta:TiO$_2$ films is discussed, with a focus on the effect of PLD background pressure of oxygen, which affects the presence of oxygen vacancies in the films favoring conductivity. As optimal synthesis conditions have been achieved, section 5.2 deals with Ta:TiO$_2$ films properties as a function of Ta content and thickness (down to ultrathin films), with a particular attention on the understanding of electrical and optical properties. Then, more complex Ta:TiO$_2$-based systems have been developed in collaboration with two Master thesis students, namely Au NPs integrated with compact Ta:TiO$_2$ films and Ta:TiO$_2$ NPs assemblies, whose results are reported in sections 5.3 and 5.4, respectively. Finally, conclusions and perspectives are summarized in section 5.5.
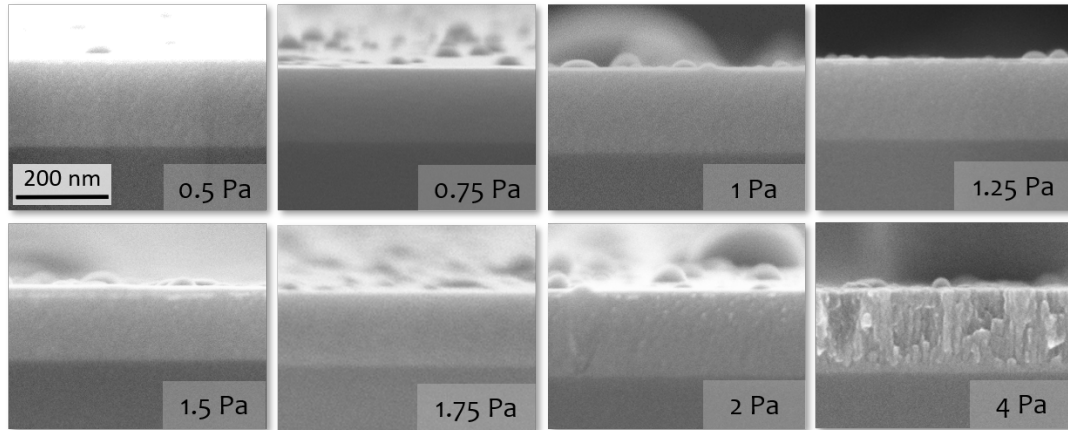
Figure 5.1: *SEM cross-section images of* Ta:TiO$_2$ *with Ta 5% at. deposited at 0.5-4 Pa of* O$_2$*, as deposited.*

5.1 Optimization of synthesis conditions

In this section, the optimal conditions for the deposition of Ta:TiO$_2$ with nominal content of Ta=5% at. are investigated. A targets of Ta$_2$O$_5$:TiO$_2$ with molar ration equal to 0.025:0.975 was employed (99.99% pure, provider *Testbourne Ltd*). Films were deposited on Si [100] and soda-lime glass substrates mounted on a rotating sample holder at a fixed target-to-substrate distance of 50 mm. For the investigation, two PLD parameters were considered, the background pressure of oxygen and the laser fluence on target. This last was chosen equal to 2.27 J/cm^2 because of an investigation in collaboration with a Master thesis student for his thesis [240]. In particular, a higher fluence was found to induce high defectivity while a lower one led to higher amount of surface droplets, both detrimental for functional properties of Ta:TiO$_2$ films.

The effect of oxygen deposition pressure presented interesting results, here reported. Indeed, as explained in section 2.2.3.1, the conductivity of Ta:TiO$_2$ thin films is favored by oxygen-poor conditions leading to oxygen vacancies, controlled in turn by oxygen background pressure during deposition and post-deposition thermal treatment in vacuum. In particular, the defect chemistry activated from oxygen-poor condition is a complex topic and, on the other hand, oxygen-rich conditions provide crystalline defects which act as electron traps [116, 118, 119]. The vacuum thermal treatment was set by Mazzolini on the basis his results and previous works [112, 117, 241]: the chosen annealing condition was in vacuum at 550°C for 1 hour, since it ensures both polycrystalline Ta:TiO$_2$ thin films in anatase phase and oxygen sub-stoichiometry. On the other hand, previous studies employed a laser wavelength equal to 266 nm for PLD synthesis, while in this work it is equal to 532 nm. This difference in PLD set up does not allow to reach either the low laser frequency employed by Mazzolini (i.e. 0.9 J/cm^2) or ensuring the lowest resistivity by depositing at 1.25 Pa [112]. Therefore, the investigation of the optimal background pressure (from 0.5 to 4 Pa) was repeated with the new laser wavelength, at laser fluence equal to 2.27 J/cm^2, while keeping the same post-deposition thermal treatment. In particular, the exact pressure tested are: 0.5,
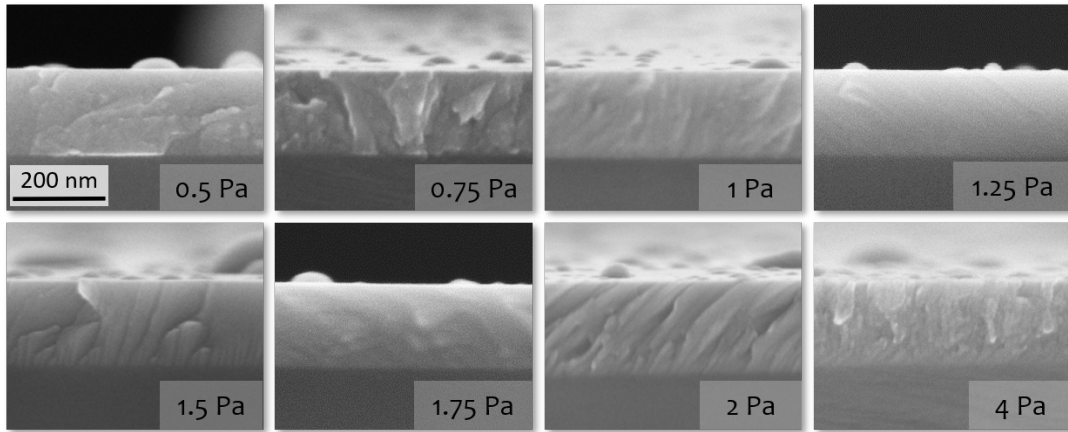
Figure 5.2: *SEM cross-section images of vacuum-annealed* Ta:TiO$_2$ *with Ta 5% at. deposited at 0.5-4 Pa of* O$_2$.

0.75, 1, 1.25, 1.5, 1.75, 2 and 4 Pa; the characterized films were all 200 nm thick. In Fig.5.1, cross-section SEM images show that before the thermal treatment, the deposits are compact and homogeneous up to 2 Pa, while at 4 Pa the film shows some structuring, although it is still compact and planar. After thermal treatment (see Fig.5.2), no significant variations of film morphology occur, except for 4 Pa-film which presents a less clear columnar structure, due to the sintering of the columns during the annealing. The effect of the thermal treatment on crystallinity was evaluated from Raman spectroscopy. Before annealing, no clear peak can be distinguished, and the spectrum only shows broad bands typical of amorphous titania materials. Raman spectra of vacuum-annealed films deposited at different pressures are reported in Fig.5.3a. The typical anatase spectrum present six well known Raman peaks: $E_g(1)$ at $144\,cm^{-1}$, $E_g(2)$ at $197\,cm^{-1}$, $B_{1g}(1)$ at $399\,cm^{-1}$, $B_{1g}(2)$ at $519\,cm^{-1}$, A_{1g} at $513\,cm^{-1}$, and $E_g(3)$ at $638\,cm^{-1}$. Since the A_{1g} and the $B_{1g}(2)$ peak are very close, they cannot be distinguished at room temperature. For films deposited at 1 Pa or higher, the spectrum shows the typical anatase Raman peaks, indicating a complete crystallization. On the other hand, below 1 Pa, the Raman spectra showed significant amorphous features. Indeed, from optical microscope images, macroscopic cracks are observable in these films after thermal treatment, likely due to the excessive sub-stoichiometry of the film. An analogous phenomenon occurs for films deposited at too high laser fluence: at low pressure (or high laser fluence) the kinetic energy of atoms in the plasma plume increases, inducing both more crystallographic defects in the deposit and higher stresses in the films. The cracks are the result of unrelieved stresses in the as deposited film, that lead to fracture when the thermal stresses of the treatment are added.

The effect of oxygen pressure is evident from the measured electrical properties. Fig 5.3b reports resistivity (ρ), charge carried density (n) and Hall mobility (μ) of the annealed films. Particularly interesting is the drop in resistivity at 1 Pa ($\rho = 8 \cdot 10^{-4}\,\Omega cm$), combined with the highest Hall mobility ($\mu = 8.4\,cm^2/Vs$) and a charge carrier density among the highest measured ($n = 9.3 \cdot 10^{20}\,cm^{-3}$). At lower pressure, resistivity sharply increases due to drastic drop in Hall mobility,
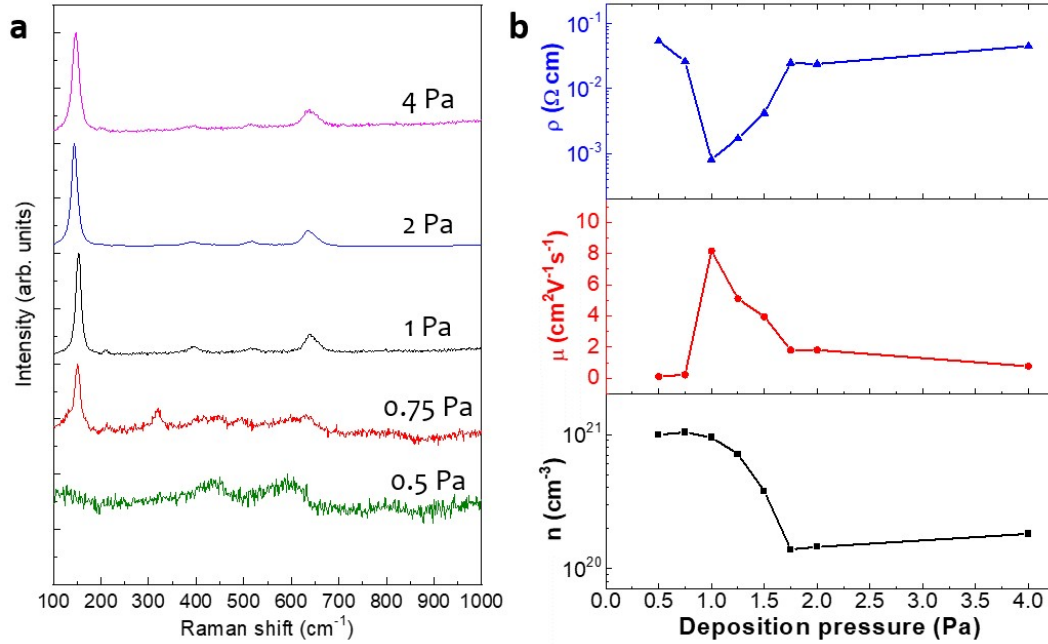
Figure 5.3: *(a) Raman spectra and (b) electrical measurements of vacuum-annealed* Ta:TiO_2 *with Ta 5% at. deposited at 0.5-4 Pa of* O_2*. Electrical measurements involve resistivity (ρ), charge carrier density (n) and Hall mobility (μ).*
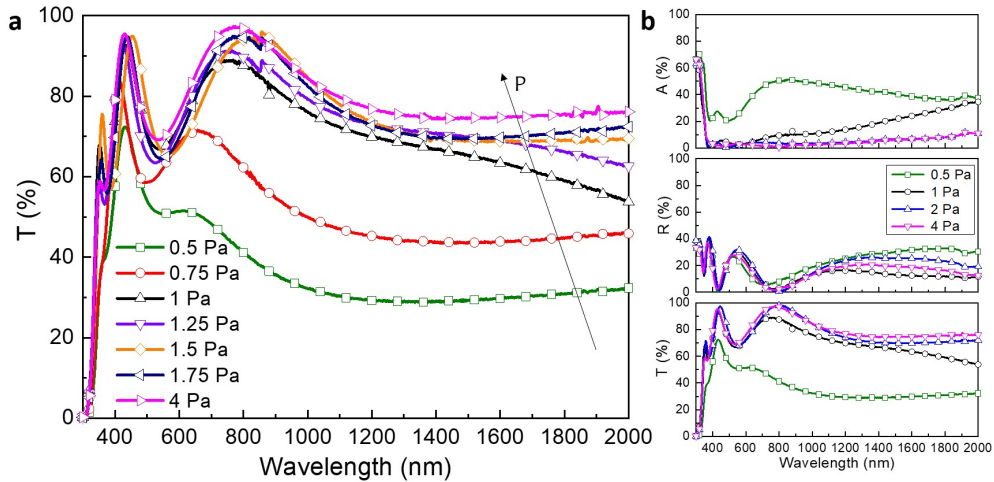
Figure 5.4: *(a) Optical transmittance (T%) of vacuum-annealed* Ta:TiO_2 *with Ta 5% at. deposited at 0.5-4 Pa of* O_2*; (b) transmittance (T%), reflectance (R%) and absorbance (A%) of selected sample deposited at different pressure to highlight different optical behavior.*

likely related to the onset of cracking and low crystallinity degree. On the other hand, from 1 to 1.75 Pa, the resistivity increases monothonically due to a decrease in both carrier density and Hall mobility, while above 2 Pa small changes occurs for all electrical properties. This behavior is associated to the increase of oxygen content in the films with the oxygen deposition pressure, leading to a reduction of the effectiveness of doping in accordance with theoretical calculations and the

increment of electron traps states due to oxygen-reach conditions [112, 116, 118, 119].

Optical behavior was considered as well. In particular, optical transmittance in visible and near-IR range increases with pressure (see Fig. 5.4a). The 0.5 Pa- and 0.75 Pa-films showed higher absorption due to their amorphous character and high quantity of defects, while if the pressure increases less deep defects are available for inter-bandgap absorption (e.g. oxygen vacancy, both neutral V_O^{2-} and ionized V_O^-/V_O, and Ti^{3+} [242]), combined with a lower density, leading to higher transparency (see Fig. 5.4b).

In conclusion, for $Ta:TiO_2$ with Ta=5% at., the optimal pressure condition was found at 1 Pa due to the best electrical properties measured, associated to a good anatase crystallization and oxygen sub-stoichiometry. Then the optimization of process parameters was repeated for $Ta:TiO_2$ thin films with nominal content of Ta = 10% at. A target of $Ta_2O_5:TiO_2$ with molar ratio equal to 0.05:0.95 was employed. The optimal condition was found again at 1 Pa of oxygen, but at a different laser fluence, namely F=2.73 J/cm^2, in order to avoid delamination of the films after vacuum thermal treatments. The effect of Ta content on film properties is presented in detail in the next section, compared to bare TiO_2 films and combined with the effect of thickness decrease (down to 10 nm).

5.2 Effect of thickness and Ta content

In this section, $Ta:TiO_2$ thin films with nominal content of Ta=5, 10% at. are investigated (referred to as $Ta(5\%):TiO_2$ and $Ta(10\%):TiO_2$, respectively) with a focus on the effect of Ta content together with the effect of thickness from 200 nm down to 10 nm. Results were compared with bare TiO_2 thin films deposited from a 99.9% pure TiO_2 target (provider *Kurt J. Lesker*) at 1 Pa and F=2.27 J/cm^2. Comparisons were performed both with vacuum-annealed TiO_2 (i.e. thermal treatment in the same condition of $Ta:TiO_2$ films) and air-annealed TiO_2 (i.e. at 500° for 2 hours), in order to take into account both sub-stoichiometric and stoichiometric TiO_2 films.

The different thicknesses, from 10 to 200 nm, were obtained by varying the deposition duration and the precise values were evaluated by means of a SEM on samples grown on silicon. The deposition rate was estimated and related to the laser fluence, resulting around 11 nm/min for TiO_2 and $Ta(5\%):TiO_2$, and 18 nm/min for $Ta(10\%):TiO_2$. Results of the investigation on the point of view of morphology, structure electrical and optical properties will be presented in the next sections.

5.2.1 Morphology and structure

Fig.5.5 shows the SEM cross-section images of vacuum-annealed $Ta(5\%):TiO_2$ thin films with different thickness, i.e. from 200 nm down to 20 nm, obtained in the same deposition conditions, while tuning the deposition time. As for $Ta(10\%):TiO_2$ and bare TiO_2 films, both as deposited and vacuum annealed films resulted compact and the observed morphology does not change significantly after thermal treatment. The estimation of amount of tantalum in $Ta:TiO_2$ films was
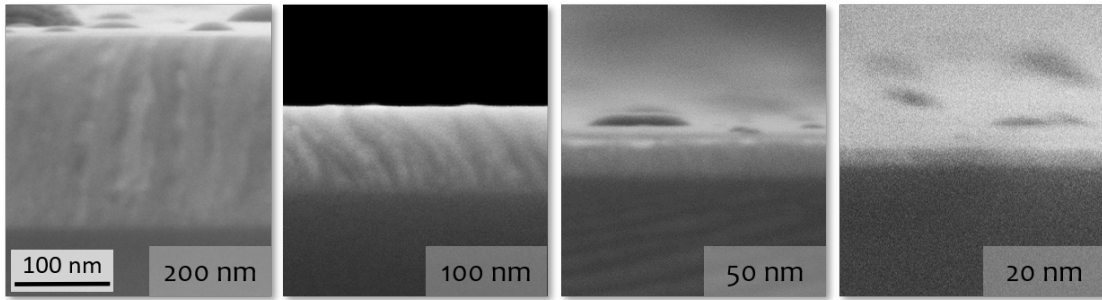
Figure 5.5: *SEM cross-section micrographs of vacuum-annealed Ta(5%):*TiO$_2$ *films deposited on Si substrate with different thickness, i.e. 200, 100, 50, 20 nm.*

performed by means of EDX, resulting in 4.5 and 9% at. for film with nominal content of Ta of 5 and 10% respectively. This result confirms the ability of PLD synthesis to preserve the cationic ratio of ablated material.

Fig.5.6 shows surface images captured by optical microscope of annealed 200nm-thick Ta:TiO$_2$ films at different Ta content and vacuum- and air-annealed TiO$_2$, deposited on glass substrate. After thermal treatment, macro-domains are observable as expected from a TiO$_2$-based film crystallized through a post-annealing [112, 243]. Optical microscopy allowed the surface investigation of films thick in the range of 50-200 nm, while thinnest films were simply not observable. Lateral domain size was measured by means of *Image J* software resulting on average 15-20 μm for Ta(5%):TiO$_2$ and 25-30 μm for Ta(10%):TiO$_2$ films. This difference in domain size is probably not ascribable to the different content of Ta, but rather to the different laser fluence employed during film depositions. As a confirmation of this, optical microscope images of bare vacuum-annealed TiO$_2$ films' surface presented domain size comparable to Ta(5%):TiO$_2$ (see Fig.5.6a,c), indeed the same laser fluence was utilized. On the other hand, air-annealed TiO$_2$ showed the same domain size, but domains are more well-defined and more easier detectable (see Fig.5.6d).

Further surface characterization was performed by SEM at high voltage (15-20 kV), distance (6-7 mm) and contrast on films deposited on Si substrate (see Fig.5.7). For films with thickness between 50-200 nm, cross-shape domains are observable, separated by smaller domains (see Fig.5.7a,b), and this feature is in accordance with previous investigation of TiO$_2$ surfaces after annealing [243]. Average domain size measured from SEM resulted smaller with respect to the films grown on glass substrates, i.e. about 5 and 9 μm for Ta(5%):TiO$_2$ and Ta(10%):TiO$_2$, respectively. Films thick 20 and 10 nm were observed as well, and a sort of uncompleted domains were found (see Fig.5.7c,d).

Structural characterization was performed via XRD, whose measurements and analysis were carried out thanks to the collaboration of G. Terraneo (experimental details of XRD measurements have been already reported in section 4.2). Fig.5.8 shows resulting diffractograms as a function of Ta content for vacuum-annealed films with nominal thickness equal to 200 nm, compared to vacuum- and air-annealed TiO$_2$. The XRD patterns highlighted that all analyzed films show only the presence of crystalline anatase phase while no rutile phase was observed. In
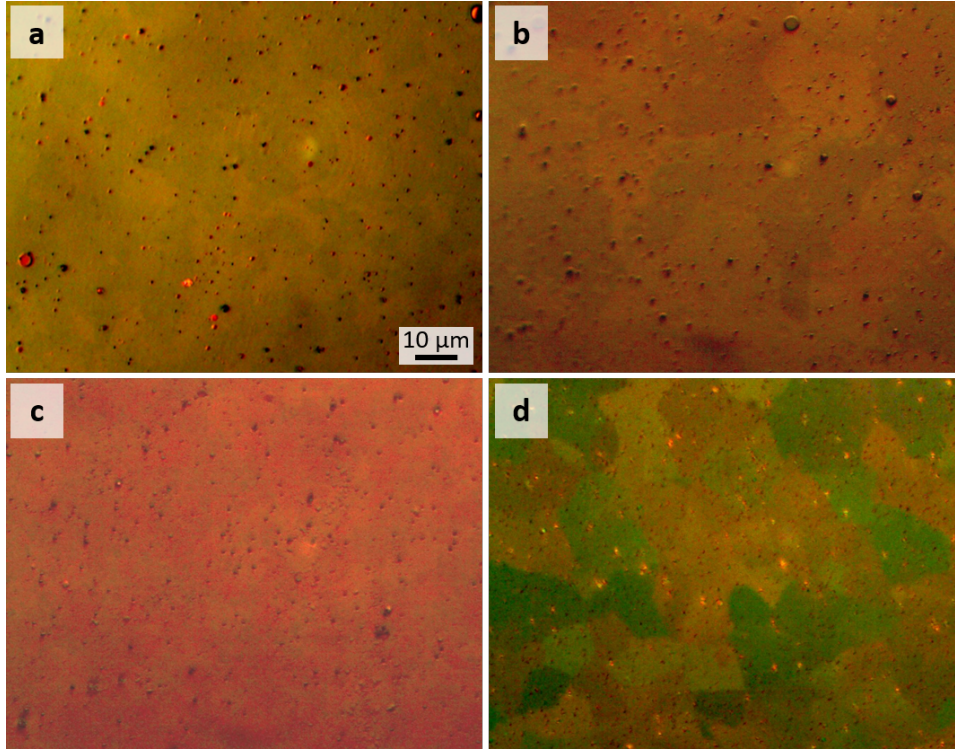
Figure 5.6: *Optical microscope images of surfaces of 200 nm-thick vacuum-annealed (a) Ta(5%):TiO$_2$, (b) Ta(10%):TiO$_2$ and (c) TiO$_2$, as well as (d) air-annealed TiO$_2$. All samples were deposited on glass substrate.*

addition, in both the tantalum-doped films neither the presence of tantalum oxide (Ta$_2$O$_5$) phases nor metallic tantalum aggregates were detected suggesting the formation of homogeneous solid solutions [224]. In all the analyzed films the more intense peak was the (101). This behavior can be explained since it is known that anatase thin films grown on amorphous substrates can form [101] preferred-oriented polycrystalline systems [244, 245]. Interestingly in both the Ta-doped films the relative intensity of the (101) peak was higher than in the TiO$_2$ samples suggesting that in these samples the effect of the doping could induce a preferential direction towards the lowest surface energy, namely the [101] (see inset of Fig.5.8).

In addition, since the atomic radius of Ta is slightly larger than the atomic radius of Ti (145 and 140 pm respectively) and, although the percentage of Ta is relative low, this could introduce some lattice modifications in the samples, which lead to a shift of the measured XRD reflections, as shown for (101) peak in the inset of Fig.5.8. A whole profile fitting performed by means of Pawley method[1] allowed to calculate the lattice parameters a and c of the tetragonal cell of the TiO$_2$ anatase phase according to

$$q_{hkl} = \frac{1}{d_{(h,k,l)}} = \sqrt{\frac{h^2}{a} + \frac{k^2}{a} + \frac{l^2}{c}} \qquad (5.1)$$

---

[1] The mean crystallite size domain and the lattice parameters were determined by using the full profile fitting Pawley method [246]. The Pawley method was carried out using the program-suite TOPAS from Bruker.
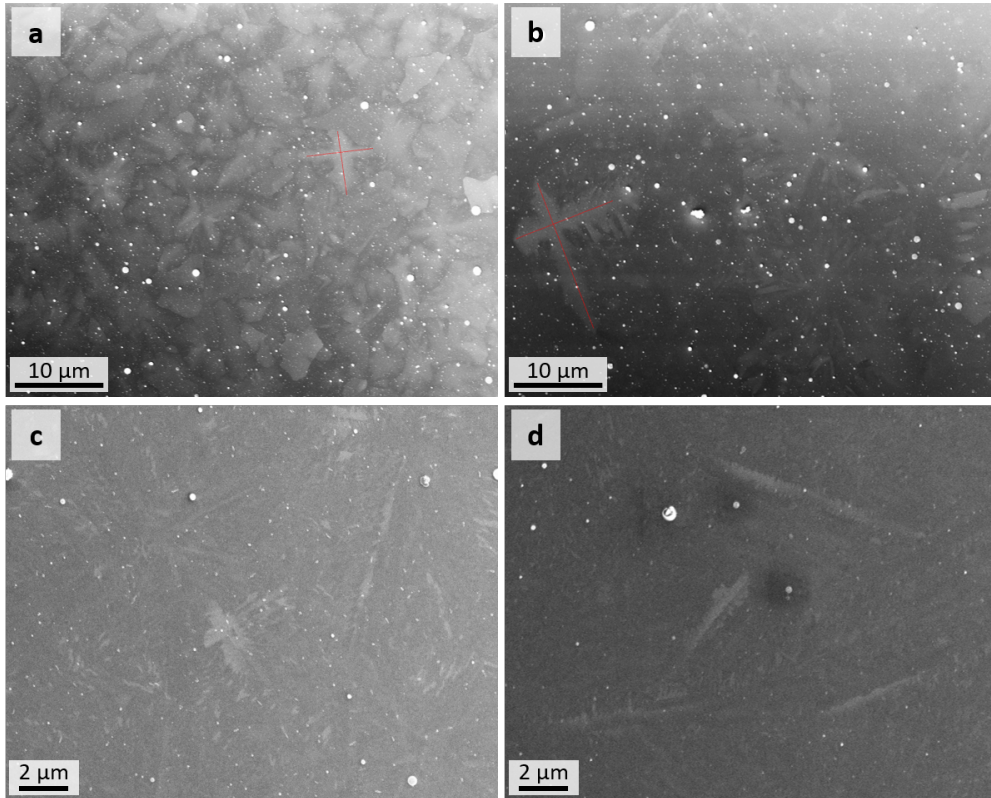
Figure 5.7: *SEM top-view images of 200 nm-thick vacuum-annealed (a) Ta(5%):TiO₂, (b) Ta(10%):TiO₂ and 20 nm-thick (c) Ta(5%):TiO₂, (d) Ta(10%):TiO₂. Cross-shape of crystalline domains of the thickest films are indicated.*

where q_{hkl} is the scattering vector (as a function of scattering angle 2θ, since $q_{hkl} = \frac{2}{\lambda}sin\theta_{hkl}$) and $d_{(h,k,l)}$ is the spacing of the (h, k, l) lattice planes. As a result, the lattice parameters showed a variation of the length in relation of the presence and percentage of Ta. Specifically in the Ta-doped films both the a and c axis were longer than the vacuum-annealed TiO₂ films, while the Ta(10%):TiO₂ film possessed larger cell parameters compared to the Ta(5%):TiO₂ sample (see Table 5.1), confirming the hypothesis of lattice expansion due to Ta incorporation in Ti substitutional sites. The presence of the doping also affected the crystallite size along film growth direction, calculated again with Pawley method. In fact both the Ta-doped films showed a slightly larger mean domain size than the undoped TiO₂ films. In particular, Ta(5%):TiO₂ films display the largest domain equal to 76 nm, while Ta(10%):TiO₂ resulted equal to 68 nm. Interesting the different annealing procedure, namely in vacuum or air, on the undoped TiO₂ films did not produce a marked influence on the mean crystallite domain that remained almost unchanged (i.e. 53 nm and 56 nm for air- and vacuum annealed TiO₂ respectively, see Table 5.1), while lattice parameters and cell volume show more notable differences, as already observed [112].

Structural characterization was supported by Raman analysis and extended down to thinnest films (i.e. 10 nm). Fig.5.9 shows the Raman spectra of Ta(5%):TiO₂ and Ta(10%):TiO₂ films after the vacuum annealing process, as a function of thick-
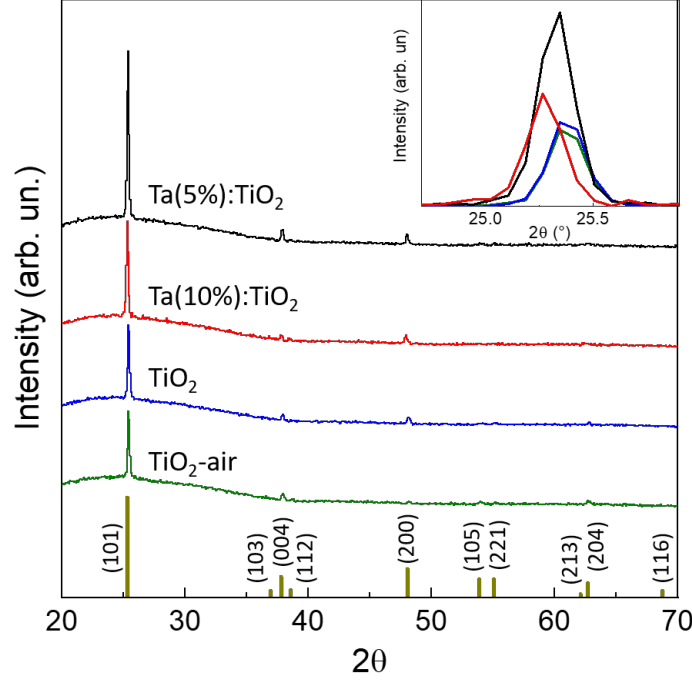
Figure 5.8: *XRD diffractograms of air- and vacuum-annealed* TiO$_2$, *Ta(5%):*TiO$_2$ *and Ta(10%):*TiO$_2$ *films thick 200 nm; the characteristic peaks of anatase are highlighted. The inset shows a magnification of the (101) peak.*

ness. All spectra display the Raman peaks of anatase, while no presence of Ta$_2$O$_5$ or other TiO$_2$ polymorphs is detected, confirming XRD results. In particular, $E_g(1)$, $B_{1g}(1)$, $B_{1g}(2)$ superimposed on A_{1g} and $E_g(3)$ peaks of anatase are evident around their nominal values, i.e. 144, 399, 519, 513 and 638 cm^{-1} [247, 248] for the thickest films (i.e. 75-200 nm). On the other hand, films with thickness in the range 10-50 nm exhibit only $E_g(1)$ and $E_g(3)$ peaks, likely because of the worse signal-to-noise ratio. As shown in Fig.5.10a, Ta content affects the position of the $E_g(1)$ peak. For films about 200 nm thick, $E_g(1)$ peak shifts from nominal position of 144 cm^{-1} to 152 and 155 cm^{-1} for Ta(5%):TiO$_2$ and Ta(10%):TiO$_2$ respectively, while peak FWHM broadens from 10 to 13-14 cm^{-1}. This trend has been already observed by Mazzolini (see section 2.2.3.1) and it was associated to a

Sample	a Å	c Å	Volume Å^3	Mean crystalline domain size nm
TiO$_2$-air	3.63444	9.59028	126.680	53
TiO$_2$	3.78336	9.48282	135.735	56
Ta(5%):TiO$_2$	3.79291	9.49844	136.646	76
Ta(10%):TiO$_2$	3.79329	9.54190	137.299	68

Table 5.1: *Lattice parameters (a and c), cell volume and mean crystalline domain size of 200 nm-thick films of air- and vacuum-annealed* TiO$_2$, *Ta(5%):*TiO$_2$ *and Ta(10%):*TiO$_2$, *calculated by Pawley method.*
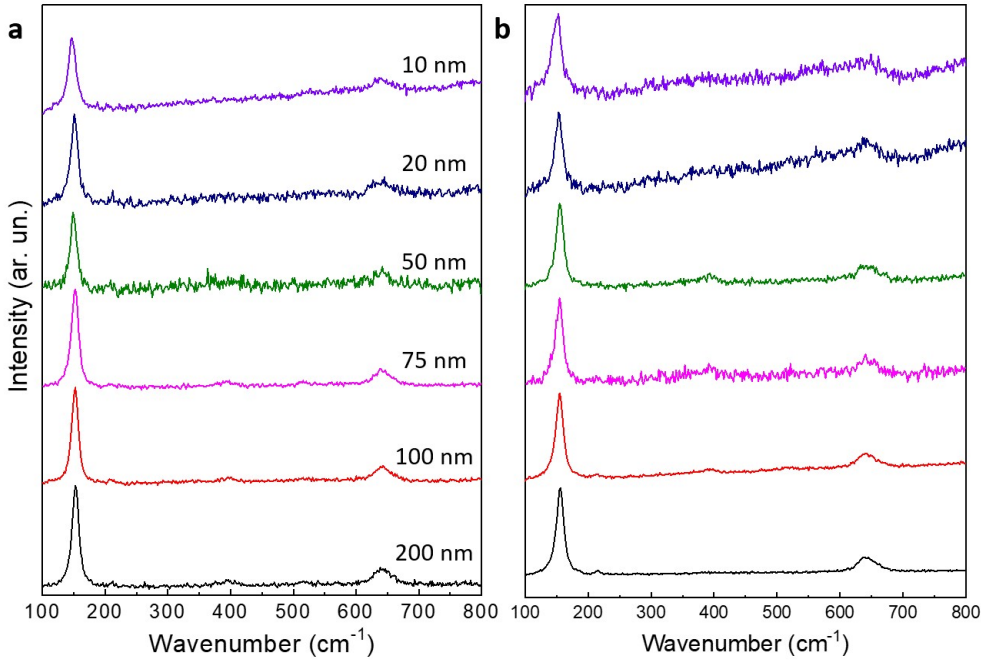
Figure 5.9: *Raman spectra of (a) Ta(5%):TiO$_2$ and (b) Ta(10%):TiO$_2$ films at different thicknesses, i.e. from 10 up to 200 nm.*

correlation between $E_g(1)$ peak position and the measured charge carrier density, independent on type and amount of extrinsic doping, or specific deposition and annealing conditions [126]. Considering these results, Raman analysis allows a qualitative estimate of charge carrier density of Ta:TiO$_2$ thin films. Fig.5.10b,c shows the $E_g(1)$ peak position and FWHM obtained by fitting with Lorentz function: the shift is larger for Ta(10%):TiO$_2$ for every thickness, while at fixed Ta content $E_g(1)$ does not depend significantly on thickness, at least down to 20 nm, in agreement with charge carrier density values (see next section). On the other hand, for 10nm-thick films the $E_g(1)$ position has a smaller shift for both Ta contents, namely to 147 and 150 cm^{-1} respectively, while the peak width increases to 17-18 cm^{-1}. This behavior can be associated to a larger film defectivity, size confinement [248] as well as a smaller charge carrier density (see next section).

5.2.2 Electrical properties

Fig.5.11 reports resistivity (ρ), charge carrier density (n) and Hall mobility (μ) measured for Ta:TiO$_2$ films as a function of thickness (from 10 to 200 nm) and Ta content. Measurements on bare vacuum-annealed TiO$_2$ films (thickness 50 and 200 nm) are reported as reference (blue triangles). Notably, stoichiometric (i.e air-annealed) TiO$_2$ is expected to be insulating (indeed, resistivity was too high for the range of available experimental setup), however, sub-stoichiometric (i.e. vacuum-annealed) TiO$_2$ films display a resistivity of the order of $10^{-2}\,\Omega$cm and charge carrier density of 5-7$\cdot10^{19}\,cm^{-3}$. This behavior is associated to anatase TiO$_2$ with oxygen vacancies, which represent an effective doubly negative charged donor state [112, 249]. For Ta:TiO$_2$ films the resistivity is up to one order of magnitude lower
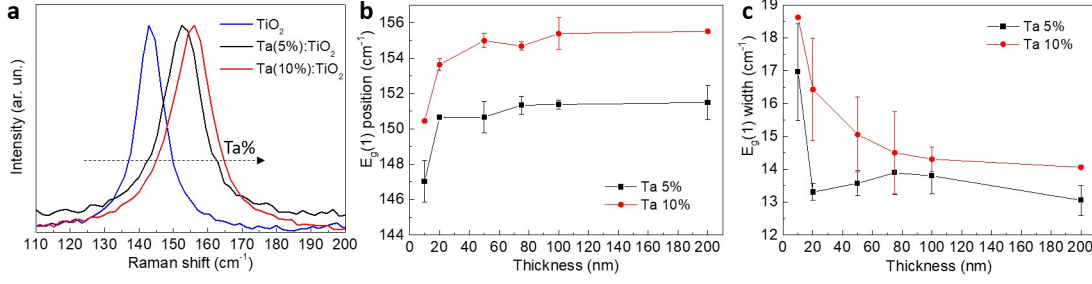
Figure 5.10: *(a) Magnification on $E_g(1)$ peak of Raman spectra of films thick 200 nm with different Ta content (5, 10 %at. and bare TiO_2); (b) position and (c) FWHM of the fitted $E_g(1)$ peak as a function of Ta content and film thickness.*

than bare TiO_2 for both Ta contents, i.e. from $10^{-2}\,\Omega$cm to $10^{-3}\,\Omega$cm, because of conduction electrons from the Ta active dopant (see Fig.5.11a). Focusing on $Ta(5\%){:}TiO_2$ films, the resistivity is almost constant for films thick from 200 down to 50 nm, with a slight increment from $8 \cdot 10^{-4}$ up to $1 \cdot 10^{-3}\,\Omega$cm, while a more evident increment occurs for 20nm-thick film, where the resistivity reaches $3 \cdot 10^{-3}\,\Omega$cm. The same trend occurs for $Ta(10\%){:}TiO_2$ films, where resistivity is around $1 \cdot 10^{-3}\,\Omega$cm for films 50-200 nm thick, while it increases to about $2 \cdot 10^{-3}\,\Omega$cm for 20nm-thick film.

For both doping contents, charge carrier density does not significantly vary with thickness down to 50 nm (see Fig.5.11b). Moreover, n of $Ta(10\%){:}TiO_2$ films is almost the double of $Ta(5\%){:}TiO_2$, indeed the average values over thickness of 50-200 nm are $1.65 \cdot 10^{21}$ and $9.95 \cdot 10^{20}\,cm^{-3}$, respectively. For 20 nm-thick films the charge carrier density is a bit smaller than thicker films for both Ta contents, but $Ta(10\%){:}TiO_2$ film still show a higher value than $Ta(5\%){:}TiO_2$. These results indicate that the charge carrier density increases proportionally with Ta content in a condition of high dopant activation efficiency as observed for thickest films as well [110]. Precisely, by considering EDX results and measured charge carrier density, dopant activation efficiency results equal to 74% and 68% for $Ta(5\%){:}TiO_2$ and $Ta(10\%){:}TiO_2$, respectively.

For 200 nm-thick films, Ta content evidently affects the Hall mobility (see Fig.5.11c). Indeed, while μ measured for $Ta(5\%){:}TiO_2$ is almost equal to bare TiO_2 (i.e. around 8 cm^2/Vs), mobility of $Ta(10\%){:}TiO_2$ is about half. This behavior is related to the higher concentration of ionized impurities in crystal lattice, which affects electron scattering, as well as the probability of carrier-carrier and carrier-defect interaction at higher value of n [80, 126]. Moreover, Hall mobility clearly decreases with thickness. For $Ta(5\%){:}TiO_2$, μ decreases gradually from about 8 to 5 cm^2/Vs by reducing thickness from 200 to 50 nm, while Hall mobility falls down to 1.5 cm^2/Vs for 20 nm-thick film. On the other hand, mobility remains almost constant and around 4 cm^2/Vs for $Ta(10\%){:}TiO_2$ films down to 50 nm, and drops to about 2 cm^2/Vs for 20 nm-thick film. This trend as a function of thickness can be related to the grain size reduction, because μ is affected by scattering at imperfections like grain boundaries or dislocation, as well as scattering at the interfaces [250]. Indeed, in section 5.2.1 the mean crystalline domain
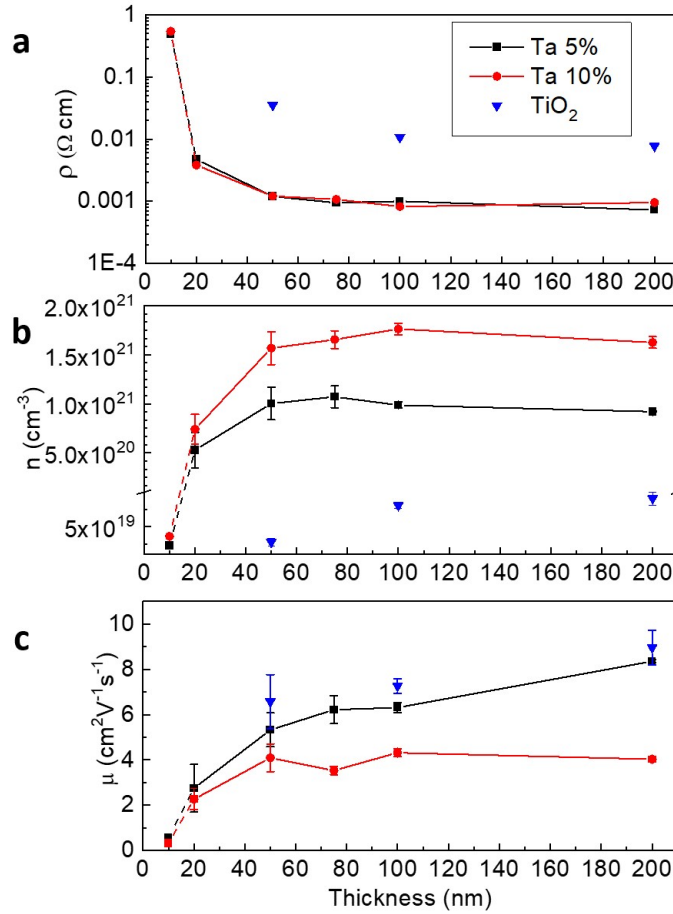
Figure 5.11: *(a) Resistivity ρ, (b) charge carrier density n and (c) Hall mobility μ as a function of film thickness (from 10 to 200 nm) and Ta content: 5% at. (black squares), 10% at. (red circles) and bare TiO_2 (blue triangles).*

size was calculated from XRD measurements on 200 nm thick-films and resulted 76 nm and 68 nm for Ta(5%):TiO_2 and Ta(10%):TiO_2 respectively. Therefore, the higher Hall mobility of Ta(5%):TiO_2 can be favored also by larger grains, moreover a significant decrease of μ with thickness reduction is expected for sizes much lower than the calculated mean domain, such as 20 nm-thick films, because crystalline grains could not grow up completely.

On the other hand, 10nm-thick films display a completely different electrical behavior, almost independent on Ta content. Indeed, for both Ta(5%):TiO_2 and Ta(10%):TiO_2 10 nm-thick films, the resistivity measured is about $0.5\,\Omega$cm, therefore more than two orders of magnitude higher than thicker Ta:TiO_2 films (see Fig.5.11a). Hall effect measurements on these films were less reliable and repeatable, likely because of the higher resistance of the film as well as the difficulty to measure such a thin film with our setup. The measured charge carrier density was 2.3 and $3.5 \cdot 10^{19}\ cm^{-3}$ for Ta of 5 and 10 % at., respectively, namely around 2 orders of magnitude smaller than thicker films (see Fig.5.11b). At the same time, Hall mobility drops by one order of magnitude with μ=0.56 cm^2/Vs for Ta(5%):TiO_2

and μ=0.31 cm^2/Vs for Ta(10%):TiO$_2$ (see Fig.5.11c). This behavior can be explained with the presence of defects at the film surface and at the interface with the substrate, causing electron trapping and scattering, and such defects become dominant in ultrathin films with a thickness of 10 nm, combined with the fact that crystal domains cannot grow up completely [250–252]. Moreover, the chosen annealing temperature for Ta:TiO$_2$ thin films is around the annealing point of the soda-lime glass substrate, therefore there could be a non-negligible exchange of species between the film and the substrate at the interface, whose effects could be significant on the properties of 10 nm-thick films.

5.2.3 Optical properties

Ellipsometric measurements[2] were performed on Ta:TiO$_2$ films with 200 nm nominal thickness, grown on Si substrates, in collaboration with M. Sygletou and F. Bisio at CNR-SPIN of Genova. Specifically, spectroscopic ellipsometry (SE) measures the change of the polarization state of light reflected at non-normal incidence off the sample surface. The result consist in the ellipsometric angles $\Psi(\lambda)$ and $\Delta(\lambda)$, defined as $\frac{r_p}{r_s} = tan\Psi \cdot e^{i\Delta}$, where r_p and r_s are the Fresnel reflection coefficients for p- and s-polarized radiation. The measured films were modeled as a stack of dielectric layers, each characterized by its thickness and complex dielectric function, representing the physical layers of the samples. The optical response of the system was calculated assuming Fresnel boundary conditions at the interface between the layers. Bottom to top, the model included: i) a semi-infinite Si substrate, ii) a native oxide layer, iii) the Ta:TiO$_2$ (or TiO$_2$) film and iv) a roughness layer (the latter modelled as a Bruggemann effective-medium layer [253] composed at 50% by Ta:TiO$_2$ and 50% by voids). For the modelling of the optical properties of Ta:TiO$_2$ films, a combination of Lorentz, Lorentz-gaussian and Parametrized SEMIconductor oscillator model (called PSEMI oscillators) were employed, together with a Drude-type contribution for representing the doping-induced free carriers. PSEMI oscillators are parameterized functions widely employed for modelling the optical response of crystalline semiconductors [254]. The oscillator parameters of the bare TiO$_2$, and the Ta:TiO$_2$, layer, as well as the thickness of all the optical layers were carefully fitted in order to achieve the best agreement between the experimental data and the simulated SE spectra. The thickness of the SiO$_2$ native oxide on a bare substrate was measured about 2 nm. Here, only measurements on films thick 200 nm are discussed, since for the thickest films (100-200 nm) the results change within the variability of the measurement, while for thinner films (lower than 50 nm) the measurements are not reliable.

Fig.5.12 reports the real (ϵ_1) and the imaginary (ϵ_2) part of the dielectric functions extracted from SE measurements by means of the described optical model. The results for Ta:TiO$_2$ films with Ta content of 5 and 10% at. are compared to bare TiO$_2$ with the same nominal thickness (i.e. 200 nm), both air-annealed and vacuum-annealed. For the real part (ϵ_1, Fig.5.12a), air-annealed TiO$_2$ shows two humps in the high-energy region (3.5-4.5 eV), while vacuum-annealed TiO$_2$ shows a unique band in the same range. In the visible range, ϵ_1 decreases for both air- and vacuum-annealed TiO$_2$ with almost the same slope.

---

[2]J.A. Woollam V-VASE ellipsometer, 0.5-5.05 eV range, incidence angle of 60°.
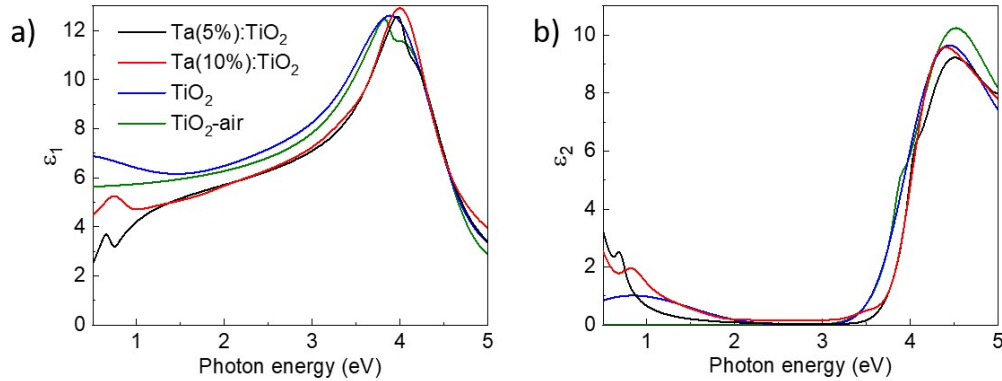
Figure 5.12: *(a) Real and (b) imaginary parts of the dielectric function of* Ta:TiO$_2$ *films with different doping contents (5, 10% at.) compared with bare vacuum-annealed (*TiO$_2$*) and air-annealed* TiO$_2$ *(*TiO$_2$*-air).*

For both samples, ϵ_1 values are in accordance with values reported in literature for anatase along the entire range, with a maximum at 3.8-3.9 eV around 12.5 and between 6 and 9 in visible range (1.7-3.3 eV) [255–258]. In the IR range, ϵ_1 is flat for air-annealed TiO$_2$, while its value increases for vacuum-annealed TiO$_2$. On the other hand, Ta doping leads to blue-shifted and narrowed bands in the UV range, while the maximum values of ϵ_1 are close to bare TiO$_2$. In the visible range, ϵ_1 curves for Ta:TiO$_2$ films almost overlap and decrease as bare TiO$_2$ but at lower values (this behavior has been already reported by Manole et al. for Nb-doped anatase [259]), while in the IR range ϵ_1 decreases and shows a small peak for both Ta-doped films (at 0.65 and 0.76 eV for Ta(5%):TiO$_2$ and Ta(10%)TiO$_2$, respectively).

In Fig.5.12b, ϵ_2 of air-annealed TiO$_2$ exhibits a band in the UV range associated to optical band gap absorption with a peak around 4.5 eV and a shoulder at 3.8 eV. This shape is associated to anisotropy of the crystal structure of anatase which results in optical properties strongly dependent on the polarization direction of the incident light beam. Indeed, the shoulder and the peak are associated to perpendicular and parallel component of dielectric tensor to c-axis [255, 256, 260]. Similar to ϵ_1, also ϵ_2 of vacuum-annealed TiO$_2$ shows a unique band in the UV range at the same energy of air-annealed TiO$_2$, but with a slightly smaller value. The effect of Ta doping is the shift of absorption band in UV at higher energy values, suggesting a higher optical band gap with respect to bare TiO$_2$ film, due to Moss-Burstein effect [82, 261] (see section 2.2.1). In the visible range, all ϵ_2 curves go to zero, suggesting no absorption as expected for TiO$_2$ and TiO$_2$-based TCO. In the lower-energy region of the visible range (below 2 eV) and in the IR range, ϵ_2 of air-annealed TiO$_2$ curve is close to zero, while for vacuum-annealed TiO$_2$ it increases to a maximum at about 0.84 eV. The different behaviour of vacuum-annealed TiO$_2$ with respect to air-annealed TiO$_2$ in this range can be associated to oxygen vacancy concentration in anatase structure (as already discussed in the previous section) [262, 263]. On the other hand, Ta:TiO$_2$ films show a larger increase of ϵ_2 in this range (occurring at lower energy for Ta(5%):TiO$_2$). Notably, as for ϵ_1 curves, both Ta:TiO$_2$ films show a peak in this range at 0.68 and 0.82 eV
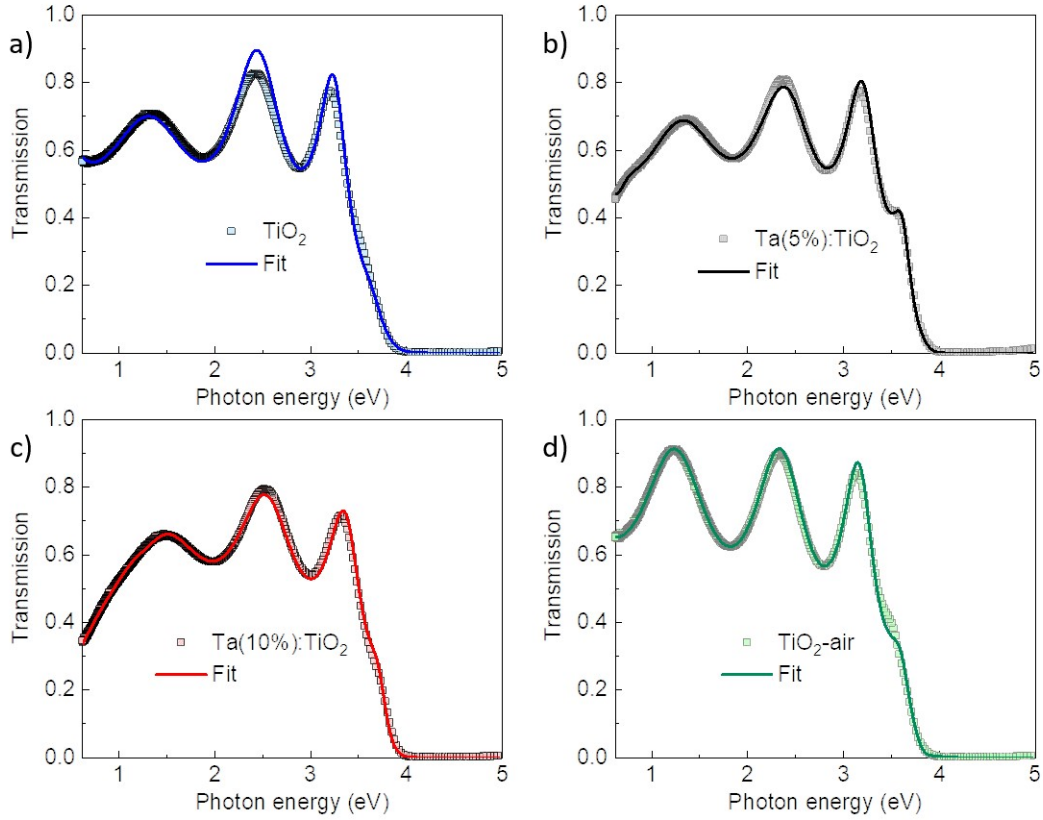
Figure 5.13: *Transmission spectra of vacuum-annealed (a) TiO$_2$, (b) Ta(5%):TiO$_2$, (c) Ta(10%):TiO$_2$ and (d) air-annealed TiO$_2$ films of 200 nm thickness, grown on soda-lime glass substrates. Squares represent the experimental data while lines the theoretical fit, as extracted from ellipsometry measurements.*

for Ta content of 5 and 10% at., respectively.

Optical properties in the IR range of both Ta:TiO$_2$ films show a behavior associated with free carrier absorption related to plasma resonance which occurs for large concentration of conduction electrons [250] and is expected to blue-shift with charge carrier density [76], as observed for Ta(10%):TiO$_2$. The explanation of the small peaks in IR range both in ϵ_1 and ϵ_2 curves is less straightforward. A hypothesis is the establishment of a strong interaction between plasma oscillation of free carriers and phonons, with a formation of longitudinal optical phonon-plasmon coupled mode. This phenomenon is typical of polar semiconductor [264, 265] and it occurs in the IR dielectric response, which can be described by a harmonic oscillator function with Lorentzian line shape [266]. However, Ta:TiO$_2$ is not a polar material, but the large carrier density due to Ta doping as well as a large degree of lattice defects could induce increasing ionic character of Ti-O covalent bond; even so, further investigations are needed to understand these phenomena.

The optical constants extracted from ellipsometry were applied for the modelling of transmission measurements. The system was modelled replacing the Si/SiO$_2$ substrate with a soda-lime glass. In Fig.5.13 experimental data from the

transmission measurements are shown (squares) along with the fit data (continuous lines) which are the outcome of the modelling. The experimental data are in a good agreement with the fit, that requires only small adjustments of the oscillator parameters with respect to the Si substrate case. Indeed, transmittance spectra confirm the optical behavior observed with dielectric function analysis. For all spectra, transmittance goes to zero in the UV range due to interband absorption at the band gap, while it increases in the visible and near-IR range. The oscillations in that range are due to thin-film interference and related to the film optical path length, namely film thickness times the refraction index [80, 267]. In accordance with ellipsometry measurements, vacuum-annealed TiO$_2$ shows lower transmittance intensity than air-annealed TiO$_2$ in the range from high-energy visible to IR associated to absorption of oxygen vacancies, while both Ta:TiO$_2$ films show a stronger decrease in transmittance in near-IR due to free carrier absorption related to plasma resonance. Furthermore, the effect of increasing Ta content is observable in a blue-shift in energy where transmittance starts to decrease in near-IR and a blue-shift of absorption edge in UV range because of free carriers absorption and Moss-Burstein effect, respectively, as previously explained.

Fig.5.14a,c show optical transmittance as a function of film thickness, from 10 up to 200 nm, of Ta(5%):TiO$_2$ and Ta(10%):TiO$_2$ films. Thickness reduction leads to an increase of transmittance intensity in visible and IR range because of absorption reduction, according to Lambert-Beer law (see Eq.3.4), while interference fringes change according to the optical path length. This modulation of fringe position is a fascinating feature which can be exploited in applications in which TCO films are employed as transparent electrodes and a fine tuning of film transparency at specific wavelengths is required. The effect of thickness in UV range is more appreciable looking at the absorption coefficient (α), reported in Fig.5.147b,d as a function of energy, evaluated from measured transmittance and reflectance spectra via Lambert-Beer law Eq.3.4. Examples of reflectance measurements are reported in inset of Fig.5.14b which shows spectra of 10, 50 and 200 nm Ta(5%):TiO$_2$ films and again the effect of thickness is observable on reflectance intensity and interference fringes. The absorption coefficient shows the onset of the absorption band, which does not depend on thickness down to 50 nm, while for 10 and 20 nm-thick films it is redshifted.

As discussed in the section 2.2.3, Ta-doped TiO$_2$ is a promising TCO, therefore optical band gap of Ta:TiO$_2$ films is an important property which we investigated as a function of Ta content and thickness. The optical gap (E_g) was calculated by means of Tauc plot of the absorption coefficient (see Eq.3.5) and results are reported in Fig.5.15a as a function of Ta content and thickness. The $(\alpha h\nu)^n$ versus $h\nu$ was plotted in the proximity of the absorption onset of the films in the UV and the exponent n was chosen equal to 0.5 because of the indirect band gap of anatase; E_g was extrapolated with the intercept in the energy axis using a linear fit (see Fig.5.15b). In Fig.5.15a, the results of 20, 50 and 200 nm-thick vacuum-annealed TiO$_2$ films are reported as reference and the calculated band gap is about 3.29 eV, in line with band gap of anatase reported in literature (3.2-3.4 eV) [55, 258]. A very similar value of E_g was obtained for air-annealed TiO$_2$ films.
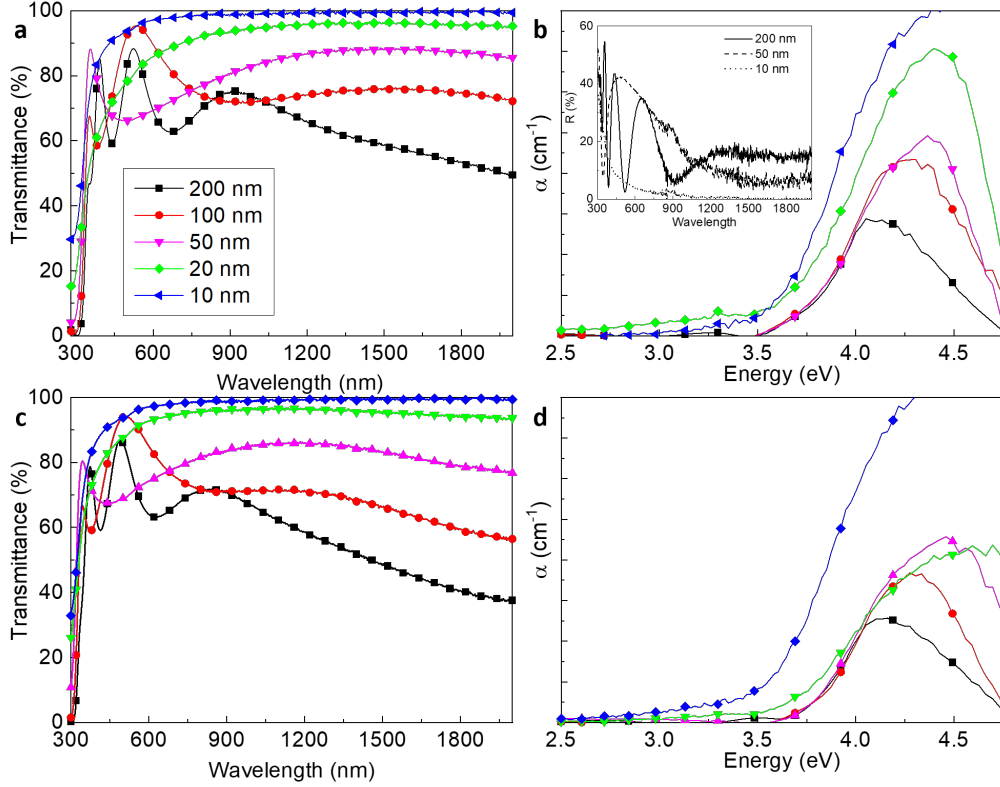
Figure 5.14: *Optical transmittance and absorption coefficient (α) as a function of thickness (10-200 nm) of (a,b) Ta(5%):TiO_2 and (c,d) Ta(10%):TiO_2 films; the legend of all images is in figure (a). Inset in figure (b) shows reflectance spectra of Ta(5%):TiO_2 film thick 10, 50 and 200 nm.*

For the thickest Ta:TiO_2 films, i.e. 50-200 nm, E_g increases with Ta content as a consequence of Moss-Burstein effect, where free carriers partially fill the conduction band forcing higher energy optical transitions [82]. Indeed, the measured charge carrier density of Ta(10%):TiO_2 almost doubles that of Ta(5%):TiO_2. Congruently, the average band gap calculated for 50-200 nm TiO_2 films doped with 5 and 10% at. of Ta was 3.48 and 3.56 eV, respectively. On the other hand, E_g calculated for films thick 10-20 nm decreases with thickness down to a value expected for an undoped film, in agreement with the measured charge carried density which starts to decrease for 20 nm films, down to a value typical of undoped TiO_2 for 10nm-thick films.

In support of this, optical band gap was calculated from ellipsometric measurements too. Indeed, refractive index (n) and extinction coefficient (k) were estimated from real (ϵ_1) and imaginary part (ϵ_2) of dielectric function according to Eq.1.10 and 1.11 (see section 1.2), then absorption coefficient is obtained according to the equation $\alpha = \frac{4\pi k}{\lambda}$. Tauc plot with α extracted from ellipsometry of 200 nm-thick films gives results in agreement with previous calculation, i.e. 3.28 eV for bare TiO_2, as well as 3.46 and 3.53 eV for Ta(5%):TiO_2 and Ta(10%):TiO_2, respectively.
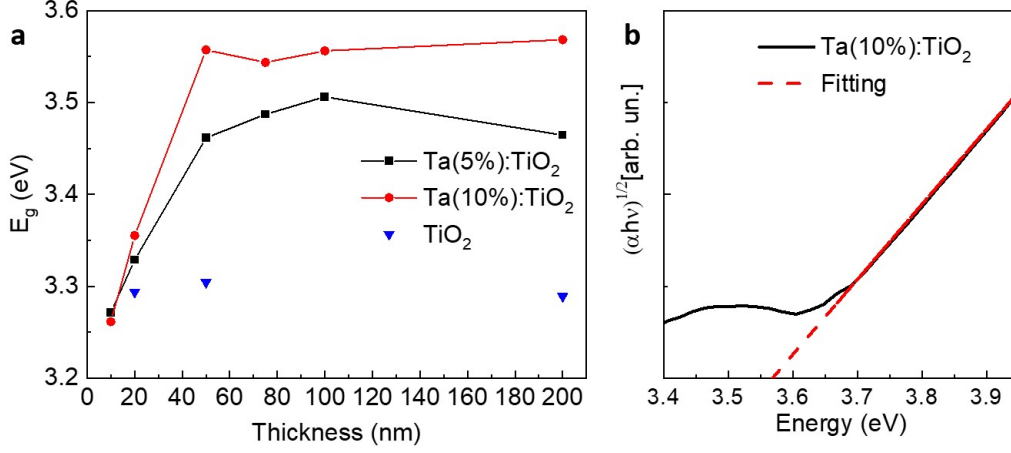
Figure 5.15: *(a) Optical band gap (E$_g$) as a function of thickness (10-200 nm) and Ta content (bare TiO$_2$, 5 and 10% at.) calculated via Tauc plot. (b) Tauc plot of a vacuum-annealed Ta(10%):TiO$_2$ thick 200 nm; the red dotted line is the linear fit exploited in the range of the linear region in correspondence of the band gap absorption.*

Optical band gap results combined with electrical properties highlight the potentiality of Ta:TiO$_2$ thin films for TCO applications, indeed we found that their optoelectronic properties remain almost unchanged down to a thickness of 50 nm and good values are obtained for 20 nm thick films too, even if electrical performance is worse and optical band gap decreases. Finally, 10nm-thick films show an optical gap comparable to bare anatase and their measured electrical properties show a further deterioration, nonetheless such ultra-thin films demonstrated still acceptable conductivity while their optical gap allows transparency in visible range.

The effective mass (m^*) of electrons in the conduction band was considered as well, being a relevant property for TCOs. For the calculation of m^* we used the Drude model (Eq.1.6) and the definition of plasma frequency (Eq.1.7). Therefore, by knowing charge carrier density measured electrically and by fitting the ellipsometric measurements with Drude model, the effective mass can be calculated. For Ta(5%):TiO$_2$, the result is that m^* varies between 2.19 and 3.6 m_e in the photon energy range 0.5-3 eV (in particular, at 0.5 eV m^*=2.41 m_e, and at 3 eV m^*=2.19 m_e); while for Ta(10%):TiO$_2$ in the same photon energy range, m^* results in the range 3.18-4.5 m_e (in particular, at 0.5 eV m^*=3.92 m_e and at 3 eV m^*=4.5 m_e). These results meet the expectations. Indeed, because of the anisotropy of the effective mass of anatase single crystals (as explained in section 2.2.3), theoretical calculations of m^* of both Nb- and Ta-doped anatase and experimental work on Nb-doped TiO$_2$ report m_x^*= 0.4-0.6 m_e and m_z^*>3.5 m_e (where m_x^* and m_z^* are the orthogonal and parallel components of m^* with respect to tetragonal axis, respectively). Moreover, calculations predict an increase of m_z^* with charge carrier concentration [121–124]. Here, taking into account that Ta:TiO$_2$ films are polycrystalline, the m^* results seem to be consistent with values reported in literature and the anisotropicity appears mediated by the different crystallites orientations, in addition m^* shows an increment with Ta content.

Furthermore, a rough estimate of m^* can also be obtained from the optical bandgap shift due to Moss-Burstein effect, under simplified hypothesis (see Eq.2.1 in section 2.2.1), by knowing charge carrier density from electrical measurements, while ΔE_g is calculated by subtracting the optical gap of bare TiO$_2$ (3.29 eV) to that of Ta:TiO$_2$ films evaluated by Tauc plot and reported in Fig.5.15a. Since electrical measurements and optical band gap calculations do not show significant dependence on thickness in the range 50-200 nm, also effective mass varies marginally with thickness; indeed, m^* values of 1.7-2.2 m_e and 1.8-2.1 m_e are obtained for Ta(5%):TiO$_2$ films and Ta(10%):TiO$_2$ films, respectively, notably almost the same for both Ta contents. These results are smaller than the effective mass reported in literature in Mazzolini's previous work on Ta:TiO$_2$ films which employed the same calculation method (i.e. 2.9 m_e) [112]. Anyhow, this calculation procedure should be considered as a qualitative description, since the effect of nonparabolicity of the bands, which could be introduced by many-body type interactions, is not considered in the model (Eq.2.1) [83, 268, 269]. For 20 nm-thick films larger values of m^* are obtained, but the result is affected by the fact that the evaluation of ΔE_g is unreliabale due to the transparency of the film, while for 10 nm films m^* cannot be estimated at all. Nonetheless, these values are underestimated with respect to m^* obtained from Drude modeling of ellipsometric measurements, especially for Ta(10%):TiO$_2$. This is not surprising, given the approximations involved in such an estimate.

Finally, according to the low frequency region of the dielectric constant and by taking into account only the free carriers due to the dopant, we calculated the plasma energy (E_P) by using Eq.1.7 of plasma frequency and by knowing $E_P = \hbar\omega_P$. The contribution of bound electrons of the semiconductor was considered by introducing ϵ_∞ (reported equal to 5.9 for anatase [270]) [271]. First, we consider the effective mass extracted from optical gap shift (Eq.2.1). As expected, the effect of thickness in the range of 50-200 nm is slight; E_P values between 0.32-0.36 eV and 0.43-0.45 eV are obtained in this thickness range for Ta(5%):TiO$_2$ and Ta(10%):TiO$_2$, respectively. In support of these results, the same calculation was performed by using m^* obtained from Drude model applied to ellipsometry, resulting E_P= 0.25-0.32 eV and 0.32-0.35 eV for Ta(5%):TiO$_2$ and Ta(10%):TiO$_2$, respectively. The E_P values in the near- and mid-IR range are expected for a TCO with charge carrier density of the order of $10^{21}cm^{-3}$, such as Ta:TiO$_2$.

Because of these results, FTIR[3] measurements were performed thanks to the collaboration of F. Rusconi and P. Biagioni, at the Department of Physics of Politecnico di Milano, in order to further investigate Ta:TiO$_2$ optical behavior in this range (i.e. 0.1-1.49 eV). The measured samples are vacuum-annealed Ta:TiO$_2$ films with different Ta content (5, 10%at.) compared with vacuum- and air-annealed TiO$_2$. For these measurements, films were deposited on CaF$_2$ substrates, which is transparent along the considered range, and the chosen thickness was around 700 nm, to detect enough signal. Specular transmittance spectra were measured; the curves are reported in Fig.5.16 (continuous lines) and compared with specular transmittance on the same samples measured with the

---

[3]FTIR spectrophotometer INVENIO-R (Bruker). Sources involve halogen lamp for near-IR (0.37-1.49 eV) and globar for mid-IR (0.1-0.62 eV); the employed detector is mercury cadmium telluride (MCT). The beam incidence on samples is almost normal and the employed aperture is equal to 1 mm.
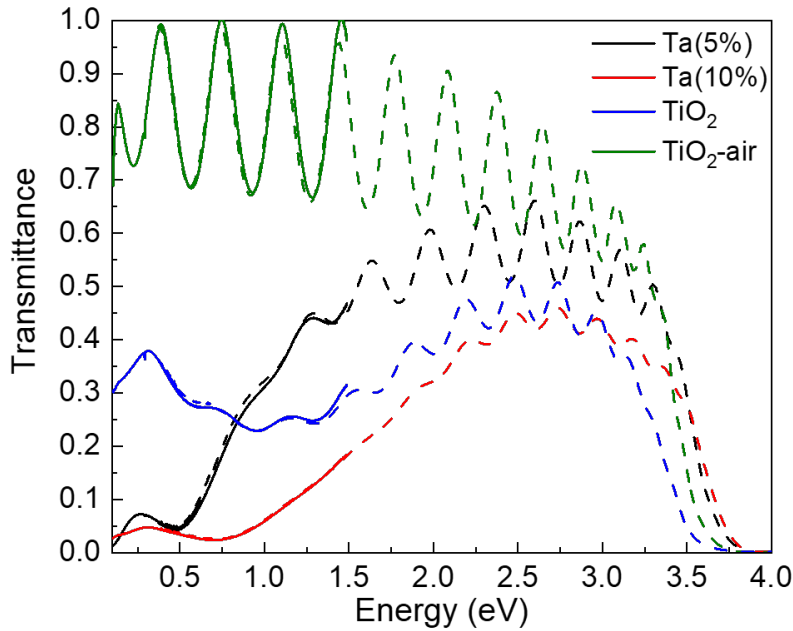
Figure 5.16: *FTIR measurements of specular transmittance of* Ta:TiO$_2$ *films with different Ta content (5, 10%at.) compared with vacuum- and air-annealed* TiO$_2$. *Dash lines represents measurements on the same sample taken by a spectrophotometer.*

spectrophotometer available at IIT (i.e. range in 0.41-4.96 eV, see section 3.3.1), corresponding to the dashed lines in the figure. Notably, the measurements taken by different instruments match and overlap for a wide range (i.e. 0.41-1.49 eV). In particular, a decrease in optical transmittance was detected for both Ta:TiO$_2$ films, and the value of energy where it occurs is considered an indication of plasma energy trend (although they do not coincide, as discussed in section 2.2.1). The transmittance dip blue-shifts with Ta content (i.e. around 0.45 and 0.66 eV for Ta(5%):TiO$_2$ and Ta(10%):TiO$_2$, respectively), however the drop resulted less sharp for Ta(10%):TiO$_2$ films with respect to Ta(5%):TiO$_2$, suggesting more free carrier absorption. Perspectives of this study includes the development of a model for fitting of the measurements, in order to estimate films optical properties in this range and compare with other kind of measurements above discussed.

5.3 Integration of Au nanoparticles with Ta:TiO$_2$ thin films

Au NPs were integrated in compact Ta:TiO$_2$ thin films with the aim to tune the plasmonic resonance of Au NPs by changing the dielectric constant of the surrounding matrix (as explained in section 2.2.2), that in this case can be done by varying Ta-doping content (as discussed in section 5.2.3). This kind of systems can be interesting for different applications, for example for sensing, optical modulators and for the integration of plasmonic functionalities in electrodes [101,103,104]. Specifically, different configurations of integration have been studied, namely Au
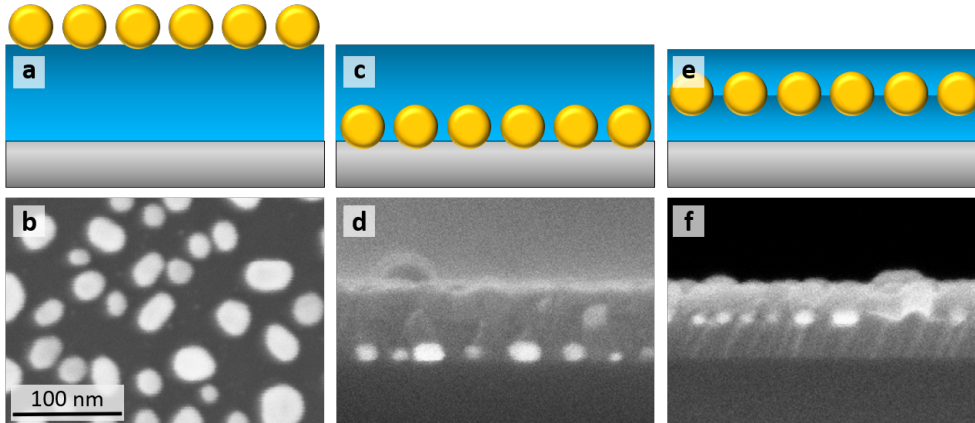
Figure 5.17: *Schematic representation of different integration configurations of Au NPs in Ta:TiO$_2$ films and respective SEM top-view or cross-section pictures: (a,b) Au-top, (c,d) Au-bottom and (e,f) Au-sandwich.*

NPs on top and on bottom of Ta:TiO$_2$ films, as well as embodied like a sandwich (see schematic representations in Fig.5.17), referred to as Au-top, Au-bottom and Au-sandwich, respectively. Moreover, the effect of Ta content (i.e. 5, 10% at., or bare TiO$_2$) and Au NPs size (diameter from 20-40 nm) were investigated.

The optimal Ta:TiO$_2$ and TiO$_2$ films were employed, deposited by PLD, according to synthesis condition presented in section 5.1. Au NPs were obtained by thermal evaporation of an Au thin film (i.e. equivalent thickness of 2-3 nm measured by means of a quartz microbalance; the chosen value depends on Au NPs size desired) and subsequent thermal treatment to allow de-wetting and Au NPs formation. This thermal treatment coincided with vacuum-annealing of Ta:TiO$_2$ and TiO$_2$ films, therefore film crystallization and Au NPs formation can be obtained in one step. However, the order of synthesis steps depends on type of integration configuration considered.

First, the effect of type of integration configuration was investigated, with Au NPs with average diameter of 20 nm integrated in Ta(5%):TiO$_2$ films thick 50 nm. The choice of TCO thickness is due to limit the presence of interference fringes in the optical spectra that can be hide the Au NPs resonance peak (see Fig.5.14a,c). SEM images of different configurations after thermal treatments are reported in Fig.5.17, in particular top-view of Au-top and cross-sections of both Au-bottom and Au-sandwich. For these last two configurations, it is observable that the addition of Au NPs provides nucleation sites for Ta:TiO$_2$ growth over them, by orienting the crystalline domains and increasing the defectivity. On the contrary, when gold is deposited on top, the morphology seems not to be affected and the film is compact, similar to the reference without gold. From Raman analysis, the presence of Au NPs do not prevent the Ta(5%):TiO$_2$ crystallization in anatase phase upon thermal treatment. From electrical measurements, the Au NPs integration leads to a drop in electrical performance for all configurations, associated mainly to additional scattering mechanisms for free electrons motion. From optical transmittance (see Fig.5.18a), the Au NPs resonance peak is observable (i.e. minimum in trasmittance in the visible range) and results red-shifted
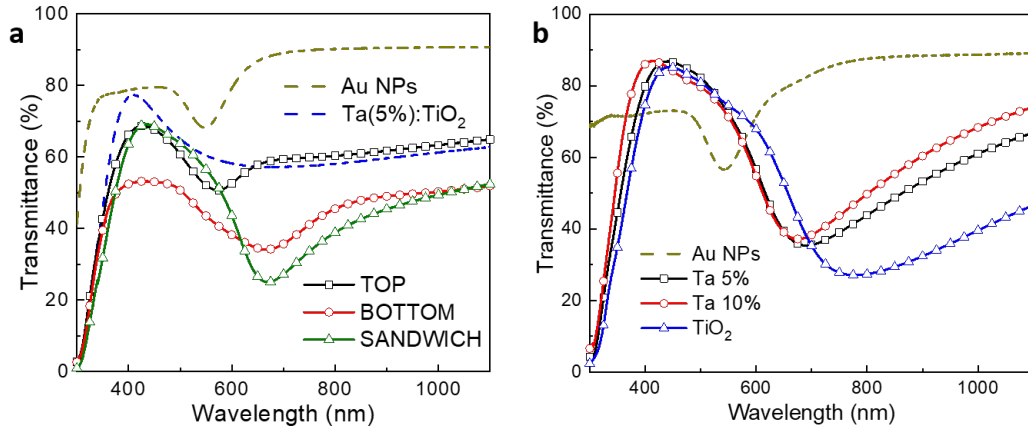
Figure 5.18: *Optical transmittance of (a) different integration configurations and (b) at different Ta content for the Au-sandwich configuration.*

and broadened with respect to bare Au NPs for all configuration types, in particular this effect increases from Au NPs on top to Au NPs on bottom configuration, while the highest effectiveness occurred for sandwich-like system.

Then, the effect of Ta content of the Ta:TiO$_2$ film on the Au NPs resonance peak position was studied, keeping constant the configuration type. As a main result, Au NPs LSPR peak is blue-shifted with increasing Ta content. For example, Fig.5.18b shows the optical transmittance spectra for sandwich-like configuration at different Ta contents. The transmittance minimum moves from 548 nm of bare Au NPs to 624 nm, 641 nm and 712 nm for Ta(5%):TiO$_2$, Ta(10%):TiO$_2$ and TiO$_2$ matrix, respectively. This behavior is expected since dielectric function decreases in visible range with Ta content (as discussed in previous section, Fig.5.12), as a consequence the resonance frequency of the embedded Au NPs blue-shift according to Eq.1.19.

Finally, the effect of Au NPs size (i.e. diameter from 20 to 40 nm) was considered as well (not shown). From electrical measurements, a higher amount of evaporated gold slightly improves the electrical performance of films. Optical characterization reveals that LSPR excitation of NPs is red-shifted and broadened by increasing Au NPs size, together with a reduction of transmittance, in accordance with literature (see section 1.3.2 and [14, 16]).

5.4   Towards Ta:TiO$_2$ NPs assemblies

A first exploration of the development of Ta:TiO$_2$ NPs assemblies in thin films has been performed, by exploiting the advantage of PLD in which the in-plume clusters formation can be triggered by an increase in the background pressure of deposition (as explained in detail in section 3.2.1). By exploring the 4-15 Pa pressure range of pure O$_2$ or mixture Ar:O$_2$ (5:1), films having different porosity were deposited and assemblies of NPs of tens nm were obtained at higher pressures (see Fig.5.19a,b). The choice of depositing in Ar:O$_2$ (5:1) is due to the goal of obtain-
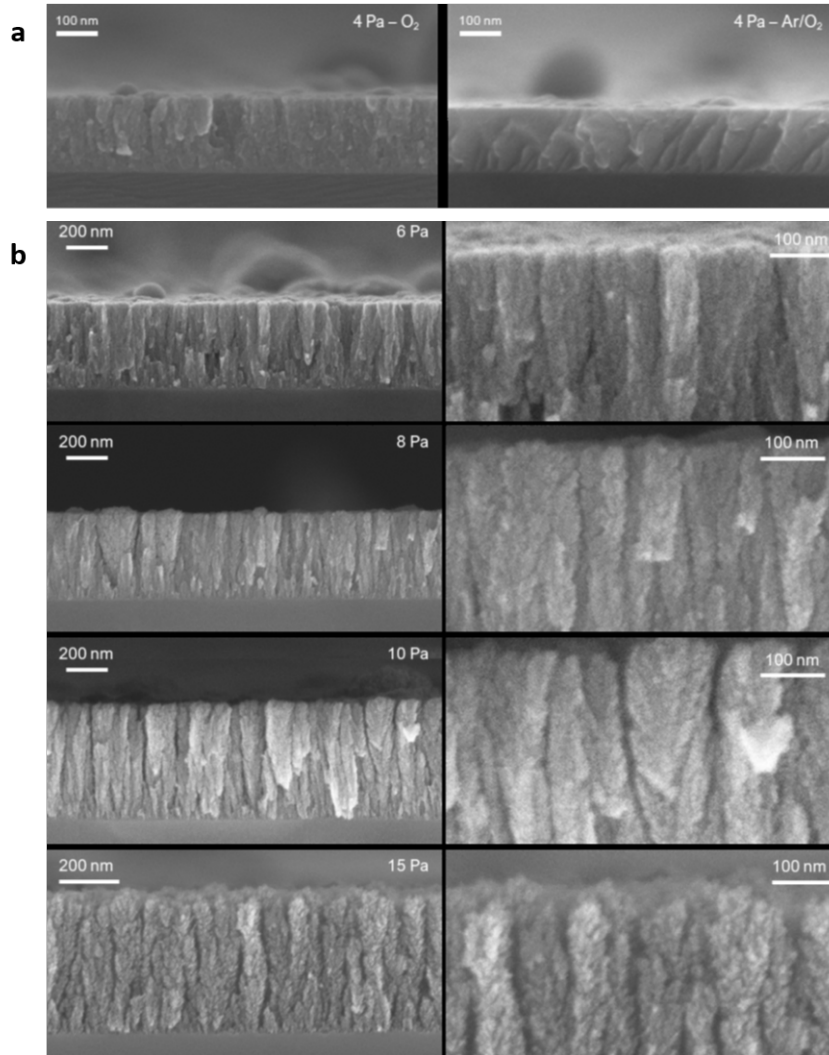
Figure 5.19: *SEM cross-section images of* Ta:TiO$_2$ *(a) deposited at 4 Pa of* O$_2$ *and mixture* Ar:O$_2$, *and (b) deposited at different pressure of mixture* Ar:O$_2$, *i.e. 6-15 Pa. Adapted from [200].*

ing hierarchical films while ensuring oxygen-poor condition which is necessary to allow successful Ta-doping (see section 2.2.3.1). By comparing films deposited at the same pressure of pure O$_2$ and Ar:O$_2$ mixture on the morphological point of view, the main difference consists in a more compact structure for film deposited in the mixture (see Fig.5.19a). The effect of an increase in the deposition pressure can also be seen in the optical properties of the samples, leading to an increase in transmittance (see Fig.5.20a). The main issue to obtain Ta:TiO$_2$ NPs assemblies effectively doped involves the difficulty to obtain a crystalline structure upon thermal treatment. After standard Ta:TiO$_2$ vacuum thermal treatment (i.e. at 550°C for 1 hour, ramp 10°C/min), Raman signal of the nanoporous films were tempered by photoluminescence effects, and showed high levels of noise, attributed to a strong amorphous fraction.

For this reason, different annealing parameters were explored; the ultrafast an-
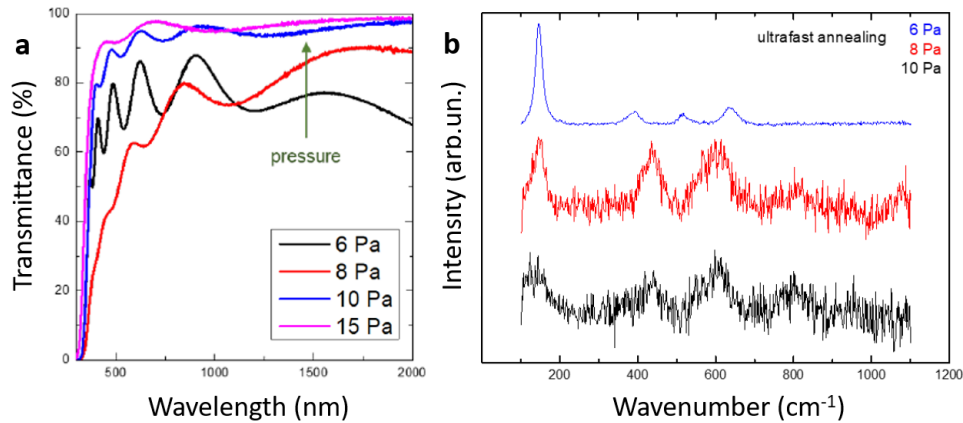
Figure 5.20: *(a) Optical transmittance and (b) Raman spectra after ultrafast annealing of Ta:TiO$_2$ films deposited at different pressures of mixture Ar:O$_2$. Adapted from [200].*

nealing in vacuum (i.e. at 550°C for 30 seconds, ramp equal to approximately one minute) was found to promote a slightly better crystallization from Raman analysis. However, while the 6 Pa spectrum is that of anatase, the same cannot be said in the case of the 8 and 10 Pa spectra. As shown in Fig.5.20b, the intensity of anatase main peak (i.e. $E_g(1)$ at $144\,cm^{-1}$) decreases with deposition pressure, while signal-to-noise ratio worsens, suggesting only partial crystallization. In addition, two broad peaks around $450\,cm^{-1}$ and $600\,cm^{-1}$ appear, related to the joint presence of anatase and rutile. The presence of rutile at high deposition pressure is not unexpected [197], indeed rutile formation was attested at an annealing temperature below the anatase-to-rutile transition temperature, because rutile nanocrystal seeds might have been already present in the as deposited film, suggesting that higher deposition pressures favor in-plume nucleation of rutile clusters that act in turn as crystallization seeds for rutile.

In conclusion, either in Raman or optical analysis of Ta:TiO$_2$ films deposited at high pressure did not show signs of successful doping. This could be either due to the deposition process or the post-annealing treatment, leading to an incomplete crystallization or issues with amount of oxygen. On the other hand, the nanoporous systems can be the intrinsic problem, since the large surface area provides many surface defects which trap free electrons, preventing a good doping activation efficiency. In order to assess this, more investigation is necessary. Depositions at different gas compositions should be performed, and the effects of different annealing cycles should be explored. Another possibility involves the employment of a capping layer which prevent oxygen excessive desorption upon thermal treatment that could be excessively reducing.

5.5   Conclusions

In this chapter the development of Ta:TiO$_2$ thin films was presented together with the characterization and understanding of their properties. After the first step of optimization of synthesis parameters to find the conditions for most conductive films, the film properties were studied as a function of Ta content (i.e. 5 and

10%at., compared with bare TiO$_2$) and thickness (from 200 down to 10 nm), with a particular focus on electrical and optical behavior.

Homogeneous and compact Ta:TiO$_2$ films were deposited on glass and silicon substrates, then vacuum annealing was performed to obtain sub-stoichiometric poly-crystalline films in anatase phase, confirmed by structural characterization. Electrical measurements show film resistivity between $8 \cdot 10^{-4}$-$1 \cdot 10^{-3} \, \Omega$cm for both Ta contents in a thickness range of 50-200 nm, while charge carrier density increases proportionally with Ta content (i.e. average values of $9.95 \cdot 10^{20} \, cm^{-3}$ and $1.65 \cdot 10^{21} \, cm^{-3}$ for 5 and 10% at., respectively) suggesting a condition of high dopant activation efficiency. On the other hand, for 200 nm-thick films, Hall mobility decreases with Ta content, indeed for Ta(5%):TiO$_2$ it is almost equal to bare TiO$_2$ (i.e. around $8 \, cm^2/Vs$), while mobility of Ta(10%):TiO$_2$ is about half, due to the higher concentration of ionized impurities in the crystal lattice, which affects electron scattering, as well as carrier-carrier and carrier-defect interaction at higher density of carriers. Finally, electrical properties deteriorate for films thinner than 20 nm almost independently from Ta content, because of the presence of defects at the film surface and at the interface with the substrate, that become dominant in ultrathin films, combined with the fact that crystal domains cannot grow up completely, however 10 nm-thick films resulted still conductive. This result highlights the possibility to design devices with ultrathin conductive films, which is a thickness difficult to achieve for metals due to their percolation threshold.

Optical characterizations showed that the Ta addition changes optical response due to the increase of charge carrier density. Indeed, optical absorption in UV range blue-shifts with Ta content, according to Moss-Burstein effect, while absorption in IR range increases because of free carriers. Optical band gaps of Ta:TiO$_2$ films were calculated by means of Tauc plot, showing an increase with Ta content (from 3.29 eV for bare TiO$_2$ to 3.48 and 3.56 for Ta(5%):TiO$_2$ and Ta(10%):TiO$_2$, respectively). In agreement with the measured charge carrier density, optical bang gap does not change in the thickness range of 50-200 nm, while it starts to decrease for 20 nm films, down to a value typical of undoped TiO$_2$ for 10nm-thick films. Effective mass was estimated both from Drude model parameters extracted from fitting of SE results and Moss-Burstein shift of optical gap. In the first case m^* varies in the range of 2.19-3.6 m_e and 3.18-4.5 m_e for Ta(5%):TiO$_2$ and Ta(10%):TiO$_2$, respectively (in the photon energy range 0.5-3eV). These results are in accordance with literature theoretical calculations for Ta-doped anatase, moreover, the predicted increment of m^* with Ta content was confirmed. On the other hand, effective mass calculated from optical gap shift is slightly underestimated and does not show a dependence on Ta content, however, it should be noticed that very similar results were obtained from two different approximated approaches of the systems. Finally, plasma energy was calculated to be in the near/mid-IR range (i.e. around 0.34 and 0.44 eV for Ta(5%):TiO$_2$ and Ta(10%):TiO$_2$, respectively) as expected for a TCO with charge carrier density of the order of $10^{21} \, cm^{-3}$.

These results make Ta:TiO$_2$ a potential candidate for plasmonic applications in IR. In comparison with other more studied TCOs in this field (e.g. ITO and

n-doped ZnO), this material ensures the fascinating advantages of TiO$_2$ (e.g. well-known material already employed for energy conversion and photocatalytic applications, low cost, non-toxic, high chemical and thermal stability), moreover in this work Ta:TiO$_2$ thin films demonstrated high doping efficiency, which leads to a easily tuning of charge carrier density by Ta content, allowing to adjust the electrical and optical properties as desired. In addition, the study of the thickness demonstrated constant electrical and optical properties down to 50 nm, which is a required size for building blocks in nanoplasmonic devices and metamaterials, e.g layered structures or metasurfaces (for example nanoantenna array, that can be obtained by exploiting lithography techniques on thin films). On the other hand, an evaluation of the plasmonic quality factors of these films for different applications should be done, while the nanocrystalline Ta:TiO$_2$ could be not the ideal choice, therefore more investigations in this direction are needed. Finally, the electrical properties of ultrathin films can be further investigated by depositing on other substrates, for example a buffer layer of insulating TiO$_2$ over the glass substrate can improve electrical response as well as allow deposition of even thinner films (i.e. <10 nm) [252].

Then, complex Ta:TiO$_2$-based systems were developed. One system involves the integration of Au NPs with compact Ta:TiO$_2$ thin films with the aim to tune the plasmonic response of Au NPs by changing the dielectric constant of the surrounding matrix. Specifically, different configurations of integration have been studied, namely Au NPs on top and on bottom of Ta:TiO$_2$ films, as well as embodied like a sandwich, together with the effect of Ta content (i.e. 5, 10% at., or bare TiO$_2$. As main results, the effect of integration on Au NPs resonance peak resulted red-shifted and broadened with respect to bare Au NPs for all configuration types, in particular this effect increases from Au NPs on top to Au NPs on bottom configuration, while the highest effectiveness occurred for sandwich-like system; moreover, keeping constant the configuration, LSPR peak blue-shifted with increasing Ta content. Perspectives of these systems include the understanding of the influence of the Ta:TiO$_2$ dielectric media on the plasmonic properties of Au NPs by employing effective medium theories as well as pump probe measurements. In addition, these systems enable the possibility of tuning of Au NPs plasmonic resonance modulating in active way the dielectric constant of the surrounding TCO by means of external stimuli such as the application of an electric field, as discussed in section 2.2.2.

Finally, a first exploration of the development of Ta:TiO$_2$ NPs assemblies in thin films has been performed. By exploring the 4-15 Pa pressure range of pure O$_2$ or mixture Ar:O$_2$, films having different porosity were deposited and assemblies of NPs of tens nm size were obtained at higher pressures. However, some issues occurred for the crystallization of more porous films upon thermal treatments (as indicated by Raman analysis). Therefore, different annealing parameters were explored and the ultrafast thermal treatment in vacuum was found to promote a slightly better crystallization; however, they did not show signs of successful doping. In order to assess this, appropriate optical and structural characterizations should be performed on samples deposited at different gas compositions, as well as the effects of different annealing cycles should be explored. Finally, a capping

layer can be employed in order to protect Ta:TiO$_2$ NPs assemblies from the highly reducing environment which could experience during the annealing treatment.

CHAPTER 6

Titanium nitride thin films

As discussed in section 2.3, transition metal nitrides are promising alternatives to metals in the plasmonic application field. Among them, titanium nitride (TiN) provides a tailored plasmonic response in the visible and near-IR range which in principle can be controlled by stoichiometry and crystalline quality. TiN is stable, hard and has the technological advantage to be currently used in silicon CMOS technology, moreover its very high melting point paves the way for high temperature and power plasmonic applications [77].

Even if TiN is one of the most studied metal nitrides for plasmonics, the understanding and the fine tuning of its electrical and optical properties have proven challenging so far, since these properties are not only affected by stoichiometry, but also by crystallinity and surface oxidation, which strictly depend on synthesis conditions. Moreover, nanostructured TiN films (i.e. assemblies of NPs with various size, shape and architectures) are fascinating systems for several plasmonic applications. However, in literature there are some examples of nanostructured TiN films and only few are investigated for plasmonics, just for SERS applications [190, 191, 195].

In this chapter, the development of TiN thin films as well as the investigation of the influences of composition and structure on their optical response is presented with the aim of tuning and understanding, while controlling the film morphology from compact to nanostructured, up to achieve the non-trivial synthesis of TiN NPs systems. In particular, the synthesis of TiN thin films was studied as a function of PLD process parameters and post-deposition thermal treatments, with a focus on background atmosphere (i.e. type of gas and pressure), in order to understand their impact on stoichiometry, structure, morphology and, as a consequence, optical and electrical properties. Since the oxidation issue during the synthesis represents a non-trivial problem (as discussed in section 2.3.3.2), particular focus was given to this topic, especially in case of porous structures and NPs assemblies with large surface area.

In section 6.1, a brief overview on the specific characterizations of TiN thin

films is introduced. In section 6.2, the morphology evolution from compact TiN thin films to porous NPs assemblies is shown as well as its effect on film composition, structure and optical response; moreover, the involved mechanisms in PLD synthesis to deposit NPs assemblies, as well as the employed strategies to overcome the oxidation-issue of nanoporous TiN films are explained. In section 6.3, the effect of different thermal treatments on both compact and nanoporous TiN films are reported, together with a preliminary study of the effect of substrate heating during films deposition. Finally, conclusions and perspectives are summarized in section 6.4.

It should be remembered that the research on TiN thin films at Nanolab was carried out in collaboration with two Master thesis student which I supervised for their thesis work [201, 272]. Moreover, PLD dynamics of TiN synthesis and the effect of substrate heating during deposition were studied at the Oak Ridge National Laboratory (ORNL, Tennessee, USA) in the framework of a user project, in cooperation with the Center for Nanophase Materials Sciences (CNMS), where I spent three months.

6.1 Chatacterization of TiN thin films

In order to understand characterization results of TiN thin films presented in this chapter, a discussion on TiN Raman analysis needs to be made. As introduced in section 2.3.3.2, Raman spectroscopy of TiN would be a useful technique to check qualitatively the stoichiometry and composition of deposited films. In principle, first-order Raman scattering is not allowed in an ideal crystal with rock-salt cubic structure like TiN (i.e. O_h symmetry). However, films deposited by means of magnetron sputtering or PLD present defects that may be generated from energetic ions or species in deposition mechanism, leading to a reduction of crystal symmetry which induces first-order Raman modes [174]. These Raman modes activated by defects and disorder make the TiN spectrum composed by broad bands instead of sharp peaks. Therefore a precise characterization of material structure is more difficult than in case of a material with active Raman modes (e.g. TiO_2), since the effects of crystallinity and stoichiometry are more indirect and tricky to be analyzed.

TiN Raman spectra have been studied by many authors [151, 163, 166, 172, 175–177, 273], who recognized three main spectral regions (refer to Fig.6.1a)

- Below $400\,cm^{-1}$, two bands are observed, associated to transverse acoustic (TA) and longitudinal acoustic (LA) phonons at $\sim 200 - 215\,cm^{-1}$ and $\sim 300 - 330\,cm^{-1}$, respectively. These bands indicate the presence of nitrogen vacancies, since they are mainly due to vibration of Ti^{4+} ions.

- At $\sim 400 - 450\,cm^{-1}$, the observed peak is associated to second order scattering of TA mode.

- In the range of $500-600\,cm^{-1}$, the observed band is associated to the optical mode (TO) due to Ti vacancies and vibration of N^{3-} ions.

Therefore, the relative intensities of acoustic bands below $400\,cm^{-1}$ and optical mode in the range of $500 - 600\,cm^{-1}$ are an indication of film stoichiometry. If
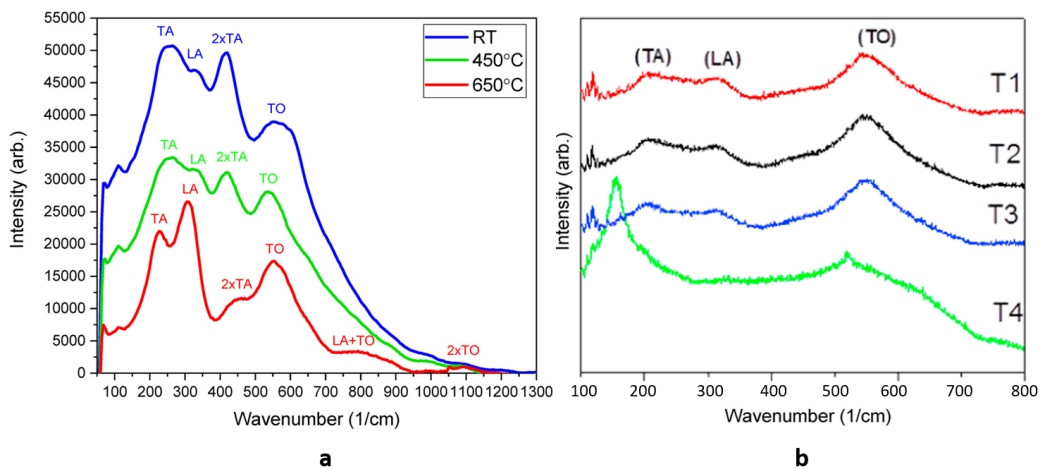
Figure 6.1: *Raman spectra of TiN thin films grown (a) at different temperatures and (b) power by means of DC reactive magnetron sputtering. Adapted from [163] and [274], respectively.*

they show the same intensity, stoichiometric TiN films are expected; on the other hand, higher acoustic bands imply nitrogen sub-stoichiometry (see red curve in Fig.6.1a), while higher TO means nitrogen over-stoichiometry (see curves of T1,T2 and T3 samples in Fig.6.1b).

In addition, Raman analysis allows to recognize partial oxidation. As discussed in section 2.3.3.2, Raman bands broad significantly with the increase of bounds of titanium atoms with oxygen, as a consequence of high content of nitrogen vacancies, but also due to a progressive amorphisation of the film [173, 275]. Another oxidation signature on Raman spectra involves the appearance of two peaks at ~ 150 and $520\,cm^{-1}$ (see curve of T4 in Fig.6.1b), attributed to vibrational modes of titanium-oxynitride (TiO_xN_y).

Moreover, the film oxidation can be recognized also from changes in optical reflectance and transmittance spectra, as discussed in section 2.3.3.2. By increasing the degree of oxidation of TiN films, the reflectance dip red-shifts and reflectance edge becomes less steep, as consequence of a reduction of free-carriers in the films [146, 147, 276]; morevoer a maximum in transmittance appears, which rises and red-shifts with oxygen content [173] (see Fig.2.19b,c).

Finally, in this work, the structural investigation of compact TiN thin films, before and after thermal treatment, was performed by means of XRD. For a rock salt structure (or face centered cubic structure, FCC) such as TiN, the plain with the lowest surface energy is (200); however, for physical vapor deposited TiN films, some research groups had reported that a crossover of the growth orientation from the (002) direction to the (111) direction occurs as the film thickness is increased to ~ 150 nm [277–279]. Initially, the (200) direction has the lowest crystallographic perpendicular growth rate, because this plane offers the highest mobility to the Ti atoms, meaning that the (200)-oriented grains will have the largest lateral growth rate [280]. Consequently, due to the anisotropy in lateral growth rate, a random out-of-plane nucleated film will evolve. Then, proceeding the thin film deposition, the (111)-oriented grains (having the largest geometric growth rate) will slowly envelop the other ones, and, at the end, their volume fraction will

become dominant.

6.2 TiN thin films morphology evolution: from compact to NPs assemblies

In this section, the morphology evolution of TiN thin films from compact to NPs assemblies is presented as a function of PLD process parameters. Different combinations of laser fluence and background atmosphere were studied in order to determine the optimum conditions to deposit adherent TiN thin films both on silicon and glass substrate, with the widest possible uniform thickness. Given the poor adhesion of TiN films on glass substrates, a pre-deposition cleaning of substrates was needed before each deposition. For this purpose, ionic bombardment was performed by using a RF Ar ion source[1], which removed moisture and contaminants from the substrate surface. Moreover, in order to limit oxidation during synthesis, a reducing atmosphere was employed for both deposition and thermal treatment in gas, namely N_2/H_2 $(95 - 5\%)$. The base pressure for all depositions was set 4-5 $\cdot 10^{-3}$ Pa (i.e. the pressure reached before starting depositions in vacuum or before gas injection), while for thermal treatment was 4-5$\cdot 10^{-5}$ Pa. The base pressure was kept constant for all samples in order to neglect the effect of this synthesis parameter since its variation to higher values can have a role in the oxidation of the films [169].

In Table 6.1, the employed combinations of laser fluences and background atmospheres during deposition are reported together with the corresponding observed morphology and stoichiometry/composition; moreover, the samples that have undergone thermal treatments or have been protected by a capping layer are indicated (which will be discussed in the next sections, as reported in the table).

6.2.1 Compact TiN thin films

PLD process parameters were chosen on the basis of previous works (summarized in section 2.3.3.1), with the aim to deposit compact and uniform TiN thin films. Laser fluence (F) on the target was set equal to 2, 3.5, and 6.5 J/cm^2. From higher fluence, a higher atomic mobility is expected during the growth process, and therefore better crystallinity, but also larger thickness gradient across the substrate, which can lead to greater growth stresses. Fig.6.2a reports cross-section SEM images of TiN films deposited in vacuum at F=2, 3.5 and 6.5 J/cm^2, showing that the film structure is columnar and rather compact and dense at all fluences, and the same was observed for TiN films deposited at 1 Pa of N_2/H_2 (see Fig.6.2b). From SEM top-view images of vacuum-deposited films (Fig.6.2c), the surface appears quite smooth, while the white dots correspond to droplets of few hundreds of nm, whose amount do not change significantly with laser fluence. All samples reported in Fig.6.2 have the thickness in the range of 200-250 nm. In general, by keeping constant background pressure during deposition, the effect of increasing fluence involves faster deposition rate as well as a more compact structure.

---

[1] Ar ions are accelerated towards the substrate by means of a RF ion gun at voltage set equal to 435 V, power 330 W and Ar gas flow fixed at 10 sccm, producing a current of $\sim 40\,mA$. The substrates undergo pre-cleaning ionic bombardment for 75 minutes.

Fluence J/cm^2	Background atmosphere Pa (N_2/H_2)	Morphology	Stoichiometry/ composition	Section	Thermal treatments (Section 6.3)	Note
2	vacuum	compact	N sub-stoichiometry	6.2.1	vacuum, N_2/H_2 at 550°C	
	1	compact	N sub-stoichiometry	6.2.1	vacuum, N_2/H_2 at 550°C	
	5	compact	N sub-stoichiometry	6.2.2		
	10	compact	amorphous oxide	6.2.2		
	20	tree-like	amorphous oxide	6.2.2		
	50	tree-like	amorphous oxide	6.2.2		
	100	foam-like	amorphous oxide	6.2.2		
3.5	vacuum	compact	N sub-stoichiometry	6.2.1		
	1	compact	N sub-stoichiometry	6.2.1		
	5	compact	N sub-stoichiometry	6.2.2		
	10	compact	TiO_xN_y	6.2.2	vacuum, N_2/H_2 at 550°C, N_2/H_2 at 300°C	capping layer (Section 6.2.2.1)
	20	compact	TiO_xN_y	6.2.2	vacuum, N_2/H_2 at 550°C, N2/H2 at 300°C	capping layer
	50	tree-like	amorphous oxide	6.2.2	vacuum, N_2/H_2 at 550°C, N2/H2 at 300°C	capping layer
	100	tree-like	amorphous oxide	6.2.2		
6.5	vacuum	compact	N sub-stoichiometry	6.2.1		
	1	compact	N sub-stoichiometry	6.2.1		
	50	tree-like	TiO_xN_y	6.2.2.1		
	100	tree-like	TiO_xN_y	6.2.2.1		

Table 6.1: *The explored PLD parameters (i.e. laser fluence and background atmosphere of N_2/H_2) for the development of TiN thin films are reported, together with the corresponding observed morphology and composition/stoichiometry. The selected samples that have undergone thermal treatments or have been protected by a capping layer are indicated with the section in which their properties are discussed.*
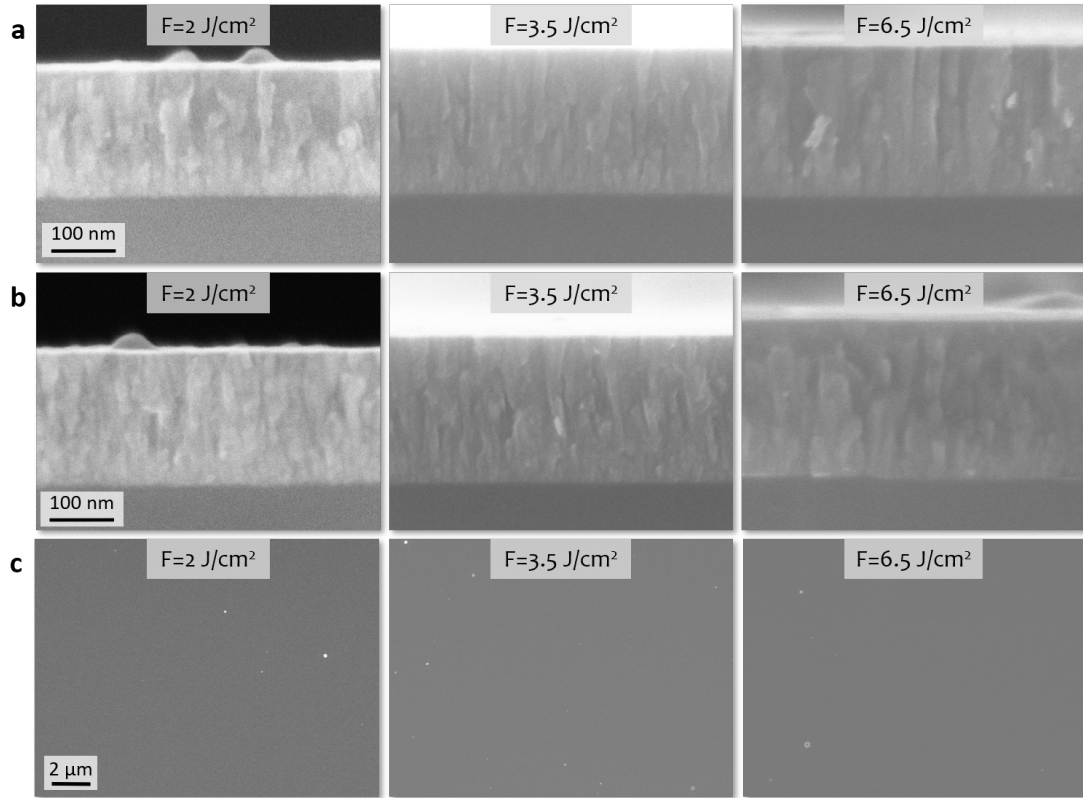
Figure 6.2: *(a,b) SEM cross-section and (c) top view images of samples deposited (a,c) in vacuum and (b) at 1 Pa of N_2/H_2 and at different laser fluence, i.e. 2, 3.5 and 6.5 J/cm^2.*

The Raman spectra of the deposited compact films are very similar and overlap. For example, Fig.6.3 shows Raman curves of the films deposited on glass substrate in vacuum with F=2, 6.5 J/cm^2 and at 1 Pa with F=2 J/cm^2. A unique broad band is observed below $400\,cm^{-1}$, which includes both LA and TA modes, while the signal around $500 - 600\,cm^{-1}$ (associated to the TO modes) is very low. The overall behavior suggests nitrogen sub-stoichiometry for all conditions. The same measurements were performed on samples deposited on Si substrates, displaying no differences (not shown).

The results of EDX measurements are reported in the Table 6.2. However, the quantitative reliability of these measurements is low because of the small atomic number of nitrogen and oxygen and the vicinity in energy of their x-ray transitions with the lower one of titanium (i.e. Kα=0392 keV and 0.525 keV for N and O atoms, respectively; Kα=4.512 keV and Lα=0.452 keV for Ti atom). Even so, EDX results can be effective to identify a trend of the atomic specie contents in the films. To have more reliable values, the nitrogen-titanium ratio (N/Ti) of the target was measured, resulting equal to 0.8 and, since the target is known to be stoichiometric (i.e. the measured number should be 1), the N/Ti ratio reported in Table 6.2 for the samples is normalized to 0.8.

Notably, by keeping constant the background pressure, the N/Ti ratio meanly increases with fluence. On the other hand, there is not a clear trend of which atmosphere promotes higher nitrogen incorporation in TiN thin films, therefore
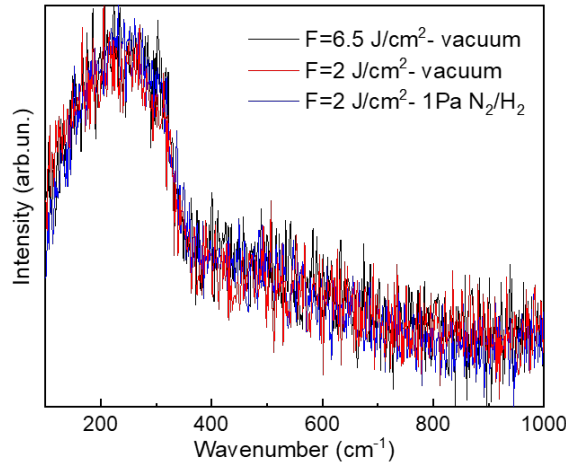
Figure 6.3: *Raman spectra of TiN thin films deposited in vacuum at F=2 and 6 J/cm^2, and at 1 Pa of N_2/H_2 and F=2 J/cm^2.*

Atmosphere	Fluence J/cm^2	Thickness nm	Ti at.%	N at.%	O at.%	Si at.%	N/Ti normalized
Vacuum	2	495	46.82	11.09	39.36	2.73	0.30
	3.5	460	49.27	11.89	34.26	4.58	0.30
	6.5	250	34.94	23.60	23.11	18.35	0.85
1 Pa N_2/H_2	2	490	43.18	16.84	38.56	1.41	0.49
	3.5	520	42,65	19.36	37.35	0.64	0.56
	6.5	515	44.16	24.08	30.62	1.14	0.69

Table 6.2: *Atomic percentage of titanium, nitrogen, oxygen and silicon detected by EDX on TiN thin films deposited at different fluences (i.e. 2, 3.5 and 6.5 J/cm^2) and atmospheres (i.e. vacuum and 1 Pa of N_2/H_2). The indicated N/Ti ratio is normalized to the value measured on stoichiometric TiN target (i.e. 0.8). The thicknesses of the measured samples are reported.*

more statistics is needed. Moreover, for all samples the substrate (i.e. silicon) is detected, especially for thinner films, therefore the high content of oxygen detected can partially be due to native oxide on the substrate surface. For a better compositional investigation, more accurate techniques are needed, e.g. x-ray photoelectron spectroscopy (XPS). In addition, it is important to know if the oxygen present in the films is bounded to Ti or adsorbed on film surface, for this purpose measurements with secondary-ion mass spectrometry (SIMS) should be performed.

Finally, the optical properties of TiN films deposited at F=2 J/cm^2 were measured in terms of reflectance (R) and transmittance (T) and relative spectra are reported in Fig.6.4. As expected for opaque TiN thin films, transmittance turned out to be zero (or very close to zero) all over the UV/Vis/NIR range. The reflectance of both TiN films deposited in vacuum and in 1 Pa N_2/H_2 show the typical TiN film curve, with the reflectance deep centered at about 330 nm and
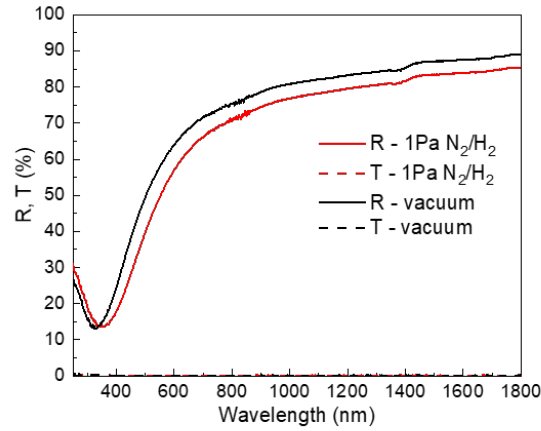
Figure 6.4: *Optical reflectance (R) and transmittance (T) spectra of TiN thin films deposited at $F=2J/cm^2$ in vacuum and at 1 Pa of N_2/H_2.*

350 nm, respectively. In addition, the reflectance intensity in the near-IR range (i.e. 800-2000 nm) is a bit higher for the vacuum-deposited sample.

6.2.2 Nanoporous TiN thin films

In order to obtain TiN NPs assembies system, the effect of the increase of background pressure was studied. Indeed, the morphological transition from compact to tree-like nanostructured thin films by increasing pressure during PLD process has been already observed for other materials (e.g. TiO_2 [197], as showed in section 4.2). By the way, it should be said that the synthesis conditions for the development of nanoporous films of this section were chosen on the basis of the investigation of the mechanisms of PLD synthesis of TiN thin films as a function of laser fluence and background atmosphere, that will be discussed in section 6.2.3.

Here, the employed background pressures are 5, 10, 20, 50 and 100 Pa of N_2/H_2, at two different fluences, i.e. 2 and 3.5 J/cm^2. The corresponding SEM cross-section images are reported in Fig.6.5. For all these samples, deposition time was set at 30 minutes, and thickness was found to increase with pressure because of porosity increment. For films deposited at F=2 J/cm^2 the morphology goes from compact (i.e. at 5-10 Pa) to porous tree-like (i.e. at 20-50 Pa) and to foam-like (i.e. at 100 Pa); while the films deposited at F=3.5 J/cm^2 follow the same morphological transition, but shifted towards higher pressure, since higher laser fluence favors the deposition of more compact structures.

Fig.6.6a shows Raman spectra of samples deposited at F=2 J/cm^2. The spectrum of the film deposited at 5 Pa shows features close to sub-stoichiometric TiN, while the film deposited at 10 Pa displays a spectrum typical of amorphous TiO_2, and the same signal was observed for films deposited at higher pressure (not reported). This behavior can be explained by considering that a higher pressure leads to films with higher porosity, implying a more disordered structure whose TiN Raman scattering is too weak and completely overcome by the stronger TiO_2 signal. In addition, the more porous films are expected to be characterized by a
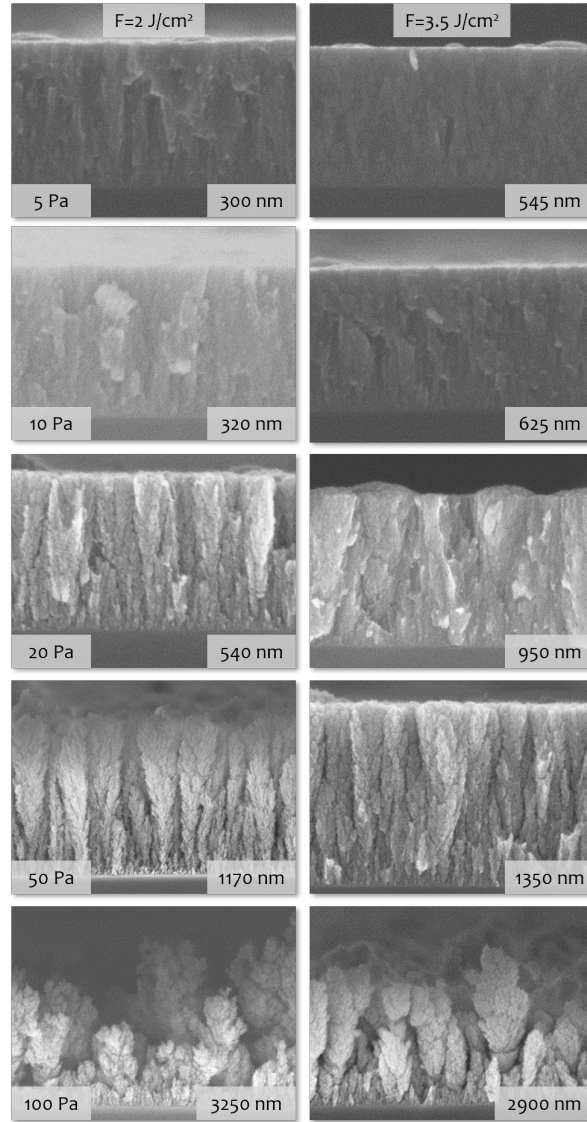
Figure 6.5: *SEM cross-section images of samples deposited at (left column) F=2 J/cm² and (right column) 3.5 J/cm², at different pressures (i.e. from 5 to 100 Pa, labeled in the left column) for 30 minutes. The measured thickness of each film is reported.*

higher oxidation extent, considering their greater specific surface area. Fig.6.6b shows the Raman spectra of films deposited at F=3.5 J/cm^2 and at a pressure of 5, 10 and 20 Pa. It can be seen that the increase of deposition pressure of N_2/H_2 from 5 to 20 Pa leads to a blue-shift of the acoustic band in the range $200 - 300\,cm^{-1}$, and the increase of the signal in the range $500 - 600\,cm^{-1}$. This last region corresponds to LO band that occurs in case of higher nitrogen content, however it is most likely the signal coming from an oxynitride phase. The higher pressures at F=3.5 J/cm^2 are not reported since their spectra show amorphous TiO_2 signal.

The change of morphology and composition with deposition pressure is reflected on the optical behavior. Fig.6.7a shows transmittance, reflectance and absorbance
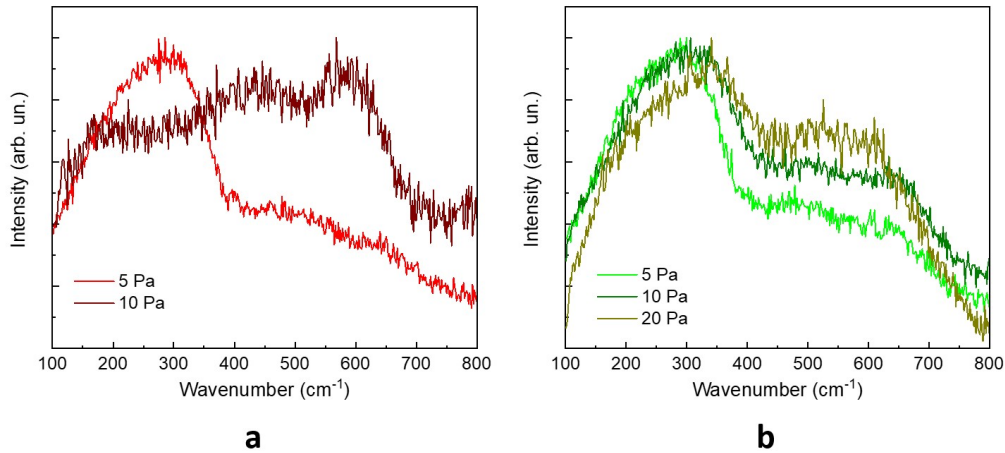
Figure 6.6: *Raman spectra of TiN films deposited at (a) F=2 J/cm^2, at 5 and 10 Pa of* N$_2$/H$_2$; *and (b) F=3.5 J/cm^2 at 5, 10 and 20 Pa of* N$_2$/H$_2$.

(i.e. $A = 100 - T - R$) of samples deposited at 2 J/cm^2, at 5 and 10 Pa. In accordance with Raman analysis, these samples show a transition from an optical behavior typical of TiN thin films at 5 Pa (i.e. high reflectance in the near-IR and a dip around 400-600 nm, while transmittance is almost zero) to a spectrum typical of amorphous TiO$_2$ for the sample deposited at 10 Pa (i.e. very high transparency and low reflectance and absorbance for wavelength above the band gap). The optical spectra of samples deposited at F=3.5 J/cm^2, at 5-50 Pa are reported in Fig.6.7b. By increasing the background pressure of deposition, the following observation can be made:

- The increase from 5 to 10 Pa leads to the appearance of a transmittance peak around 480 nm (see 6.7b, T%). At 20 Pa, such transmittance peak rises in intensity and red-shifts to about 550 nm. This behavior is associated to an increase of oxygen incorporation within the TiN crystal lattice, forming TiO$_x$N$_y$ (as introduced in section 2.3.3.2, [173]).

- The reflectance decreases with pressure increment (see Fig.6.7b, R%). In particular, the reflectance edge typical of compact TiN thin films becomes less steep, and finally disappears at 20 Pa.

- The absorbance increases with pressure, while the qualitative behavior of the spectra changes (see 6.7b, A%). At 5 Pa, there is a well-defined narrow peak (i.e. maximum at $\lambda = 472nm$). At 10 Pa two peaks are visible, one narrower at shorter wavelength and the other broader and red-shifted (i.e. maximum at $\lambda = 612nm$). At 20 Pa, the two peaks are more separated, and the maximum of the broader peak is around 719 nm. An hypothesis for this absorption band splitting consists in the separation of two contributions, namely the inter-band (at shorter wavelength) and the intra-band (at longer wavelength) transitions. Indeed, for compact TiN thin films, the two contributions are expected in the same wavelength interval, giving one stronger peak (i.e. the theoretical cut-off energy for inter-band transitions occurs at 2.48 eV, corresponding to λ=500 nm, while the screened plasma wavelength
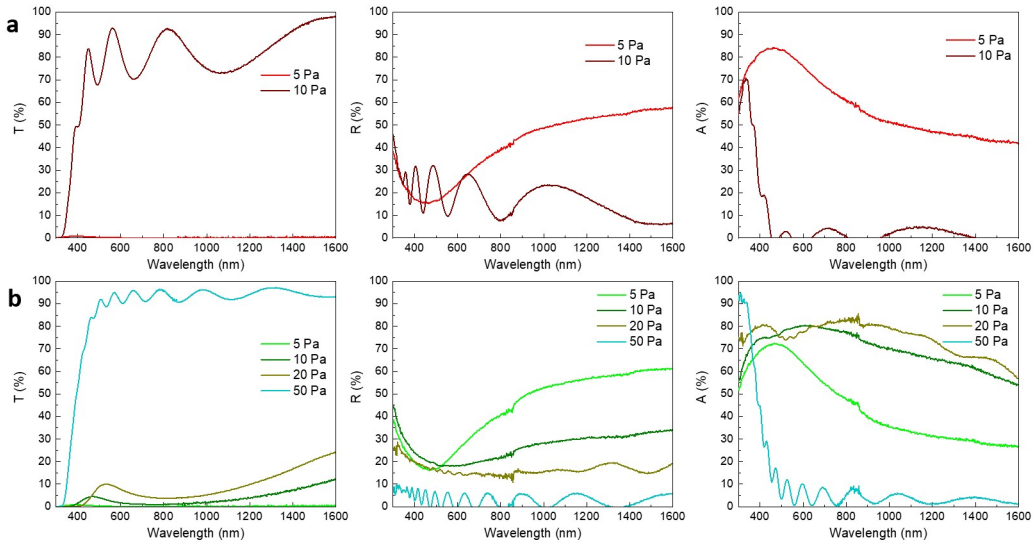
Figure 6.7: *Optical transmittance (T), reflectance (R) and absorbance (A) of films deposited at (a) F=2 J/cm², at 5 and 10 Pa of* N_2/H_2*; and (b) F=3.5 J/cm² at 5, 10, 20 and 50 Pa of* N_2/H_2*.*

depends on TiN stoichiometry and typically it varies between 420-620 nm, as discussed in section 2.3.1) [78, 281, 282]. On the other hand, in the case of TiN NPs the contribution of inter-band transitions can be observed at shorter wavelengths, exhibiting a higher intensity with respect to the LSPR peak located at longer wavelength, whose weaker intensity decreases with oxidation [189]. In the present case, nanostructured TiN films are consti-tuted by NPs or clusters assemblies, therefore the observed behavior can be associated qualitative to an intermediate situation, where the intra-band and inter-band contributions have similar intensity, and are located in a nearby spectral region. The more porous is the film, the more the intra-band ab-sorbance peak red-shifts and the contribution given by inter-band transitions starts to appear. However, it should be stressed that this explanation is only hypothetical and other optical investigations are needed to verify the nature of the two absorption peaks, e.g ellipsometry and pump probe measurements.

Finally, the spectra of samples deposited at F=3.5 J/cm^2 and 50-100 Pa showed optical behavior typical of amorphous TiO_2 (like the film deposited at F=2 J/cm^2 and 10 Pa), analogously to Raman results.

6.2.2.1 Strategies to reduce oxidation of nanoporous TiN films

Up to this point, the most porous samples resulted amorphous TiO_2 (i.e. de-posited above 10 Pa for F=2 J/cm^2, and above 50 Pa for F=3.5 J/cm^2), while the most compact films showed sub-stoichiometric TiN behavior (i.e. films de-posited below 5 Pa), finally also an intermediate situation was found, depositing titanium oxynitride films (i.e. at 10-20 Pa for F=3.5 J/cm^2). Two strategies have been explored in order to reduce the oxygen incorporation, especially for more porous films, by considering that oxidation can occur mainly in two ways

1. During the deposition, due to poor vacuum environment or impurities in background pressure

2. After deposition, since oxygen atoms can bond to uncoordinated Ti atoms upon air exposure

Oxidation reduction during deposition. For this case, the strategy involves the exploitation of a higher laser fluence during deposition. Even in case of compact TiN films, an increment of N/Ti ratio with fluence was observed by qualitative EDX measurements (see section 6.2.1). Moreover, by comparing samples with similar morphology and density (measured by means of a quartz crystal microbalance, QCM[2], in PLD apparatus), for which a similar surface-to-volume ratio and, as a consequence, comparable surface oxidation upon air exposure are expected (as discussed in section 2.3.3.2), features more close to TiN rather than amorphous TiO_2 occur for higher fluences. For example, the film deposited at F=3.5 J/cm^2 and 20 Pa of N_2/H_2 showed Raman and optical signals typical of TiO_xN_y, while sample deposited at F=2 J/cm^2 and 10 Pa (similar in morphology and density) displayed amorphous TiO_2 behavior for the same characterization techniques. The hypothesis might be that the increase in laser fluence enhances the nitrogen spiecies reactivity in the plasma plume, and as a consequence nitrogen incorporation is more favored with respect to oxygen coming from either gas impurities or residual contamination in the chamber [161, 162, 188]. In addition, the higher nitrogen incorporation during deposition may also contribute to the reduction of air-exposure oxidation. However, to better understand what occurs during deposition by raising the laser energy density, other measurements such as in-situ Raman spectroscopy should be performed.

The laser fluence was set equal to 6.5 J/cm^2 and the explored background pressures were 50 and 100 Pa N_2/H_2, considered to have similar morphology and density as some samples deposited at F=3.5 J/cm^2. Namely, comparisons were performed between samples deposited at 6.5 J/cm^2-50 Pa with 3.5 J/cm^2-20 Pa, whose estimated density was about 2 g/cm^3 and similar morphology is observable in Fig.6.8a,c and Fig.6.5 (right column, 3rd line); and 6.5 J/cm^2-100 Pa with 3.5 J/cm^2-50 Pa, whose estimated density was about 1g/cm^3 and similar morphology is observable in Fig.6.8b,d and Fig.6.5 (right column 4th line).

Fig.6.9 reports Raman spectra of the selected samples. The film deposited at 6.5 J/cm^2-50 Pa shows a very similar signal to films at 3.5 J/cm^2-20 Pa (see Fig.6.9a). On the other hand, the increase in laser fluence resulted more effective in reducing oxidation for more porous films (see Fig.6.9b). Indeed, while the sample obtained at 3.5 J/cm^2-50 Pa shows amorphous TiO_2 signal, the film deposited at 6.5 J/cm^2-100 Pa displays spectra more similar to TiO_xN_y.

The optical characterization revealed some unexpected but interesting results. Both films deposited at F=6.5 J/cm^2 reported a very low transmittance and reflectance (see Fig.6.10a,b) and, as a consequence, a very high and broad-band absorbance (i.e.$\sim$ 85 $-$ 96%) all over the UV/Vis/NIR range (i.e. 270-2000

---

[2]QCM device consists in a vibrating quartz piece placed in a region considered to undergo the same level of covering as the actual film. The increase in film thickness results in a change in the vibration frequency, as the crystal gets covered. In this work, the measured densities should be not considered as the actual density value of the films, but a qualitative means to compare density of films deposited in different conditions.
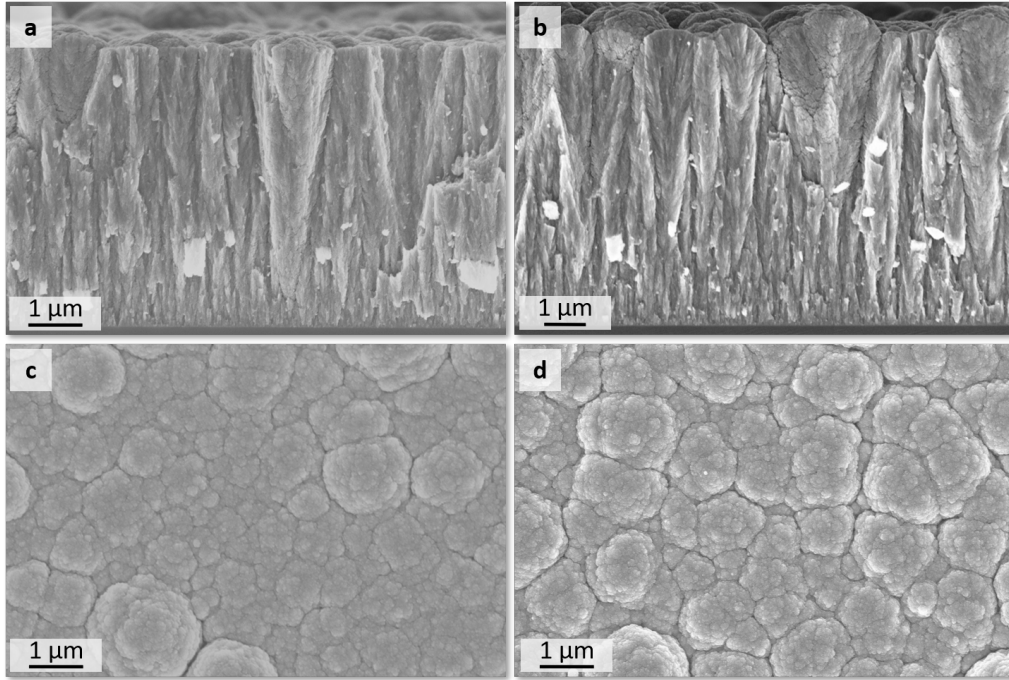
Figure 6.8: *(a,b) SEM cross-section and (c,d) top-view images of films deposited at F=6.5 J/cm^2, at (a,c) 50 Pa and (b,d) 100 Pa of* N$_2$/H$_2$.

nm), as shown in Fig.6.10c. Yan *et al.* obtained similar results for highly substoichiometric TiO$_2$ NPs random assemblies [283] and the broadband absorption was associated to the plasmon hybridization (i.e. interaction of elementary plasmons supported by nanostructures of elementary geometries [284]) and hot spot generation arising from near-touching [283, 285]. Moreover, the porous nanostructure promotes light trapping due to multiple reflections and scattering of light as well as the reduced reflectance at the air-solid interface due to an effective graded refractive index layer [283, 286]. In the present case, this fascinating result is comparable to broadband absorbers made of complex TiN metamaterial structures, discussed in section 2.3.2 [155, 287]. Typically, a complex structure is needed since the existing absorber usually suffer from limited wavelength-range where absorption is high (i.e. >90%). Here, titanium oxynitride nanoporous films could represent a promising alternative in terms of rather simple structure, in particular the tree-like film deposited at 100 Pa shows an absorbance higher than 90% in the wide range 270-2000 nm and an average absorbance of 94.8%. Such high broadband absorber can find application in solar cells, thermal photovoltaics and hot electron devices [288].

Oxidation reduction upon air exposure. For this issue, the strategy involves a capping layer. In particular, a compact layer of aluminum nitride (AlN) was chosen since it is known as an efficient oxygen diffusion layer that forms a very stable AlO$_x$N$_y$ in contact with air, which is a passivating protective layer [289]. Here, a uniform and compact capping layer thick 200 nm was obtained by ablating an Al target (purity 99.9%) with laser fluence equal to 2 J/cm^2, at 1 Pa of N$_2$/H$_2$.
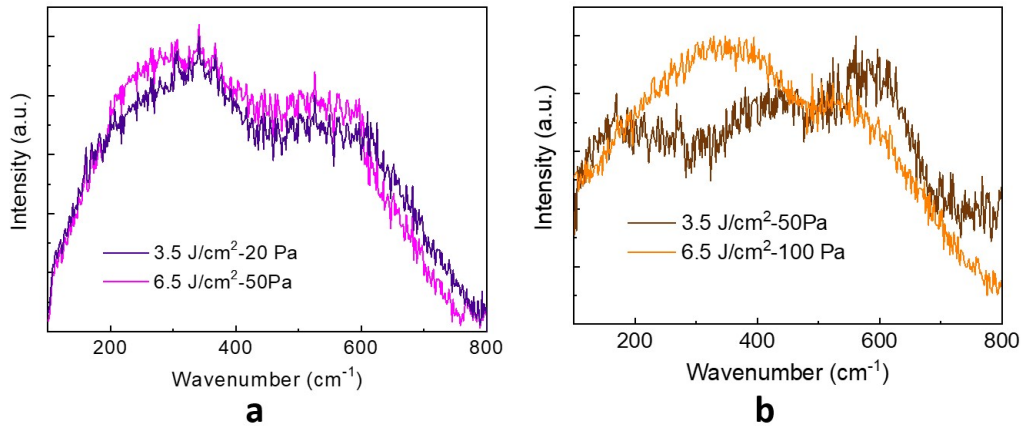
Figure 6.9: *Raman of films deposited at F=6.5 J/cm² at (a) 50 Pa and (b) 100 Pa of* N_2/H_2, *compared with films deposited at F=3.5 J/cm² at 20 and 50 Pa, respectively.*

The bare capping layer deposited on glass substrate showed very high transparency and low reflectivity and absorbance all over the UV/Vis/NIR range, as shown on Fig.6.11a; moreover no Raman signal was detected in the range of interest (not shown). Therefore, even if the exact composition of this capping layer is unknown, such layer is functional for the purpose and, in addition, it is not expected to affect neither Raman nor optical spectra of the underlying TiN. The capping layer was deposited on top of the films, without opening the vacuum chamber, by employing a composite target made of TiN target (diameter of 1 inch) attached on the Al target (diameter of 2 inch), as shown in the Fig.6.11b. In this way, first the TiN target is ablated at the wanted laser fluence and pressure, then the Al target is ablated without opening vacuum chamber at the pressure and fluence condition described above.

The investigated capped samples are the films deposited at F=3.5 J/cm^2 and at 10-50 Pa of N_2/H_2, and they were compared to corresponding uncapped films. Fig.6.11c shows SEM cross-section image of the capped film deposited at 50 Pa. For all pressure conditions, the morphology of the underlying nanoporous film does not change by adding the capping, while this last resulted compact and uniform all over the film surface. From Raman spectra (see Fig.6.12a,b), it is observed that the presence of the capping layer does not affect the signal of the two more compact films (i.e. deposited at 10 and 20 Pa), while optical absorbance shows some differences, as shown in Fig.6.13a,b. By comparing with uncapped films, the contributions of the two absoption peaks (already observed, as discussed in previous section) are more separated, since the peak at larger wavelength results red-shifted. However, a blue-shift for this peak was expected with respect to the uncapped one, because a lower oxygen incorporation would lead to a higher charge carrier concentration. The observed red-shift could be explained by considering that the presence of a high refractive index ($\sim$ 2.01 for AlN) cap layer may affect the underlying film's optical behavior.

On the other hand, for the most porous sample (i.e. deposited at 50 Pa), the cap layer resulted to be highly effective in reducing air-exposure oxidation, likely because it is the more porous film and, therefore, more subjected to this kind of
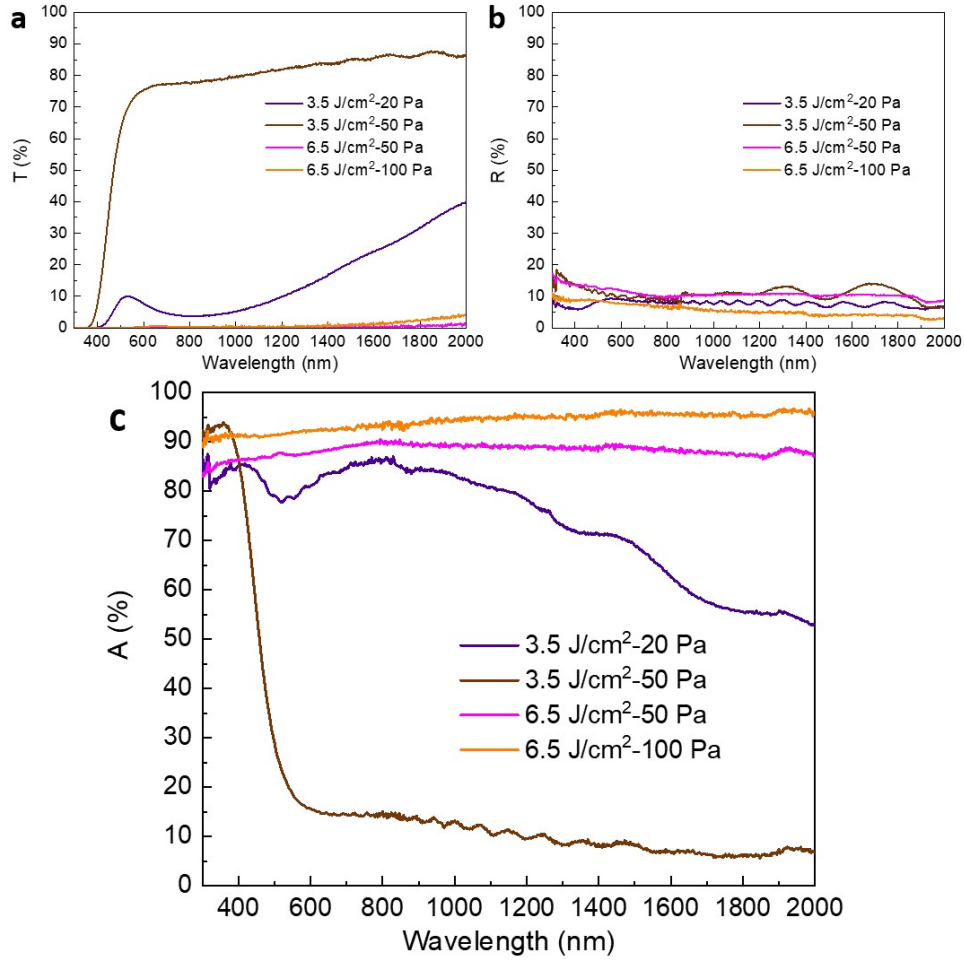
Figure 6.10: *(a) Optical transmittance, (b) reflectance and (c) absorbance of films deposited at F=6.5 J/cm², at 50 Pa and 100 Pa of N_2/H_2, compared with films deposited at F=3.5 J/cm² and 20 and 50 Pa, respectively.*

oxidation mechanism. Indeed, while corresponding uncapped film shows a Raman signal typical of amorphous TiO_2, the capped one displays a spectrum associated to TiO_xN_y (see Fig.6.12c). Moreover, while uncapped film has very low absorbance and very high transmittance in Vis-NIR (as expected for amorphous TiO_2), the capped one shows an optical behavior typical of a partially oxidized TiN film (see Fig.6.13c,d); in particular, a transmittance peak occurs at $\lambda = 685\,nm$, while two absorption peaks occur at $\sim 450\,nm$ and $\sim 925\,nm$. It should be specified that all peak positions can be influenced by the capping layer refractive index. Notably, considering all the capped films, the absorption peak located at shorter wavelength raises in intensity and red-shifts by increasing deposition pressure; at the same time, the absorption peak located at longer wavelength decreases in intensity and red-shifts.

In conclusion, the two adopted strategies resulted to be effective in reducing oxygen incorporation within the nanoporos films. Specifically, by employing a fluence equal to 6.5 J/cm^2 and depositing at 50 and 100 Pa, TiO_xN_y films with
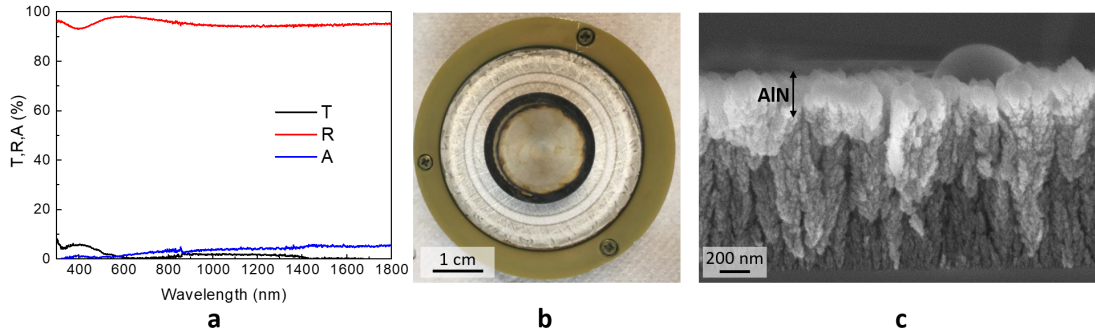
Figure 6.11: *(a) Optical transmittance (T), reflectance (R) and absorbance (A) of bare capping layer of AlN deposited on glass substrate; (b) picture of assembled target of TiN and Al; (c) SEM cross-section image of capped film deposited at F=3.5 J/cm² and 50 Pa of* N_2/H_2.
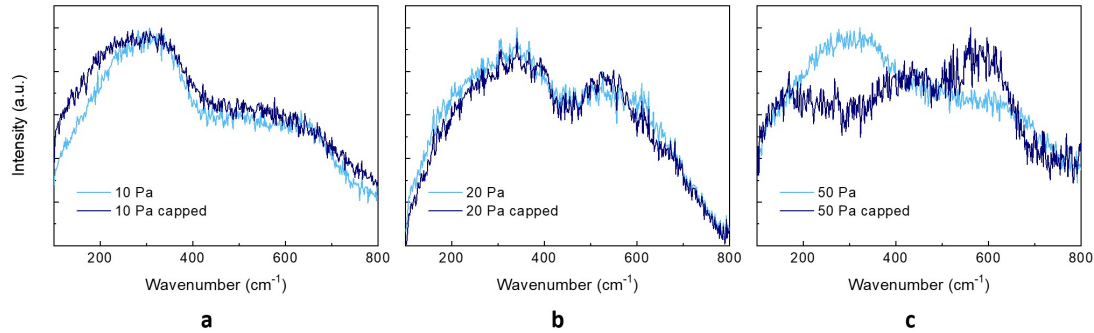
Figure 6.12: *Raman spectra of capped and corresponding uncapped films deposited at (a) 10 Pa, (b) 20 Pa and (c) 50 Pa of* N_2/H_2.

tree-like structure were obtained, showing a very high and broad-band absorption all over the UV/Vis/NIR interval. On the other hand, by capping films deposited at F=3.5 J/cm^2 with a AlN 200 nm-thick compact layer, an effective oxidation reduction was achieved for the more porous film (i.e. deposited at 50 Pa), which presents again TiO_xN_y signals as well as the tree-like structure.

6.2.3 Mechanisms in TiN pulsed laser deposition

During my period at CNMS, I focused on the mechanisms occurring during deposition of TiN by means of PLD, aimed to the development of TiN NPs assemblies systems. Indeed, the corresponding results were employed as a foundation for the development and the study of TiN nanoporous films (i.e. deposited at pressure above 5 Pa) performed at NanoLab and discussed in section 6.2.2.

The mechanism of plasma plume expansion, which occurs when the laser pulses hit the material target (i.e. TiN), was investigated with specific in-situ characterization techniques available at CNMS as a function of background atmosphere and laser fluence. In-situ diagnostics involves ion probe time-of-flight current measurement[3] and gated intensified charge coupled device (ICCD) imaging[4], that

---

[3] A floating wire ion probe (detector area 1 mm^2) was biased at -40 V by a battery and 1 mF capacitor which was terminated at a digital oscilloscope (typically 50 W, but up to 500 W for smaller currents) to record the ion flux current as a voltage for each laser shot.

[4] Princeton Instruments, PI-MAX, with variable gating (minimum 5 ns). A Nikon camera lens was positioned
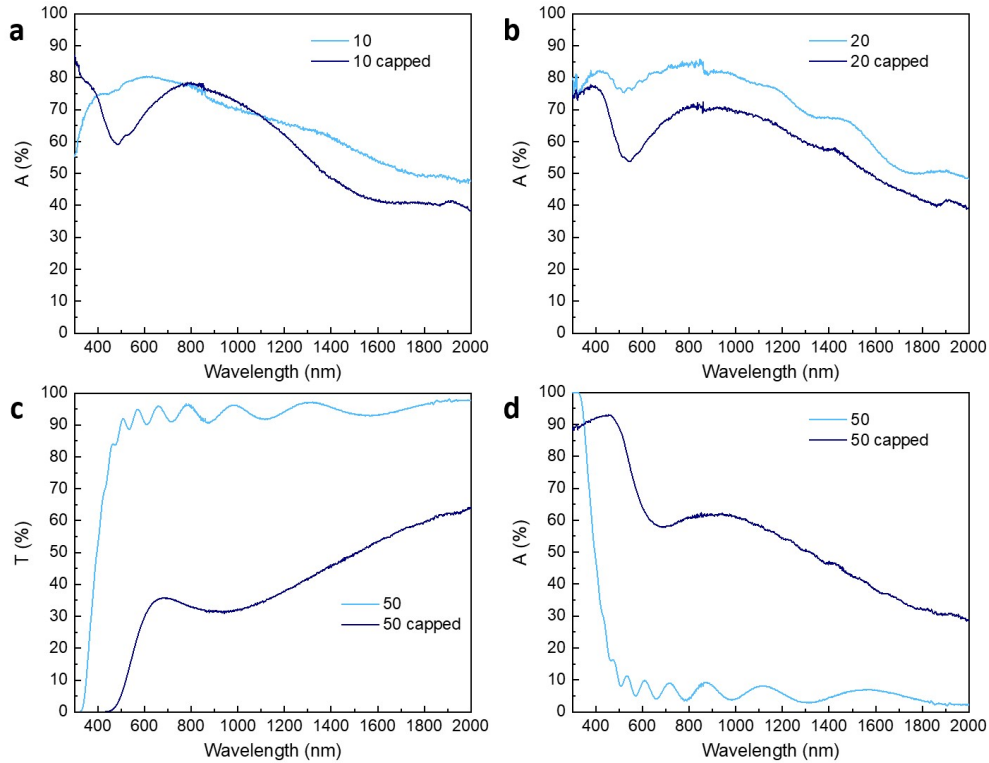
Figure 6.13: *Optical absoption of capped and corresponding uncapped films deposited at (a) 10 Pa and (b) 20 Pa of* N_2/H_2*; (c) optical transmittance and (d) absorption of capped and uncapped film deposited at 50 Pa of* N_2/H_2*.*

were carried out in a PLD apparatus with a KrF-laser (λ=248 nm , as described in section 3.2.1). In particular, the ion probe time-of-flight current measurement is time-resolved and it allows to record the temporal profile of the ion flux of the plasma, coming from the ablated target, by means of a probe placed at the same position and distance of the target; on the other hand, ICCD imaging captures the emitting radiation stimulated by electron impact collisions in the weakly ionized plasma. For these measurements, two laser fluences where considered (i.e. 2 and 3 J/cm^2) and the employed background atmospheres were N_2 and N_2/H_2 (4% of H_2), while the repetition rate of the pulsed laser was set equal to 1Hz. For better understanding the mechanisms described below, refer to the brief description of the fundamental PLD process in section 3.2.1.

Fig.6.14 shows the ion probe measurements at 2 and 3 J/cm^2 as a function of N_2 pressure. The peaks or bands in ion probe plots are associated to the arrival time of ions to the detector placed at the same position and distance of the substrate (i.e. 5 cm). At vacuum and 1 Pa, only a single peak is visible, known as *fast component* [290], whose intensity decreases by increasing background pressure during deposition. Notably, the position of this component does not shift significantly with pressure, suggesting that these ions can reach the substrate without

---

outside the deposition chamber, at a distance of 46 cm from the plume center, focusing on the plasma plume through a 5.08 cm x 20.32 cm Suprasil window. The exposure time and lens aperture (f-stop) were varied according to the plume conditions, from 100 ns to 100 μs and from f4.5 to f32, respectively.
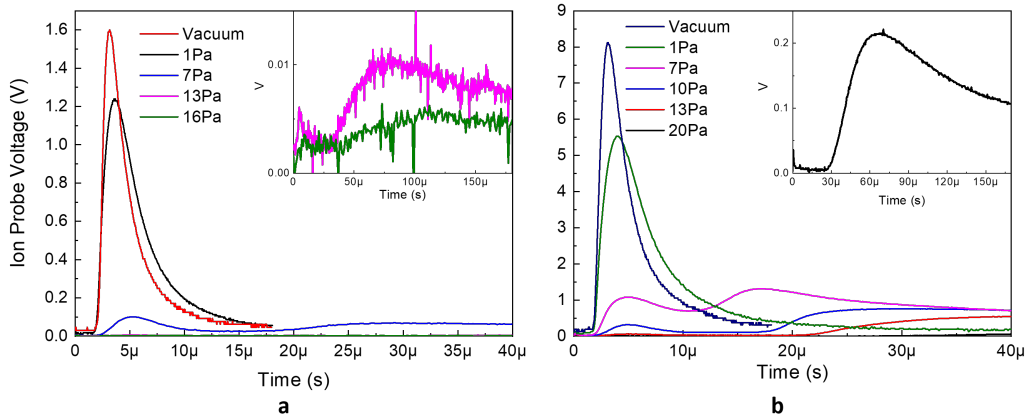
Figure 6.14: *Ion probe measurements at laser fluence equal to (a) 2 J/cm^2 and (b) 3 J/cm^2, as a function of background pressure of N_2.*

being slowed down by collisions with background gas molecules. Indeed, at F=2 J/cm^2 the maximum was found at 3.1 μs in vacuum and 3.5 μs at 1Pa, while at F=3 J/cm^2 it was found at 3.1 μs in vacuum and 4.0 μs at 1Pa. By further increasing the pressure, the intensity of the fast component decreases, while a *second component* appears at longer time, according to the *plume splitting* collisional model [291, 292]. The second component is associated to ions slowed down by collision upon pressure increase and, in addition, it shifts to longer times with pressure. Finally, at higher pressure (e.g. at 20 Pa for F=3 J/cm^2 and above 13 Pa for F=2 J/cm^2) the fast component is not more observable, while the second one is still present. This is the desired condition to deposited NPs assemblies [290], which is needed to achieve the development of TiN NPs systems (aim of this work).

Then, ICCD pictures were taken at successive delays (setting zero the time when the laser hits the target) for selected conditions, namely at 20 and 50 Pa of N_2 at F=3 J/cm^2 (see Fig.6.15a,b), to better understand the involved processes. From these images, it is observable that the laser ablation of TiN target results in a rapidly expanding, forward-directed plasma plume containing atoms, ions, and molecules ejected from the target. By increasing pressure from 20 to 50 Pa, a slight delay is observable in the plasma plume expansion, moreover a larger spatial confinement occurs at the higher pressure. In Fig.6.15, the *shock front* of plasma plume is recognized due to the bright fluorescence [290, 293]. At 20 Pa, the shock front hits the substrate at a delay of 35-40 μs, while the plume edge at 50 Pa never reaches the substrate. However, the clusters and NPs that are formed in the expanding plume can propagate well beyond the shock front, indeed NPs can be deposited just past the edge of the visible plume, up to several centimeters further away from the target (as already observed for other materials [290]). In this condition, if the ablated species can be collected on a substrate, mesoporous and nanoporous films can be obtained. In this case, the samples deposited in the two selected conditions showed a morphology and structure very similar to films deposited at NanoLab at F=3.5 and at 20 and 50 Pa (whose SEM cross-section
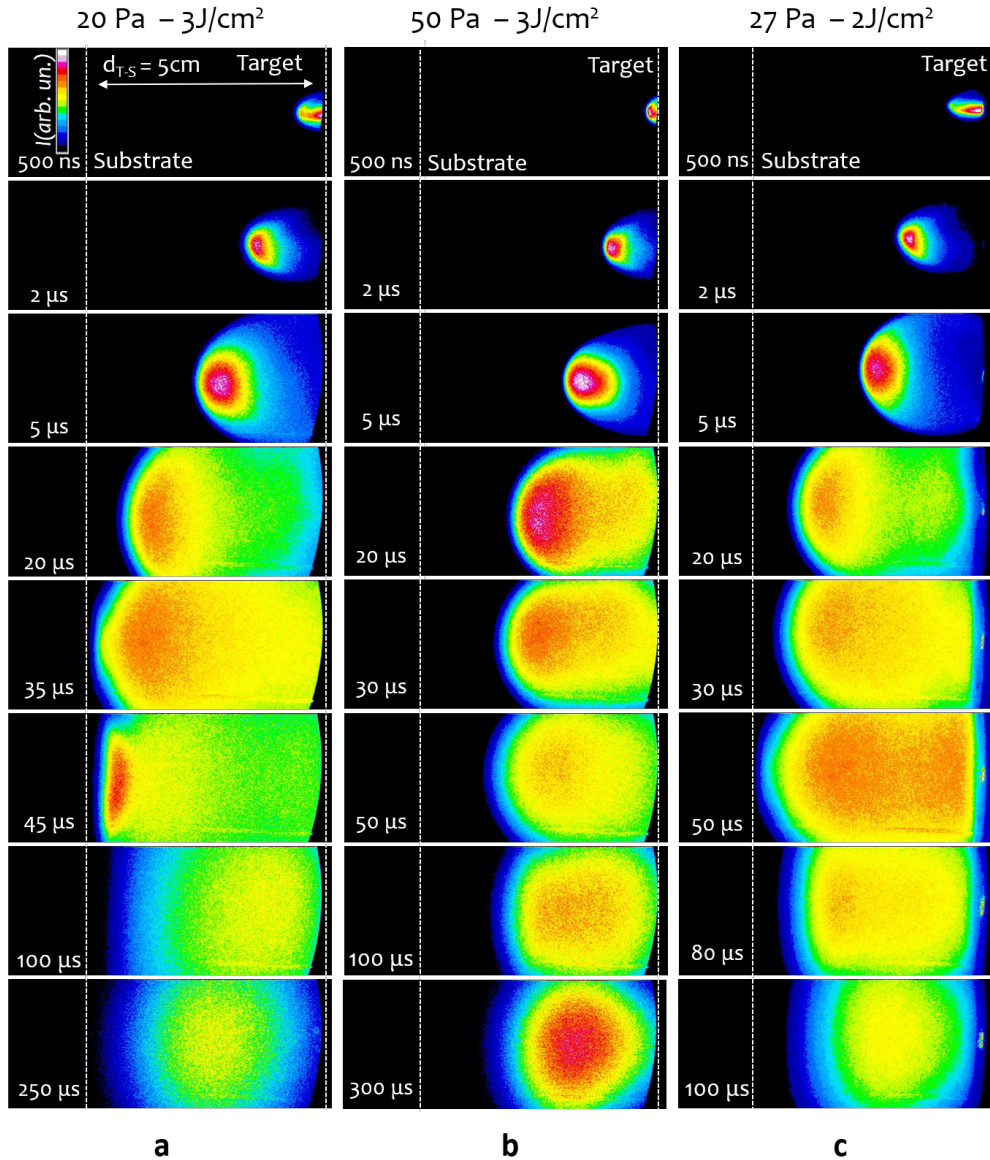
Figure 6.15: *ICCD pictures taken at (a) 20 Pa and (b) 50 Pa of* N_2 *at F=3* J/cm^2*, and (c) at 27 Pa and F=2* J/cm^2*.*

images are reported in Fig.6.5), showing a more porous tree-like structure for the film deposited at the higher pressure. Finally, a correlation between ICCD pictures and ion probe measurements can be done, indeed the time when plume edge reaches the substrate corresponds to the onset of the second component, as can be seen at 20 Pa (see inset Fig.6.14b).

In addition, the intermediate condition $L \simeq 1$, corresponding to the plume edge tangent to the substrate (as discussed in section 3.2.1), was searched with the aim to deposit films with hierarchical morphology (tree-like structure). This condition was found at 27 Pa and F=2 J/cm^2, and the corresponding ICCD images and ion probe measurement are reported in Fig.6.15c and 6.16a, respectively. From ICCD,
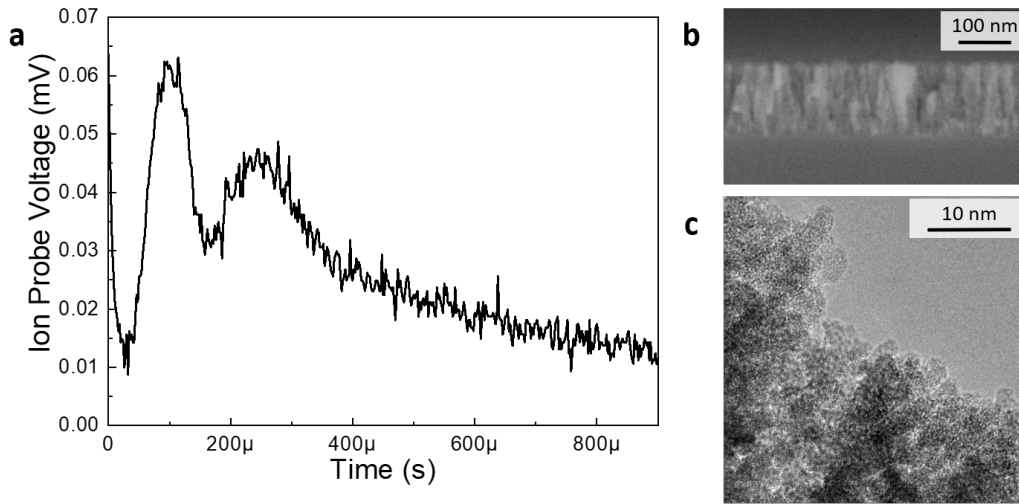
Figure 6.16: *(a) Ion probe measurement in the condition of 27 Pa and F=2 J/cm^2; (b) SEM cross-section and (c) TEM images of the films deposited in the same condition.*

the plasma edge achieves the condition of tangency to the substrate at around 50 μs, corresponding to the onset of the second component in the ion probe graph. In addition, while the fast component is not visible, a *third component* appears at longer time. This is associated to the fact that not all the ablated material sticks to the substrate, therefore incoming ablated species can collide with rebounded materials, slowing down furtherly and splitting the ion probe signal in another component [291]. Moreover, in case of 20 Pa and F=3 J/cm^2, which is a condition where the plasma edge hits the substrate (i.e. $L < 1$), the third component is not clearly observable as a separated band from the ion probe measurement, but it is still present and visible from ICCD at 45 μs as a bright zone of emission near the substrate.

Finally, the $L \simeq 1$ condition (i.e. 27 Pa and F= $2J/cm^2$) was employed to deposit films thick 150 nm, whose SEM and TEM images are shown in Fig.6.16b,c. It should be specified that for depositions of these samples, the background atmosphere was changed from N_2 to N_2/H_2; however, no changes in deposition mechanisms were found by checking with ion probe measurements and ICCD imaging. In Fig.6.16b,c, the deposited film shows a fluffy tree-like morphology and structure composed by NPs with average diameter around 3 nm. More details about this sample will be discuss in section 6.3.3, in comparison to the corresponding annealed film and to the film deposited at the same condition but with the substrate heated at 500°C.

6.3   Effects of thermal treatment

In this section, the effect of thermal treatments on the properties of both compact and nanoporous TiN films is studied. The effects of two different annealing atmospheres are considered, namely vacuum and N_2/H_2. In both cases, an increase of

film crystallinity is expected, moreover in case of N_2/H_2-annealing, an enrichment in nitrogen content is desired. For compact TiN thin films the annealing temperature was chosen equal to 550°C in order to promote crystal domain enlargement while keeping low thermal oxidation, according to [167]. For nanoporous TiN films two temperatures were employed, namely 300 and 550°C. Indeed, since these films are expected to be constituted by very small crystallites (i.e. size of few nm) immersed in an amorphous matrix [194], the thermal budget for oxidation would be lower than for compact TiN films. For this reason, temperatures lower than 400°C may be used [167, 170], namely 300°C for this work.

6.3.1 Thermal treatment of compact TiN thin films

The effect of post-deposition thermal treatments in vacuum or over-pressure of N_2/H_2 (at 550°C for 1 hour; for more details refer to section 3.2.2) was studied on compact TiN thin films deposited at 1 Pa of N_2/H_2 or vacuum at laser fluence equal to $2J/cm^2$, with the aim to improve crystallinity.

However, during thermal treatment, the TiN films grown on silicon substrates developed circular hollows on the surface (see Fig.6.17), that were ascribed to possible strains due to the thermal expansion mismatch between film and substrate, while this problem does not occur on glass substrate. Indeed, TiN and Si have quite dissimilar coefficient of thermal expansion (i.e. $9.35 \cdot 10^{-6}\,K^{-1}$ for TiN and $2.6 \cdot 10^{-6}\,K^{-1}$ for Si, at room temperature) [163, 294]. Therefore, trying to avoid this phenomenon, thermal SiO_2 film 350 nm-thick was grown on silicon substrate via air-thermal treatment before TiN deposition. Indeed, the coefficient of thermal expansion of SiO_2 is equal to 8-14 $\cdot 10^{-6}\,K^{-1}$, therefore more similar to TiN. This strategy was effective, in fact the annealing process did not cause TiN film dewetting from the SiO_2 substrates. This result is relevant because it means that silicon substrate can be replaced by thermal SiO_2/Si while allowing characterizations which need a semiconducting substrate (e.g. SEM, EDX). Moreover, the thermal stability of SiO_2 gives the opportunity to perform thermal treatments at much higher temperatures than 550°C, which is the highest temperature feasible for glass substrates.

Structural analysis was performed via XRD (see section 4.2 for XRD experimental details) on as deposited and annealed TiN films (about 500 nm thick), whose diffractograms are reported in Fig.6.18. All XRD patterns reveal crystalline face-centered cubic (FCC) structures typical of TiN films, while the absence of titanium and oxide-related peaks suggests that if oxygen is present, it is in non-crystalline superficial oxynitride (or low degree of crystalline phase), not detectable by XRD.

First, the effect of substrate on as deposited TiN films (at 1Pa of N_2/H_2) was studied, in particular glass and thermal SiO_2/Si were considered (see Fig.6.18a). Both curves have a preferred (111) orientation, as expected from TiN films much thicker than $\sim$ 150 nm and deposited via physical vapor deposition (see section 6.1), and films deposited on SiO_2 shows a more intense and sharp (111) peak, suggesting a more crystalline structure with respect to the corresponding TiN films on glass. The Scherrer's equation (see Eq.4.1) was applied to (111) peaks in order to evaluate the average crystalline domain size, equal to 10.1 and 4.2
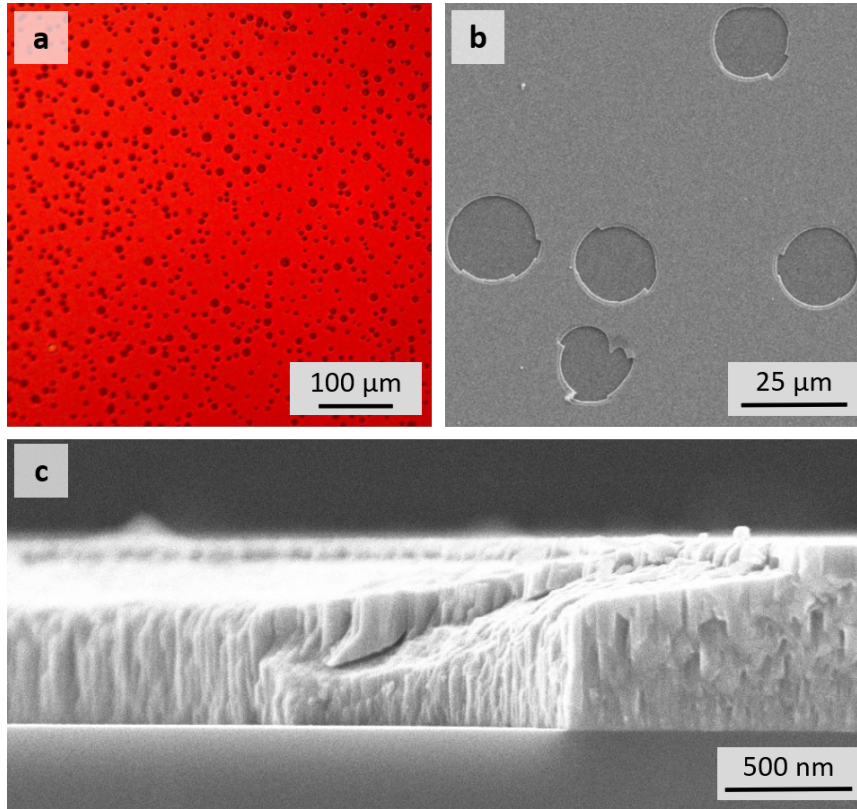
Figure 6.17: *(a) Optical microscope, (b) SEM top-view and (c) SEM cross-section images of a compact TiN film deposited on silicon substrate after annealing.*

nm for the films deposited on SiO_2 and glass substrate, respectively. In addition, the position of the (111) peak for both films is slightly left-side shift with respect to the reference value (i.e. 36.302° and 36.256° for films deposited on SiO_2 and glass, respectively, which means a shift of 0.424-0.470° from reference position of 36.726°). This shift implies a variation of lattice parameter, which can be calculated with Bragg's law for cubic crystal system as follows

$$a = \frac{\lambda\sqrt{h^2 + k^2 + l^2}}{2sin\theta} \tag{6.1}$$

where λ is the X-ray wavelength, θ is the diffraction angle and h,k and l are the Miller indices. The lattice constant results equal to 4.283Åand 4.288Åfor film deposited on SiO_2 and glass respectively, therefore a bit larger than the reference of 4.235 Å. This variation of a leads to a macro-strain which gives an indication on the intrinsic stress in the films, that is typically due to the lattice mismatch between TiN and substrate material and it is associated to a compressive stress (in-plane compression, which is commonly observed in TiN_x films produced by physical vapor deposition techniques) as well as to variation in film stoichiometry [282, 295–297].

Then, the effect of different annealings (i.e. vacuum- and N_2/H_2-annealings at 550°C) on TiN thin films deposited deposited at 1Pa of N_2/H_2 on glass substrate is considered, and the corresponding diffractograms are shown in Fig.6.18b. Both
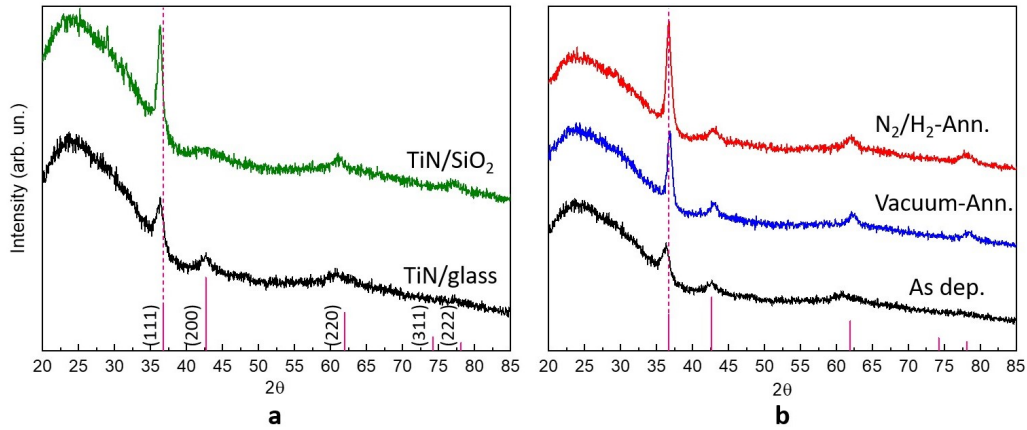
Figure 6.18: *XRD diffractograms of compact TiN films deposited at 1Pa of* N_2/H_2 *as a function of (a) different substrates (i.e. glass and* SiO_2*) and (b) different thermal treatments (i.e. vacuum- and* N_2/H_2*-annealings). The characteristic XRD peaks of TiN are reported in (a). In (b) As dep. means as deposited, i.e. before thermal treatment.*

the annealings did not modify the preferred orientation of the films, while smaller grains with other orientations grew up since the heat treatment provides thermal energy to facilitate the atom rearrangement by diffusion in the thin film [168, 298]. By using Scherrer's equation on (111) peak, the average crystalline domain size was estimated equal to 9.0 and 9.2 nm for vacuum- and N_2/H_2-annealed film, respectively. Therefore, both annealings lead to a slight enhancement of film crystallinity as well as to an increase of the domain size. Indeed, in literature thermal treatments have shown more effectiveness when the as deposited films are quite amorphous and thinner than 200 nm [167, 171], while here as deposited 500 nm thick-films show already FCC structure, therefore a more slight effect of the annealing is expected. Finally, another effect of the annealing involve the right-side shift of the (111) peak to 36.692° and 36.826° for N_2/H_2- and vacuum-annealed films, respectively, meaning a lattice constant of 4.239 Åand 4.224 Å. This shift can be associated to a relaxation of the compressive stress or to a partial oxidation of the film, since a solid solution of TiN-TiO crystallize in the same cubic structure as TiN with a slightly smaller lattice constant a_{TiO}=4.1766 Å [180].

Fig.6.19 shows Raman spectra before and after thermal treatment of TiN thin films deposited at 1 Pa of N_2/H_2. The Raman analysis resulted not dependent on the employed substrate, therefore only results of films deposited on glass are reported. In section 6.2, it was shown that the Raman spectrum of as deposited compact TiN films suggests nitrogen sub-stoichiometry, moreover no differences were found in Raman signals of films deposited in vacuum or at 1 Pa of N_2/H_2. Both the annealings lead to a blue-shift of the acoustic band (i.e. the band below 400 cm^{-1}). This behavior is more pronounced for N_2/H_2-annealed films and in literature this has been associated to a partial oxidation of the film [173, 275], since a blue-shift can be due to a decrease in the lattice parameter, which is confirmed by XRD. In addition, a slight intensity increase in the range of 500-600 cm^{-1} is observed, which can be associated again to a partial oxidation rather than to an increment of nitrogen content. Finally, both annealings resulted in a better
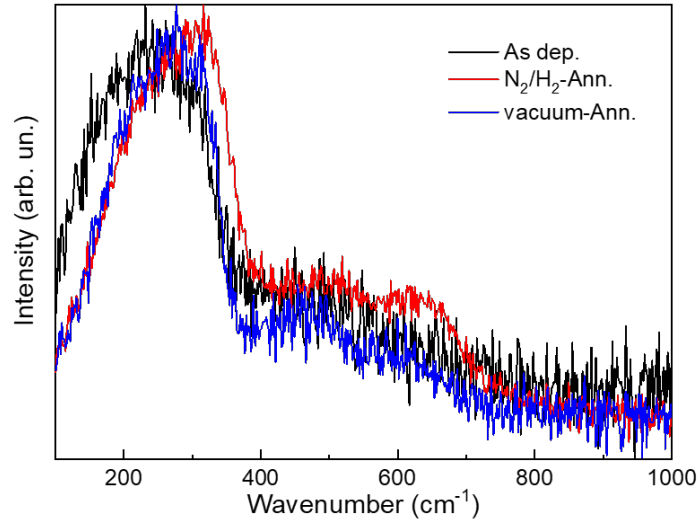
Figure 6.19: *Raman spectra of compact TiN films deposited at 1 Pa N$_2$/H$_2$ before (As dep.) and after vacuum- and N$_2$/H$_2$-annealings.*

signal-to-noise ratio and in a narrower acoustic band, suggesting a more ordered structure (confirmed by XRD analysis), especially for the vacuum-annealed film. The combination of XRD and Raman results indicate that thermal treatment is a way to improve crystallinity, while a certain degree of (surface) oxidation is unavoidable, therefore a compromise needs to be made depending on the specific goal.

For electrical and optical characterizations a total of three different synthesis conditions were investigated: (i) deposition and annealing in N$_2$/H$_2$, (ii) deposition in N$_2$/H$_2$ and vacuum-annealing and (iii) deposition in vacuum followed by N$_2$/H$_2$-annealing.

The electrical measurements were performed on compact 200 nm-thick TiN thin films grown on glass substrates. Here, preliminary results are presented in terms of resistivity (ρ), charge carrier density (n) and mobility (μ) and are shown in Fig6.20. The main faced issue involves the reliability of Hall measurements, indeed, only few measurements reported a Figure-of-Merit (FoM, defined in section 3.3.2) smaller than 1. In particular, in case of vacuum-annealed TiN film deposited at 1 Pa of N$_2$/H$_2$ only one measurement was reliable, indeed no error bars are shown for this sample in Fig.6.20. For other samples, even if Hall measurements with FoM<1 are reported, both charge carrier density and mobility present very large error bars, especially for vacuum-deposited films, suggesting bad repeatibility and reliability of these measurements. On the other hand, resistivity measurements demonstrated good repeatability for all samples.

As deposited films show similar resistivity, while the effect of annealing is different for each condition. For TiN film deposited at 1 Pa the resistivity increase upon both vacuum and N$_2$/H$_2$-annealings, moving from $2.7 \cdot 10^{-4}$ Ωcm to
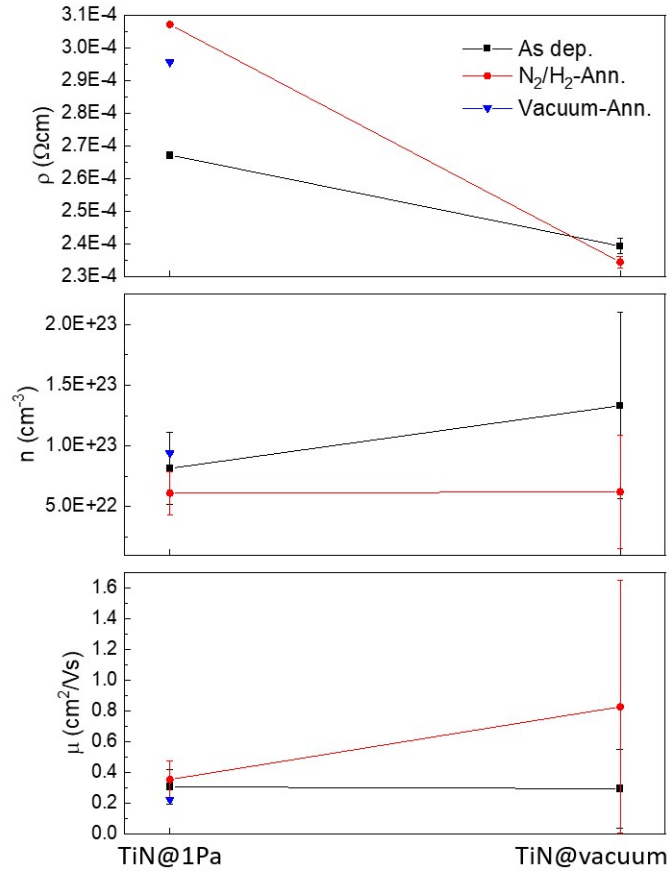
Figure 6.20: *Resistivity (ρ), charge carrier density (n) and Hall mobility of compact TiN films deposited at 1 Pa of N_2/H_2, before and after vacuum- and N_2/H_2-annealings, and vacuum-deposited, before and after N_2/H_2-annealing.*

$2.96 \cdot 10^{-4}\,\Omega cm$ for vacuum-annealing and to $3.1 \cdot 10^{-4}\,\Omega cm$ for N_2/H_2-annealing. On the other hand, vacuum-deposited TiN film shows a slight decrease of resistivity upon N_2/H_2-annealing, namely from $2.4 \cdot 10^{-4}\,\Omega cm$ to $2.3 \cdot 10^{-4}\,\Omega cm$. In literature, resistivity is expected to decrease upon thermal treatment as a consequence of a significant enhancement of the crystalline structure [172], however for slight crystalline changes, resistivity varies moderately [171]. Here, a deterioration of resistivity with thermal treatment is observed and it can be associated to the increase of surface oxidation (as observed from Raman spectroscopy), while the slight enhancement of crystallinity (as observed from XRD) has a side effect. Notably, the lowest resistivity values found in this work ($\sim 200\,\mu\Omega cm$) is one order of magnitude higher than the epitaxial or good quality polycrystalline TiN films deposited through physical vapor depositions [148, 150].

As regard Hall measurements, the charge carrier density of the as deposited samples was a bit higher than the high quality and almost stoichiometric TiN films deposited by physical vapor deposition techniques reported in literature [299, 300], however the very large error bars should be taken into consideration. For TiN film deposited at 1 Pa, the vacuum-annealing leads to an increase of carrier density, i.e.

from $8.2 \cdot 10^{22} \, cm^{-3}$ to $9.3 \cdot 10^{22} \, cm^{-3}$, while the N$_2$/H$_2$-annealing leads to a decrease down to $6.1 \cdot 10^{22} \, cm^{-3}$. Moreover, the N$_2$/H$_2$-annealing leads to a decrease of carrier density of the vacuum-deposited film too, moving from $1.3 \cdot 10^{23} \, cm^{-3}$ down to $4.6 \cdot 10^{22} \, cm^{-3}$.

The measured Hall mobility was very similar for both as deposited TiN films, around $0.3 \, cm^2/Vs$. The effect of vacuum-annealing leads to a decrease of Hall mobility (i.e. from $0.31 \, cm^2/Vs$ to $0.22 \, cm^2/Vs$), while N$_2$/H$_2$-annealing leads to an increase (i.e. from $0.31 \, cm^2/Vs$ to $0.36 \, cm^2/Vs$ for TiN film deposited at 1Pa, and from $0.29 \, cm^2/Vs$ to $0.83 \, cm^2/Vs$ for vacuum-deposited TiN film), however error bars are very large, especially for vacuum-deposited TiN films before and after annealing (where the lower end of the error bar goes even to zero). However, since XRD analysis suggests a slight improvement of crystallinity structure upon both vacuum- and N$_2$/H$_2$-annealings as well as an increase of the estimated average domain size, an improvement of Hall mobility was expected. Even if the highest Hall mobility achieved is much lower than the μ of an epitaxial crystalline TiN thin film (e.g. μ=6.7 cm^2/Vs [134]), the measured μ are in accordance with Hall mobility reported in literature for polycrystalline TiN films with (111) preferred orientation, e.g Yang *et al.* measured $0.15 \, cm^2/Vs$ for 300 nm-thick films deposited by reactive sputtering [301], and Yu *et al.* found 0.15-0.4 cm^2/Vs for 40-60 nm-thick films deposited by RF magnetron sputtering [302].

Finally, by considering that Raman spectroscopy showed an increment of surface oxidation, and since the 4-point probe van der Pauw configuration implies that contacts are placed on the edge on the surface of the samples (see section 3.3.2), the surface oxidation can prevent a reliable Hall measurement. Therefore, to better understand the electrical behavior of these compact TiN thin films, before and after annealing, an optimization of apparatus of measurement is needed (e.g. growing TiN thin films on electrical contacts) as well as more statistics.

The optical spectra were measured on compact TiN thin films about 200 nm-thick and grown on both glass and SiO$_2$/Si substrates. The reflectance spectra of all synthesis condition are reported in Fig.6.21. The vacuum-annealing left the reflectivity of the TiN film deposited at 1 Pa of N$_2$/H$_2$ basically unchanged, the reflectance dip moderately red-shifts from 350 to 359 nm as well as reflectance intensity slightly decreases all over the spectrum (see Fig.6.21a). On the other hand, N$_2$/H$_2$-annealing causes a strong shift of the dip position towards longer wavelengths, i.e. from 330 nm to 390 nm for the TiN film deposited in vacuum and from 350 nm to 473 nm for the TiN film deposited at 1 Pa of N$_2$/H$_2$, as well as lower reflectance intensity in near-IR range. This behavior is associated to a reduction of free-carriers in TiN films [146, 147], that can be due to a partial oxidation of the film upon N$_2$/H$_2$-annealing rather than an increment in nitrogen content, in agreement with other characterizations. In particular, a comparison between reflectance dip position and the measured charge carried density can be made by considering that reflectance minimum is an indication of the film plasma frequency, which is affected in turn by carrier density (see section 1.2). This correlation is observable already from as deposited films. Indeed, reflectance minima of vacuum-deposited films is slightly blue-shifted with respect the film deposited at 1 Pa, in agreement the higher charge carrier density measured for the vacuum-deposited
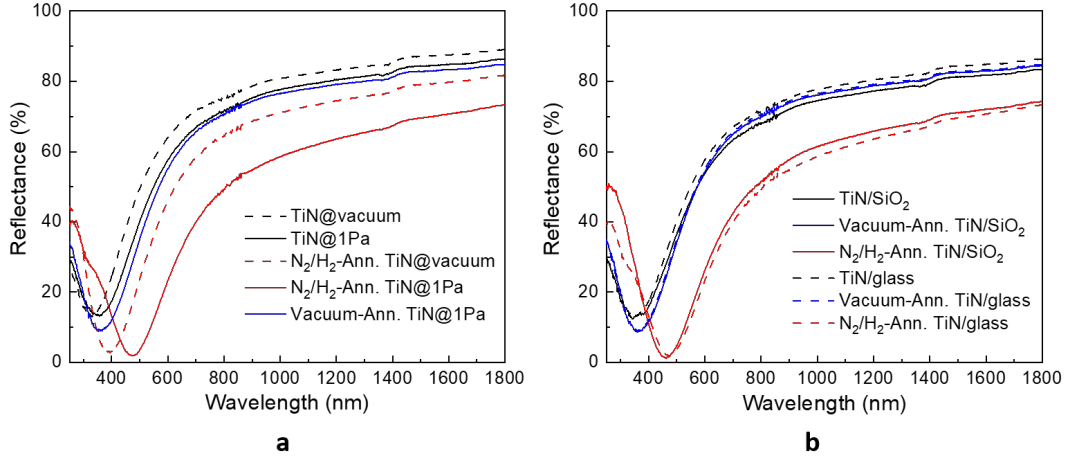
Figure 6.21: *Optical reflectance spectra of compact TiN films grown on glass and SiO_2/Si substrates, before and after thermal treatments. In (a) the effect of vacuum- and N_2/H_2-annealings on samples deposited on glass is shown; in (b) the effect of different substrates is shown before and after annealings.*

sample. Moreover, N_2/H_2-annealing leads to a red-shift of both as deposited samples, as well as a decrease of the measured charge carried density in both cases. However, even if the highest red-shift was found for N_2/H_2-annealed film deposited at 1 Pa, the smaller n was measured for the N_2/H_2-annealed vacuum-deposited films, nevertheless the large error bar of the Hall measurements should be taken into account. For the same reason, it is not surprising the contradiction between the slight increase of carrier density measured after vacuum-annealing of the film deposited at 1 Pa and the moderate red-shift of reflectance minimum upon this thermal treatment.

Finally, changing the substrate from glass to SiO_2/Si does not affect optical reflectance spectra, as clearly observable in Fig.6.21b. The effect of thermal treatments remains the same and the reflectance curves almost overlap with spectra taken on the corresponding samples deposited on glass, both before and after annealing. This means that optical features are more affected by changes in stoichiometry and composition rather than crystal structure (observed from XRD), that in this case is just a moderate modification.

Ellipsometric measurements were performed on the same set of samples, deposited on silicon substrate.[5] The pseudo-dielectric permittivity was retrieved by direct inversion of the ellipsometric quantities as

$$\langle\tilde{\epsilon}\rangle = sin^2\phi[1 + tan^2\phi(\frac{1-\rho}{1+\rho})] \tag{6.2}$$

where $\langle\tilde{\epsilon}\rangle = \langle\epsilon_1\rangle + i\langle\epsilon_2\rangle$, $\rho = tan\Psi e^{i\Delta} = \frac{r_p}{r_s}$ (Fresnel reflection coefficients for p- and s- polarized radiation) and ϕ is the incident angle [303]. The measured

---

[5]The ellipsometric measurements were performed in collaboration with L. Mascaretti at Regional Centre of Advanced Technologies and Materials, Faculty of Science, Palacký University of Olomouc. The data were collected with a J. A. Woollam variable-angle spectroscopic ellipsometer (VASE), range 0.5-6.5 eV, at the angle of incidence 65° and 75°. Data analysis and fitting were performed by WVASE32 (J. A. Woollam Co.) software.

Pressure (Pa)	Thermal treatment	TiO_2 thickness (nm)	λ_{ps} (nm)	E_{ps} (eV)	Q_{SPP} at 1550 nm	Q_{LSPR} Max	ρ_D ($\mu\Omega$cm)	n_D (cm^{-3})	μ_D (cm^2/Vs)	MFP (nm)
1	No	3	461	2.70	6.16	0.59 (827 nm)	197.72	$4.08 \cdot 10^{22}$	0.71	3.23
1	N_2/H_2	10	475	2.61						
1	Vacuum	1.3	463	2.68	8.08	0.71 (827 nm)	205.07	$4.43 \cdot 10^{22}$	0.83	3.52
Vacuum	No	1.5	410	3.02	10.75	0.78 (729 nm)	160.95	$3.69 \cdot 10^{22}$	0.80	3.74
Vacuum	N_2/H_2	24	541	2.50	1.52	0.19 (954 nm)				

Table 6.3: *The TiN thin films properties extracted from the modeling and the fitting of el-lipsometric measurements before and after thermal treatment: the estimated thickness of the TiO_2 superficial layer, the screened plasma wavelength (λ_{ps}) and energy (E_{ps}), the plasmonic quality factors (Q_{SPP}, Q_{LSPR}) and the electrical properties calculated from the parameters of Drude oscillator, i.e. the resistivity (ρ_D), charge carrirer density (n_D), mobility (μ_D) and the mean free path (MFP).*

films were modeled with a two-layer model consists in a TiN film covered by a TiO_2 layer. The optical properties of the TiN layer were modeled by Drude-Lorentz model with only one Lorentz oscillator [78], while for the oxide layer the Tauc-Lorentz model was employed, in which the light is absorbed above the band gap (fixed at 3.2 eV) and is transmitted below [304]. The oxide thickness was estimated from the modeling and the results are reported in Table6.3. The oxide layer was found equal to 1.5 nm and 3 nm for the film deposited in vacuum and at 1 Pa of N_2/H_2, respectively. After vacuum-annealing, the oxide does not thicken, while after the N_2/H_2-annealing it was calculated significantly thicker and equal to 10 and 24 nm. In particular, the fitting of both N_2/H_2-annealed films was very difficult, and results do not appear completely reliable. Likely, the two layer model is not effective for these films, since the oxidation can be so high that the film is an oxynitride for the whole thickness. For a better fitting, more complex model can be used (e.g. Maxwell-Garnett formalism, which is an effective medium model where the oxynitride films can be treated as a composite of different phases such as TiN inclusion in TiO_2 films or vice versa [146]) or a composition analysis through the thickness may be necessary by means of depth profiling XPS, SIMS or Rutherford backscattering spectrometry. The calculated real and imaginary parts of the pseudo-dielectric permittivity of the TiN layer are reported in Fig.6.22a,b. The as deposited and the vacuum-annealed films show a metallic behavior typical of TiN films, indeed the real part changes from positive to negative values in the visible region as a consequence of free-carrier absorption (Fig.6.22a). The vacuum-deposited sample exhibits the lowest $\langle \epsilon_1 \rangle$. The effect of vacuum annealing on the film deposited at 1 Pa leads to a lowering of $\langle \epsilon_1 \rangle$ for wavelength longer than about 1000 nm. The N_2/H_2-annealed films show the higher $\langle \epsilon_1 \rangle$, but it should be taken in account that the curve of the N_2/H_2-annealed film deposited at 1 Pa is not reliable, especially in the visible range. In Fig.6.22b, the imaginary part increases monotonically with the wavelength after showing a minimum around 320 nm (except for the N_2/H_2-annealed films). The highest $\langle \epsilon_2 \rangle$ is showed by the N_2/H_2-annealed film deposited in vacuum, followed by the vacuum-deposited film and the films deposited at 1 Pa; in this case the effect of vacuum-annealing is not significant. The value at which $\langle \epsilon_1 \rangle = 0$ is the crossover wavelength (λ_{ps}, corresponding to the screened plasma energy E_{ps}, see section 2.3.1), which are shown in the inset of Fig.6.22a and reported in the Table6.3.
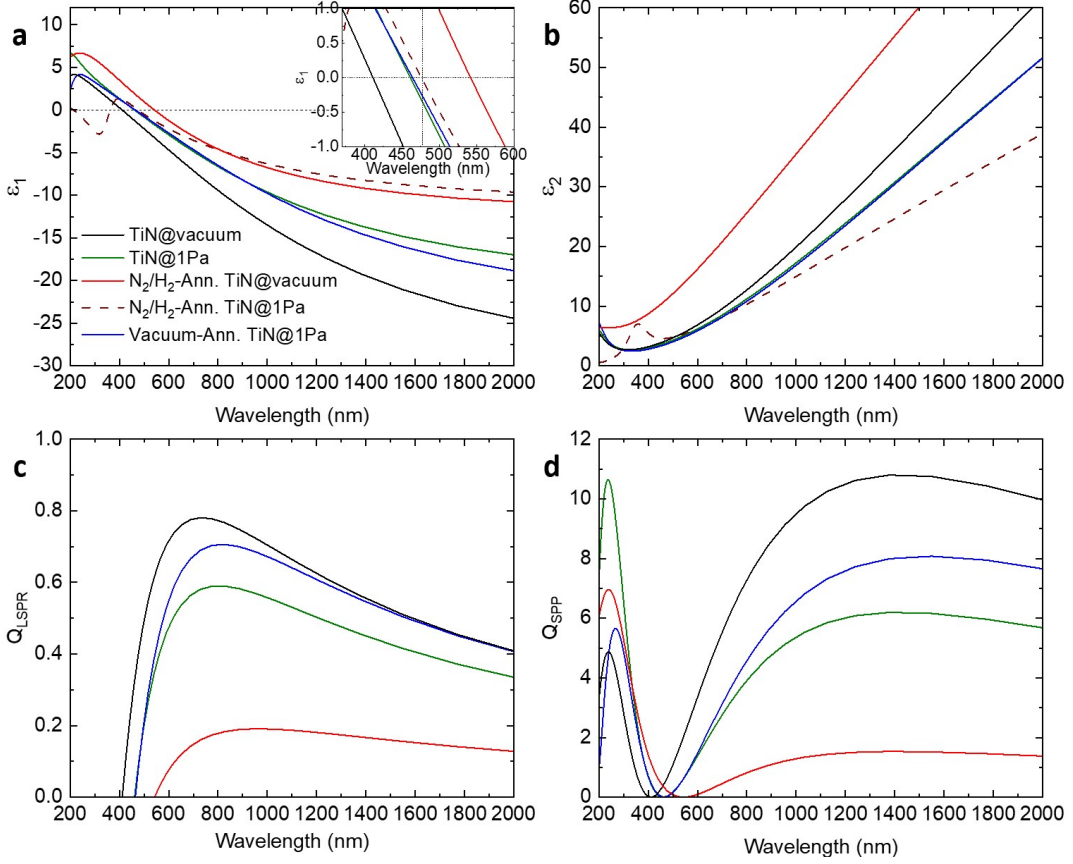
Figure 6.22: *(a) Real and (b) imaginary parts of the pseudo-dielectric permittivity of compact TiN films deposited at 1 Pa of N_2/H_2, before and after vacuum- and N_2/H_2-annealings, and vacuum-deposited, before and after N_2/H_2-annealing; the inset in (a) is a magnification of the crossover wavelength λ_{ps}. (c,d) Quality factors for localized surface plasmons (Q_{LSPR}) and surface plasmon polaritons (Q_{SPP}) calculated from ϵ_1 and ϵ_2.*

As discussed in section 2.3.1, the value of λ_{ps} for a stoichiometric TiN film is known to be equal to 478 nm (i.e. E_{ps}=2.65 eV), while smaller values imply a substoichiometric TiN and larger values mean overstoichiometry. In this case, the as deposited and vacuum-annealed films show substoichiometry, in accordance with Raman measurements, on the other hand, the N_2/H_2-annealed films show almost stoichiometric and overstoichiometric behavior, but this result is probably unreliable for the reasons explained before. The relative position of λ_{ps} is in agreement with the reflectance minimum measured with the spectrophotometer: the lowest values was found for the vacuum-deposited film, the vacuum-annealing leads to a slight red-shif, while the N_2/H_2-annealing leads to a substantial red-shift.

The real and imaginary parts of the pseudo-dielectric permittivity were employed to calculate the plasmonic properties of the films in terms of the quality factor for LSPRs (Q_{LSPR}) and SPP (Q_{SPP}) introduced in section 1.4, and resuts are reported in Fig.6.22c,d. In both cases, the best plasmonic behavior was found for the vacuum-deposited film, whose maximum Q_{LSPR} is equal to 0.78 at

729 nm and the Q_{SPP} at 1550 nm (i.e. communication wavelength) is equal to 10.75 (the results for the other samples are reported in Table 6.3). As expected, these values are much smaller than those reported for epitaxial TiN thin films deposited at high temperature on MgO (Q_{LSPR}=3.4 at 1200 nm and Q_{SPP}=213 at 1550 nm) [305], however they are also much smaller than the best achieved by TiN films deposited by PLD at room temperature (Q_{LSPR}=1.9 at 855 nm and Q_{SPP}=113 at 1550 nm) [153]. Instead, these results are similar to those obtained for TiN thin fims with a resistivity of the same order of magnitude (around 100-500 $\mu\Omega$cm) obtained by ion beam assisted deposition [306], whose results were justified with a low content of crystalline phase and high defects and oxygen concentration (around 25%at.) in the samples, and by atomic layer deposition [307]. Moreover, the vacuum-annealing of the film deposited at 1 Pa leads to a better plasmonic behavior for both LSPR and SPP, while N_2/H_2-annealing shows a worsening.

In order to compare ellipsometric results with electrical properties previously analyzed, the parameters of Drude oscillator are employed, since they account the metallic character of the TiN films. Indeed, the unscreened plasma frequency is directly correlated to conduction electron density (n_D) according to Eq.1.7. In addition resistivity (ρ_D), optical mobility (μ_D) and mean free path (MFP) can be calculated from Drude parameters according to

$$\rho_D = \frac{\hbar\gamma_D}{E_{pu}^2\epsilon_0} \cdot 10^8 \tag{6.3}$$

$$MFP = (\frac{2\pi^2\epsilon_0\hbar^4}{e^2m*^2})^{1/3}\frac{E_{pu}^{2/3}}{\gamma_D} \cdot 10^9 \tag{6.4}$$

$$\mu_D = \frac{e}{m^*\gamma_D} \tag{6.5}$$

where the effective mass was approximated from stroichiometric TiN, i.e. $m^* = 1.15\,m_e$ [282,307].

The results are reported in Table 6.3 (except for N_2/H_2-annealed samples since not reliable). As for optical properties, the best electrical behavior was found for the vacuum-deposited sample, i.e. the lowest resistivity and highest MFP. The film deposited at 1 Pa shows a bit worsening of these properties, but a slight higher charge carrier density. The vacuum-annealing of this sample leads to an increase in resistivity, but also in charge carrier density and MFP. These data are consistent with electrical properties measured by Van der Pauw method in d.c. current. The two types of resistivity show the same order of magnitude, and an increase after vacuum-annealing occurs in both cases. However, the underestimation of resistivity from Drude parameters can be ascribed to the electron scattering effects at grain boundary and interfaces that are not taken into account, or for the presence of macroscopic defects which increases the d.c.-resistivity, but having much less influence on the polarizibility at optical frequencies [306,308]. Even the n_D is underestimated, especially for the vacuum-deposited sample, but the order of magnitude is the same of d.c.-charge carrier density and the trend with the vacuum-annealing is confirmed. Finally the μ_D and MFP are very similar in all conditions and this in accordance with the trend of the Hall mobility. Comparing the MFP, which is around 3.5 nm for all samples, with the average crystalline do-

main size calculated by Scherrer equation from (111) peaks of XRD diffractograms (i.e. 4.2 nm for the film deposited at 1 Pa and 9 nm after vacuum-annealing), it can suggest that for as deposited sample the scattering sites occur at the grain boundary and point defects, while for vacuum-annealed sample scattering centers may be dispersed within the grains. However, it should be taken into account that two different substrates were employed (i.e. glass for XRD and silicon for ellipsometry) which can affect the crystalline structure of the films.

6.3.2 Thermal treatment of nanoporous TiN thin films

The effect of thermal treatment at different temperatures (300 and 550°C) in vacuum and over-pressure of N_2/H_2 was studied on nanoporous films deposited at 10, 20 and 50 Pa, F=$3.5 J/cm^2$, with the aim to favor desorption of surface oxygen, to improve the crystallization and, in the case of annealing in N_2/H_2 overpressure, enrich the films with nitrogen. Fig.6.23 shows the Raman spectra of annealed samples with the different thermal treatments (i.e. in vacuum at 550°C and in N_2/H_2 at both 300 and 550°C), compared with as deposited films. The following considerations can be made:

- For samples deposited at 10 and 20 Pa the annealing in N_2/H_2 at 300°C leads to a higher relative intensity of the acoustic band at 250-350 cm^{-1} (see Fig.6.23a,b). This could be related to a greater concentration of nitrogen vacancies or to a decrease of oxygen content within the film. Indeed, the broad band at 450-650 cm^{-1}, which can be associated to the presence of an underlying amorphous TiO_2 Raman signal, decreases in intensity. Moreover, the acoustic band of sample deposited at 10 Pa gets narrower and this may be due to the higher crystallinity of the annealed film. Finally, for the film deposited at 20 Pa, the appearance of the transverse acoustic mode contribution around 250 cm^{-1} may indicate a slightly improved crystallization [173].

- For samples deposited at 10 Pa, both annealing treatments at 550°C (i.e. in vacuum and in N_2/H_2 overpressure) do not give any evident difference in terms of Raman spectrum (Fig.6.23a). On the other hand, for films deposited at 20 Pa, the two treatments affect Raman signal in a different way (Fig.6.23b). Precisely, the annealing in vacuum gives an amorphous TiO_2 spectrum, while the one in N_2/H_2 gives broader and more undefined bands.

- For samples deposited at 50 Pa, all the thermal treatments lead to the crystallization of the amorphous TiO_2 already present and none of three annealings seem to have been successful in reducing oxidation (see Fig.6.23c).

In summary, from Raman analysis, the annealing in N_2/H_2 at 300°C seems to have improved the crystallinity of the films deposited at 10 and 20 Pa. However, this hypothesis should be further verified with other techniques, e.g. XRD. In addition, no evidences of nitrogen content increase was observed after the annealing in N_2/H_2 overpressure, instead a suggestion of oxidation reduction was observed for the less porous samples after annealing in N_2/H_2 at 300°C.

Fig.6.24 shows the transmittance, reflectance and absorbance curves for the considered samples before and after the three different thermal treatments. The

135
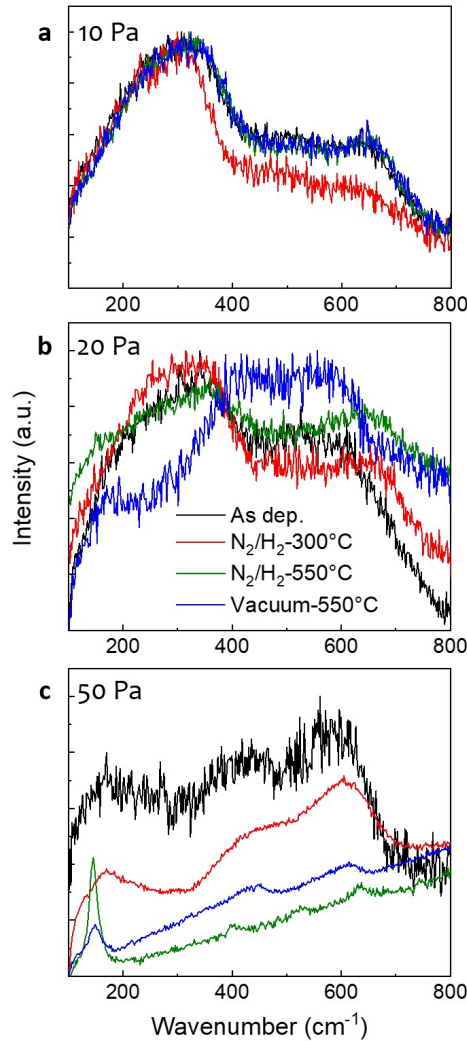
Figure 6.23: *Raman spectra of films deposited at (a) 10, (b) 20 and (c) 50 Pa, before (black lines) and after different annealings: vacuum-annealing at 550° C (blue lines), N_2/H_2-annealings at 550° C (green lines) and 300° C (red lines).*

optical measurements confirm the observations made for Raman analysis:

- For samples deposited at 10 and 20 Pa (Fig.6.24a,b), the N_2/H_2-annealing at 300°C is the thermal treatment that most reduces the transmittance peak, and it is the only one to blue-shift this peak (i.e. from $\lambda \approx 500\,nm$ to $\lambda \approx 380\,nm$ and from $\lambda \approx 550\,nm$ to $\lambda \approx 480\,nm$ for films deposited at 10 and 20 Pa, respectively). As discussed in section 2.3.3.2, this behavior can be associated to a decrease of oxygen content in the films. Moreover, the transmittance tail at longer wavelengths reduces. In accordance with Raman spectra analysis, the lower temperature adopted for the thermal treatment in N_2/H_2 seems to have reduced the oxidation within these films.

- The reflectance of the sample deposited at 10 Pa significantly changes after N_2/H_2-annealing at 300°C (Fig.6.24a). A well-defined reflectance dip appears next to a more steep plasma reflectance edge, while reflectance intensity in-

136
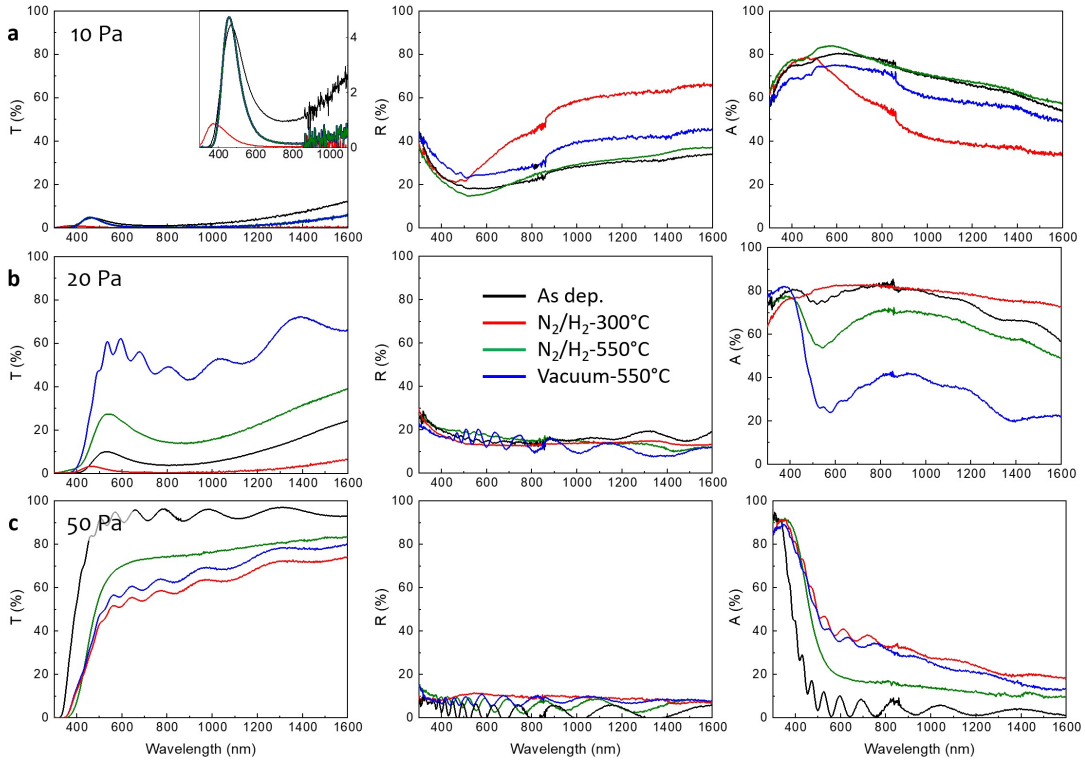
Figure 6.24: *Optical transmittance (T%), reflectance (R%) and absorbance (A%) of films deposited at (a) 10, (b) 20 and (c) 50 Pa, before (black lines) and after different annealings: vacuum-annealing at $550°C$ (blue lines), N_2/H_2-annealings at $550°C$ (green lines) and $300°C$ (red lines).*

creases at longer wavelengths, reaching values around 65%. This behavior can be associated to an increase of the carrier density of the film, therefore the annealing may have reduced either oxidation or nitrogen incorporation, or both. However, because of Raman analysis previously discussed, the oxidation reduction is more probable.

The absorbance peak of the sample deposited at 10 Pa becomes narrower and blue-shifted after the same annealing. Furthermore, instead of the two absorbance maxima of the as deposited TiN film, a single peak is observable upon this annealing. It can be assumed that the contributions to absorption given by inter and intra-band transitions overlap in the same wavelength range.

- For sample deposited at 20 Pa the reflectance does not change upon any annealings, and it stays low and constant along the whole wavelength range (Fig.6.24b). On the other hand, considering that the transmittance peak decreases, the two absorbance maxima of the as deposited film almost completely overlap into one single-peak after after N_2/H_2-annealing at 300°C. Moreover, this single-peak is broad and with an intensity around 80% for almost the whole analyzed wavelength interval.

- For sample deposited at 10 Pa (Fig.6.24a), both annealings at 550°C do
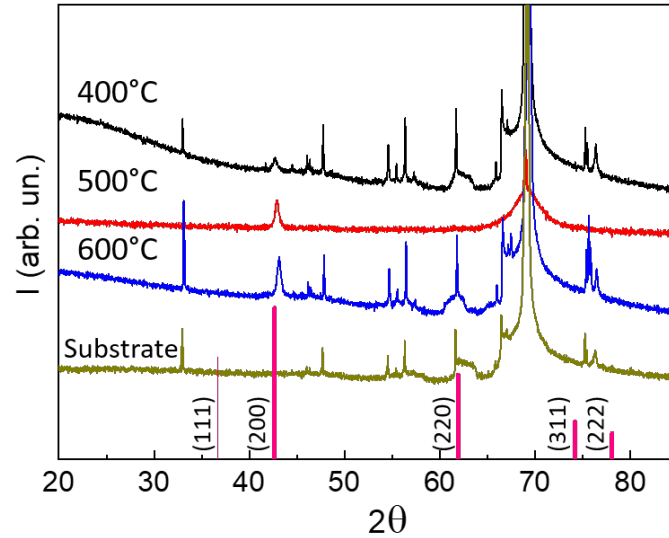
Figure 6.25: *XRD diffractograms of compact TiN deposited on silicon substrate heated at 400, 500 and 600°C. The substrate spectrum and TiN characteristic XRD peaks are reported.*

not evidently affect the optical curves, in accordance with Raman spectra, which suggests no clear structural modification. On the other hand, for samples deposited at 20 Pa (Fig.6.24b), these thermal treatments lead to higher transmittance peaks and lower intra-band absorption intensities, indicating a great oxidation extent. This is in accordance with Raman analysis, where a typical signal of amorphous TiO_2 was measured for that samples.

• For sample deposited at 50 Pa, all the three thermal treatments do not lead to any optical feature that can be associated to TiN (Fig.6.24c). This is in accordance with Raman analysis, where the spectra of either amorphous or crystalline TiO_2 were obtained.

In conclusion, in the case of nanoporous thin films, lowering the annealing temperature (i.e. 300°C instead of 550°C) gave more substantial differences in terms of Raman and optical spectra with respect to changing the annealing atmosphere; in fact, for films deposited at 10 Pa and 20 Pa, a reduction of oxidation and an increment of crystallinity were observed. However, this hypothesis should be further verified with other characterizations, e.g. XPS and XRD. Finally, for sample deposited at 50 Pa, all the three thermal treatments do not show any optical feature that can be associated to TiN, therefore the adopted thermal annealings are not effective in reducing the high oxidation extent.

6.3.3   Effects of substrate heating

At CNMS, it was possible to study the effect of substrate heating during deposition both for compact and nanoporous TiN thin films.

In literature, heating the substrate during PLD synthesis was found as an effective way to improve microstucture, stoichiometry and, as a consequence, to better electrical properties of TiN thin films. Xiang *et al.* [134] studied the effect of substrate temperature (T_{sub}) from 500 to 800°C on 200 nm-thick TiN films deposited on silicon substrate. They found an optimal condition at 700°C, in which XRD analysis showed the highest and narrower (200) peak, as well as the best electrical properties (i.e. ρ=25.7 $\mu\Omega$cm and n=6.7 · 10^{20} cm^{-3}). The enhancement in crystalline structure with T_{sub} was explained by considering its direct influence on the diffusion and aggregation of adatoms (coming from the ablated target) on the substrate during deposition. At low temperatures, the adatoms have difficultly to find the suitable surface sites due to their low diffusion. Therefore, islands nucleate leading to many structural defects in the final film. On the other hand, the crystalline structure and surface roughness of TiN films is improved by increasing T_{sub}. Similar results were found by Lee *et al.* [150], which deposited 150-200 nm-thick TiN films and studied the effect of T_{sub} from room temperature to 650°C. They found the lowest resistivity for films deposited at 650°C; in addition, they found that the (200) orientation of the TiN film is promoted with respect to the (111) direction by increasing T_{sub}, since (200) is the thermodynamically most favored and the increase of T_{sub} facilitate the growth of films with structure closer to thermodynamic equilibrium. Moreover, Chowdhury *et al.* [151] showed that substrate heating affect the oxygen incorporation during the deposition. The oxygen content was found to decrease by increasing T_{sub}, up to oxygen-free TiN films at T_{sub}>600°C. In this case, the decrease of resistivity with T_{sub} was associated both to an enhanced structure as well as to a more stoichiometric film. Finally, Rasic *et al.* [163] detected a decrease of residual strain in the deposited TiN films when the T_{sub} was increased from room temperature to 450°C and 650°C. This residual stress was explained by a lower defect mobility and by the reduced energy budget available to drive the relaxation of the lattice, leading to the promotion of defects and vacancies that are dentrimental for electrical properties of the films.

Here, the effect of T_{sub} on the structure of compact film is discussed. The films were deposited at 1 Pa of N_2, F=3 J/cm^2 and 500 shots, with substrate heated at three different temperatures, namely 400, 500 e 600°C. In all cases, very compact films around 130 nm thick were obtained. Fig.6.25 shows the XRD diffractograms of these samples. Since films were grown on silicon oriented (100), the peaks at 32.9° and 69.1° are associated to its (200) and (400) peaks of the substrate, while other sharp peaks have a not clear origin, that can be due to some substrate inclusions, to the sample holder or to a non-perfectly monochromatic incident radiation (e.g. Kα1-2 Kβ lines). However, the (200) peak of TiN is clearly recognized at 42.67°. This preferred orientation of growth was expected because of film thickness (i.e. below 150 nm). Moreover, the intensity of (200) peak increases with substrate temperature, while becoming sharper, suggesting an increase in crystallinity.

Then, the effect of substrate heating was studied on the fluffy tree-like structure deposited in the conditions identified in section 6.2.3 (i.e. at 27 Pa of N_2/H_2 and F=2 J/cm^2). In particular, three synthesis conditions were compared:

1. Tree-like film deposited at room temperature (Fluffy-T_{room})
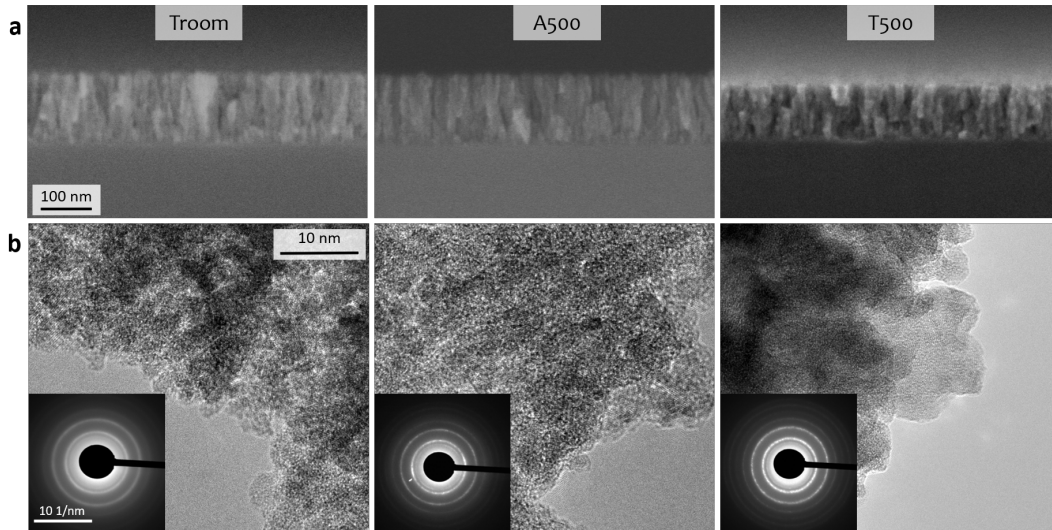
Figure 6.26: *(a) SEM and (b) TEM images of Fluffy-T_{room} (Troom), Fluffy-A500 (A500) and Fluffy-T_{500} (T500) samples. Insets in (b) show the corresponding SAED patterns.*

2. Tree-like film deposited at room temperature and post-annealed in N_2/H_2 at 500°C for 1 hour, without opening vacuum chamber (Fluffy-A500)

3. Tree-like film deposited with substrate heated at 500°C (Fluffy-T_{500})

The samples were deposited by keeping fixed laser shot number at 10000 and thickness was measured by SEM cross-section images, resulting equal to 150 nm, 140 nm and 115 nm for Fluffy-T_{room}, Fluffy-A500 and Fluffy-T_{500}, respectively. Fig.6.26 shows SEM and TEM images as well as selected area electron diffraction (SAED)[6] pattern of all considered samples. For the Fluffy-T_{room} sample, tree-like structure is composed by NPs with average size of about 3 nm. The SAED pattern shows blurry diffraction rings associated to poorly crystalline and defective nanostructures. For Fluffy-A500, the overall structure remains the same, while a slight sintering of NPs is observed from TEM images, as a consequence of post-deposition annealing effect. In addition, SAED pattern shows more distinct rings, but not assignable to a FCC structure as found for the TiN compact films. Finally, the Fluffy-T_{500} shows a more compact structure, where the single building NPs are difficult to be distinguished, and SAED rings are more clear, but still not a FCC structure was observed. The electron energy loss spectroscopy (EELS) was employed to qualitative check the atomic species present in the films. In all cases, Ti, N and O atoms were found; moreover, the intensity of the N peak decreases in favor of the O peak moving from Fluffy-T_{room}, to Fluffy-A500 and to Fluffy-T_{500}. However, a EELS quantitative analysis is needed to estimate the film stoichiometry. In Fig.6.27, Raman analysis[7] shows a spectrum similar to the characteristic TiN curve for Fluffy-T_{500}, while other films are slighlty detectable, by taking into account that the more sharp peaks are associated to the silicon

---

[6] HR-TEM micrographs, SAED patterns and EELS characterization were obtained with a Carl Zeiss LIBRA 200MC TEM operated at 200 kV. The samples were deposited directly on lacey carbon TEM grid. The measurements were performed thanks to the collaboration of Chenze Liu and Gerd Duscher.

[7] Exciting radiation with λ=785 nm and spectra acquired by a 1200 greeds/mm grating.
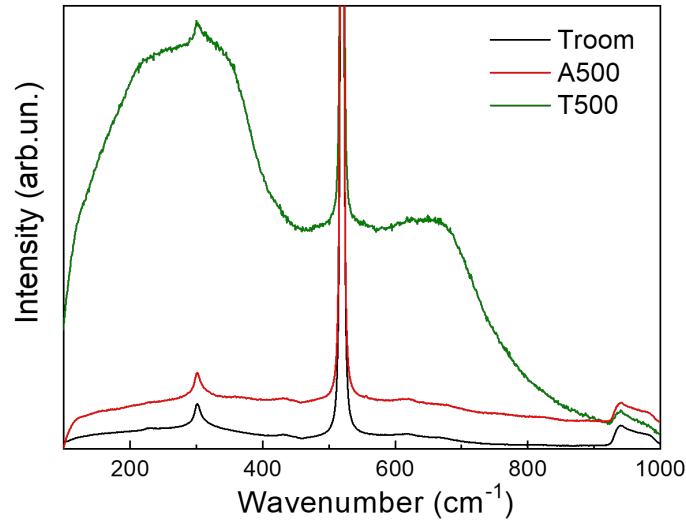
Figure 6.27: *Raman spectra of Fluffy-T_{room} (Troom), Fluffy-A500 (A500) and Fluffy-T_{500} (T500) samples.*

substrate. Even if Fluffy-T_{500} is the thinner film, the higher Raman signal can be due to the more compact and ordered structure.

In conclusion, this preliminary study of the substrate heating effect resulted promising to finely tune the crystalline structure of both compact and nanoporous TiN films, suggesting to be more effective than post-deposition thermal treatments.

6.4 Conclusions

In this chapter, TiN thin films were developed and investigated with the aim of tuning and understanding the influences of composition and structure on the optical response, while controlling the film morphology from compact to nanostructured, up to achieve the non-trivial synthesis of TiN NPs systems. The synthesis of TiN thin films was studied as a function of PLD process parameters and post-deposition thermal treatments, with a focus on the effect of background atmosphere (i.e. type of gas and pressure). Even if TiN is a very stable material, the oxidation issue during the synthesis represented a non-trivial problem, especially in case of porous structure and NPs assemblies with large surface area.

The main achievements of this chapter are summarized as follows:

- The optimum conditions to deposit adherent and compact films both on silicon and glass substrate, with uniform thickness on the widest possible area, were found by studying different combinations of laser fluences (i.e. F=2, 3.5, 6.5 J/cm^2) and background atmosphere (i.e. vacuum and 1Pa of N_2/H_2).

- The morphology evolution from compact-columnar to nanoporous tree-like

141

and to foam-like films was found as a function of background pressure (i.e. from 5 to 100 Pa of N_2/H_2, at F=2 and 3.5 J/cm^2). In particular, the development of TiN NPs assemblies systems was possible thanks to a specific investigation on PLD mechanisms in TiN synthesis performed at CNMS, with specific in-situ characterization techniques.

- The oxidation control/reduction of nanoporous TiN films was performed by means of two strategies:

  - Deposition at high laser fluence (F=6.5 J/cm^2 at 50 and 100 Pa), with the aim to lead to higher nitrogen radicals reactivity in the plasma plume and reduction of oxygen incorporation during deposition. TiO_xN_y films with tree-like structure were obtained, with a peculiar high and broadband absorption spectra all over the UV-Vis-NIR spectrum (i.e. higher than 90% in the wide range 270-2000 nm and an average absorbance of 94.8%). This is a fascinating result which is comparable to broadband absorbers made of TiN complex metamaterial structure, with a complex fabrication procedure [155,287], for applications in solar energy harvesting and hot electron devices.

  - Protection of the TiN NPs assemblies with a capping layer, in order to reduce surface oxidation due to air exposure. Such strategy was effective in reduce oxidation in the more porous films, by employing a 200 nm-thick aluminum nitride diffusion barrier deposited on top.

  For a better understanding of oxidation process, in-situ Raman spectroscopy during deposition should be performed, as well as more precise compositional characterizations after deposition, e.g. x-ray photoelectron spectroscopy (XPS), secondary-ion mass spectrometry (SIMS) and quantitative electron energy loss spectroscopy (EELS).

- The effect of thermal treatments (at 550°C in vacuum and N_2/H_2) was studied on compact films deposited at 1 Pa or in vacuum and at laser fluence equal to 2 J/cm^2.

  - XRD analysis revealed TiN films with FCC structure and a slight improvement in crystalline order upon annealing was observed; on the other hand, Raman spectroscopy suggests an increase of surface oxidation. As a consequence, electrical properties did not improve significantly with thermal treatment and the lowest resistivity achieved ($\sim 200\,\mu\Omega cm$) was one order of magnitude higher than good crystalline quality TiN thin films in literature.

  - Thermal treatment resulted a good way to tune optical response of the films, tuning film reflectivity (i.e. reflectance dip and intensity) by acting on free carriers, which depend in turn on oxygen and nitrogen content of the film.

  - The properties extracted from ellipsometric measurements imply that the best metallic behavior is attributed to the vacuum-deposited TiN thin film. The effect of the vacuum thermal treatment consists in an

improvement of plasmonic quality factors, while N_2/H_2-annealing leads to a worsening. In addition, the fitting of N_2/H_2-annealed films do not lead to completely reliable results, suggesting that these films cannot be modeled as a two-layer (i.e. TiN film covered by a TiO_2 layer), but more likely a titanium oxynitride phase is present for the whole thickness.

- The effect of thermal treatments (i.e. in N_2/H_2 at 300 and 550°C, in vacuum at 550°C) was studied on nanoporous films, and the annealing at 300°C resulted effective for films deposited at 10 and 20 Pa, implying higher TiN crystallization and a reduced oxidation.

- Preliminary results of the effect of substrate heating during deposition of both compact and nanoporous films were shown, resulting a more promising approach in finely tuning the crystalline structure than post-deposition thermal treatments. For compact thin films, degree of crystallinity was found to increase with substrate temperature; for nanoporous films, the morphology of TiN NP assemblies becomes less fluffy, promoting strong NPs sintering.

Finally, perspectives of this study involve:

- Further studies on stoichiometry/composition of both compact and nanoporous TiN thin films by different techniques (e.g. depth profiling XPS, SIMS or Rutherford backscattering spectrometry) in order to better understanding the optical and electrical measurements of the films.

- Thermal treatments of compact TiN thin films at higher temperature in vacuum (which demonstrated to be more promising in the plasmonic response while bringing less oxidation than N_2/H_2-annealing) to achieve more effective tuning of crystalline structure.

- Synthesis of compact TiN thin films via nitrogen ion assisted pulsed laser deposition (or ion beam assisted deposition, IBAD), which has been already employed coupled with magnetron sputtering [309–311], while it is totally new in PLD synthesis. The aim is to tune the composition, structure and crystalline properties of the samples by controlling ion species, current (i.e. the number of ions colliding with the sample per unit time) and the kinetic energy of the ions. In addition, the employment of N ions can allow their implantation in the TiN films, leading to further stoichiometric control.

- Systematic investigation about the effect of thickness on TiN films, down to ultra-thin films (i.e. <10 nm), which is of great interest in plasmonic applications. In particular, compact TiN thin films have already demonstrated to have plasmonic properties tunable by thickness at few nanometers [312], and this fascinating property can be attractive for sub-wavelength optical structures (i.e. metamaterials) and nanoelectronics.

CHAPTER 7

Conclusions and perspectives

This PhD project was aimed to the development and investigation of nanostructured thin films based on titanium oxides and nitrides, focused to achieve a fine control of their physical properties (i.e. morphology, structure, composition) as well as the understanding of the material optical and electrical behavior and their potential application in the plasmonic field. The specific systems investigated were: Au NPs integrated with TiO_2 nanostructured thin films (aimed to enhance light harvesting of the oxide for photoanode applications) and thin films and NPs assemblies based on alternative plasmonic materials, namely Ta:TiO_2 and TiN. These systems were grown via physical vapor deposition techniques, in particular pulsed laser deposition (PLD), followed by post-deposition thermal treatments to crystallize the materials in the desired phase, or to modify their functional properties. The properties of the obtained systems were studied with a focus on the optical and electrical response and their relation with the system structure, from atomic to nano/masoscale, aimed to understand and to optimize the system behavior in view of possible plasmonic applications, such as sensing, surface enhanced Raman scattering (SERS) and photoconversion. The main achievements for each system are here listed:

1. Au NPs integrated with TiO_2 hierarchical films

- The integration was successfully realized with an original single-step pulsed lased co-deposition procedure, leading to Au NPs homogeneously dispersed through the whole thickness of the TiO_2 film.

- The control of process parameters allowed a fine tuning of film properties in terms of porosity, crystalline structure as well as Au NP size and number density, which in turn affect the optical response of the entire Au-TiO_2 system, giving the possibility of controlling Au NP plasmonic resonance over a certain wavelength range.

- The high porosity was interesting for several applications, indeed preliminary tests of photocatalysis and SERS experiments have been performed in collaboration with external research groups, leading to promising results.

2. Ta:TiO$_2$ thin films

After the first step of optimization of the synthesis parameters to find the conditions for the most conductive Ta:TiO$_2$ thin films (for Ta content of 5% at., the lowest resistivity was found equal to $8 \cdot 10^{-4} \, \Omega cm$), the film properties were studied as a function of Ta content and thickness (down to ultrathin films), with a focus on the understanding of electrical and optical behavior.

- Conductive films were obtained down to 10 nm-thickness (i.e. resistivity of $0.5 \, \Omega cm$), usually unaffordable for metals, but particularly attractive for sub-wavelength optical structures and nanoelectronics.

- The high dopant activation efficiency demonstrated by Ta-doping offers the possibility of fine tuning both electrical and optical properties by handling Ta content. Indeed, the charge carrier density was measured equal to $9.95 \cdot 10^{20} \, cm^{-3}$ and $1.65 \cdot 10^{21} \, cm^{-3}$ for 5 and 10% at. respectively, while affecting optical band gap (from 3.29 eV for bare TiO$_2$ to 3.48 and 3.56 for Ta 5 and 10% at. respectively) and effective mass (calculated in the range of 2.19-3.6 m_e and 3.18-4.5 m_e for Ta 5 and 10% at. respectively).

- The plasma frequency of Ta:TiO$_2$ films was estimated to be in the near/mid-IR range, paving the way to IR plasmonic applications, difficult to reach for metals.

Then, complex Ta:TiO$_2$-based systems were developed:

- Au NPs were integrated with compact Ta:TiO$_2$ thin films, with the aim to tune the plasmonic response of Au NPs by changing the dielectric constant of the surrounding matrix. As main results, the Au NPs resonance peak resulted tunable in the range of 550-800 nm by the type of integration configuration and by the doping content of the surrounding matrix.

- A first exploration of the development of Ta:TiO$_2$ NPs assemblies in thin films was performed, by exploiting the advantage of PLD in which the in-plume clusters formation can be triggered by an increase in the background pressure of deposition. NPs with a size of tens nm were obtained, however some issues occurred for the crystallization and no evidence of successful doping was observed.

3. TiN thin films

- The correlation between synthesis process parameters with morphology (from compact-columnar to nanoporous tree-like and to foam-like) and stoichiometry/composition was established, while the oxidation-issue was handled with different strategies depending on film morphology.

- Nanoporous hierarchical films formed by titanium nitride (or titanium oxynitride, TiO_xN_y) NPs assemblies were successfully obtained thanks to a specific investigation on PLD mechanisms in TiN synthesis with in-situ characterization techniques (available at CNMS), and this kind of morphology is quite new in the plasmonic framework.

- For particular synthesis conditions, the obtained TiO_xN_y NPs assemblies exhibit an excellent broadband absorption along a wide optical range (i.e. absorbance >90% in the range 270-2000 nm), currently achieved only by very complex TiN-based systems and promising for application such as solar energy harvesting and hot electron devices.

- The employed post-deposition thermal treatments promoted a slight crystallization of the films, while substrate heating during deposition showed to be more effective on the crystal structure. On the other hand, the post-annealing resulted a good way to tune optical response of the films, by acting on free carriers, which depend in turn on oxygen and nitrogen content. From the properties extracted from ellipsometric measurements, the vacuum thermal treatment appears to improve the plasmonic response of the film, while N_2/H_2-annealing leads to a worsening (likely because of partial oxidation and TiO_xN_y phase formation).

Finally, perspectives of this work are listed according to the type of system:

1. **Au NPs integrated with TiO_2 hierarchical films**

- The potentiality of the employed integration approach can be extended to other NP/oxide systems with controlled properties thanks to the versatility of the laser ablation process.

- Au-TiO_2 systems can be exploited for other plasmonic applications, especially those requiring nanoscale porosity and light scattering, such as chemical sensors and photovoltaics. In addition, these systems are a promising SERS substrate to detect molecules that cannot bind directly to Au NPs, but to TiO_2 (e.g. silane molecules).

2. **Ta:TiO_2 thin films**

- The plasmonic quality factors need to be evaluated in the range of the plasmonic response (near- and mid-IR) in view of possible applications. In addition, the estimated quality factors can be a guideline to a further optimization of film synthesis conditions and properties.

- The electrical properties of ultrathin films can be further explored by depositing on different substrates. For example a buffer layer of insulating TiO_2 over the glass substrate can improve electrical response and allow the deposition of even thinner films (i.e. <10 nm).

- The influence of the Ta:TiO_2 matrix on the plasmonic properties of Au NPs in Au NPs-compact Ta:TiO_2 systems needs to be clarified, for example by

employing effective medium theories and pump probe measurements, which probe the dynamics of a possible charge transfer between the two materials. Indeed, the increase of chemical potential of Ta:TiO$_2$ due to doping may promote a charge carrier accumulation on the Au NPs, leading to the observed blue-shift of the plasmonic resonance. In addition, these systems enable the possibility of tuning of Au NPs plasmonic resonance by active modulation of the dielectric constant of the surrounding TCO by means of external stimuli such as the application of an electric field.

- To obtain plasmonic Ta:TiO$_2$ NPs with controlled localized surface plasmon resonance (LSPR), the crystalline structure needs to be improved and the doping activation needs to be verified. For these purposes, different background gasses and mixtures during deposition and different annealing cycles can be performed. Finally, a capping layer can be employed in order to protect Ta:TiO$_2$ NPs assemblies from the highly reducing environment during the annealing treatment.

3. TiN thin films

- Deeper study of stoichiometry/composition in nanoporous films are needed, aimed to a better understanding of the role of oxygen (i.e. bonded or adsorbed) as well as the oxidation process (both during deposition and upon air exposure), by means of precise techniques such as x-ray photoelectron spectroscopy (XPS), secondary-ion mass spectrometry (SIMS), electron energy loss spectroscopy (EELS) and in-situ Raman spectroscopy.

- Exploring of other synthesis conditions for compact TiN thin films, such as thermal treatments at higher temperature and ion assisted pulsed laser deposition (employing nitrogen ions), which allows an additional control on composition and structure of the deposited films.

- Systematic study of the effect of film thickness on optical and electrical properties down to ultrathin films.

Finally, thin and ultrathin films of both Ta:TiO$_2$ and TiN would be employed for the development of sub-wavelength optical structures, i.e. metameterials and metasurfaces, and nanoelectronics. In addition, in a long-term view, being both these materials a good alternative to metals in several plasmonic applications (e.g. in IR and high temperature/power plasmonics), it will be necessary to design devices which incorporate them by means of scalable synthesis techniques and common microfabrication processes.

This PhD project fit into the context of the research of new materials and new combinations of materials for applications in the plasmonic field, aimed to enhance the plasmonic response of already existing devices and to pave the way to other applications that are unaffordable by traditional plasmonic systems. As a continuation of this line of research, other materials can be explored, both TCOs (e.g. CdO-based and Ga$_2$FeO$_4$, a p-type semiconductor which in principle can excite surface plasmon polaritons in near-IR) and metal nitrides (e.g ZrN,

HfN and ternary conductive nitrides, composed by nitrides of the group IVb, Vb and VIb metals, which result in some cases more stable and with less structural defects than binary nitrides). Moreover, the thin films studied in this work can be employed to develop multilayer systems when combined with thin layers of dielectric materials that provide lattice matching, for example TiO_2 for $Ta:TiO_2$ and AlN for TiN, aimed to develop hyperbolic metameterials with engineered optical response.

List of Figures

List of Tables

Bibliography

[1] C. Kittel, P. McEuen, and P. McEuen, *Introduction to solid state physics*, vol. 8. Wiley New York, 1996.

[2] J. M. Ziman, *Principles of the Theory of Solids*. Cambridge university press, 1972.

[3] A. W, N. Ashcroft, N. Mermin, N. Mermin, and B. P. Company, *Solid State Physics*. HRW international editions, Holt, Rinehart and Winston, 1976.

[4] S. V. Gaponenko, *Introduction to nanophotonics*. Cambridge University Press, 2010.

[5] S. A. Maier, *Plasmonics: fundamentals and applications*. Springer Science & Business Media, 2007.

[6] M. P. Givens, "Optical properties of metals," in *Solid state physics*, vol. 6, pp. 313–352, Elsevier, 1958.

[7] P. B. Johnson and R.-W. Christy, "Optical constants of the noble metals," *Physical review B*, vol. 6, no. 12, p. 4370, 1972.

[8] R. P. Prasankumar and A. J. Taylor, *Optical techniques for solid-state materials characterization*. CRC Press, 2016.

[9] L. Mascaretti, A. Dutta, Š. Kment, V. M. Shalaev, A. Boltasseva, R. Zbořil, and A. Naldoni, "Plasmon-enhanced photoelectrochemical water splitting for efficient renewable energy storage," *Advanced Materials*, vol. 31, no. 31, p. 1805513, 2019.

[10] J. Zhang, L. Zhang, and W. Xu, "Surface plasmon polaritons: physics and applications," *Journal of Physics D: Applied Physics*, vol. 45, no. 11, p. 113001, 2012.

[11] P. Zhang, T. Wang, and J. Gong, "Mechanistic understanding of the plasmonic enhancement for solar water splitting," *Advanced Materials*, vol. 27, no. 36, pp. 5328–5342, 2015.

[12] U. Kreibig and M. Vollmer, *Optical properties of metal clusters*, vol. 25. Springer Science & Business Media, 2013.

[13] S. Linic, U. Aslam, C. Boerigter, and M. Morabito, "Photochemical transformations on plasmonic metal nanoparticles," *Nature materials*, vol. 14, no. 6, pp. 567–576, 2015.

[14] K. L. Kelly, E. Coronado, L. L. Zhao, and G. C. Schatz, "The optical properties of metal nanoparticles: the influence of size, shape, and dielectric environment," 2003.

[15] V. Amendola, R. Pilot, M. Frasconi, O. M. Maragò, and M. A. Iatì, "Surface plasmon resonance in gold nanoparticles: a review," *Journal of Physics: Condensed Matter*, vol. 29, no. 20, p. 203002, 2017.

[16] L. M. Liz-Marzán, "Tailoring surface plasmons through the morphology and assembly of metal nanoparticles," *Langmuir*, vol. 22, no. 1, pp. 32–41, 2006.

[17] A. Kinkhabwala, Z. Yu, S. Fan, Y. Avlasevich, K. Müllen, and W. Moerner, "Large single-molecule fluorescence enhancements produced by a bowtie nanoantenna," *Nature Photonics*, vol. 3, no. 11, pp. 654–657, 2009.

[18] C. Clavero, "Plasmon-induced hot-electron generation at nanoparticle/metal-oxide interfaces for photovoltaic and photocatalytic devices," *Nature Photonics*, vol. 8, no. 2, pp. 95–103, 2014.

[19] S. Mubeen, G. Hernandez-Sosa, D. Moses, J. Lee, and M. Moskovits, "Plasmonic photosensitization of a wide band gap semiconductor: converting plasmons to charge carriers," *Nano letters*, vol. 11, no. 12, pp. 5548–5552, 2011.

[20] E. Heilweil and R. Hochstrasser, "Nonlinear spectroscopy and picosecond transient grating study of colloidal gold," *The Journal of chemical physics*, vol. 82, no. 11, pp. 4762–4770, 1985.

[21] T. Klar, M. Perner, S. Grosse, G. Von Plessen, W. Spirkl, and J. Feldmann, "Surface-plasmon resonances in single metallic nanoparticles," *Physical Review Letters*, vol. 80, no. 19, p. 4249, 1998.

[22] I. V. Bondarev and V. M. Shalaev, "Universal features of the optical properties of ultrathin plasmonic films," *Optical Materials Express*, vol. 7, no. 10, pp. 3731–3740, 2017.

[23] S. A. Maier and H. A. Atwater, "Plasmonics: Localization and guiding of electromagnetic energy in metal/dielectric structures," *Journal of applied physics*, vol. 98, no. 1, p. 10, 2005.

[24] P. Anger, P. Bharadwaj, and L. Novotny, "Enhancement and quenching of single-molecule fluorescence," *Physical review letters*, vol. 96, no. 11, p. 113002, 2006.

[25] S. Schietinger, M. Barth, T. Aichele, and O. Benson, "Plasmon-enhanced single photon emission from a nanoassembled metal- diamond hybrid structure at room temperature," *Nano letters*, vol. 9, no. 4, pp. 1694–1698, 2009.

[26] D. O. Melville, R. J. Blaikie, and C. R. Wolf, "Submicron imaging with a planar silver lens," *Applied Physics Letters*, vol. 84, no. 22, pp. 4403–4405, 2004.

[27] M. Svedendahl, S. Chen, A. Dmitriev, and M. Kall, "Refractometric sensing using propagating versus localized surface plasmons: a direct comparison," *Nano letters*, vol. 9, no. 12, pp. 4428–4433, 2009.

[28] K. Saha, S. S. Agasti, C. Kim, X. Li, and V. M. Rotello, "Gold nanoparticles in chemical and biological sensing," *Chemical reviews*, vol. 112, no. 5, pp. 2739–2779, 2012.

[29] M. Jahn, S. Patze, I. J. Hidi, R. Knipper, A. I. Radu, A. Mühlig, S. Yüksel, V. Peksa, K. Weber, T. Mayerhöfer, *et al.*, "Plasmonic nanostructures for surface enhanced spectroscopic methods," *Analyst*, vol. 141, no. 3, pp. 756–793, 2016.

[30] R. Carles, M. Bayle, P. Benzo, G. Benassayag, C. Bonafos, G. Cacciato, and V. Privitera, "Plasmon-resonant raman spectroscopy in metallic nanoparticles: Surface-enhanced scattering by electronic excitations," *Physical Review B*, vol. 92, no. 17, p. 174302, 2015.

[31] S. A. Maier, P. G. Kik, H. A. Atwater, S. Meltzer, E. Harel, B. E. Koel, and A. A. Requicha, "Local detection of electromagnetic energy transport below the diffraction limit in metal nanoparticle plasmon waveguides," *Nature materials*, vol. 2, no. 4, pp. 229–232, 2003.

[32] H. A. Atwater and A. Polman, "Plasmonics for improved photovoltaic devices," in *Materials for Sustainable Energy: A Collection of Peer-Reviewed Research and Review Articles from Nature Publishing Group*, pp. 1–11, World Scientific, 2011.

[33] P. R. West, S. Ishii, G. V. Naik, N. K. Emani, V. M. Shalaev, and A. Boltasseva, "Searching for better plasmonic materials," *Laser & Photonics Reviews*, vol. 4, no. 6, pp. 795–808, 2010.

[34] M. Rycenga, C. M. Cobley, J. Zeng, W. Li, C. H. Moran, Q. Zhang, D. Qin, and Y. Xia, "Controlling the synthesis and assembly of silver nanostructures for plasmonic applications," *Chemical reviews*, vol. 111, no. 6, pp. 3669–3712, 2011.

[35] M.-C. Daniel and D. Astruc, "Gold nanoparticles: assembly, supramolecular chemistry, quantum-size-related properties, and applications toward biology, catalysis, and nanotechnology," *Chemical reviews*, vol. 104, no. 1, pp. 293–346, 2004.

[36] J. A. Schuller, E. S. Barnard, W. Cai, Y. C. Jun, J. S. White, and M. L. Brongersma, "Plasmonics for extreme light concentration and manipulation," *Nature materials*, vol. 9, no. 3, pp. 193–204, 2010.

[37] K. Catchpole, , and A. Polman, "Plasmonic solar cells," *Optics express*, vol. 16, no. 26, pp. 21793–21800, 2008.

[38] D. B. Ingram, P. Christopher, J. L. Bauer, and S. Linic, "Predictive model for the design of plasmonic metal/semiconductor composite photocatalysts," *Acs Catalysis*, vol. 1, no. 10, pp. 1441–1447, 2011.

[39] A. Naldoni, F. Riboni, U. Guler, A. Boltasseva, V. M. Shalaev, and A. V. Kildishev, "Solar-powered plasmon-enhanced heterogeneous catalysis," *Nanophotonics*, vol. 5, no. 1, pp. 112–133, 2016.

[40] J. Li, S. K. Cushing, F. Meng, T. R. Senty, A. D. Bristow, and N. Wu, "Plasmon-induced resonance energy transfer for solar energy conversion," *Nature Photonics*, vol. 9, no. 9, pp. 601–607, 2015.

[41] H. Inouye, K. Tanaka, I. Tanahashi, and K. Hirao, "Ultrafast dynamics of nonequilibrium electrons in a gold nanoparticle system," *Physical Review B*, vol. 57, no. 18, p. 11334, 1998.

[42] F. Ladstädter, U. Hohenester, P. Puschnig, and C. Ambrosch-Draxl, "First-principles calculation of hot-electron scattering in metals," *Physical Review B*, vol. 70, no. 23, p. 235125, 2004.

[43] E. Thimsen, F. Le Formal, M. Gratzel, and S. C. Warren, "Influence of plasmonic Au nanoparticles on the photoactivity of Fe2O3 electrodes for water splitting," *Nano letters*, vol. 11, no. 1, pp. 35–43, 2011.

[44] I. Thomann, B. A. Pinaud, Z. Chen, B. M. Clemens, T. F. Jaramillo, and M. L. Brongersma, "Plasmon enhanced solar-to-fuel energy conversion," *Nano letters*, vol. 11, no. 8, pp. 3440–3446, 2011.

[45] T. Torimoto, H. Horibe, T. Kameyama, K.-i. Okazaki, S. Ikeda, M. Matsumura, A. Ishikawa, and H. Ishihara, "Plasmon-enhanced photocatalytic activity of cadmium sulfide nanoparticle immobilized on silica-coated gold particles," *The journal of physical chemistry letters*, vol. 2, no. 16, pp. 2057–2062, 2011.

[46] D. B. Ingram and S. Linic, "Water splitting on composite plasmonic-metal/semiconductor photoelectrodes: evidence for selective plasmon-induced formation of charge carriers near the semiconductor surface," *Journal of the American Chemical Society*, vol. 133, no. 14, pp. 5202–5205, 2011.

[47] S. K. Cushing, J. Li, F. Meng, T. R. Senty, S. Suri, M. Zhi, M. Li, A. D. Bristow, and N. Wu, "Photocatalytic activity enhanced by plasmonic resonant energy transfer from metal to semiconductor," *Journal of the American Chemical Society*, vol. 134, no. 36, pp. 15033–15041, 2012.

[48] J. S. DuChene, B. P. Williams, A. C. Johnston-Peck, J. Qiu, M. Gomes, M. Amilhau, D. Bejleri, J. Weng, D. Su, F. Huo, *et al.*, "Elucidating the sole contribution from electromagnetic near-fields in plasmon-enhanced Cu2O photocathodes," *Advanced Energy Materials*, vol. 6, no. 1, p. 1501250, 2016.

[49] J. K. Kim, X. Shi, M. J. Jeong, J. Park, H. S. Han, S. H. Kim, Y. Guo, T. F. Heinz, S. Fan, C.-L. Lee, *et al.*, "Enhancing Mo: BiVO4 solar water splitting with patterned au nanospheres by plasmon-induced energy transfer," *Advanced Energy Materials*, vol. 8, no. 5, p. 1701765, 2018.

[50] M. Valenti, E. Kontoleta, I. A. Digdaya, M. P. Jonsson, G. Biskos, A. Schmidt-Ott, and W. A. Smith, "The role of size and dimerization of decorating plasmonic silver nanoparticles on the photoelectrochemical solar water splitting performance of BiVO4 photoanodes," *ChemNanoMat*, vol. 2, no. 7, pp. 739–747, 2016.

[51] L. Zhang, L. O. Herrmann, and J. J. Baumberg, "Size dependent plasmonic effect on BiVO4 photoanodes for solar water splitting," *Scientific reports*, vol. 5, no. 1, pp. 1–12, 2015.

[52] P. Peerakiatkhajohn, T. Butburee, J.-H. Yun, H. Chen, R. M. Richards, and L. Wang, "A hybrid photoelectrode with plasmonic Au@TiO2 nanoparticles for enhanced photoelectrochemical water splitting," *Journal of Materials Chemistry A*, vol. 3, no. 40, pp. 20127–20133, 2015.

[53] T. Wang, R. Lv, P. Zhang, C. Li, and J. Gong, "Au nanoparticle sensitized ZnO nanopencil arrays for photoelectrochemical water splitting," *Nanoscale*, vol. 7, no. 1, pp. 77–81, 2015.

[54] S. C. Warren and E. Thimsen, "Plasmonic solar water splitting," *Energy & Environmental Science*, vol. 5, no. 1, pp. 5133–5146, 2012.

[55] H. Tang, K. Prasad, R. Sanjines, P. Schmid, and F. Levy, "Electrical and optical properties of TiO2 anatase thin films," *Journal of applied physics*, vol. 75, no. 4, pp. 2042–2047, 1994.

[56] A. Primo, A. Corma, and H. García, "Titania supported gold nanoparticles as photocatalyst," *Physical Chemistry Chemical Physics*, vol. 13, no. 3, pp. 886–910, 2011.

[57] Y. Tian and T. Tatsuma, "Plasmon-induced photoelectrochemistry at metal nanoparticles supported on nanoporous tio 2," *Chemical communications*, no. 16, pp. 1810–1811, 2004.

163

[58] Y. Tian and T. Tatsuma, "Mechanisms and applications of plasmon-induced charge separation at TiO2 films loaded with gold nanoparticles," *Journal of the American Chemical Society*, vol. 127, no. 20, pp. 7632–7637, 2005.

[59] F. Su, T. Wang, R. Lv, J. Zhang, P. Zhang, J. Lu, and J. Gong, "Dendritic Au/TiO2 nanorod arrays for visible-light driven photoelectrochemical water splitting," *Nanoscale*, vol. 5, no. 19, pp. 9001–9009, 2013.

[60] M. S. Rodrigues, D. Costa, R. Domingues, M. Apreutesei, P. Pedrosa, N. Martin, V. Correlo, R. Reis, E. Alves, N. Barradas, *et al.*, "Optimization of nanocomposite Au/TiO2 thin films towards lspr optical-sensing," *Applied Surface Science*, vol. 438, pp. 74–83, 2018.

[61] V. M. Shalaev, "Transforming light," *Science*, pp. 384–386, 2008.

[62] H. Chen, C. T. Chan, and P. Sheng, "Transformation optics and metamaterials," *Nature materials*, vol. 9, no. 5, pp. 387–396, 2010.

[63] M. Kauranen and A. V. Zayats, "Nonlinear plasmonics," *Nature photonics*, vol. 6, no. 11, pp. 737–748, 2012.

[64] T. Hanke, G. Krauss, D. Träutlein, B. Wild, R. Bratschitsch, and A. Leitenstorfer, "Efficient nonlinear light emission of single gold optical antennas driven by few-cycle near-infrared pulses," *Physical Review Letters*, vol. 103, no. 25, p. 257404, 2009.

[65] J. B. Khurgin, "How to deal with the loss in plasmonics and metamaterials," *Nature nanotechnology*, vol. 10, no. 1, pp. 2–6, 2015.

[66] G. V. Naik, V. M. Shalaev, and A. Boltasseva, "Alternative plasmonic materials: beyond gold and silver," *Advanced Materials*, vol. 25, no. 24, pp. 3264–3294, 2013.

[67] P. Clegg, "The optical constants of thin metallic films deposited by evaporation," *Proceedings of the Physical Society. Section B*, vol. 65, no. 10, p. 774, 1952.

[68] L. Yau and C. Sah, "Measurement of trapped-minority-carrier thermal emission rates from Au, Ag, and Co traps in silicon," *Applied Physics Letters*, vol. 21, no. 4, pp. 157–158, 1972.

[69] G. V. Naik, J. Kim, and A. Boltasseva, "Oxides and nitrides as alternative plasmonic materials in the optical range," *Optical materials express*, vol. 1, no. 6, pp. 1090–1099, 2011.

[70] I. Kriegel, F. Scotognella, and L. Manna, "Plasmonic doped semiconductor nanocrystals: Properties, fabrication, applications and perspectives," *Physics Reports*, vol. 674, pp. 1–52, 2017.

[71] D. H. Kim, S. Lee, J. H. Park, J. H. Noh, I. J. Park, W. M. Seong, and K. S. Hong, "Transmittance optimized Nb-doped TiO2/Sn-doped In2O3 multilayered photoelectrodes for dye-sensitized solar cells," *Solar energy materials and solar cells*, vol. 96, pp. 276–280, 2012.

[72] S. Dias, S. Chirakkara, N. Patel, and S. Krupanidhi, "Gallium and indium co-doped ZnO as a transparent conducting oxide for Cu2SnS3 photodetectors," *Journal of Materials Science: Materials in Electronics*, vol. 29, no. 3, pp. 2131–2139, 2018.

[73] T. Hanada, T. Negishi, I. Shiroishi, and T. Shiro, "Plastic substrate with gas barrier layer and transparent conductive oxide thin film for flexible displays," *Thin Solid Films*, vol. 518, no. 11, pp. 3089–3092, 2010.

[74] S. H. Park, J. B. Park, and P. K. Song, "Characteristics of Al-doped, Ga-doped and In-doped zinc-oxide films as transparent conducting electrodes in organic light-emitting diodes," *Current Applied Physics*, vol. 10, no. 3, pp. S488–S490, 2010.

[75] S. C. Dixon, D. O. Scanlon, C. J. Carmalt, and I. P. Parkin, "n-type doped transparent conducting binary oxides: an overview," *Journal of Materials Chemistry C*, vol. 4, no. 29, pp. 6946–6961, 2016.

[76] A. Agrawal, R. W. Johns, and D. J. Milliron, "Control of localized surface plasmon resonances in metal oxide nanocrystals," *Annual Review of Materials Research*, vol. 47, pp. 1–31, 2017.

[77] P. Patsalas, N. Kalfagiannis, and S. Kassavetis, "Optical properties and plasmonic performance of titanium nitride," *Materials*, vol. 8, no. 6, pp. 3128–3154, 2015.

[78] P. Patsalas, N. Kalfagiannis, S. Kassavetis, G. Abadias, D. Bellas, C. Lekka, and E. Lidorikis, "Conductive nitrides: Growth principles, optical and electronic properties, and their perspectives in photonics and plasmonics," *Materials Science and Engineering: R: Reports*, vol. 123, pp. 1–55, 2018.

[79] F. Wang, M. Wu, Y. Wang, Y. Yu, X. Wu, and L. Zhuge, "Influence of thickness and annealing temperature on the electrical, optical and structural properties of AZO thin films," *Vacuum*, vol. 89, pp. 127–131, 2013.

[80] G. Wan, S. Wang, X. Zhang, M. Huang, Y. Zhang, W. Duan, and L. Yi, "Transparent conductive Nb-doped TiO2 films deposited by rf magnetron co-sputtering," *Applied Surface Science*, vol. 357, pp. 622–625, 2015.

[81] R. Moss, E. Tzimas, H. Kara, P. Willis, and J. Kooroshy, "Critical metals in strategic energy technologies," *Publications Office of the European Union, Luxembourg*, 2011.

[82] E. Burstein, "Anomalous optical absorption limit in InSb," *Physical Review*, vol. 93, no. 3, p. 632, 1954.

[83] B. E. Sernelius, K.-F. Berggren, Z.-C. Jin, I. Hamberg, and C. G. Granqvist, "Band-gap tailoring of ZnO by means of heavy al doping," *Physical Review B*, vol. 37, no. 17, p. 10244, 1988.

[84] D. S. Ginley, H. Hosono, and D. C. Paine, *Handbook of transparent conductors*. Springer Science & Business Media, 2010.

[85] R. G. Gordon, "Criteria for choosing transparent conductors," *MRS bulletin*, vol. 25, no. 8, pp. 52–57, 2000.

[86] T. J. Coutts, D. L. Young, and X. Li, "Characterization of transparent conducting oxides," *Mrs Bulletin*, vol. 25, no. 8, pp. 58–65, 2000.

[87] K. Ellmer, "Past achievements and future challenges in the development of optically transparent electrodes," *Nature Photonics*, vol. 6, no. 12, pp. 809–817, 2012.

[88] J. A. Nelson, *The physics of solar cells*. World Scientific Publishing Company, 2003.

[89] S. Franzen, "Surface plasmon polaritons and screened plasma absorption in indium tin oxide compared to silver and gold," *The Journal of Physical Chemistry C*, vol. 112, no. 15, pp. 6027–6032, 2008.

[90] C. Rhodes, M. Cerruti, A. Efremenko, M. Losego, D. Aspnes, J.-P. Maria, and S. Franzen, "Dependence of plasmon polaritons on the thickness of indium tin oxide thin films," *Journal of Applied Physics*, vol. 103, no. 9, p. 093108, 2008.

[91] C. Rhodes, S. Franzen, J.-P. Maria, M. Losego, D. N. Leonard, B. Laughlin, G. Duscher, and S. Weibel, "Surface plasmon resonance in conducting metal oxides," *Journal of Applied Physics*, vol. 100, no. 5, p. 054905, 2006.

[92] M. Noginov, L. Gu, J. Livenere, G. Zhu, A. Pradhan, R. Mundle, M. Bahoura, Y. A. Barnakov, and V. Podolskiy, "Transparent conductive oxides: Plasmonic materials for telecom wavelengths," *Applied Physics Letters*, vol. 99, no. 2, p. 021101, 2011.

[93] J. Kim, G. V. Naik, N. K. Emani, U. Guler, and A. Boltasseva, "Plasmonic resonances in nanostructured transparent conducting oxide films," *IEEE Journal of Selected Topics in Quantum Electronics*, vol. 19, no. 3, pp. 4601907–4601907, 2013.

[94] E. Della Gaspera, A. S. Chesman, J. van Embden, and J. J. Jasieniak, "Non-injection synthesis of doped zinc oxide plasmonic nanocrystals," *ACS nano*, vol. 8, no. 9, pp. 9154–9163, 2014.

[95] E. Feigenbaum, K. Diest, and H. A. Atwater, "Unity-order index change in transparent conducting oxides at visible frequencies," *Nano letters*, vol. 10, no. 6, pp. 2111–2116, 2010.

[96] Z. Yang, S. Han, T. Yang, L. Ye, H. Ma, and C. Cheng, "ITO films deposited on water-cooled flexible substrate by bias rf magnetron sputtering," *Applied surface science*, vol. 161, no. 1-2, pp. 279–285, 2000.

[97] S. Fernández, A. Martínez-Steele, J. Gandia, and F. Naranjo, "Radio frequency sputter deposition of high-quality conductive and transparent ZnO:Al films on polymer substrates for thin film solar cells applications," *Thin Solid Films*, vol. 517, no. 10, pp. 3152–3156, 2009.

[98] R. Kamakura, T. Takeishi, S. Murai, K. Fujita, and K. Tanaka, "Surface-enhanced infrared absorption for the periodic array of indium tin oxide and gold microdiscs: Effect of in-plane light diffraction," *ACS Photonics*, vol. 5, no. 7, pp. 2602–2608, 2018.

[99] C. Chen and H. Ye, "Fabrication and optimization of ITO-Ag co-sputtered nanocomposite films as plasmonic materials in the near-infrared region," in *Photonic and Phononic Properties of Engineered Nanostructures VII*, vol. 10112, p. 101121I, International Society for Optics and Photonics, 2017.

[100] C. K. Chew, C. Salcianu, P. Bishop, C. J. Carmalt, and I. P. Parkin, "Functional thin film coatings incorporating gold nanoparticles in a transparent conducting fluorine doped tin oxide matrix," *Journal of Materials Chemistry C*, vol. 3, no. 5, pp. 1118–1125, 2015.

[101] V. Cantale, F. C. Simeone, R. Gambari, and M. A. Rampi, "Gold nano-islands on FTO as plasmonic nanostructures for biosensors," *Sensors and Actuators B: Chemical*, vol. 152, no. 2, pp. 206–213, 2011.

[102] G. Ruffato, D. Garoli, S. Cattarin, S. Barison, M. Natali, P. Canton, A. Benedetti, D. De Salvador, and F. Romanato, "Patterned nanoporous-gold thin layers: Structure control and tailoring of plasmonic properties," *Microporous and mesoporous materials*, vol. 163, pp. 153–159, 2012.

[103] P.-S. Huang, D. Hoe Kim, and J.-K. Lee, "Electron emission of Au nanoparticles embedded in ZnO for highly conductive oxide," *Applied Physics Letters*, vol. 104, no. 14, p. 142102, 2014.

[104] M. Huang, Z. Hameiri, H. Gong, W.-C. Wong, A. G. Aberle, and T. Mueller, "Hybrid silver nanoparticle and transparent conductive oxide structure for silicon solar cell applications," *physica status solidi (RRL)–Rapid Research Letters*, vol. 8, no. 5, pp. 399–403, 2014.

[105] A. Hagfeldt, G. Boschloo, L. Sun, L. Kloo, and H. Pettersson, "Dye-sensitized solar cells," *Chemical reviews*, vol. 110, no. 11, pp. 6595–6663, 2010.

[106] T. Bak, J. Nowotny, M. Rekas, and C. Sorrell, "Photo-electrochemical hydrogen generation from water using solar energy. materials-related aspects," *International journal of hydrogen energy*, vol. 27, no. 10, pp. 991–1022, 2002.

[107] A. Fujishima, T. N. Rao, and D. A. Tryk, "Titanium dioxide photocatalysis," *Journal of photochemistry and photobiology C: Photochemistry reviews*, vol. 1, no. 1, pp. 1–21, 2000.

[108] X. Chen and S. S. Mao, "Titanium dioxide nanomaterials: synthesis, properties, modifications, and applications," *Chemical reviews*, vol. 107, no. 7, pp. 2891–2959, 2007.

[109] Y. Furubayashi, T. Hitosugi, Y. Yamamoto, K. Inaba, G. Kinoda, Y. Hirose, T. Shimada, and T. Hasegawa, "A transparent metal: Nb-doped anatase TiO2," *Applied Physics Letters*, vol. 86, no. 25, p. 252101, 2005.

[110] T. Hitosugi, Y. Furubayashi, A. Ueda, K. Itabashi, K. Inaba, Y. Hirose, G. Kinoda, Y. Yamamoto, T. Shimada, and T. Hasegawa, "Ta-doped anatase TiO2 epitaxial film as transparent conducting oxide," *Japanese journal of applied physics*, vol. 44, no. 8L, p. L1063, 2005.

[111] Y. Sato, H. Akizuki, T. Kamiyama, and Y. Shigesato, "Transparent conductive Nb-doped TiO2 films deposited by direct-current magnetron sputtering using a TiO2-x target," *Thin Solid Films*, vol. 516, no. 17, pp. 5758–5762, 2008.

[112] P. Mazzolini, P. Gondoni, V. Russo, D. Chrastina, C. S. Casari, and A. Li Bassi, "Tuning of electrical and optical properties of highly conducting and transparent Ta-doped TiO2 polycrystalline films," *The Journal of Physical Chemistry C*, vol. 119, no. 13, pp. 6988–6997, 2015.

[113] U. Diebold, "The surface science of titanium dioxide," *Surface science reports*, vol. 48, no. 5-8, pp. 53–229, 2003.

[114] M. Landmann, E. Rauls, and W. Schmidt, "The electronic structure and optical response of rutile, anatase and brookite TiO2," *Journal of physics: condensed matter*, vol. 24, no. 19, p. 195503, 2012.

[115] L. Mascaretti, *Hydrogen-treated titanium dioxide hierarchical nanostructures for water splitting applications*. PhD thesis, Italy, 2018.

[116] J. Osorio-Guillén, S. Lany, and A. Zunger, "Atomic control of conductivity versus ferromagnetism in wide-gap oxides via selective doping: V, nb, ta in anatase tio2," *Physical review letters*, vol. 100, no. 3, p. 036601, 2008.

[117] M. Neubert, S. Cornelius, J. Fiedler, T. Gebel, H. Liepack, A. Kolitsch, and M. Vinnichenko, "Overcoming challenges to the formation of high-quality polycrystalline TiO2:Ta transparent conducting films by magnetron sputtering," *Journal of Applied Physics*, vol. 114, no. 8, p. 083707, 2013.

[118] D.-C. Qi, A. R. Barman, L. Debbichi, S. Dhar, I. Santoso, T. C. Asmara, H. Omer, K. Yang, P. Krüger, A. T. Wee, *et al.*, "Cationic vacancies and anomalous spectral-weight transfer in Ti1-xTaxO2 thin films studied via polarization-dependent near-edge x-ray absorption fine structure spectroscopy," *Physical Review B*, vol. 87, no. 24, p. 245201, 2013.

[119] H. Kamisaka, T. Hitosugi, T. Suenaga, T. Hasegawa, and K. Yamashita, "Density functional theory based first-principle calculation of Nb-doped anatase TiO2 and its interactions with oxygen vacancies and interstitial oxygen," *The Journal of chemical physics*, vol. 131, no. 3, p. 034702, 2009.

[120] D.-m. Chen, G. Xu, L. Miao, S. Nakao, and P. Jin, "Sputter deposition and computational study of M-TiO2 (M= Nb, Ta) transparent conducting oxide films," *Surface and Coatings Technology*, vol. 206, no. 5, pp. 1020–1023, 2011.

[121] H. Anh Huy, B. Aradi, T. Frauenheim, and P. Deák, "Comparison of Nb-and Ta-doping of anatase TiO2 for transparent conductor applications," 2012.

[122] H. A. Huy, B. Aradi, T. Frauenheim, and P. Deák, "Calculation of carrier-concentration-dependent effective mass in Nb-doped anatase crystals of TiO2," *Physical Review B*, vol. 83, no. 15, p. 155201, 2011.

[123] Y. Hirose, N. Yamada, S. Nakao, T. Hitosugi, T. Shimada, and T. Hasegawa, "Large electron mass anisotropy in a d-electron-based transparent conducting oxide: Nb-doped anatase TiO2 epitaxial films," *Physical Review B*, vol. 79, no. 16, p. 165108, 2009.

[124] C. J. Dahlman, A. Agrawal, C. M. Staller, J. Adair, and D. J. Milliron, "Anisotropic origins of localized surface plasmon resonance in n-type anatase TiO2 nanocrystals," *Chemistry of Materials*, vol. 31, no. 2, pp. 502–511, 2019.

[125] P. Mazzolini, *Functional properties control of doped TiO2 for transparent electrodes and photoanodes*. PhD thesis, Italy, 2015.

[126] P. Mazzolini, V. Russo, C. S. Casari, T. Hitosugi, S. Nakao, T. Hasegawa, and A. Li Bassi, "Vibrational–electrical properties relationship in donor-doped TiO2 by raman spectroscopy," *The Journal of Physical Chemistry C*, vol. 120, no. 33, pp. 18878–18886, 2016.

[127] P. Mazzolini, T. Acartürk, D. Chrastina, U. Starke, C. S. Casari, G. Gregori, and A. Li Bassi, "Controlling the electrical properties of undoped and Ta-Doped TiO2 polycrystalline films via ultra-fast-annealing treatments," *Advanced Electronic Materials*, vol. 2, no. 3, p. 1500316, 2016.

[128] S. H. Kim, H. Park, K. H. Lee, S. H. Jee, D.-J. Kim, Y. S. Yoon, and H. B. Chae, "Structure and mechanical properties of titanium nitride thin films grown by reactive pulsed laser deposition," *Journal of Ceramic Processing Research*, vol. 10, no. 1, pp. 49–53, 2009.

[129] J. Lackner, W. Waldhauser, R. Berghauser, R. Ebner, B. Major, and T. Schöberl, "Structural, mechanical and tribological investigations of pulsed laser deposited titanium nitride coatings," *Thin Solid Films*, vol. 453, pp. 195–202, 2004.

[130] Z. Peng, H. Miao, L. Qi, S. Yang, and C. Liu, "Hard and wear-resistant titanium nitride coatings for cemented carbide cutting tools by pulsed high energy density plasma," *Acta Materialia*, vol. 51, no. 11, pp. 3085–3094, 2003.

[131] S. Niyomsoan, W. Grant, D. Olson, and B. Mishra, "Variation of color in titanium and zirconium nitride decorative thin films," *Thin Solid Films*, vol. 415, no. 1, pp. 187 – 194, 2002.

[132] T. Tang, C.-C. Wei, R. Haken, T. Holloway, C.-F. Wan, and M. Douglas, "Vlsi local interconnect level using titanium nitride," in *1985 International Electron Devices Meeting*, pp. 590–593, IEEE, 1985.

[133] P. Ruterana, G. Nouet, T. Kehagias, P. Komninou, T. Karakostas, M. di Forte Poisson, F. Huet, and H. Morkoc, "The microstructure of Ti/Al and TiN ohmic contacts to gallium nitride," *physica status solidi (a)*, vol. 176, no. 1, pp. 767–771, 1999.

[134] W. Xiang, Y. Liu, and J. Zhang, "Influence of microstructure on the electrical properties of heteroepitaxial TiN films," *Electronic Materials Letters*, vol. 14, no. 3, pp. 314–318, 2018.

[135] A. Serro, C. Completo, R. Colaço, F. Dos Santos, C. L. Da Silva, J. Cabral, H. Araújo, E. Pires, and B. Saramago, "A comparative study of titanium nitrides, TiN, TiNbN and TiCN, as coatings for biomedical applications," *Surface and Coatings Technology*, vol. 203, no. 24, pp. 3701–3707, 2009.

[136] U. Guler, J. C. Ndukaife, G. V. Naik, A. A. Nnanna, A. V. Kildishev, V. M. Shalaev, and A. Boltasseva, "Local heating with lithographically fabricated plasmonic titanium nitride nanoparticles," *Nano letters*, vol. 13, no. 12, pp. 6078–6083, 2013.

[137] L. Gui, S. Bagheri, N. Strohfeldt, M. Hentschel, C. M. Zgrabik, B. Metzger, H. Linnenbank, E. L. Hu, and H. Giessen, "Nonlinear refractory plasmonics with titanium nitride nanoantennas," *Nano letters*, vol. 16, no. 9, pp. 5708–5713, 2016.

[138] H. Reddy, U. Guler, Z. Kudyshev, A. V. Kildishev, V. M. Shalaev, and A. Boltasseva, "Temperature-dependent optical properties of plasmonic titanium nitride thin films," *ACS photonics*, vol. 4, no. 6, pp. 1413–1420, 2017.

[139] S. Ishii, R. P. Sugavaneshwar, K. Chen, T. D. Dao, and T. Nagao, "Sunlight absorbing titanium nitride nanoparticles," in *2015 17th International Conference on Transparent Optical Networks (ICTON)*, pp. 1–3, IEEE, 2015.

[140] A. Naldoni, U. Guler, Z. Wang, M. Marelli, F. Malara, X. Meng, L. V. Besteiro, A. O. Govorov, A. V. Kildishev, A. Boltasseva, *et al.*, "Broadband hot-electron collection for solar water splitting with plasmonic titanium nitride," *Advanced Optical Materials*, vol. 5, no. 15, p. 1601031, 2017.

[141] D. R. Lide, *CRC handbook of chemistry and physics*, vol. 85. CRC press, 2004.

[142] C. Stampfl, W. Mannstadt, R. Asahi, and A. J. Freeman, "Electronic structure and physical properties of early transition metal mononitrides: Density-functional theory lda, gga, and screened-exchange lda flapw calculations," *Physical Review B*, vol. 63, no. 15, p. 155106, 2001.

[143] Y. Ren, X. Gao, C. Zhang, X. Liu, and S. Sun, "The electronic and elastic properties of Si atom doping in TiN: A first-principles calculation," *Coatings*, vol. 8, no. 1, p. 4, 2018.

[144] S. Logothetidis, I. Alexandrou, and A. Papadopoulos, "In situ spectroscopic ellipsometry to monitor the process of TiNx thin films deposited by reactive sputtering," *Journal of applied physics*, vol. 77, no. 3, pp. 1043–1047, 1995.

[145] U. Guler, V. M. Shalaev, and A. Boltasseva, "Nanoparticle plasmonics: going practical with transition metal nitrides," *Materials Today*, vol. 18, no. 4, pp. 227–237, 2015.

[146] L. Braic, N. Vasilantonakis, A. Mihai, I. J. Villar Garcia, S. Fearn, B. Zou, N. M. Alford, B. Doiron, R. F. Oulton, S. A. Maier, *et al.*, "Titanium oxynitride thin films with tunable double epsilon-near-zero behavior for nanophotonic applications," *ACS applied materials & interfaces*, vol. 9, no. 35, pp. 29857–29862, 2017.

[147] L.-J. Meng and M. Dos Santos, "Characterization of titanium nitride films prepared by dc reactive magnetron sputtering at different nitrogen pressures," *Surface and Coatings Technology*, vol. 90, no. 1-2, pp. 64–70, 1997.

[148] N. Arshi, J. Lu, Y. K. Joo, C. G. Lee, J. H. Yoon, and F. Ahmed, "Study on structural, morphological and electrical properties of sputtered titanium nitride films under different argon gas flow," *Materials Chemistry and Physics*, vol. 134, no. 2-3, pp. 839–844, 2012.

[149] F. Marchetti, M. Dapor, S. Girardi, F. Giacomozzi, and A. Cavalleri, "Physical properties of TiN thin films," *Materials Science and Engineering: A*, vol. 115, pp. 217–221, 1989.

[150] M. B. Lee, M. Kawasaki, M. Yoshimoto, M. Kumagai, and H. Koinuma, "Epitaxial growth of highly crystalline and conductive nitride films by pulsed laser deposition," *Japanese journal of applied physics*, vol. 33, no. 11R, p. 6308, 1994.

[151] R. Chowdhury, R. Vispute, K. Jagannadham, and J. Narayan, "Characteristics of titanium nitride films grown by pulsed laser deposition," *Journal of materials research*, vol. 11, no. 6, pp. 1458–1469, 1996.

[152] I. Mihailescu, E. Gyorgy, N. Chitica, V. Teodorescu, G. Mavin, A. Luches, A. Perrone, M. Martino, and J. Neamtu, "A parametric study of the deposition of the TiN thin films by laser reactive ablation of titanium targets in nitrogen: the roles of the total gas pressure and the contaminations with oxides," *Journal of materials science*, vol. 31, no. 11, pp. 2909–2915, 1996.

[153] R. P. Sugavaneshwar, S. Ishii, T. D. Dao, A. Ohi, T. Nabatame, and T. Nagao, "Fabrication of highly metallic tin films by pulsed laser deposition method for plasmonic applications," *ACS Photonics*, vol. 5, no. 3, pp. 814–819, 2017.

[154] G. V. Naik, J. L. Schroeder, X. Ni, A. V. Kildishev, T. D. Sands, and A. Boltasseva, "Titanium nitride as a plasmonic material for visible and near-infrared wavelengths," *Optical Materials Express*, vol. 2, no. 4, pp. 478–489, 2012.

[155] W. Li, U. Guler, N. Kinsey, G. V. Naik, A. Boltasseva, J. Guan, V. M. Shalaev, and A. V. Kildishev, "Refractory plasmonics with titanium nitride: broadband metamaterial absorber," *Advanced Materials*, vol. 26, no. 47, pp. 7959–7965, 2014.

[156] G. Zhao, T. Zhang, T. Zhang, J. Wang, and G. Han, "Electrical and optical properties of titanium nitride coatings prepared by atmospheric pressure chemical vapor deposition," *Journal of non-crystalline solids*, vol. 354, no. 12-13, pp. 1272–1275, 2008.

[157] A. Lousa, J. Esteve, J. Mejia, and A. Devia, "Influence of deposition pressure on the structural mechanical and decorative properties of tin thin films deposited by cathodic arc evaporation," *Vacuum*, vol. 81, no. 11-12, pp. 1507–1510, 2007.

[158] J. Paulitsch, M. Schenkel, T. Zufraß, P. H. Mayrhofer, and W.-D. Münz, "Structure and properties of high power impulse magnetron sputtering and DC magnetron sputtering crn and tin films deposited in an industrial scale unit," *Thin Solid Films*, vol. 518, no. 19, pp. 5558–5564, 2010.

[159] C. M. Zgrabik and E. L. Hu, "Optimization of sputtered titanium nitride as a tunable metal for plasmonic applications," *Optical Materials Express*, vol. 5, no. 12, pp. 2786–2797, 2015.

[160] H. Gu, K. Leung, C. Chung, and X. Han, "Room-temperature growth of high-purity titanium nitride by laser ablation of titanium in a nitrogen atmosphere," *Surface and Coatings Technology*, vol. 110, no. 3, pp. 153–157, 1998.

[161] R. Krishnan, T. Mathews, A. Balamurugan, S. Dash, A. Tyagi, B. Raj, and V. Jayaram, "Reactive pulsed laser deposition of titanium nitride thin film: Optimization of process parameters using secondary ion mass spectrometry," *Applied surface science*, vol. 256, no. 10, pp. 3077–3080, 2010.

[162] D. Craciun, G. Socol, N. Stefan, G. Dorcioman, M. Hanna, C. Taylor, E. Lambers, and V. Craciun, "The effect of deposition atmosphere on the chemical composition of TiN and ZrN thin films grown by pulsed laser deposition," *Applied Surface Science*, vol. 302, pp. 124–128, 2014.

[163] D. Rasic, R. Sachan, M. F. Chisholm, J. Prater, and J. Narayan, "Room temperature growth of epitaxial titanium nitride films by pulsed laser deposition," *Crystal Growth & Design*, vol. 17, no. 12, pp. 6634–6640, 2017.

[164] J.-S. Chun, P. Desjardins, I. Petrov, J. Greene, C. Lavoie, and C. Cabral Jr, "Interfacial reaction pathways and kinetics during annealing of epitaxial Al/TiN (001) model diffusion barrier systems," *Thin Solid Films*, vol. 391, no. 1, pp. 69–80, 2001.

[165] H. Guo, W. Chen, Y. Shan, W. Wang, Z. Zhang, and J. Jia, "Microstructures and properties of titanium nitride films prepared by pulsed laser deposition at different substrate temperatures," *Applied Surface Science*, vol. 357, pp. 473–478, 2015.

[166] B. Subramanian and M. Jayachandran, "Characterization of reactive magnetron sputtered nanocrystalline titanium nitride (TiN) thin films with brush plated Ni interlayer," *Journal of applied electrochemistry*, vol. 37, no. 9, pp. 1069–1075, 2007.

[167] A. Tarniowy, R. Mania, and M. Rekas, "The effect of thermal treatment on the structure, optical and electrical properties of amorphous titanium nitride thin films," *Thin Solid Films*, vol. 311, no. 1-2, pp. 93–100, 1997.

[168] Y. Xi, H. Fan, and W. Liu, "The effect of annealing treatment on microstructure and properties of TiN films prepared by unbalanced magnetron sputtering," *Journal of alloys and compounds*, vol. 496, no. 1-2, pp. 695–698, 2010.

[169] F.-H. Lu and H.-Y. Chen, "XPS analyses of TiN films on Cu substrates after annealing in the controlled atmosphere," *Thin Solid Films*, vol. 355, pp. 374–379, 1999.

[170] J. Wang, W. Liu, and T. Mei, "The effect of thermal treatment on the electrical properties of titanium nitride thin films by filtered arc plasma method," *Ceramics international*, vol. 30, no. 7, pp. 1921–1924, 2004.

[171] J.-H. Huang, K.-J. Yu, P. Sit, and G.-P. Yu, "Heat treatment of nanocrystalline TiN films deposited by unbalanced magnetron sputtering," *Surface and Coatings Technology*, vol. 200, no. 14-15, pp. 4291–4299, 2006.

[172] A. Achour, M. Chaker, H. Achour, A. Arman, M. Islam, M. Mardani, M. Boujtita, L. Le Brizoual, M. Djouadi, and T. Brousse, "Role of nitrogen doping at the surface of titanium nitride thin films towards capacitive charge storage enhancement," *Journal of Power Sources*, vol. 359, pp. 349–354, 2017.

[173] A. Trenczek-Zajac, M. Radecka, K. Zakrzewska, A. Brudnik, E. Kusior, S. Bourgeois, M. M. de Lucas, and L. Imhoff, "Structural and electrical properties of magnetron sputtered Ti(ON) thin films: the case of TiN doped in situ with oxygen," *Journal of Power Sources*, vol. 194, no. 1, pp. 93–103, 2009.

[174] R. Dhanaraj, S. Mohamed, M. Kamruddin, K. Kaviyarasu, and P. Manojkumar, "Structural properties of TiN thin films prepared by RF reactive magnetron sputtering," *Materials Today: Proceedings*, 2020.

[175] W. Spengler and R. Kaiser, "First and second order Raman scattering in transition metal compounds," *Solid State Communications*, vol. 18, no. 7, pp. 881–884, 1976.

[176] W. Spengler, R. Kaiser, A. Christensen, and G. Müller-Vogt, "Raman scattering, superconductivity, and phonon density of states of stoichiometric and nonstoichiometric TiN," *physical review b*, vol. 17, no. 3, p. 1095, 1978.

[177] Z. Ding, B. Yao, L. Qiu, and T. Lv, "Raman scattering investigation of nanocrystalline δ-TiNx synthesized by solid-state reaction," *Journal of alloys and compounds*, vol. 421, no. 1-2, pp. 247–251, 2006.

[178] P. Padmavathy, R. Ananthakumar, B. Subramanian, C. Ravidhas, and M. Jayachandran, "Structural and electrochemical impedance spectroscopic studies on reactive magnetron sputtered titanium oxynitride (TiON) thin films," *Journal of Applied Electrochemistry*, vol. 41, no. 6, p. 751, 2011.

[179] R. R. M. d. Sousa, F. O. d. Araújo, T. H. d. C. Costa, I. O. Nascimento, F. E. P. Santos, C. Alves Júnior, and M. C. Feitor, "Thin TiN and TiO2 film deposition in glass samples by cathodic cage," *Materials Research*, vol. 18, no. 2, pp. 347–352, 2015.

[180] M. Radecka, E. Pamula, A. Trenczek-Zajac, K. Zakrzewska, A. Brudnik, E. Kusior, N.-T. Kim-Ngan, and A. Balogh, "Chemical composition, crystallographic structure and impedance spectroscopy of titanium oxynitride TiNxOy thin films," *Solid State Ionics*, vol. 192, no. 1, pp. 693–698, 2011.

[181] C. Ernsberger, J. Nickerson, T. Smith, A. Miller, and D. Banks, "Low temperature oxidation behavior of reactively sputtered TiN by X-ray photoelectron spectroscopy and contact resistance measurements," *Journal of Vacuum Science & Technology A: Vacuum, Surfaces, and Films*, vol. 4, no. 6, pp. 2784–2788, 1986.

[182] I. Milošev, H.-H. Strehblow, and B. Navinšek, "Comparison of TiN, ZrN and CrN hard nitride coatings: Electrochemical and thermal oxidation," *Thin solid films*, vol. 303, no. 1-2, pp. 246–254, 1997.

[183] J. Li, L. Gao, J. Sun, Q. Zhang, J. Guo, and D. Yan, "Synthesis of nanocrystalline titanium nitride powders by direct nitridation of titanium oxide," *Journal of the American Ceramic Society*, vol. 84, no. 12, pp. 3045–3047, 2001.

[184] J. Tavares, S. Coulombe, and J. Meunier, "Synthesis of cubic-structured monocrystalline titanium nitride nanoparticles by means of a dual plasma process," *Journal of Physics D: Applied Physics*, vol. 42, no. 10, p. 102001, 2009.

[185] S. M. Kumar, K. Murugan, S. Chandrasekhar, N. Hebalkar, M. Krishna, B. Satyanarayana, and G. Madras, "Synthesis and characterization of nano silicon and titanium nitride powders using atmospheric microwave plasma technique," *Journal of Chemical Sciences*, vol. 124, no. 3, pp. 557–563, 2012.

[186] N. Takada, T. Sasaki, and K. Sasaki, "Synthesis of crystalline TiN and Si particles by laser ablation in liquid nitrogen," *Applied Physics A*, vol. 93, no. 4, pp. 833–836, 2008.

[187] U. Guler, S. Suslov, A. V. Kildishev, A. Boltasseva, and V. M. Shalaev, "Colloidal plasmonic titanium nitride nanoparticles: properties and applications," *Nanophotonics*, vol. 4, no. 3, pp. 269–276, 2015.

[188] S. Yick, A. Murdock, P. Martin, D. Kennedy, T. Maschmeyer, and A. Bendavid, "Tuning the plasmonic response of TiN nanoparticles synthesised by the transferred arc plasma technique," *Nanoscale*, vol. 10, no. 16, pp. 7566–7574, 2018.

[189] A. J. Alvarez Barragan, *Nanomaterials for Energy Applications: From Photovoltaics to Plasmonic Catalysis*. PhD thesis, UC Riverside, 2019.

[190] N. Kaisar, Y.-T. Huang, S. Jou, H.-F. Kuo, B.-R. Huang, C.-C. Chen, Y.-F. Hsieh, and Y.-C. Chung, "Surface-enhanced Raman scattering substrates of flat and wrinkly titanium nitride thin films by sputter deposition," *Surface and Coatings Technology*, vol. 337, pp. 434–438, 2018.

[191] Z. Dong, H. Wei, Y. Chen, R. Wang, J. Zhao, J. Lin, J. Bu, Y. Wei, Y. Cui, and Y. Yu, "Surface enhanced Raman scattering activity of TiN thin film prepared via nitridation of sol-gel derived TiO2 film," in *AOPC 2015: Advanced Display Technology; and Micro/Nano Optical Imaging Technologies and Applications*, vol. 9672, p. 967209, International Society for Optics and Photonics, 2015.

[192] F. Liu, X. Yang, D. Dang, and X. Tian, "Engineering of hierarchical and three-dimensional architectures constructed by titanium nitride nanowire assemblies for efficient electrocatalysis," *ChemElectroChem*, vol. 6, no. 8, pp. 2208–2214, 2019.

[193] S. Gbordzoe, R. Kotoka, E. Craven, D. Kumar, F. Wu, and J. Narayan, "Effect of substrate temperature on the microstructural properties of titanium nitride nanowires grown by pulsed laser deposition," *Journal of Applied Physics*, vol. 116, no. 6, p. 064310, 2014.

[194] A. Perego, G. Giuffredi, P. Mazzolini, M. Colombo, R. Brescia, M. Prato, D. C. Sabarirajan, I. V. Zenyuk, F. Bossola, V. Dal Santo, *et al.*, "Hierarchical TiN nanostructured thin film electrode for highly stable PEM fuel cells," *ACS Applied Energy Materials*, vol. 2, no. 3, pp. 1911–1922, 2019.

[195] C. Xu, G. Qiu, S. P. Ng, and C.-M. L. Wu, "Nanostructured titanium nitride for highly sensitive localized surface plasmon resonance biosensing," *Ceramics International*, 2020.

[196] F. Sauvage, F. Di Fonzo, A. Li Bassi, C. S. Casari, V. Russo, G. Divitini, C. Ducati, C. E. Bottani, P. Comte, and M. Graetzel, "Hierarchical TiO2 photoanode for dye-sensitized solar cells," *Nano letters*, vol. 10, no. 7, pp. 2562–2567, 2010.

[197] F. Di Fonzo, C. S. Casari, V. Russo, M. F. Brunella, A. Li Bassi, and C. E. Bottani, "Hierarchically organized nanostructured TiO2 for photocatalysis applications," *Nanotechnology*, vol. 20, no. 1, p. 015604, 2008.

[198] A. BROGNARA, "Integration of plasmonic Au nanoparticles in nanostructured TiO2 films for surface enhanced raman scattering," 2018.

[199] C. MANCARELLA, "Development of plasmonic gold nanostructures with tunable optical and electrical properties," 2019.

[200] F. GAETANI, "Development of tantalum-doped titanium oxide nanostructures for plasmonic applications," 2019.

[201] S. GARATTONI, "Synthesis of titanium nitride thin films with tunable optical and electrical properties," 2019.

[202] D. Chrisey and G. Hubler, *Pulsed Laser Deposition of Thin Films*. Wiley, 1994.

[203] R. Eason, *Pulsed Laser Deposition of Thin Films: Applications-Led Growth of Functional Materials*. John Wiley & Sons, 2007.

[204] C. S. Casari and A. Li Bassi, *Advances in Laser and Optics Research*, vol. 7. Nova Science Publishers, 2011.

[205] J. Tauc, R. Grigorovici, and A. Vancu, "Optical properties and electronic structure of amorphous germanium," *physica status solidi (b)*, vol. 15, no. 2, pp. 627–637, 1966.

[206] D. B. Buchholz, J. Liu, T. J. Marks, M. Zhang, and R. P. Chang, "Control and characterization of the structural, electrical, and optical properties of amorphous zinc- indium- tin oxide thin films," *ACS applied materials & interfaces*, vol. 1, no. 10, pp. 2147–2153, 2009.

[207] V. der Pauw, "A method of measuring specific resistivity and Hall effect of discs of arbitrary shape," *Philips Res. Rep*, vol. 13, no. 1, pp. 1–9, 1958.

[208] J. Lindemuth, *Hall Effect Measurement Handbook - A Fundamental Tool for Semiconductor Material Characterization*. 2020.

[209] B. L. Cushing, V. L. Kolesnichenko, and C. J. O'connor, "Recent advances in the liquid-phase syntheses of inorganic nanoparticles," *Chemical reviews*, vol. 104, no. 9, pp. 3893–3946, 2004.

[210] G. Valverde-Aguilar, J. García-Macedo, V. Rentería-Tapia, and M. Aguilar-Franco, "Photoconductivity studies on amorphous and crystalline tio 2 films doped with gold nanoparticles," *Applied Physics A*, vol. 103, no. 3, pp. 659–663, 2011.

[211] J. Qi, X. Dang, P. T. Hammond, and A. M. Belcher, "Highly efficient plasmon-enhanced dye-sensitized solar cells through metal@oxide core–shell nanostructure," *ACS nano*, vol. 5, no. 9, pp. 7108–7116, 2011.

[212] L. Passoni, F. Ghods, P. Docampo, A. Abrusci, J. Marti-Rujas, M. Ghidelli, G. Divitini, C. Ducati, M. Binda, S. Guarnera, *et al.*, "Hyperbranched quasi-1D nanostructures for solid-state dye-sensitized solar cells," *ACS nano*, vol. 7, no. 11, pp. 10023–10031, 2013.

[213] R. Matarrese, I. Nova, A. Li Bassi, C. S. Casari, and V. Russo, "Hierarchical nanostructured TiO2 films prepared by reactive pulsed laser deposition for photoelectrochemical water splitting," 2014.

[214] B. I. Kharisov, O. V. Kharissova, B. O. García, Y. P. Méndez, and I. G. de la Fuente, "State of the art of nanoforest structures and their applications," *RSC advances*, vol. 5, no. 128, pp. 105507–105523, 2015.

[215] M. Fusi, E. Maccallini, T. Caruso, C. S. Casari, A. Li Bassi, C. E. Bottani, P. Rudolf, K. Prince, and R. Agostino, "Surface electronic and structural properties of nanostructured titanium oxide grown by pulsed laser deposition," *Surface Science*, vol. 605, no. 3-4, pp. 333–340, 2011.

[216] G. Divitini, O. Stenzel, A. Ghadirzadeh, S. Guarnera, V. Russo, C. S. Casari, A. Li Bassi, A. Petrozza, F. Di Fonzo, V. Schmidt, *et al.*, "Nanoscale analysis of a hierarchical hybrid solar cell in 3D," *Advanced functional materials*, vol. 24, no. 20, pp. 3043–3050, 2014.

[217] L. Mascaretti, S. Ferrulli, P. Mazzolini, C. S. Casari, V. Russo, R. Matarrese, I. Nova, G. Terraneo, N. Liu, P. Schmuki, *et al.*, "Hydrogen-treated hierarchical titanium oxide nanostructures for photoelectrochemical water splitting," *Solar Energy Materials and Solar Cells*, vol. 169, pp. 19–27, 2017.

[218] B. R. Bricchi, M. Ghidelli, L. Mascaretti, A. Zapelli, V. Russo, C. S. Casari, G. Terraneo, I. Alessandri, C. Ducati, and A. L. Bassi, "Integration of plasmonic Au nanoparticles in TiO2 hierarchical structures in a single-step pulsed laser co-deposition," *Materials & Design*, vol. 156, pp. 311–319, 2018.

[219] R. Matarrese, I. Nova, A. Li Bassi, C. S. Casari, V. Russo, and S. Palmas, "Preparation and optimization of TiO2 photoanodes fabricated by pulsed laser deposition for photoelectrochemical water splitting," *Journal of Solid State Electrochemistry*, vol. 21, no. 11, pp. 3139–3154, 2017.

[220] M. Ghidelli, L. Mascaretti, B. R. Bricchi, A. Zapelli, V. Russo, C. S. Casari, and A. Li Bassi, "Engineering plasmonic nanostructured surfaces by pulsed laser deposition," *Applied Surface Science*, vol. 434, pp. 1064–1073, 2018.

[221] J. Borges, M. Rodrigues, T. Kubart, S. Kumar, K. Leifer, M. Evaristo, A. Cavaleiro, M. Apreutesei, R. Pereira, M. Vasilevskiy, *et al.*, "Thin films composed of gold nanoparticles dispersed in a dielectric matrix: The influence of the host matrix on the optical and mechanical responses," *Thin Solid Films*, vol. 596, pp. 8–17, 2015.

[222] S. C. Parker and C. T. Campbell, "Kinetic model for sintering of supported metal particles with improved size-dependent energetics and applications to Au on TiO2 (110)," *Physical Review B*, vol. 75, no. 3, p. 035430, 2007.

[223] S. Moldovan, L. Roiban, D. Georgescu, L. Baia, and O. Ersen, "Thermal evolution of silver nanoparticles onto porous TiO2 nanostructures," *Catalysis Today*, vol. 284, pp. 221–228, 2017.

[224] A. Chichagov, "Information-calculating system on crystal structure data of minerals (mincryst)," in *Materials Science Forum*, vol. 166, pp. 193–198, Trans Tech Publ, 1994.

[225] D. M. Moore, R. C. Reynolds Jr, *et al.*, *X-ray Diffraction and the Identification and Analysis of Clay Minerals*. Oxford University Press (OUP), 1989.

[226] J. Manifacier, J. Gasiot, and J. Fillard, "A simple method for the determination of the optical constants n, k and the thickness of a weakly absorbing thin film," *Journal of Physics E: Scientific Instruments*, vol. 9, no. 11, p. 1002, 1976.

[227] M. Torrell, R. Kabir, L. Cunha, M. Vasilevskiy, F. Vaz, A. Cavaleiro, E. Alves, and N. Barradas, "Tuning of the surface plasmon resonance in TiO2/Au thin films grown by magnetron sputtering: the effect of thermal annealing," *Journal of Applied Physics*, vol. 109, no. 7, p. 074310, 2011.

[228] M. Torrell, L. Cunha, M. R. Kabir, A. Cavaleiro, M. Vasilevskiy, and F. Vaz, "Nanoscale color control of TiO2 films with embedded Au nanoparticles," *Materials Letters*, vol. 64, no. 23, pp. 2624–2626, 2010.

[229] S. Al-Qaradawi and S. R. Salman, "Photocatalytic degradation of methyl orange as a model compound," *Journal of Photochemistry and photobiology A: Chemistry*, vol. 148, no. 1-3, pp. 161–168, 2002.

[230] J. Gjipalaj and I. Alessandri, "Easy recovery, mechanical stability, enhanced adsorption capacity and recyclability of alginate-based TiO2 macrobead photocatalysts for water treatment," *Journal of environmental chemical engineering*, vol. 5, no. 2, pp. 1763–1770, 2017.

[231] K. Parida, N. Sahu, N. Biswal, B. Naik, and A. Pradhan, "Preparation, characterization, and photocatalytic activity of sulfate-modified titania for degradation of methyl orange under visible light," *Journal of colloid and interface science*, vol. 318, no. 2, pp. 231–237, 2008.

[232] L.-N. Ho, S.-A. Ong, H. Osman, and F.-M. Chong, "Enhanced photocatalytic activity of fish scale loaded TiO2 composites under solar light irradiation," *Journal of Environmental Sciences*, vol. 24, no. 6, pp. 1142–1148, 2012.

[233] K. Azad and P. Gajanan, "Photodegradation of methyl orange in aqueous solution by the visible light active Co: La: TiO2 nanocomposite," *Chem. Sci. J*, vol. 164, 2017.

[234] X. Pan, M.-Q. Yang, X. Fu, N. Zhang, and Y.-J. Xu, "Defective TiO2 with oxygen vacancies: synthesis, properties and photocatalytic applications," *Nanoscale*, vol. 5, no. 9, pp. 3601–3614, 2013.

[235] M. Tsuji, K. Matsuda, M. Tanaka, S. Kuboyama, K. Uto, N. Wada, H. Kawazumi, T. Tsuji, H. Ago, and J.-i. Hayashi, "Enhanced photocatalytic degradation of methyl orange by Au/TiO2 nanoparticles under neutral and acidic solutions," *ChemistrySelect*, vol. 3, no. 5, pp. 1432–1438, 2018.

[236] G. L. Chiarello, E. Selli, and L. Forni, "Photocatalytic hydrogen production over flame spray pyrolysis-synthesised TiO2 and Au/TiO2," *Applied Catalysis B: Environmental*, vol. 84, no. 1-2, pp. 332–339, 2008.

[237] M. D. Porter, T. B. Bright, D. L. Allara, and C. E. Chidsey, "Spontaneously organized molecular assemblies. 4. structural characterization of n-alkyl thiol monolayers on gold by optical ellipsometry, infrared spectroscopy, and electrochemistry," *Journal of the American Chemical Society*, vol. 109, no. 12, pp. 3559–3568, 1987.

[238] R. Matarrese, M. Mascia, A. Vacca, L. Mais, E. M. Usai, M. Ghidelli, L. Mascaretti, B. R. Bricchi, V. Russo, C. S. Casari, *et al.*, "Integrated Au/TiO2 nanostructured photoanodes for photoelectrochemical organics degradation," *Catalysts*, vol. 9, no. 4, p. 340, 2019.

[239] J. Zhao, M. Milanova, M. M. Warmoeskerken, and V. Dutschk, "Surface modification of tio2 nanoparticles with silane coupling agents," *Colloids and surfaces A: Physicochemical and engineering aspects*, vol. 413, pp. 273–279, 2012.

[240] L. ORNAGO, "Synthesis of tantalum-doped titanium oxide thin films: a bridge to infrared plasmonics," 2018.

[241] S. Seeger, K. Ellmer, M. Weise, D. Gogova, D. Abou-Ras, and R. Mientus, "Reactive magnetron sputtering of Nb-doped TiO2 films: relationships between structure, composition and electrical properties," *Thin Solid Films*, vol. 605, pp. 44–52, 2016.

[242] L. Mascaretti, V. Russo, G. Zoppellaro, A. Lucotti, C. S. Casari, S. Kment, A. Naldoni, and A. Li Bassi, "Excitation wavelength-and medium-dependent photoluminescence of reduced nanostructured TiO2 films," *The Journal of Physical Chemistry C*, vol. 123, no. 17, pp. 11292–11303, 2019.

[243] V. Pore, M. Ritala, M. Leskelaa, T. Saukkonen, and M. Jarn, "Explosive crystallization in atomic layer deposited mixed titanium oxides," *Crystal Growth and Design*, vol. 9, no. 7, pp. 2974–2978, 2009.

[244] E. áToby Kelsey *et al.*, "Atomistic simulation of the surface structure of the TiO2 polymorphs rutileand anatase," *Journal of Materials Chemistry*, vol. 7, no. 3, pp. 563–568, 1997.

[245] C. Yang, Y. Hirose, S. Nakao, and T. Hasegawa, "c-axis-oriented growth of anatase TiO2 thin films on glass substrate with SrTiO3/TiN template," *Journal of crystal growth*, vol. 376, pp. 66–69, 2013.

[246] G. Pawley, "Unit-cell refinement from powder diffraction scans," *Journal of Applied Crystallography*, vol. 14, no. 6, pp. 357–361, 1981.

[247] U. Balachandran and N. Eror, "Raman spectra of titanium dioxide," *Journal of Solid State Chemistry*, vol. 42, no. 3, pp. 276–282, 1982.

[248] A. Li Bassi, D. Cattaneo, V. Russo, C. E. Bottani, E. Barborini, T. Mazza, P. Piseri, P. Milani, F. Ernst, K. Wegner, *et al.*, "Raman spectroscopy characterization of titania nanoparticles produced by flame pyrolysis: the influence of size and stoichiometry," *Journal of Applied Physics*, vol. 98, no. 7, p. 074305, 2005.

[249] P. Deák, B. Aradi, and T. Frauenheim, "Quantitative theory of the oxygen vacancy and carrier self-trapping in bulk TiO2," *Physical Review B*, vol. 86, no. 19, p. 195206, 2012.

[250] B.-Z. Dong, G.-J. Fang, J.-F. Wang, W.-J. Guan, and X.-Z. Zhao, "Effect of thickness on structural, electrical, and optical properties of ZnO:Al films deposited by pulsed laser deposition," *Journal of Applied Physics*, vol. 101, no. 3, p. 033713, 2007.

[251] "Model for thickness dependence of mobility and concentration in highly conductive zinc oxide," *Optical Engineering*, vol. 52, no. 3, 2013.

[252] D. C. Look, "Mobility vs thickness in n+-ZnO films: Effects of substrates and buffer layers," *Materials Science in Semiconductor Processing*, vol. 69, pp. 2–8, 2017.

[253] V. D. Bruggeman, "Berechnung verschiedener physikalischer konstanten von heterogenen substanzen. i. dielektrizitätskonstanten und leitfähigkeiten der mischkörper aus isotropen substanzen," *Annalen der physik*, vol. 416, no. 7, pp. 636–664, 1935.

[254] B. Johs, C. Herzinger, J. Dinan, A. Cornfeld, and J. Benson, "Development of a parametric optical constant model for Hg1-xCdxTe for control of composition by spectroscopic ellipsometry during MBE growth," *Thin Solid Films*, vol. 313, pp. 137–142, 1998.

[255] G. Jellison Jr, L. Boatner, J. Budai, B.-S. Jeong, and D. Norton, "Spectroscopic ellipsometry of thin film and bulk anatase (TiO2)," *Journal of Applied Physics*, vol. 93, no. 12, pp. 9537–9541, 2003.

[256] S. Tanemura, L. Miao, P. Jin, K. Kaneko, A. Terai, and N. Nabatova-Gabain, "Optical properties of polycrystalline and epitaxial anatase and rutile TiO2 thin films by rf magnetron sputtering," *Applied Surface Science*, vol. 212, pp. 654–660, 2003.

[257] N. Martin, C. Rousselot, D. Rondot, F. Palmino, and R. Mercier, "Microstructure modification of amorphous titanium oxide thin films during annealing treatment," *Thin solid films*, vol. 300, no. 1-2, pp. 113–121, 1997.

[258] L. Sun and P. Hou, "Spectroscopic ellipsometry study on e-beam deposited titanium dioxide films," *Thin Solid Films*, vol. 455, pp. 525–529, 2004.

[259] A. Manole, M. Dobromir, M. Girtan, R. Mallet, G. Rusu, and D. Luca, "Optical properties of Nb-doped TiO2 thin films prepared by sol–gel method," *Ceramics International*, vol. 39, no. 5, pp. 4771–4776, 2013.

[260] Y. R. Park and K. J. Kim, "Structural and optical properties of rutile and anatase TiO2 thin films: Effects of co doping," *Thin Solid Films*, vol. 484, no. 1-2, pp. 34–38, 2005.

[261] W. Zhao, L. He, X. Feng, C. Luan, and J. Ma, "Structural, electrical and optical properties of epitaxial Ta-doped titania films by MOCVD," *CrystEngComm*, vol. 20, no. 36, pp. 5395–5401, 2018.

[262] H. Poelman, H. Tomaszewski, D. Poelman, D. Depla, and R. De Gryse, "Effect of the oxygen deficiency of ceramic TiO2-x targets on the deposition of TiO2 thin films by DC magnetron sputtering," *Surface and Interface Analysis: An International Journal devoted to the development and application of techniques for the analysis of surfaces, interfaces and thin films*, vol. 36, no. 8, pp. 1167–1170, 2004.

[263] A. Brudnik, H. Czternastek, K. Zakrzewska, and M. Jachimowski, "Plasma-emission-controlled dc magnetron sputtering of tio2-x thin films," *Thin Solid Films*, vol. 199, no. 1, pp. 45–58, 1991.

[264] B. Varga, "Coupling of plasmons to polar phonons in degenerate semiconductors," *Physical Review*, vol. 137, no. 6A, p. A1896, 1965.

[265] A. Mooradian and G. Wright, "Observation of the interaction of plasmons with longitudinal optical phonons in gaas," *Physical Review Letters*, vol. 16, no. 22, p. 999, 1966.

[266] M. Schubert, *Infrared ellipsometry on semiconductor layer structures: phonons, plasmons, and polaritons*, vol. 209. Springer Science & Business Media, 2004.

[267] M. Bass, O. S. of America Staff, O. S. of America, E. Van Stryland, W. Wolfe, and D. Williams, *Handbook of Optics: Fundamentals, techniques, and design*. Handbook of Optics, McGraw-Hill, 1995.

[268] A. A. Ziabari and S. Rozati, "Carrier transport and bandgap shift in n-type degenerate ZnO thin films: The effect of band edge nonparabolicity," *Physica B: Condensed Matter*, vol. 407, no. 23, pp. 4512–4517, 2012.

[269] A. Jain, P. Sagar, and R. Mehra, "Band gap widening and narrowing in moderately and heavily doped n-ZnO films," *Solid-state electronics*, vol. 50, no. 7-8, pp. 1420–1424, 2006.

[270] R. Gonzalez, R. Zallen, and H. Berger, "Infrared reflectivity and lattice fundamentals in anatase TiO2s," *Physical Review B*, vol. 55, no. 11, p. 7014, 1997.

[271] M. Eldlio, F. Che, and M. Cada, "Drude-Lorentz model of semiconductor optical plasmons," in *IAENG Transactions on Engineering Technologies*, pp. 41–49, Springer, 2014.

[272] M. MAZZA, "Synthesis and optical properties of titanium nitride nanostructured thin films," 2020.

[273] W. Spengler, R. Kaiser, and H. Bilz, "Resonant Raman scattering in a superconducting transition metal compound TiN," *Solid State Communications*, vol. 17, no. 1, pp. 19–22, 1975.

[274] A. Achour, R. L. Porto, M.-A. Soussou, M. Islam, M. Boujtita, K. A. Aissa, L. Le Brizoual, A. Djouadi, and T. Brousse, "Titanium nitride films for micro-supercapacitors: effect of surface chemistry and film morphology on the capacitance," *Journal of Power Sources*, vol. 300, pp. 525–532, 2015.

[275] E. P. Quijorna, V. T. Costa, F. Agulló-Rueda, P. H. Fernández, A. Climent, F. Rossi, and M. M. Silván, "TiNxOy/TiN dielectric contrasts obtained by ion implantation of; structural, optical and electrical properties," *Journal of Physics D: Applied Physics*, vol. 44, no. 23, p. 235501, 2011.

[276] A. Bittar, D. Cochrane, S. Caughley, and I. Vickeridge, "Study of TiO x N y thin film selective surfaces produced by ion assisted deposition," *Journal of Vacuum Science & Technology A: Vacuum, Surfaces, and Films*, vol. 15, no. 2, pp. 223–229, 1997.

[277] J. Je, D. Noh, H. Kim, and K. Liang, "Preferred orientation of TiN films studied by a real time synchrotron x-ray scattering," *Journal of applied physics*, vol. 81, no. 9, pp. 6126–6133, 1997.

[278] U. Oh and J. H. Je, "Effects of strain energy on the preferred orientation of TiN thin films," *Journal of applied physics*, vol. 74, no. 3, pp. 1692–1696, 1993.

[279] G. Abadias and Y. Tse, "Diffraction stress analysis in fiber-textured TiN thin films grown by ion-beam sputtering: Application to (001) and mixed (001)+(111) texture," *Journal of applied physics*, vol. 95, no. 5, pp. 2414–2428, 2004.

[280] S. Mahieu, D. Depla, and R. De Gryse, "Modelling the growth of transition metal nitrides," in *Journal of Physics: Conference Series*, vol. 100, p. 082003, IOP Publishing, 2008.

[281] M. Kumar, N. Umezawa, S. Ishii, and T. Nagao, "Examining the performance of refractory conductive ceramics as plasmonic materials: a theoretical approach," *ACS Photonics*, vol. 3, no. 1, pp. 43–50, 2016.

[282] P. Patsalas and S. Logothetidis, "Optical, electronic, and transport properties of nanocrystalline titanium nitride thin films," *Journal of Applied Physics*, vol. 90, no. 9, pp. 4725–4734, 2001.

[283] J. Yan, P. Liu, C. Ma, Z. Lin, and G. Yang, "Plasmonic near-touching titanium oxide nanoparticles to realize solar energy harvesting and effective local heating," *Nanoscale*, vol. 8, no. 16, pp. 8826–8838, 2016.

[284] E. Prodan, C. Radloff, N. J. Halas, and P. Nordlander, "A hybridization model for the plasmon response of complex nanostructures," *science*, vol. 302, no. 5644, pp. 419–422, 2003.

[285] J. B. Lassiter, J. Aizpurua, L. I. Hernandez, D. W. Brandl, I. Romero, S. Lal, J. H. Hafner, P. Nordlander, and N. J. Halas, "Close encounters between two nanoshells," *Nano letters*, vol. 8, no. 4, pp. 1212–1218, 2008.

[286] Z. Xu, Y. Yao, E. P. Brueckner, L. Li, J. Jiang, R. G. Nuzzo, and G. L. Liu, "Black silicon solar thin-film microcells integrating top nanocone structures for broadband and omnidirectional light-trapping," *Nanotechnology*, vol. 25, no. 30, p. 305301, 2014.

[287] H. Gao, W. Peng, W. Cui, S. Chu, L. Yu, and X. Yang, "Ultraviolet to near infrared titanium nitride broadband plasmonic absorber," *Optical Materials*, vol. 97, p. 109377, 2019.

[288] G. Baffou, F. Cichos, and R. Quidant, "Applications and challenges of thermoplasmonics," *Nature Materials*, pp. 1–13, 2020.

[289] M. Pons, R. Boichot, N. Coudurier, A. Claudel, E. Blanquet, S. Lay, F. Mercier, and D. Pique, "High temperature chemical vapor deposition of aluminum nitride, growth and evaluation," *Surface and Coatings Technology*, vol. 230, pp. 111–118, 2013.

[290] M. Mahjouri-Samani, M. Tian, A. A. Puretzky, M. Chi, K. Wang, G. Duscher, C. M. Rouleau, G. Eres, M. Yoon, J. Lasseter, *et al.*, "Nonequilibrium synthesis of TiO2 nanoparticle building blocks for crystal growth by sequential attachment in pulsed laser deposition," *Nano Letters*, vol. 17, no. 8, pp. 4624–4633, 2017.

[291] G. Giuffredi, A. Mezzetti, A. Perego, P. Mazzolini, M. Prato, F. Fumagalli, Y.-C. Lin, C. Liu, I. N. Ivanov, A. Belianinov, *et al.*, "Non-equilibrium synthesis of highly active nanostructured, oxygen-incorporated amorphous molybdenum sulfide her electrocatalyst," *Small*, p. 2004047, 2020.

[292] R. Wood, J. Leboeuf, K.-R. Chen, D. Geohegan, and A. Puretzky, "Dynamics of plume propagation, splitting, and nanoparticle formation during pulsed-laser ablation," *Applied surface science*, vol. 127, pp. 151–158, 1998.

[293] D. B. Geohegan, "Time-resolved diagnostics of excimer laser-generated ablation plasmas used for pulsed laser deposition," in *Excimer Lasers*, pp. 165–185, Springer, 1994.

[294] Y. Okada and Y. Tokumaru, "Precise determination of lattice parameter and thermal expansion coefficient of silicon between 300 and 1500 K," *Journal of applied physics*, vol. 56, no. 2, pp. 314–320, 1984.

[295] P. Patsalas, C. Gravalidis, and S. Logothetidis, "Surface kinetics and subplantation phenomena affecting the texture, morphology, stress, and growth evolution of titanium nitride films," *Journal of applied physics*, vol. 96, no. 11, pp. 6234–6246, 2004.

[296] G. Martinez, V. Shutthanandan, S. Thevuthasan, J. Chessa, and C. Ramana, "Effect of thickness on the structure, composition and properties of titanium nitride nano-coatings," *Ceramics International*, vol. 40, no. 4, pp. 5757–5764, 2014.

[297] P. Patsalas and S. Logothetidis, "Interface properties and structural evolution of TiN/Si and TiN/GaN heterostructures," *Journal of applied physics*, vol. 93, no. 2, pp. 989–998, 2003.

[298] A. Kavitha, R. Kannan, P. S. Reddy, and S. Rajashabala, "The effect of annealing on the structural, optical and electrical properties of titanium nitride (TiN) thin films prepared by DC magnetron sputtering with supported discharge," *Journal of Materials Science: Materials in Electronics*, vol. 27, no. 10, pp. 10427–10434, 2016.

[299] A. Torgovkin, S. Chaudhuri, A. Ruhtinas, M. Lahtinen, T. Sajavaara, and I. Maasilta, "High quality superconducting titanium nitride thin film growth using infrared pulsed laser deposition," *Superconductor Science and Technology*, vol. 31, no. 5, p. 055017, 2018.

[300] B. Johansson, J.-E. Sundgren, J. Greene, A. Rockett, and S. Barnett, "Growth and properties of single crystal TiN films deposited by reactive magnetron sputtering," *Journal of Vacuum Science & Technology A: Vacuum, Surfaces, and Films*, vol. 3, no. 2, pp. 303–307, 1985.

[301] X. Yang, W. Liu, M. De Bastiani, T. Allen, J. Kang, H. Xu, E. Aydin, L. Xu, Q. Bi, H. Dang, *et al.*, "Dual-function electron-conductive, hole-blocking titanium nitride contacts for efficient silicon solar cells," *Joule*, vol. 3, no. 5, pp. 1314–1327, 2019.

[302] J. Yu, P. Phang, C. Samundsett, R. Basnet, G. P. Neupane, X. Yang, D. MacDonald, Y. Wan, D. Yan, and J. Ye, "Titanium nitride electron-conductive contact for silicon solar cells by RF sputtering from a TiN target," *ACS Applied Materials & Interfaces*, 2020.

[303] H. G. Tompkins and J. N. Hilfiker, *Spectroscopic Ellipsometry: Practical Application to Thin Film Characterization*. Momentum Press, 2015.

[304] G. Jellison Jr and F. Modine, "Parameterization of the optical functions of amorphous materials in the interband region," *Applied Physics Letters*, vol. 69, no. 3, pp. 371–373, 1996.

[305] J. A. Briggs, G. V. Naik, Y. Zhao, T. A. Petach, K. Sahasrabuddhe, D. Goldhaber-Gordon, N. A. Melosh, and J. A. Dionne, "Temperature-dependent optical properties of titanium nitride," *Applied Physics Letters*, vol. 110, no. 10, p. 101901, 2017.

[306] J. Humlíček, A. Nebojsa, J. Hora, M. Stráský, J. Spousta, and T. Šikola, "Ellipsometry and transport studies of thin-film metal nitrides," *Thin Solid Films*, vol. 332, no. 1-2, pp. 25–29, 1998.

[307] E. Langereis, S. Heil, H. Knoops, W. Keuning, M. Van de Sanden, and W. Kessels, "In situ spectroscopic ellipsometry as a versatile tool for studying atomic layer deposition," *Journal of Physics D: Applied Physics*, vol. 42, no. 7, p. 073001, 2009.

[308] H. Van Bui, A. Y. Kovalgin, and R. A. Wolters, "On the difference between optically and electrically determined resistivity of ultra-thin titanium nitride films," *Applied surface science*, vol. 269, pp. 45–49, 2013.

[309] L. Zhang, S. Tong, H. Liu, Y. Li, and Z. Wang, "Effects of sputtering and assisting ions on the orientation of titanium nitride films fabricated by ion beam assisted sputtering deposition from metal target," *Materials Letters*, vol. 171, pp. 304–307, 2016.

[310] L.-a. Zhang, H.-n. Liu, X.-x. Suo, S. Tong, Y.-l. Li, Z.-t. Jiang, and Z. Wang, "Ion beam modification of plasmonic titanium nitride thin films," *Journal of Materials Science*, vol. 52, no. 11, pp. 6442–6448, 2017.

[311] E. Ribeiro, L. Rebouta, S. Carvalho, F. Vaz, G. Fuentes, R. Rodriguez, M. Zazpe, E. Alves, P. Goudeau, and J. Riviere, "Characterization of hard DC-sputtered Si-based TiN coatings: the effect of composition and ion bombardment," *Surface and Coatings Technology*, vol. 188, pp. 351–357, 2004.

[312] D. Shah, H. Reddy, N. Kinsey, V. M. Shalaev, and A. Boltasseva, "Optical properties of plasmonic ultrathin tin films," *Advanced Optical Materials*, vol. 5, no. 13, p. 1700065, 2017.